INTERNATIONAL DOCTORAL
SCHOOL OF THE USC

José
Paredes Pacheco

PhD Thesis

Development of a simulation platform for the evaluation of PET neuroimaging protocols in epilepsy

Santiago de Compostela, 2022

Doctoral Programme in Neuroscience and Clinical Psychology

TESIS DE DOCTORADO

DEVELOPMENT OF A SIMULATION PLATFORM FOR THE EVALUATION OF PET NEUROIMAGING PROTOCOLS IN EPILEPSY

José Paredes Pacheco

ESCUELA DE DOCTORADO INTERNACIONAL DE LA UNIVERSIDAD DE SANTIAGO DE COMPOSTELA

PROGRAMA DE DOCTORADO EN NEUROCIENCIA Y PSICOLOGÍA CLÍNICA

SANTIAGO DE COMPOSTELA / LUGO

2022

DECLARACIÓN DEL AUTOR/A DE LA TESIS

D./Dña. **José Paredes Pacheco**

Título da tese: **Development of a simulation platform for the evaluation of PET neuroimaging protocols in epilepsy**

Presento mi tesis, siguiendo el procedimiento adecuado al Reglamento y declaro que:

1) La tesis abarca los resultados de la elaboración de mi trabajo.
2) De ser el caso, en la tesis se hace referencia a las colaboraciones que tuvo este trabajo.
3) Confirmo que la tesis no incurre en ningún tipo de plagio de otros autores ni de trabajospresentados por mí para la obtención de otros títulos.
4) La tesis es la versión definitiva presentada para su defensa y coincide la versión impresa con lapresentada en formato electrónico.

Y me comprometo a presentar el Compromiso Documental de Supervisión en el caso que el original noesté depositado en la Escuela.

En **Santiago de Compostela, 20 de junio de 2022.**

Firma electrónica

AUTORIZACIÓN DEL DIRECTOR / TUTOR DE LA TESIS

Development of a simulation platform for the evaluation of PET neuroimaging protocols in epilepsy

D./Dª. Pablo Aguiar Fernández.....

D./Dª. Núria Roé Vellvé.....

INFORMA/N:

Que la presente tesis, se corresponde con el trabajo realizado por D/Dª. José Paredes Pacheco, bajo mi dirección/tutorización, y autorizo su presentación, considerando que reúne los requisitos exigidos en el Reglamento de Estudios de Doctorado de la USC, y que como director de esta no incurre en las causas de abstención establecidas en la Ley 40/2015.

De acuerdo con lo indicado en el Reglamento de Estudios de Doctorado, declara también que la presente tesis doctoral es idónea para ser defendida en base a la modalidad de Monográfica con reproducción de publicaciones, en los que la participación del doctorando/a fue decisiva para su elaboración y las publicaciones se ajustan al Plan de Investigación.

En Santiago de Compostela, 20 de junio de 2022

AGRADECIMIENTOS

Realizar una tesis doctoral no es un trabajo fácil y más a distancia y con la situación de pandemia que nos ha tocado vivir. Sin embargo, puedo decir que me siento muy orgulloso y feliz por el trabajo realizado, no solo por el aporte que hago a la comunidad científica con los trabajos desarrollados en esta tesis, sino también por haberlos realizado con el apoyo de muchas personas importantes que siempre han estado ahí para mí.

Agradecer a mis padres, hermana y tía Paqui por el amor, apoyo e interés que siempre han tenido por mí, por estar conmigo y por querer que sea feliz con lo que haga. También agradecerles por todo lo que día a día se han esforzado y se siguen esforzando para que hoy esté yo escribiendo esta tesis. Creo que nunca podré devolverles todo lo que me han dado.

Agradecer a mi pareja Rocío por su ayuda y estar a mi lado, sufrir y vivir conmigo cada pequeño avance que iba consiguiendo en la tesis. Desde que la tengo siempre ha sido un gran apoyo y, en particular, en el desarrollo de esta tesis. Con su ayuda y cariño siempre hace que cualquier carga sea menos pesada. La quiero mucho. También gracias a sus padres y hermano por preocuparse, ayudarme o escucharme siempre que ha hecho falta.

Agradecer a mi gran amigo y compañero de peripecias Fran, que ha estado desde mi paso por la universidad ahí, apoyándome y ayudándome, tanto en lo personal como en lo profesional. Espero tenerlo siempre cerca porque es una persona de las que se cruza uno pocas veces en la vida. También a mis compañeros de carrera Carlos y Karl, por los divertidos momentos que pasamos y porque sin ellos tampoco habría llegado hasta aquí.

Agradecer a los diferentes colaboradores de la Universidade de Santiago de Compostela, del Instituto de Investigación Sanitaria de Santiago de Compostela, del Centro de Investigaciones Médico-Sanitarias, de Qubiotech, del Hospital Clinic de Barcelona y de la Universidad de Hull por su contribución a mi trabajo y por contar conmigo para tantos otros.

Agradecer a la Universidade de Santiago de Compostela y a la Fundación General de la Universidad de Málaga por acogernos y ofrecer todo el soporte y facilidades necesarias para poder realizar esta tesis.

Agradecer a mis directores, Pablo y Núria, y a mi compañero Jesús por estar pendientes de mi trabajo y dedicar mucho de su tiempo y energía a que esta tesis llegara a buen puerto. Son un ejemplo de dedicación, esfuerzo y trabajo bien hecho que siempre tendré presente.

Finalmente agradecer a quien lea este trabajo por tomarse la molestia e interesarse por lo que aquí se desarrolla. Espero que le guste y le sea de gran utilidad.

Nos vemos en otro proyecto,

José

RESUMO

A tomografía por emisión de positrones (PET) é unha técnica de imaxe non invasiva que permite visualizar os cambios metabólicos no corpo dun suxeito mediante a inxección dunha molécula radiomarcada cun radioisótopo (radiofármaco), obtendo información funcional e molecular dos diferentes tecidos que o forman. O proceso de adquisición dunha imaxe PET consiste na inxección do radiofármaco, que se distribúe por todo o corpo do suxeito seguindo a vía metabólica que corresponde á molécula radiomarcada. O radioisótopo que forma parte do radiofármaco emite positróns que interactúan cos electróns do tecido para desintegrarse e xerar pares opostos de fotóns. Estes fotóns viaxan en forma de radiación gamma que atravesa os tecidos do suxeito para acabar saíndo do corpo e chegando ás paredes dos aneis que forman o escáner PET. Estes aneis están formados por bloques detectores de cristais centelleadores que reciben raios gamma e absorben toda ou parte da súa enerxía para xerar fotóns de luz visible. Estes fotóns de luz entran en contacto cun fotocátodo, provocando a emisión de electróns no interior dun tubo chamado tubo fotomultiplicador que é capaz de xerar un pulso eléctrico que é amplificado e posteriormente analizado para rexistrar a detección dun fotón. Cando se rexistran dous fotóns dentro dunha xanela de tempo, considérase que proceden da mesma aniquilación e cóntanse como un evento que se usa para xerar a imaxe PET e que se denomina coincidencia verdadeira. Non obstante, debido ás limitacións técnicas e especialmente debido a resolución temporal limitada dos distintos compoñentes do escáner PET, ademais destas coincidencias verdadeiras, tamén se detectan outros tipos de coincidencias, como coincidencias dispersas (un dos fotóns interaciona e cambia a súa dirección), coincidencias aleatorias (coincidencia formada por dous fotóns que non veñen da mesma aniquilación) e coincidencias múltiples (coincidencia formada por máis de dous fotóns), que poden degradar significativamente a imaxe PET (perda de contraste principalmente). Por este motivo, é necesario aplicar diferentes métodos de corrección para reducir o efecto destas coincidencias sobre os datos adquiridos. Despois disto, os datos corrixidos almacénanse en histogramas chamados sinogramas. Estes sinogramas utilízanse para recuperar a verdadeira distribución tridimensional do radiofármaco por todo o organismo mediante un proceso chamado reconstrución tomográfica. Segundo o método de reconstrución empregado, o estudo PET necesitará menos tempo para xerarse a cambio de ter unha calidade inferior (métodos analíticos) ou precisará máis tempo e recursos para reconstruílo, pero obtendo un resultado máis realista (métodos estatísticos).

Dentro do estudo do cerebro, as imaxes PET, xunto coa resonancia magnética (RM), xogan un papel fundamental no diagnóstico de diferentes enfermidades neurolóxicas, como pode ser a enfermidade na que se centra a presente tese de doutoramento, a epilepsia, xa que proporcionan información complementaria sobre os cambios experimentados no cerebro. A RM é considerada o tipo de imaxe por excelencia para o estudo das estruturas cerebrais, grazas ao seu alto contraste entre tecidos e á súa gran resolución espacial e temporal, que permite a diferenciación entre enfermidades neuropsicolóxicas. Do mesmo xeito, os estudos de PET cerebral que utilizan o radiofármaco 18F-fludesoxiglucosa (FDG) están moi presentes na rutina clínica, xa que permiten estudar os cambios no metabolismo celular in vivo asociados a casos de epilepsia, así como o diagnóstico precoz e diferencial entre enfermidades neurolóxicas. No campo da epilepsia, os estudos PET-FDG son unha indicación clínica aprobada para a detección de rexións hipometabólicas asociadas á presenza dun foco epileptoxénico. Localizar o foco é fundamental en pacientes con epilepsia resistente a tratamentos farmacolóxicos, xa que a resección cirúrxica de dito foco é a única opción terapéutica para estes pacientes. Os estudos PET-FDG en epilepsia son especialmente relevantes naqueles casos nos que o estudo estrutural mediante resonancia magnética non mostra ningunha lesión, polo que o PET-FDG convértese na única ferramenta capaz de propoñer unha localización do foco epileptoxénico. A avaliación das imaxes PET-FDG na rutina clínica realízana os especialistas en medicina nuclear a partir

dunha avaliación visual, achegando información cualitativa sobre o metabolismo cerebral e as rexións onde se produce un descenso, de forma complementaria á información morfolóxica que proporciona a RM. Non obstante, en moitas situacións isto non é suficiente para chegar a un diagnóstico preciso, xa que a natureza ou estadio de desenvolvemento da enfermidade, a escasa calidade dalgúns estudos PET ou os propios criterios do médico nuclear poden condicionar a detección e avaliación da enfermidade. Por este motivo, numerosos estudos suxiren o uso da análise cuantitativa nos estudos PET-FDG para complementar a análise visual e sacar o máximo proveito da imaxe, permitindo un mellor diagnóstico e detección. As directrices da Asociación Europea de Medicina Nuclear (EANM) xa recomendan realizar unha análise baseada nunha aproximación cuantitativa na rutina clínica. A pesar diso, a análise cuantitativa da PET cerebral aínda non está moi presente na rutina clínica debido principalmente a dous factores: non contar con bases de datos propias de persoas sans coas que comparar (cuestión esencial na cuantificación de imaxes), limitándose a utilizar bases de datos públicas que non se axustan totalmente ao datos adquiridos no centro (dependen do tipo e modelo de escáner); e máis importante, non contar con protocolos estandarizados para a adquisición, procesado e análise dos estudos de imaxe PET, xa que varían entre cada centro, fabricante ou software. En epilepsia existen estudos que, polo pequeno tamaño da súa lesión ou pola súa localización menos frecuente, dependen moito de empregar un método de análise cuantitativo para a súa correcta avaliación e, polo tanto, están moi influenciados polos protocolos considerados.

Para avanzar cara a unha maior estandarización nas cuestións anteriores é necesario o uso de maniquíes físicos de cerebro (phantoms en inglés). Estes maniquíes físicos permiten realizar estudos de PET cunha distribución do radiofármaco coñecida a priori e, polo tanto, validar diferentes protocolos de adquisición e procesamento utilizando estes valores como referencia (ground-truth). Porén, ao tratarse de modelos físicos, a súa configuración é moi limitada, tanto en xeometría como en materiais de fabricación, o que adoita dar lugar a imaxes PET do cerebro pouco realistas (formadas por figuras xeométricas en moitos casos). Ademais, a realización de estudos con maniquíes físicos son actividades laboriosas e lentas que en xeral supoñen unha importante exposición radioactiva para os técnicos que as realizan. Por iso, nos últimos anos comezou a cobrar forza o uso dos métodos de simulación de Monte Carlo (MC) como alternativa aos maniquíes físicos para xerar imaxes PET a partir de maniquíes dixitais do cerebro, tamén chamados mapas (moito máis flexibles para crear un mapa realista). Con estas ferramentas é posible simular bases de datos de pacientes con epilepsia cortical, con características únicas, xa que se trata de imaxes PET obtidas a partir dun mapa teórico de distribución do radiofármaco coñecido a priori. A pesar do enorme interese e da súa versatilidade, a simulación MC ten importantes limitacións que son un gran obstáculo para o seu uso xeneralizado ata o momento. En primeiro lugar, cabe mencionar que é necesaria unha importante potencia computacional para poder executarse nun tempo razoable e práctico, sobre todo se é necesario xerar maniquís dixitais que representen a distribución do radiofármaco real dun paciente. En segundo lugar, existen moitos códigos de simulación en liña dispoñibles que permiten realizar este tipo de simulacións en PET, pero requiren importantes coñecementos en programación, matemáticas ou física para que se podan utilizar, o que limita de maneira importante a súa difusión e uso para a comunidade científica.

Todo isto levou a necesidade de implementar novas ferramentas que permitan o uso das técnicas de simulación MC por parte de persoas non expertas en áreas técnicas, de fácil e doada utilización, cun tempo de execución razoable e cun alto grao de personalización e soporte que favoreza a estandarización deste tipo de técnicas para a avaliación de diferentes protocolos de imaxe PET. Por este motivo, o obxectivo principal desta tese de doutoramento é o deseño, desenvolvemento e validación dunha plataforma web (SimPET) para a xeración de estudos

simulados de PET cerebral mediante técnicas de simulación de MC. En particular, o primeiro obxectivo foi validar os modelos de simulación necesarios para a implantación de tres escáneres PET comerciais. A continuación, o segundo obxectivo foi deseñar e desenvolver a propia plataforma web, integrando os modelos de escáner validados na primeira fase nunha interface gráfica con múltiples opcións para a realización dos estudos de simulación. O terceiro obxectivo foi xerar tres bases de datos simuladas de controis sans, unha para cada un dos escáneres implementados na primera parte da tese, co fin de validar o rendemento da plataforma e poñer a disposición do público en xeral estas bases de datos de imaxes PET libres. Finalmente, o cuarto obxectivo foi utilizar a plataforma para realizar un traballo de aplicación baseado na simulación dunha base de datos de estudos PET-FDG con epilepsia cortical para a súa utilización na avaliación de protocolos de PET.

A primeira parte desta tese consistiu na validación dos modelos de simulación MC de diferentes escáneres PET comerciais (o GE Discovery ST, o GE Advance NXi e o Siemens Biograph mCT). Co fin de garantir que as imaxes PET simuladas fosen o máis semellantes posible ás adquiridas nun escáner PET real, as características técnicas de cada escáner real configuráronse no seu modelo simulado correspondente para posteriormente caracterizar cada escáner real e modelo simulado mediante National Electrical Manufacturers Association (NEMA). Estas probas teñen como obxectivo avaliar que o rendemento dun escáner PET se corresponde co indicado polo fabricante, establecendo os parámetros axeitados para cada adquisición. En concreto, as probas NEMA utilizadas neste traballo para as diferentes caracterizacións foron: unha proba de resolución espacial, unha proba de sensibilidade e unha proba de calidade de imaxe. Así, no caso do escáner GE Discovery ST, puidemos validar o seu modelo de simulación MC, obtendo diferenzas aceptables entre as probas NEMA reais e as probas NEMA simuladas. Estas diferenzas débense principalmente ás limitacións actuais que temos no modelo que describe a xeometría do bloque detector empregado no software de simulación e ao uso dun método de reconstrución similar ao código de reconstrucción privado (ao que non temos acceso) integrado no escáner PET real, que obviamente non é o mesmo. En canto á validación do modelo de simulación MC do escáner GE Advance NXi, esta xa foi realizada en varios traballos anteriores dentro do noso grupo de investigación, polo que adaptamos directamente estas configuracións validadas á configuración da simulación e reconstrución utilizada. No que respecta ao escáner mCT de Siemens Biograph, a validación do seu modelo de simulación MC realizouse a través de diferentes probas internas realizadas por colaboradores do Hospital Clínic de Barcelona e traballos previos doutros autores, permitíndonos integrar directamente os parámetros validados no software de simulación e de reconstrución tomográfica.

O segundo e principal traballo desta tese doutoral foi o deseño e desenvolvemento da plataforma web para a simulación MC de imaxes PET: SimPET (www.sim-pet.org). Esta aplicación consiste nunha plataforma web gratuíta, accesible, eficiente, e dedicada á xeración de maniquíes dixitais e imaxes simuladas de PET, especialmente orientadas ás imaxes PET do cerebro. Para o seu desenvolvemento utilizáronse varias linguaxes de programación, como HTML5, CSS, Javascript e PHP para o front-end, MATLAB, Bash, Python e C para o back-end e Laravel como framework; ademais de bibliotecas como Brain-VISET para a xeración de mapas de actividade e atenuación, SimSET para a simulación de sinogramas a partir de maniquíes de actividade e atenuación, STIR para a reconstrución das imaxes PET simuladas e SPM, FSL e NiBabel para o pre e posprocesamento das diferentes imaxes coas que se traballa. A plataforma ofrece unha interface gráfica de usuario (GUI) que permite a xeración de mapas de actividade e atenuación, sinogramas e as correspondentes imaxes PET simuladas mediante calquera dos modelos de simulación validados previamente. Ademais, conta con outras

utilidades coma un visor en liña para previsualizar as imaxes xeradas na plataforma e un apartado de descrición da análise realizada. Por outra banda, o código fonte utilizado para a simulación de MC e a reconstrución tomográfica está dispoñible gratuitamente en Github e é modificable (https://github.com/txusser/brainviset_simset), o que permite que diferentes usuarios ou desenvolvedores propoñan novos modelos de simulación e de reconstrucción tomográfica, así como novas funcións que melloren as funcións actuais da plataforma.

Unha vez que tivemos a plataforma implementada e a pleno funcionamento, o terceiro traballo consistiu en simular tres bases de datos de controis sans nos diferentes escáneres dispoñibles na plataforma SimPET para posteriormente validalo mediante diferentes análises estatísticas de comparación entre datos simulados e datos reais. Para xerar estudos de PET simulados o máis realistas posible, consideráronse como imaxes de entrada os mapas de actividade e os mapas de atenuación xerados co modelo GE Discovery ST, e os parámetros de entrada para a simulación (dose inxectada ao paciente, duración do estudo PET, nivel de ruído, etc.) os mesmos valores que os utilizados nos protocolos habituais de adquisición de cada un dos escáneres PET reais nos seus respectivos centros médicos. Deste xeito, xerouse unha base de datos de 25 imaxes PET do cerebro simuladas co GE Discovery ST, outra base de datos de 25 imaxes PET simuladas co GE Advance NXi e outra base de datos de 25 imaxes PET simuladas co Siemens Biograph mCT. Para validar o rendemento da plataforma, estudáronse as diferenzas entre as bases de datos simuladas e as imaxes reais de cada escáner mediante o método Bland-Altman. Ademais, tamén se realizou análise a nivel de voxel con SPM para observar diferenzas rexionais entre os grupos de imaxes reais e simulados. Como resultado de ambas análises estatísticas, obtivéronse diferenzas moi pequenas para o escáner GE Discovery ST (o 98 % dos vóxeles mostran diferenzas por debaixo do 10 %) e diferenzas relativamente pequenas para os outros dous escáneres (o 94-95 % dos vóxeles con diferenzas de menos do 10%), o que nos permitiu considerar a plataforma validada como ferramenta para xerar imaxes PET realistas do cerebro nos tres escáneres comerciais implantados.

Coa plataforma SimPET xa validada con datos de controis, o cuarto e último traballo desta tese de doutoramento consistiu en simular unha base de datos de diferentes casos de pacientes que mostran regións de hipometabolismo cortical para a avaliación de protocolos en epilepsia. A metodoloxía empregada para a creación de cada un destes estudos simulados consistiu no seguinte. En primeiro lugar, seleccionouse aleatoriamente unha rexión de interese (ROI) dun atlas cerebral que contén únicamente a corteza cerebral. Unha vez seleccionada a ROI da materia gris na que queriamos inducir unha zona de hipometabolismo, consideráronse dous tipos de hipometabolismo: un deles máis focal e reducido con tres posibles niveis de afectación (60, 75 ou 90%) e outro deles máis extenso que compromete rexións con dous posibles niveis de afección (30 ou 40%). Segundo os casos, a ROI enmascarouse cun ou outro tipo de hipometabolismo e, unha vez que tivemos a ROI hipometabólica, aplicouse aos mapas de actividade realistas que xa tiñamos dispoñibles no traballo anterior para obter mapas de actividade con diferentes hipometabolismos inducidos. Estes mapas de actividade, e os correspondentes mapas de atenuación, consideráronse como entrada na plataforma SimPET para xerar estudos simulados de PET-FDG con diferentes niveis de hipometabolismo inducido utilizando o modelo GE Discovery ST. Para ter a base de datos o máis equilibrada e realista posible, inicialmente xerouse o mesmo número de estudos PET simulados para cada nivel de hipometabolismo considerado. Non obstante, tras varias revisións visuais por parte dun especialista en medicina nuclear, conseguimos afinar os hipometabolismos inducidos e obter unha base de datos formada por: 25 estudos PET cun 60% de hipometabolismo focal inducido, 31 estudos PET cun 75% de hipometabolismo focal, 19 estudos. cun hipometabolismo focal do 90%, 10 estudos PET cun hipometabolismo extenso do 30% e 15 estudos PET cun

hipometabolismo extenso do 40%. A estes estudos engadimos os 25 controis simulados previamente co GE Discovery ST para ter unha base de datos total de 125 estudos de PET simulados, sendo 100 deles casos con hipometabolismo cortical simulado. Para validar esta base de datos de epilepsia cortical, realizamos unha análise cuantitativa a nivel de vóxel con SPM comparando o grupo de controis simulados fronte a cada un dos estudos de hipometabolismo simulado. Como resultado, puidemos verificar a gran semellanza entre os clusters hipometabólicos detectados por SPM nestas comparacións e a ROI hipometabólica creada para inducir hipometabolismo nos mapas de actividade orixinais. Deste xeito, non só validamos a base de datos simulada de PET-FDG na epilepsia cortical, senón que esa base de datos constitúe unha verdadeira referencia para todo tipo de traballos de avaliación de protocolos de neuroimaxe en epilepsia, xa que está formada por estudos con hipometabolismo inducido coñecido e controlado. Actualmente, esta base de datos estase a utilizar nun estudo de detectabilidade internacional realizado entre colaboradores de varios países e que ten como obxectivo avaliar a capacidade visual dos especialistas en medicina nuclear para localizar focos e zonas epileptoxénicas. Este traballo é posible grazas ao desenvolvemento dunha plataforma web desde a que colaboradores expertos poden descargar o noso conxunto de datos simulados de casos de epilepsia, realizar un informe por cada suxeito simulado indicando onde localizaron visualmente o hipometabolismo e o grao de confianza no seu diagnóstico, así como como descargar as correspondentes análises estatísticas despois do envío do informe no caso de querer comprobar a localización real e o grao de extensión do hipometabolismo inducido. Por outra banda, a plataforma SimPET tamén se utilizou para outros traballos de simulación con outros radiofármacos, como estudos de imaxe PET simulados con Florbetapir (Amiloide) ou para a simulación de bases de datos doutras enfermidades neurolóxicas tan importantes como a enfermidade de Alzheimer e a epilepsia do lóbulo temporal. Todos estes traballos demostraron a versatilidade e o potencial da plataforma SimPET como ferramenta para simular e xenerar estudos de imaxe PET, utilizando diferentes configuracións de radiofármacos e modelos de escáneres validados, e como ferramenta para avaliar protocolos de neuroimaxes PET. En definitiva, o desenvolvemento da plataforma SimPET constitúe a base dun marco no que se poden implementar futuros equipos comerciais de PET e mesmo prototipos, novos radiofármacos adicionais que xa se están a utilizar nos estudos de PET cerebral, e mesmo novas ferramentas para realizar simulacións de imaxes PET de corpo enteiro co seus radiofármacos correspondentes.

Content

INTRODUCTION

1 INTRODUCTION

1.1 POSITRON EMISSION TOMOGRAPHY

Positron Emission Tomography (PET) is a non-invasive nuclear imaging technique used to measure the metabolic activity of different processes in the body. PET takes advantage of the nature of radiotracers (molecules marked with a radioactive isotope) to detect changes at the biochemical and functional level. When the radiotracer is injected intravenously, it is distributed throughout the body by emitting positrons. These positrons will annihilate with matter electrons generating two back-to-back 511 keV annihilation photons. These gamma rays are detected by the scintillator crystals of the scanner and reconstructed producing a PET image (Figure 1).

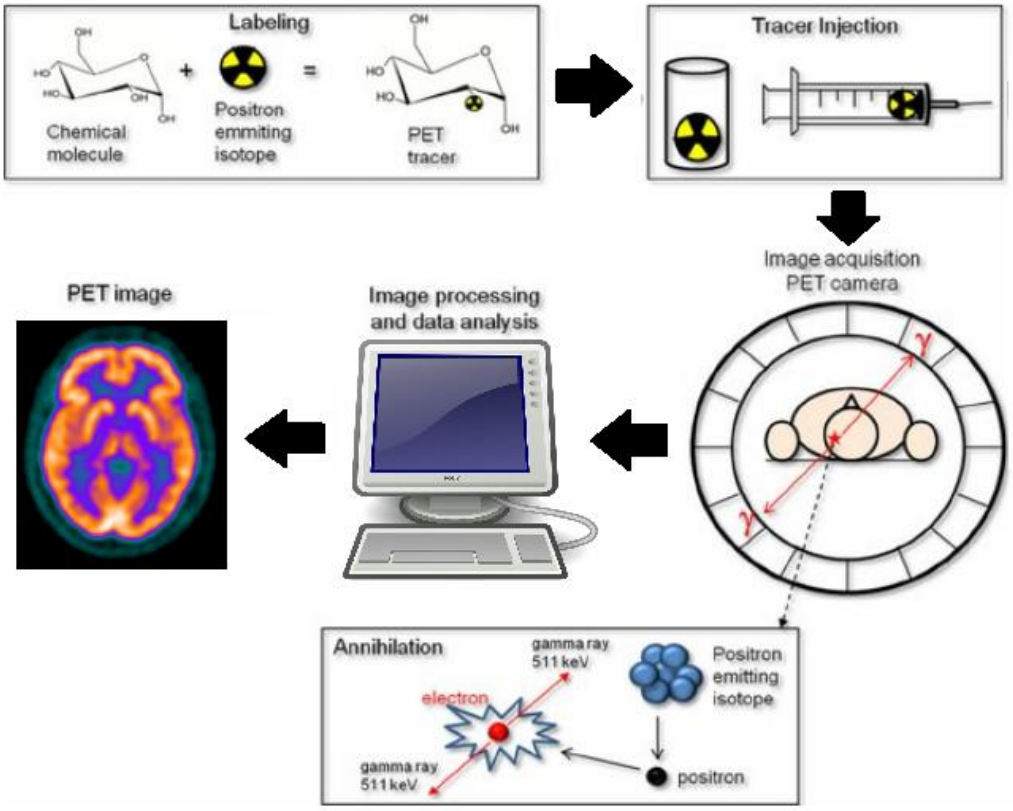

Figure 1: Procedures for acquiring a PET study.

The first human positron imaging machine was developed by Gordon Brownell and William Sweet at the Massachusetts General Hospital in 1952. Their device used two sodium iodide (NaI) detectors to detect brain tumors. Different refinements led to the creation of the PC-1 scanner, which featured an array of detectors significantly improving sensitivity (Brownell, 1999). In 1974, Brownell met with the nuclear physicist Michael Ter-Pogossian at Washinton University in St. Louis to discuss the possibility of designing hexagonal detectors. One year

later, in 1975, Michael Phelps and Edward Hoffman, assistant professors in Ter-Pogossian laboratory, created a PET scanner with hexagonal detectors (Phelps et al., 1975). This allowed Ter-Pogossian to develop a ring-shaped PET scanner (PCR-1 in 1985) and another with a cylindrical shape (PCR-2 in 1988), gaining in resolution and sensitivity (Portnow et al., 2013). Since then, the evolution of PET technologies and radiotracers has led to the use of PET as a clinical tool to improve the diagnosis, follow-up and treatment of patients in areas such as oncology, neuropsychiatry and cardiology (Maisey, 2005).

1.1.1 PET Physics

1.1.1.1 Radioisotopes and beta decay

The first approach to the positron was made by Paul AM Dirac in 1928 when he found a subatomic particle similar in mass to the electron but with a positive charge. In 1932 Carl Anderson would call these particles positrons after studying the gamma radiation of cosmic rays using cloud chambers (Anderson, 1932; Bailey et al., 2005). Today, we know that these particles are produced naturally during the beta decay of different radioisotopes. Radioactive isotopes are atoms whose nucleus is unstable due to excess energy and are very rare to find in the nature. For this reason they are produced artificially in laboratories with particle accelerators by proton bombardment. These isotopes undergo different decays to change the composition and properties of their nucleus to arrive a more stable state. In the case of the radioisotopes used in PET imaging, the nucleus converts one of its protons (p) into a neutron (n), emitting a positron β^+ and a neutrino (ν), respecting the physics conservation laws: $p \rightarrow n + \beta^+ + \nu$. This is known as β^+ decay. The positron travels a certain distance before reaching an electron of the matter. This path depends on the type of radioisotope and the materials it passes through. The combination of a positron with an electron is called annihilation, through which the mass of both particles is converted into energy, emitting two 511 keV photons in opposite directions (R. Schmitz et al., 2013). The positron-emitter radioisotopes most currently used in PET are ^{18}F and ^{11}C, and to a lesser extend also ^{13}N, ^{15}O, ^{18}F, ^{68}Ga , ^{68}Ga , ^{89}Zr, ^{64}Zr, ^{82}Rb…

1.1.1.2 Photon-matter interaction

The annihilation photons will interact with the matter losing energy and changing their direction. Due to the energy ranges involved the most relevant interaction process with matter in human tissue is Compton scattering. In this process the photon collides with an electron weakly attached to an atom of the tissue (practically a free electron) and transfers part of its energy to it. Then the photon undergoes a change of direction losing part of its energy, while the electron separates from the atom (Figure 2). Other types of photon-matter interaction can occur as well, such as photo-electric effect and pair productions, but much less likely.

The energy of the photon after Compton scattering follows the equation:

$$E'_\gamma = \frac{E_\gamma}{1 + \frac{E_\gamma}{m_0 c^2}(1 - \cos(\theta))} \qquad (1)$$

where E_γ is the incident energy of the photon, E'_γ the outgoing photon energy, m_0 the electron rest mass, c the speed of light, and θ is the scattering angle.

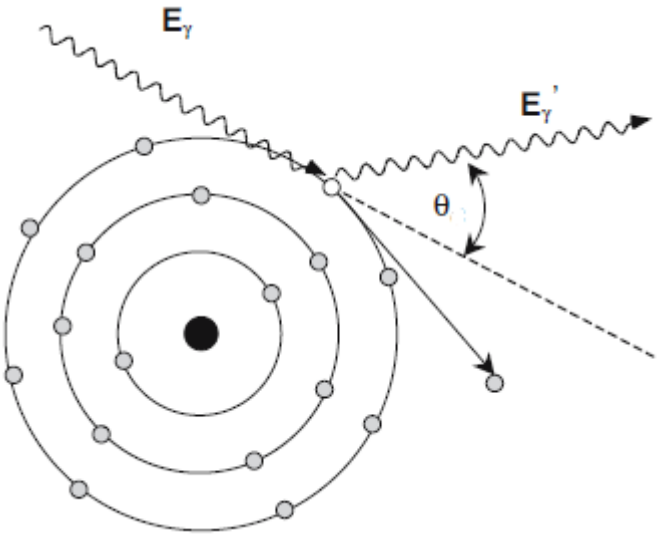

Figure 2: Compton scattering. Adapted with permission of Springer Nature from (Bailey et al., 2005).

The photon-matter interaction can be modelled in terms of the probability of the interaction of the photon with the atoms of the matter through the concept of atomic cross section (σ), expressed as cm^2/atom. The total atomic cross section σ_{total} are given by the sum of the cross sections of the different photon-matter interactions:

$$\sigma_{total} = \sigma_{pe} + \sigma_{cs} + \sigma_{pair} + \sigma_{others} \qquad (2)$$

where σ_{pe} is the cross sections for the photoelectric effect, σ_{cs} is the cross sections for the Compton scattering, σ_{pair} is the cross sections for the pair production effect and σ_{others} is the sum of others minor effects.As we discussed above, σ_{cs} is the main interaction effect for 511 keV photons of PET and therefore $\sigma_{total} = \sigma_{cs}$. In the Figure 3, we can see the contribution of the cross section of each effect to the total atomic cross sections depending on the level of energy that interacts.

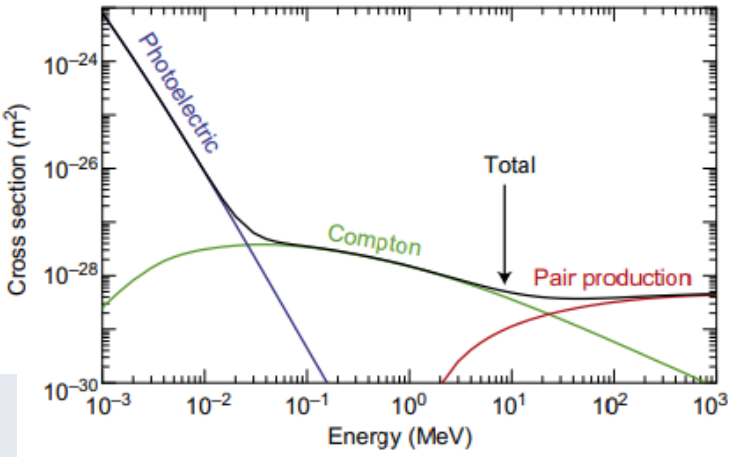

Figure 3: Atomic cross sections of photon-matter interaction, including photoelectric effect (blue), pair production effect (red) and Compton scattering (green). The total atomic cross section is in black. Adapted with permission of Elsevier from (Marshall & Cully, 2020).

The total atomic cross sections allows to describe the mass attenuation coefficient by:

$$\mu/\rho\ (cm^2 \cdot g^{-1}) = \frac{\sigma_{total}}{u(g) * A} \qquad (3)$$

where A is the atomic mass of the material element and $u(g) = 1.661 \times 10^{-24} g$ is the atomic mass unit. Using the mass attenuation coefficient and dividing it by the density of matter (ρ) we obtain the linear attenuation coefficient of the material (μ) in cm-1. For a collimated source of photons, μ allows to calculate the intensity of a photon beam passing through the material:

$$I_x = I_0 e^{-\mu \Delta x} \qquad (4)$$

where I_0 is the photon beam intensity before interacting, Δx is the width of the material and I_x is the remaining intensity of the photons after passing through the material (Cherry & Dahlbom, 2006). This attenuation will be a crucial factor during the acquisition of the PET image and will be discussed in detail later.

1.1.2 PET Instrumentation

The acquisition of the PET data is carried out by detecting the back-to-back photons. These photons interact with scintillation detectors generating low-energy photons (visible light). These photons of light are converted into an electrical signal or pulse by photodetectors based on photomultiplier tubes (PMTs) or recently solid-state photomultipliers. The electric signals or pulses are amplified and finally registered as a count (Saha, 2010a). The classic detection process based on the use of PMTs can be observed in Figure 4.

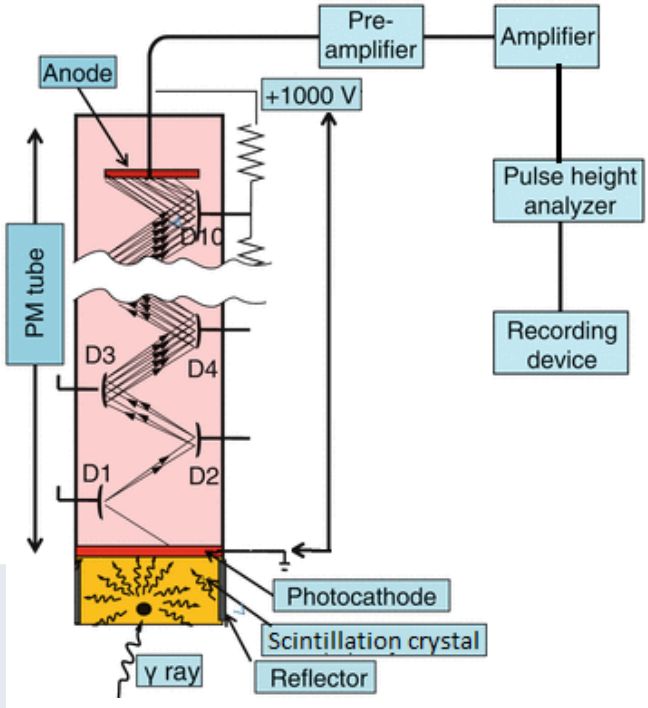

Figure 4: Photon detection process. Adapted with permission of Springer Nature from (Saha, 2010b).

1.1.2.1 Scintillation detectors

Multiple types of scintillation detectors have been used in different PET prototypes, such as those based on gases (Freon, CO_2…), liquids (Xenon) and solids (crystals, plastics…). However solid scintillation detectors have been used in commercial PET systems so far, mainly due to their higher efficiency in photon detection. When the photon interacts with the solid scintillator, it can transfer all or part of its energy to the detector crystal by successive Compton interactions or a single interaction by photoelectric effect. If the photon transfers all its energy, it is absorbed in the scintillator, but if the photon only transfers part of its energy, it will leave the scintillator with the remaining energy (Humm et al., 2003). In both cases, energy transferred to the scintillator results in an emission of light photons that are collected by the photodetectors.

These solid scintillation detectors can have different characteristics and compositions that will be crucial for the good performance of the PET scanner. The main characteristics that influence when choosing one detector or another are: the stopping power of PET photons, the decay time of the scintillation crystal, the visible light output per MeV of photon energy and directly related to the latter, the energy resolution. The stopping power of a scintillator depends directly on the density and the effective atomic number (Z_{eff}) of the crystal. A high density increases the photon probability to undergo the Compton effect and deposit part of its energy on the crystal, while a high Z_{eff} favors the photon would transfer all its energy to the crystal through the photoelectric effect. The decay time is the time it takes for the crystal to absorb the energy of the photons inside it, transmit it to the photodetector, and go back to stable state to receive the next photon interaction. A short decay time is desirable to have a high efficiency at high count rates. The light output is the amount of visible photons that are generated for each unit of energy received by the scintillator (photons/MeV). The light output is directly related to better energy resolution. The energy resolution is essential for rejecting those photons which achieve the detector after Compton interactions in the tissue (Bailey et al., 2005). However, a high light output usually causes a longer decay time, for this reason a certain balance is usually sought between both characteristics.

Some of the most common scintillation detectors in PET and their properties can be seen in Table 1. Historically, one of the most widespread scintillators in PET equipment has been the BGO because it has a good stopping power and is cheaper than other options. The NaI(Tl) has a large light-output value leading to good energy and spatial resolution but a lower stopping power than BGO. Currently, the main type of scintillator used in PET scanners is LSO and its variants (e.g. LSO, LYSO and LFS) because it has a good balance between the qualities of the previous two (high light output, good stopping power, and short decay time) (CITA https://www.ajronline.org/doi/10.2214/AJR.10.4741). GSO is another detector developed for commercial systems, with better energy resolution but with lower stopping power and light output than LSO. In addition to all these models, there are other scintillators under development based on other chemical elements (Bailey et al., 2005).

Table 1: More common scintillation detectors in PET scanners from (R. Schmitz et al., 2013).

Material	*Cost*	*Light Output*	*Effective Density*	*Decay Time*
NaI(Tl)	Cheap (relatively)	Highest	Lowest	Long
BGO	Expensive	Lowest	Highest	Long
LSO	More expensive	High	High	Very short
GSO	More expensive	Very high	Lower than LSO	Very short

1.1.2.2 Photomultiplier tube

As we mentioned earlier, the function of the PMT is to convert the visible light photons generated by the scintillating crystal into an electrical pulse. The PMT is a vacuum glass tube formed by a photocathode (electrode) in contact with the scintillating crystal, a series of dynodes in the middle, and an anode at the end of the tube. When photons of light from the scintillating detector hit the photocathode, it emits electrons. These electrons are accelerated from dynode to dynode by the difference in voltage, generating with each impact enough energy to produce more electron emissions from each dynode. This continues until a torrent of electrons is produced that are drawn to the anode (Saha, 2010a). The electrical pulse that is generated is amplified to be detectable and analyzed by a pulse height analyzer. This process can be seen in Figure 4.

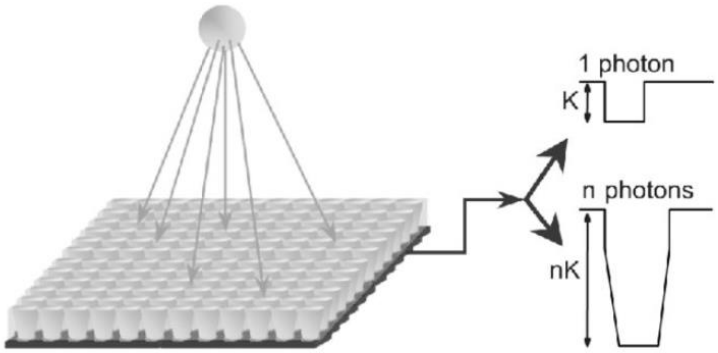

Figure 5: Scheme of a silicon photomultiplier based on a matrix of SPAD sensors. Reproduced with permission of IEEE from (Finocchiaro et al., 2006).

In recent years, solid-state/silicon photomultipliers (SiPMs) have been developed. SiMP are formed by a matrix of special diodes (SPAD: Single Photon Avalanche Diode) connected by a common silicon substrate and which function as photon counters. When a photon reaches one of the diodes, a current avalanche of electron-hole pairs is produced. After detection, this current is reduced by a resistor. As a result the diode is reset and is ready to count another photon. All the outputs of the diodes are connected, so the SiMP behaves as a proportional device for photon streams (see Figure 5). These detectors have a number of advantages over traditional PMTs: higher internal gain, smaller size, good single-photon timing resolution and low bias voltage. These advantages together with their compatibility with magnetic fields, make these detectors are progressively replacing PMTs in current PET and PET/MR equipment (Lecoq & Gundacker, 2021; Mazzillo et al., 2011).

1.1.2.3 Electronic collimation

The output signal of the photomultipliers is shaped and amplified before reaching the pulse height analyzer (PHA). The PHA is a discriminator that filters out photons of different energies. This device accepts or rejects photons through an energy detection window. The narrower the PHA window, the more accurate the filtration, but the more the photon detection efficiency decreases. In PET systems, this window has a width of 350-650 keV with a center at 511 keV. The PHA also assigns a digital time stamp to each photon to be able to if two photons detected in opposite detectors have occurred in the same coincidence timing window (on the order of 6-10 ns) (R. Schmitz et al., 2013). This process is called electronic collimation (see Figure 6) and is essential to reject scattered photons.

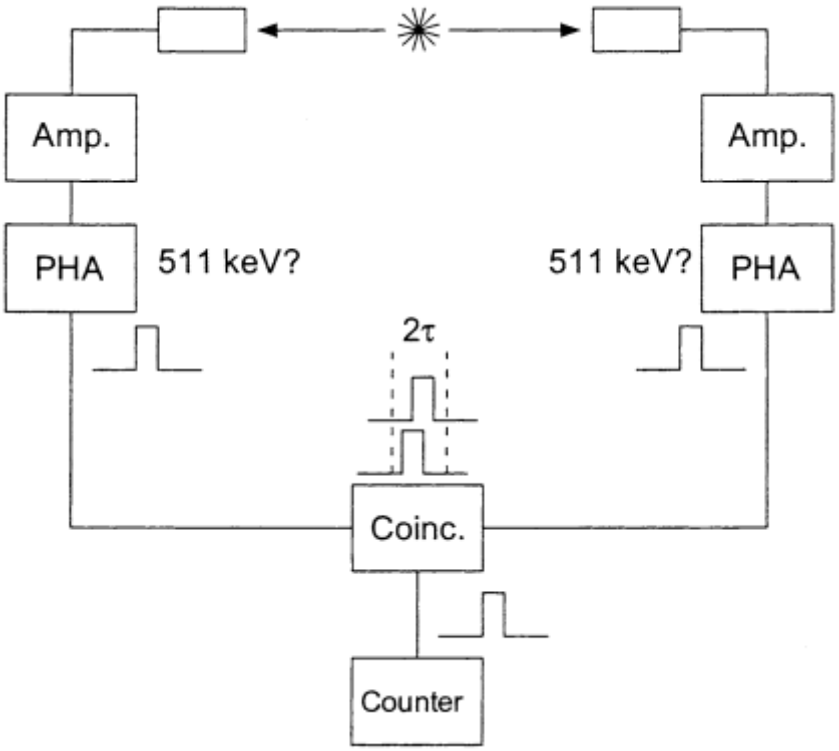

Figure 6: Diagram of a coincidence detection. Reproduced with permission of Springer Nature from (Cherry & Dahlbom, 2006).

1.1.2.4 Scintillator crystal performance

There are certain detector properties that determine the performance of the PET scanner and will influence the quality of your images:

a) The time resolution is the statistical uncertainty or timing error between the arrival of a photon at the scintillator and output pulse leading edge. When a photon is detected by a scintillator crystal, the system initiates a coincidence time window. If another photon is received within this time window, it will be considered that both photons come from the same annihilation. The composition of the scintillator crystal, and in particular, the decay time, is directly related the timing resolution of the detector block and thus the coincidence time window. The short decay times lead to better timing resolution and shorter coincidence time window (Bailey et al., 2005).

b) The intrinsic efficiency is the ability to detect photons reaching the scintillator detector per unit of activity. It is mainly determined by the stopping power of the crystals, which is related to the composition of the scintillator crystal.

c) The energy resolution is the ability of a detector to estimate the energy of an arriving photon. This is essential in PET detectors for detecting separately (and then removing) those photons that achieve the detector after Compton interactions in the tissue. High light output from scintillation crystals lead to better energy resolution.

d) Regarding the material used, BGO has been one of the most used due to its high stopping power, but its long decay time and low light output is a huge limitation, and nowadays LSO and GSO are usually preferred (see Table 1) (Saha, 2010a).

1.1.2.5 PET scanner configurations

As we have seen, a PET scanner is made up of detector blocks grouped into arrays. The distribution of these sets of detectors determines the geometry of the PET scanner. The most common design is the ring geometry around the radioactive source. However, the first scanners were two flat detectors facing each other and later they evolved to other designs such as a rotating partial ring system, a hexagonal array of panel detectors or continuous curved panel systems (see Figure 7).

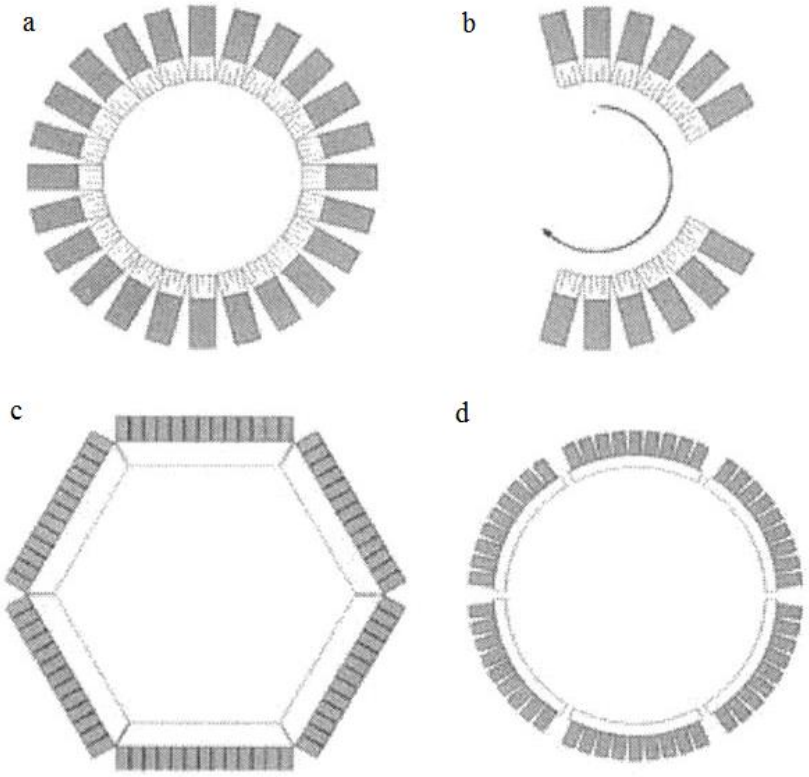

Figure 7: Four different PET scanner designs: fixed ring design (a), rotating partial ring system (b), fixed system with six flat detectors (c) and fixed system using continuous curved panels. Reproduced with permission of Springer Nature from (Cherry & Dahlbom, 2006).

The geometry of a PET scanner is of paramount importance as the overall detection efficiency of scanner is directly related to the distance between the source and the detectors (transverse or transaxial plane), the diameter of the ring, the number of detector blocks per ring, and the number of consecutive rings in the direction of the patient's body (axial plane). Nonetheless, the angular coverage of the current PET scanners is limited and the scanner only covers a small part of the patient's body, so they are usually equipped with beds to move the patient along the detector, so that whole-body PET studies have to be acquired by using multiple bed positions (Cherry & Dahlbom, 2006).

1.1.3 PET acquisition

1.1.3.1 Line-of-response (LOR)

Once two photons are detected in coincidence, it can be defined the line that joins the two centers of the detectors that receive the photons. It is called line of response (LOR) and represents the line where the annihilation has occurred. Due to limitations in energy and timing resolution mentioned above, different types of LORs can be detected (Bailey, 2005):

a) Singles (Figure 8a), when only one photon is detected in the coincidence time window. It occurs when the other photon coming from the same annihilation is lost (outside of the angular coverage of the detectors). It is a fairly frequent event in PET.

b) True coincidences (Figure 8b), when two photons generated from the same annihilation reach two opposite detectors without matter interaction and are registered within the same coincidence time window. In this case, the LOR corresponds to the path followed by the photons and that joins the two detectors.

c) Scatter coincidences (Figure 8c), when one or both photons detected within the same coincidence have been scattered by Compton effect, losing a small part of the energy. Most PET scanners do not have enough energy resolution to discard these scattered photons. These scatter coincidences produces a loss of image contrast (Humm et al., 2003).

d) Random coincidences (Figure 8d), when two photons generated from different annihilations are detected within the same coincidence time window. This generates an incorrect LOR that produces a background constant signal in the final image. If a and b are the detectors that register both photons, the random event count rate (R_{ab}) can be expressed as a function of the number of photons that a and b can detect (N_a and N_b) and the coincidence window width (2τ):

$$R_{ab} = 2\tau * N_a * N_b \quad (5)$$

As R_{ab} is proportional to 2τ, the better timing resolution the detector has, the fewer randoms events are generated.

e) Multiple coincidences (Figure 8e), when three or more photons are detected within the same coincidence time window. They are normally discarded without degradation effects on image quality, but results in loss of true coincidences.

For the calculation of the prompt count rate, in addition to the true coincident events, the random and scatter events are also considered valid since only two photons are detected in the same coincident time window. Instead, single and multiple events are directly discarded from the data. The best performance is achieved when true events are recorded and used for image formation, and, therefore, various correction methods for random and scatter events have to be applied.

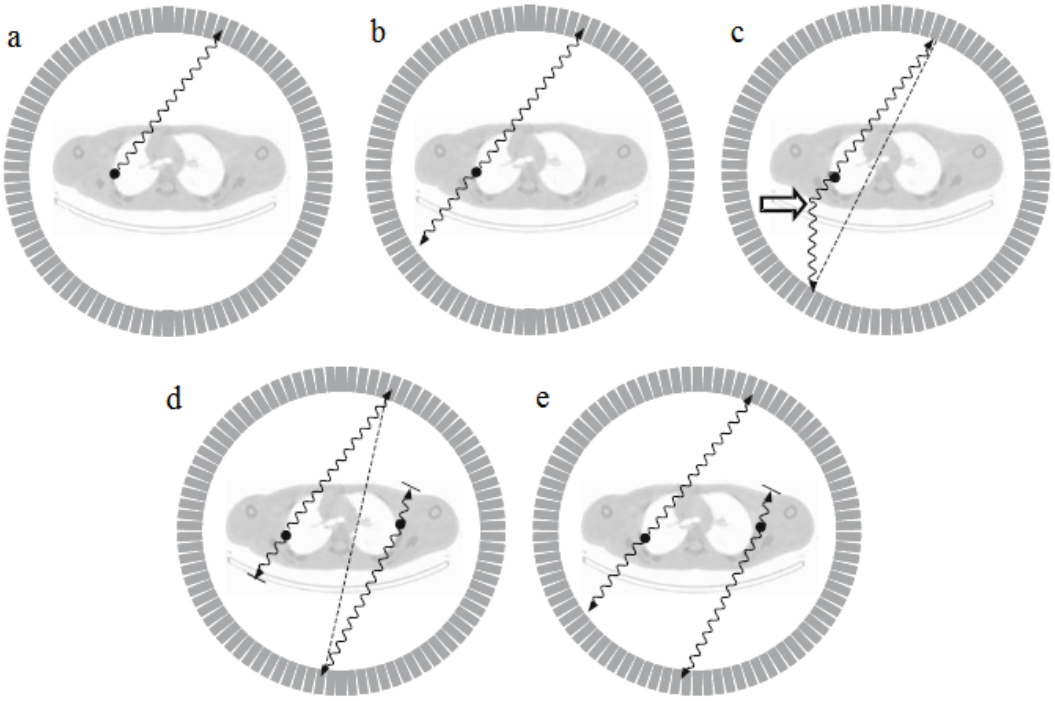

Figure 8: Types of coincident events in PET: Singles (a), trues (b), scatter (c), random (d) and multiple (e) Adapted with permission of Springer Nature from (Bailey, 2005).

1.1.3.2 Sinogram

The last step in PET data acquisition is storing the accepted data. All the LORs passing through the patient are stored and defined by an orientation angle (ϕ) with respect to the axial plane and a distance to the center of the scanner (s), forming a histogram of the LORs called sinogram (R. Schmitz et al., 2013). If for each point of the patient we represent the detected LORs as a function of these two parameters in a two-dimensional x-y graph, we will form the sinogram for that transaxial plane (Figure 9). Each value of the sinogram represents the number of matches detected along the LOR defined by the angle (x-axis) and the distance to the center of the scanner (y-axis).

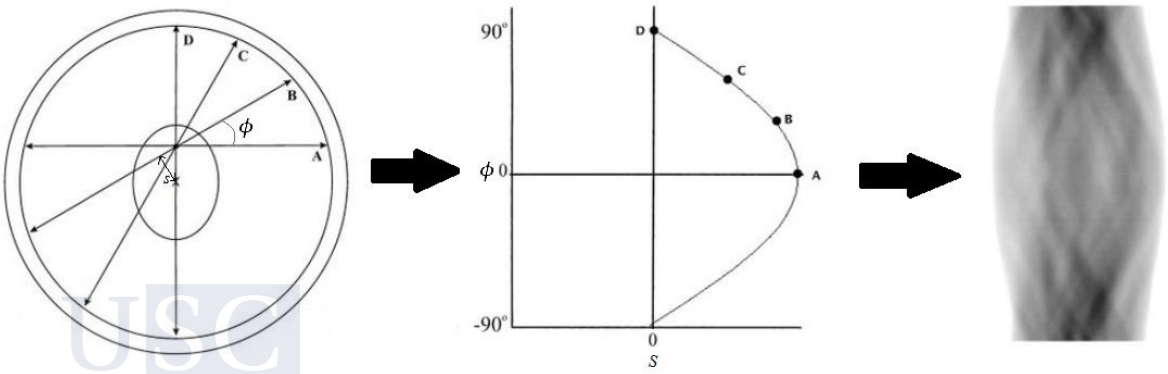

Figure 9: Conversion of detected raw data to a sinogram. Adapted with permission of JNMT from (Fahey, 2002).

In addition to the sinograms, the information detected in the LORs can also be saved as projections. These projections $p(s,\phi)$ represent the parallel line integrals of the activity for each given angle ϕ. They can be obtained by going through each row of the sinogram.

The clinical scanners are made up of several consecutive rings and, therefore, LORs have to be defined based on more parameters than for a single full ring of detectors. In this case, a LOR can be defined as $L(s,\phi,\theta,z)$ where s and ϕ are the variables that we saw previously and that define the plane of the sinogram, θ is the angle of inclination with respect to the axial plane (z-axis) and z is the position on the z-axis (see Figure 10). This allows different ways of acquiring PET images. The two-dimensional mode only accepts coincident events in direct planes (polar angle $\theta = 0$), i.e. between detectors of the same ring (see Figure 11a). In this mode N sinograms are acquired, where N is the number of rings. Therefore the sensitivity of the scanner is limited to N times the sensitivity of a ring. A more standard 2D mode is the one that accepts the coincidences generated in the direct planes, but also in the crossed planes, that is, between detectors of two adjacent rings. Thus, in a scanner with N rings, we can define N direct planes plus N-1 crossed planes, being a total of 2N-1 planes of coincidences, improving the sensitivity (Cherry & Dahlbom, 2006). Initially thin tungsten shields, known as septa, were placed between the rings to reduce the detection of photons from larger angles and minimize the number of scattered and random photons in early 2D mode scanners (see Figure 11b) but currently it is not like that.

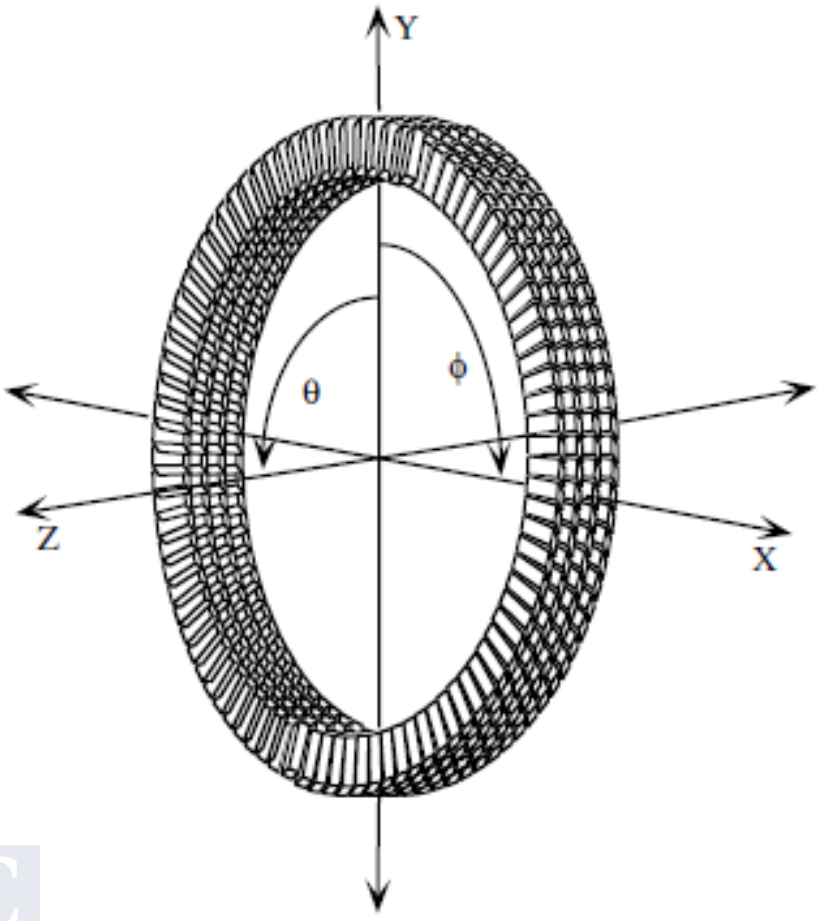

Figure 10: Diagram for a multi-ring PET camera. Reproduced with permission of Springer Nature from (Bailey, 2005).

Increasing the number of coincidence planes significantly improves the sensitivity of the PET scanner. For this reason, today most of the PET scanners acquire in three-dimensional mode (fully 3D mode). In this mode there are no septa and coincident event planes are allowed between any combinations of rings (see Figure 11c). This leads to N^2 sinograms being generated. Despite generating a lot of redundant information, this improvement in sensitivity relies on a better SNR in the image, reducing the acquisition time and the amount of injected dose (Cherry & Dahlbom, 2006).

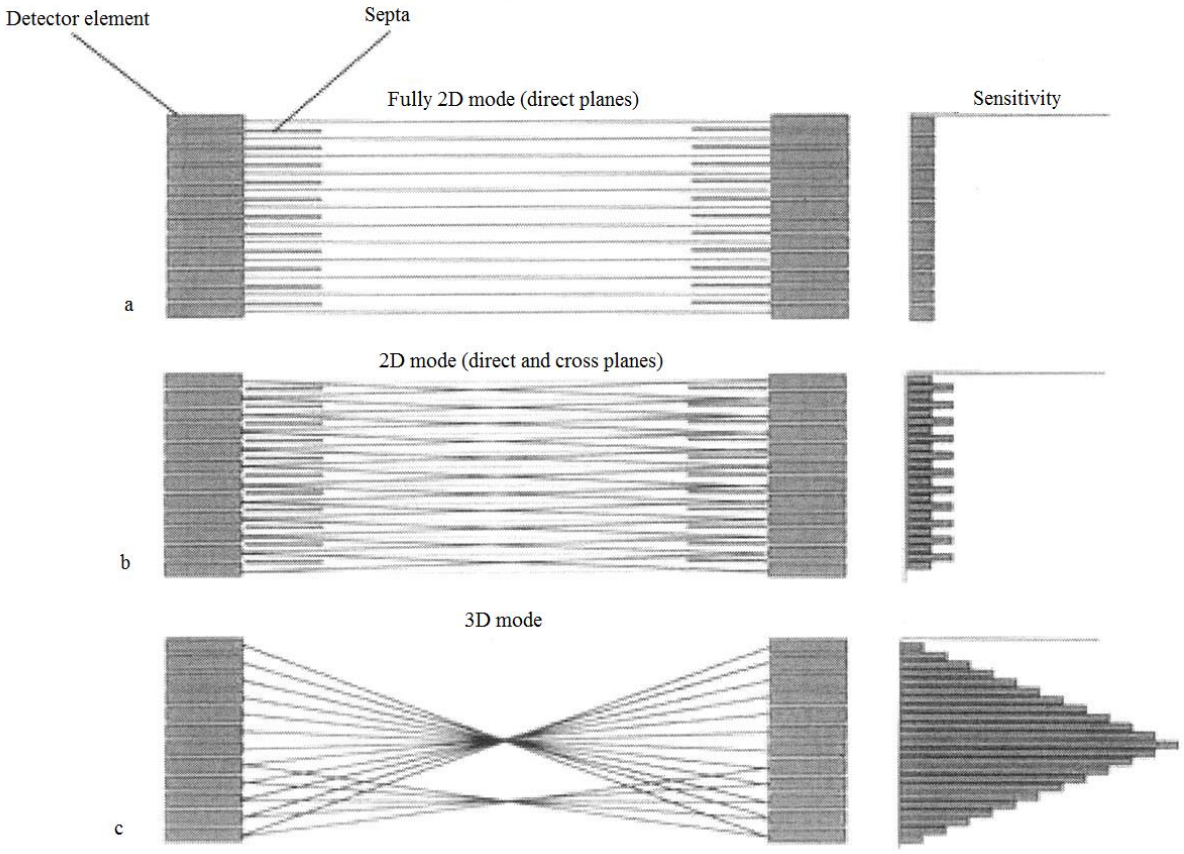

Figure 11: More common acquisition modes: Fully 2D (a), 2D (b) and 3D (c). Adapted with permission of Elsevier from (Zanzonico, 2004).

1.1.4 PET Reconstruction

Tomographic reconstruction consists of recovering the 3D distribution of the radiotracer using the projections or sinograms. This section discusses the reconstruction problem and the most common types of reconstruction methods. We start with analytical reconstruction to go on to reconstruction with statistical methods.

1.1.4.1 Reconstruction problem

PET reconstruction consists of solving the following linear problem:

$$p = Hf + n \quad (6)$$

where p are the acquired data, H is known as the system response matrix (SRM), f is the unknown 3D distribution of the radiotracer and n are the possible errors in the observation.

The goal is to use p to obtain f. Although the acquired data are stochastic variables, as a first approximation, we can assume that the data are deterministic, that is, without a source of error. Therefore, in equation 6, n would be a known number and we could find the exact solution of the equation for f. Analytical reconstruction methods use this to find a direct solution through the image f from the projections p. The advantage of assuming deterministic data is that it greatly simplifies the reconstruction process, making it faster. The bad part is that noise information is discarded.

1.1.4.2 Analytical reconstruction methods

In 2D analytical reconstruction methods the basic step is backprojection. This procedure consists of placing each value of a projection $p(s,\phi)$ back to its corresponding LOR. However, we do not know how the values were distributed in the original LOR, so the approach we can do is to put a constant value along the entire LOR. In Figure 12 we can see an example of backprojection $b(x,y,\phi)$ for a specific angle ϕ.

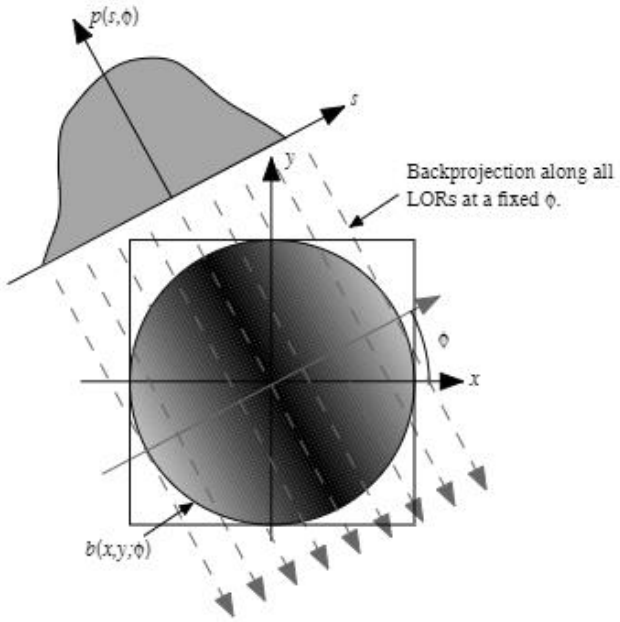

Figure 12: Backprojecton of all values of a projection $p(s,\phi)$ for a fixed value of ϕ. Reproduced from (Alessio & Kinahan, 2005).

Mathematically, for a given angle ϕ, a projection can be defined by the Radon transform of the radiotracer distribution $f(x,y)$, as follows (Kak & Slaney, 2001):

$$p(s,\phi) = \int_{-\infty}^{\infty}\int_{-\infty}^{\infty} f(x,y)\cdot\delta(x\,cos\phi + y\,sin\phi - s)dxdy \qquad (7)$$

where δ is the Delta function, so the integral is always zero except in the LOR $L(s,\phi)$. If we integrate along all the angles, we get the backprojected image $b(x,y)$:

$$b(x,y) = \int_0^{\pi} p(s,\phi)|_{s=xcos\phi+ysin\phi}\,d\phi \qquad (8)$$

The integral travels 180º since the other angles do not give new information.

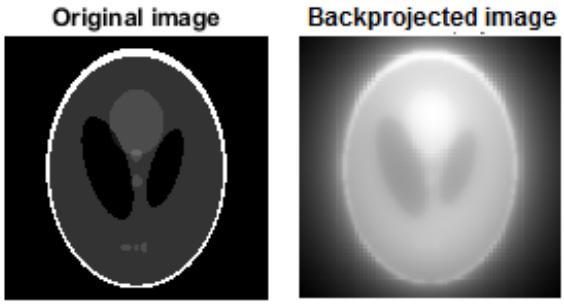

Figure 13: Original image VS Backprojected image. Adapted from (Zvolský, 2014).

If the backprojection is calculated for all the required angles, we might think that we would recover the image with the radiotracer distribution, however, this is not the case. Basic backprojection has the problem of intensity oversampling in the center of the image and less sampling at the edges, producing a blurring effect (see Figure 13).

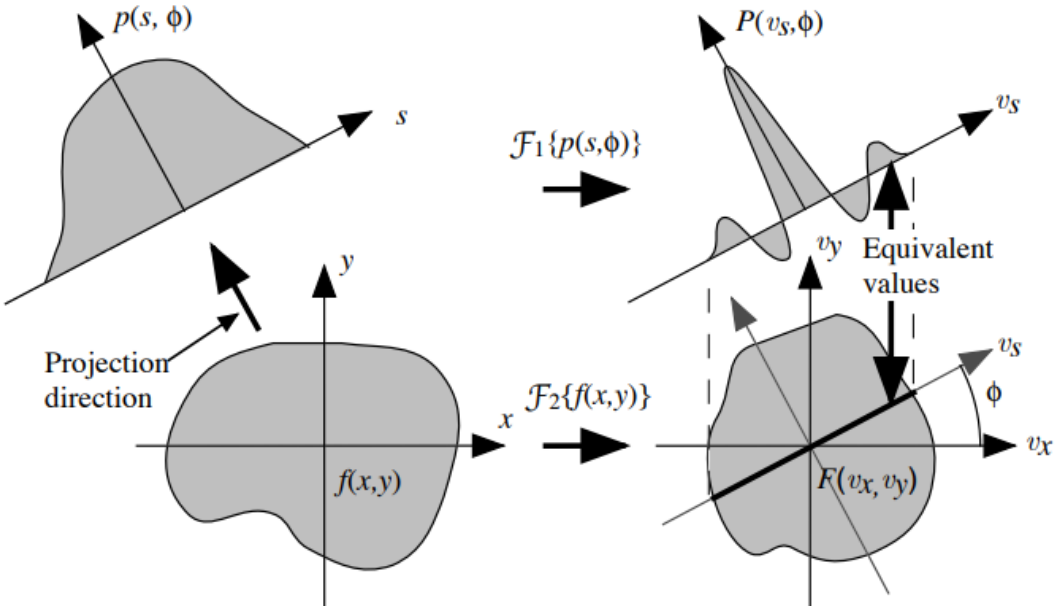

Figure 14: Two-dimensional CST where the 1-D Fourier transform of a projection at angle ϕ is equivalent to the 2-D Fourier transform of the central section at the same angle of the radioactive source. Adapted with permission of Elsevier from (Kinahan et al., 2004).

This blurring effect can be minimized by applying a filter to the data during acquisition. This filtered data is then backprojected to reconstruct an image more similar to the original source. This reconstruction method is called Filtered Backprojection (FBP) and it is one of the 2D reconstruction methods most used today due to its efficiency and better precision. The FBP method is based on the Fourier transform of the acquired data as well as the central slice theorem (CST). According to the CST (Kinahan et al., 2004), it is verified that:

$$\mathcal{F}_1\{p(s,\phi')\} = \mathcal{F}_2\{f(x,y)\}|_{\phi=\phi'} \quad (9)$$

where $\mathcal{F}_1$ is the 1-D Fourier transform of the projection $p(s,\phi)$ and $\mathcal{F}_2$ is the 2-D Fourier transform of the radiotracer distribution $f(x,y)$. This implies that doing the 1-D Fourier transform of the projection p for an angle ϕ' is equivalent to doing the 2-D Fourier transform of the data $f(x,y)$ and taking a slice through the origin with the same angle ϕ'. A schematic graph of this can be seen in Figure 14.

Following the CST, using the inverse Fourier transform and switching to polar coordinates, the real distribution, $f(x,y)$, can be expressed as:

$$f(x,y) = \mathcal{F}_2^{-1}\{F(v_x,v_y)\} = \int_0^{\pi} d\phi \left[\int_{-\infty}^{\infty} dw|w|P(w)e^{2\pi iws}\right] = \int_0^{\pi} d\phi p'(s,\phi) \qquad (10)$$

where we $F(v_x,v_y)$ is the Fourier transform of $f(x,y)$, P is the Fourier transform of $p(s,\phi)$ and $p'(s,\phi)$ is the original projection but multiplied by a ramp frecuency filter $|w|$ in the Fourier space (Zvolský et al., 2017). In this way, the FBP method consists of applying the Fourier transform to the projection $p(s,\phi)$, applying the ramp filter $|w|$, coming back to the initial space with the inverse of the Fourier transform, this filtered projection is backprojected and then all the backprojected projections are added to generate the FBP image (see Figure 15).

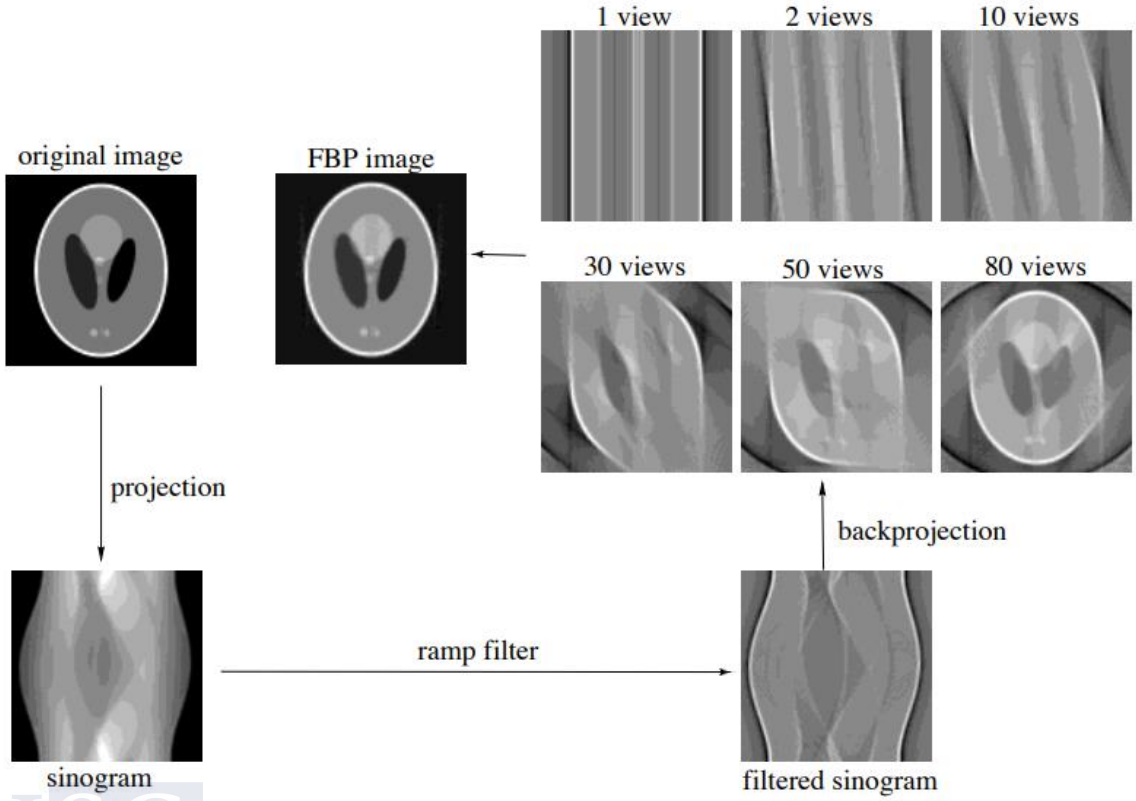

Figure 15: Filtered backprojection method. Reproduced from (Zvolský, 2014).

The FBP method is widely used for 2D reconstruction thanks to its simplicity and easy implementation. However, operating in 2D mode is not the most appropriate, since working in 3D mode takes more advantage of the radiation emitted by the patient, increasing the sensitivity of the scanner. For this reason, various reconstruction methods take advantage of data acquired in 3D and putting them together in parallel transverse sinograms ($\theta = 0$) so that they can be reconstructed with the traditional FBP method. These algorithms are known as rebinning algorithms. The simplest of these algorithms is the single-slice rebinning (SSRB), which takes the mean position where an event has occurred in the axial plane and adds it to the corresponding direct sinogram closest to that axial position. However, this algorithm only works well when the radioactive source is small, but in the case of patients some blurring of the data occurs in the axial direction (Cherry & Dahlbom, 2006). Another method is multi-slice rebinning (MSRB), where the LORs are rebinned at different direct sinograms, increasing the resolution but being too sensitive to noise artifacts (Biersack & Freeman, 2008). The most widely accepted rebinning algorithm is the Fourier rebinning (FORE). This algorithm is based on relating the 2D Fourier transform of the oblique sinograms ($\theta > 0$) with the 2D Fourier transform of the transverse sinograms ($\theta = 0$). In particular, Fourier transformed oblique sinograms can be rebinned into direct sinograms and, after sample normalization in the Fourier space, the inverse transform can be applied to retrieve direct sinograms (Alessio & Kinahan, 2005). FORE was the rebinning method implemented in most scanners instead of SSRB and MSRB, since it supports greater angles and is more accurate in larger radioactive sources.

Another option for analytical 3D image reconstruction is the 3-D reprojection algorithm (3DRP). It is considered as an extension of the FBP method. The difference between 2D and 3D acquisition is that, while in 2D you have the information of all the projections for any angle (ϕ ranging from 0 to 180º), in 3D mode different projections are truncated during the acquisition when $\theta > 0$ (see Figure 16). This is due to the cylindrical geometry of most PET scanners. The solution is the data redundancy presents in 3D acquisition. Incorporating oblique sinograms improves the SNR of the reconstructed image and, in this case, allows to solve the problem of truncated projections. In the 3DRP method the 2D sinograms ($\theta = 0$) are extracted and reconstructed using FBP to get a 3D image volume. This image can be projected to add activity in oblique LORs lost during acquisition and remove truncation. This is called reprojection or forward-projection. Now the projections are 2D and represent the activity for a particular ϕ and θ. The 2D Fourier transform is applied to these projections. Then, they are multiplied by a 2D filter and return to the original space taking inverse 2D Fourier transform to finally be backprojected into a 3D image matrix. The final reconstructed 3D image is obtained repeating this process for each supported ϕ and θ (Cherry & Dahlbom, 2006).

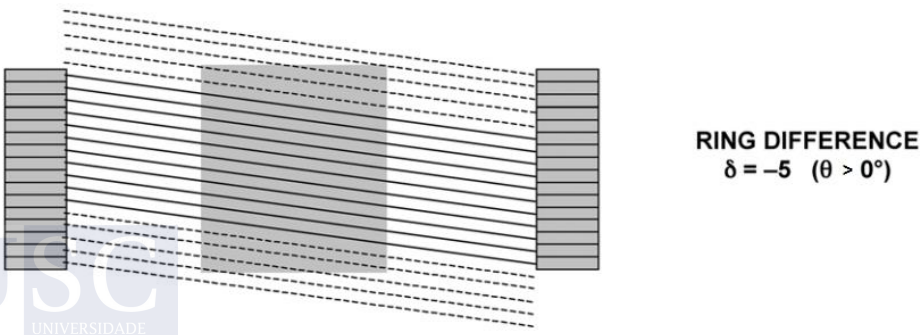

Figure 16: Truncation of projections in axial plane when $\theta > 0$. Modified with permission of Springer Nature from (Cherry & Dahlbom, 2006).

1.1.4.3 Statistical reconstruction methods

Analytical reconstruction methods have an important handicap: they do not take into account noise in the data and it is a factor that must be taken into account in PET. For this reason, images reconstructed with analytical methods often have low contrast, noise, and even artifacts. This leads to the development of statistical methods that consider projections as stochastic data taking into account the noise structure to achieve more realistic reconstructions. The most common in PET are iterative reconstruction methods. These methods try to find approximate solutions to the problem (Alessio & Kinahan, 2005). They consist of an iterative algorithm whose goal is the best estimate of the reconstructed image. This provides greater precision than analytical methods. On the other hand, these models have a higher mathematical complexity, since they do not have a direct analytical solution, and therefore a higher computational cost. However, nowadays it is not a big problem thanks to advances in computing, favoring their presence in most PET scanners.

The basic pipeline of iterative methods consists can be seen on Figure 17. An initial image $f^*(x,y)$ is estimated (usually an image with constant or blank values). Then a forward-projection $p^*(r,\phi)$ is applied to this image. This process is the inverse of backprojection and consists of adding all the activity data of the voxels that intersect with each LOR to estimate the projections. Once all the estimated projections are calculated, they are compared with the actual projections $p(r,\phi)$ measured from the acquired data. Depending on the differences found between the estimated and measured projections, the estimated initial image is updated to generate a new estimated image. This process is repeated until the estimated projections are quite similar to the real projections measured (within the characteristics and limitations of each scanner) and then the reconstructed image is generated (Cherry & Dahlbom, 2006).

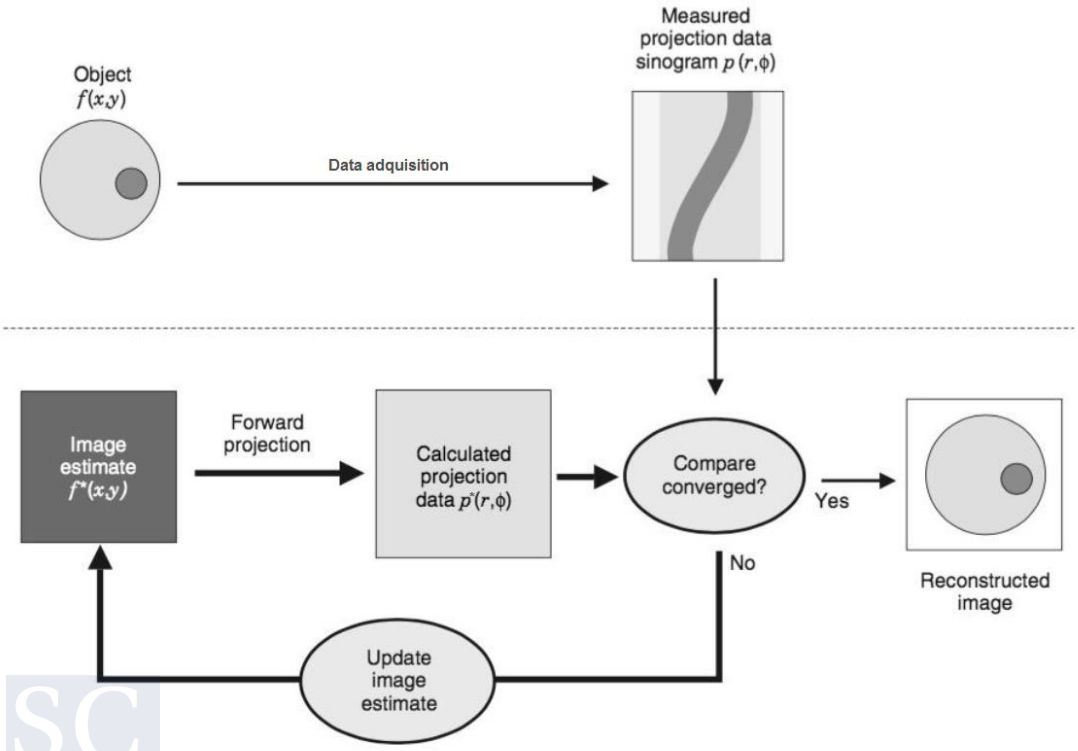

Figure 17: Basic pipeline of iterative reconstruction methods. Modified with permission of Springer Nature from (Cherry & Dahlbom, 2006).

The most used iterative reconstruction methods are those based on maximum likelihood (ML) methods. Likelihood is a statistical measure that is maximized when the difference between the measured and estimated projections is minimized. The maximum likelihood expectation maximization (ML-EM) is an iterative algorithm that maximizes likelihood under the assumption that the data are distributed according to a Poisson model (Shepp & Vardi, 1982). This algorithm seeks to converge towards a solution where the estimated images produce projections similar to the measured projections (see Figure 17). In this case, in each iteration, the estimated image values are updated like this:

$$f_j^{k+1} = \frac{f_j^k}{\sum_i a_{ij}} \sum_i \frac{p_i a_{ij}}{\sum_m a_{im} f_m^k} \qquad (11)$$

where a_{ij} is the element of the SRM that represents the probability that an annihilation in voxel j is detected in LOR i, f_j^k is the radiotracer distribution estimate in voxel j at iteration k and p_i is the measured projection i (Alessio & Kinahan, 2005). This method requires many interactions for the estimated data to converge towards the measured projections. As a consequence, the inherent noise of PET images increases with each iteration causing variance in the images (Saha, 2010a). For this reason, a balance must be reached between likelihood and noise level when selecting the number of iterations. In addition, this method requires a lot of processing time.

To reduce computation time, the ordered subsets expectation maximization (OSEM) (Hudson & Larkin, 1994), was implemented as a modification of the MLEM method. In this method the projections are grouped into disjoint subsets, so that MLEM is applied to each subset (called a sub-iteration) using the estimated LORs in the measured subset instead of to each individual projection. A single iteration is completed when all sub-iterations are processed in the form:

$$f_j^{k+1} = \frac{f_j^k}{\sum_{i \in S_n} a_{ij}} \sum_{i \in S_n} \frac{p_i a_{ij}}{\sum_m a_{im} f_m^k} \qquad (12)$$

where S_n is each of the N subsets. In this way, an updated image is generated in each subiteration, with N images after a complete iteration. Convergence is similar to ML-EM but is N times faster (Alessio & Kinahan, 2005). This improvement in the efficiency of iterative methods allows for greater use in clinical practice. For this reason, the OSEM method is today integrated into most commercial scanners.

1.1.5 PET corrections

As we have seen in previous sections, the data acquired in a PET scanner can be affected by multiple factors, such as the geometry or composition of the scanner and the interaction of photons with matter. In this section, we are going to comment on the main corrections made to minimize variability or errors in the acquired data.

1.1.5.1 Normalization correction

Factors such as the geometry of the scanner, the physical differences in the detectors, intrinsic efficiency, the variation in the gain of the PMTs, or the variations in the sensitivity of the LORs not perpendicular to the surface of the detectors result in an acquisition of non-

uniform data. To correct this effect, normalization is used. Data normalization consists of exposing all pairs of detectors to a uniform 511 keV photon source (usually a ^{18}Ge source) with no other source in the field of view (FOV) of the scanner (blank scan). Normalization coefficients are calculated for each LOR by dividing the mean counts of all LORs by the number of counts of the particular LOR:

$$F_i = \frac{A_{mean}}{A_i} \qquad (13)$$

where F_i is the normalization coefficient of the ith LOR, A_{mean} are the mean counts of all LORs in the plane of the ith LOR and A_i is the number of counts of the ith LOR. Then this normalization coefficients are applied to the acquired sinograms, to obtain the normalized sinograms. This calculation process is usually carried out weekly or monthly due to the fact that several hours are needed for an accurate estimate of the required counts (Saha, 2010a).

1.1.5.2 Attenuation correction

The photons produced during the annihilation lose energy as they pass through the different tissues of the subject. Previously we saw that among all the possible interactions at the microscopic level between photons and matter, the Compton effect is the most common, where photons transfer and lose part of the energy. At the macroscopic level, we saw that if a collimated source of photons passes through a material, knowing the thickness and the linear attenuation coefficient of the material in addition to the intensity of the photon beam, we can calculate the intensity of the beam after passing through the material according to Equation 4. If two annihilation photons are produced inside a subject and they have to pass through different tissues with different thicknesses (a and b) until they reach the detectors, and μ is the linear attenuation coefficient of a tissue that they traverse along the LOR, then the count rate or probability P that both photons are detected is:

$$P = e^{-\mu a} \times e^{-\mu b} = e^{-\mu D} \qquad (14)$$

where D is the total thickness traversed by the photons. If instead of a single tissue, the photons pass through organs or tissues with different attenuation coefficients, the previous equation remains as (Saha, 2010a):

$$P = e^{-\sum_{i=0}^{n} \mu_i D_i} \qquad (15)$$

where, n is the number of organs or tissues traversed and μ_i and D_i the linear attenuation coefficients and the thicknesses of each one. Some of the most common tissues, their densities and their linear attenuation coefficients can be seen in Table 2.

Photon attenuation causes inhomogeneities in the acquired data and must be corrected. Based on the previous expression, attenuation correction only requires the estimation of the μ linear attenuation coefficient of each tissue. The original method used a transmission image generated from a radioactive source rotating around the center of the scanner, exposing all detectors to uniform radiation, but it is a time consuming process. An extended alternative in standalone PET units is the post-injection transmission scan. This eliminates the need to correct for patient movement, but detectors need to efficiently distinguish transmission and emission activities (Daube-Witherspoon et al., 1988).

Table 2: Density and linear attenuation coefficients for most common tissues in PET. Modified with permission of Springer Nature from (Bailey et al., 2005).

Material	*Density (p) [g*cm-3]*	*μ [cm-1]*
Adipose tissue	*0.95*	*0.090*
Water	*1*	*0.095*
Lung	*1.05*	*0.03*
Smooth muscle	*1.05*	*0.101*
Cortical bone	*1.92*	*0.178*
NaI(Tl)	*3.67*	*0.34*
Bismuth germinate (BGO)	*7.13*	*0.95*
Lead	*11.35*	*1.75*

The expansion of dual PET/CT scanners led to the implementation of an attenuation correction method based on the x-ray CT transmission scan. The main advantages offered by this method are: it is much faster than the previous method, since a CT scan only needs one or two minutes while the standard PET transmission scan needs between 20-40 minutes, and on the other hand, the CT data brings much less noise to the acquisition. In addition, CT transmission scans can be acquired after the injection of the radiotracer, allowing to acquire unbiased transmission scans and taking better advantage of the scanning time. All this has led to significant improvements in PET image quality thanks to the CT-based attenuation correction method, making it a gold standard for PET/CT scanners. However, there are factors for improvement such as respiratory movements or difficulties in converting the low-energy CT data to estimate the attenuation coefficients for 511 keV, which can cause some artifacts in the PET image (R. Schmitz et al., 2013).

Recently, the development of PET/MR scanners poses a challenge in attenuation correction, since MR does not acquire information on attenuation coefficients. The main difficulty in determining attenuation coefficients is locating the most attenuating structures in the body and assigning them an attenuation coefficient at 511 keV. There are different approaches based on the segmentation of the different structures of the body, but it remains challenging (Zaidi et al., 2007).

1.1.5.3 Randoms correction

Random coincidences are an important part of the data acquired in PET imaging, since they generate a signal uniformly distributed in the background of the image, leading to significant quantitative errors.

Efforts are been made to reduce the coincident time window with more efficient electronics or with crystals with shorter scintillation decay times. However, this time window should be kept long enough not to lose any true coincidences. Therefore, the selection of the time window will have to maintain a balance between the sensitivity to detect true events and decrease the acceptance of randoms.

Different randoms correction methods have been proposed:

a) A first way of correcting these coincidences is estimating the distribution of the randoms within the body by fitting a parabolic or Gaussian function to the tails outside the body. Thus a ratio of the randoms that can be eliminated is calculated from the acquired sinograms. In addition, it is necessary that the body does not cover the entire FOV so the tails have a certain length, contain a good number of counts and can be fitted reasonably well (Meikle & Badawi, 2005).

b) Another correction option is using the detected single events. In Equation 5 we saw how the random event count rate could be calculated for each LOR for a given time window. These measurements can be subtracted from the acquired data to correct them. The main disadvantage of this method is that measuring single events is very inefficient and the data measured by this method is affected by the electronic limitations of the PET scanner as the dead time of detectors or the sensitivity (Saha, 2010a).

c) One of the most accurate and frequent methods to correct the effect of randoms is the delayed channel method. In this process, the channel through which one of the annihilation photons is recorded is delayed several times the duration of the coincidence window. This delay in the detection of events leads to any coincidences detected are random. Then these matches can be removed from the acquired data. The advantage of this method is that the delayed channel matches assume the same dead-time as the prompt channel matches. However, the delayed coincidences contribute to increasing the dead-time of the system and, more importantly, the estimation of randoms in each LOR adds noise to the data. In this sense, the estimate is poorer than the previous method. To solve this, most implementations of the delayed channel method allow the data of the delayed channel and the prompt channel to be acquired separately. This allows the estimated randoms to be post-processed to reduce noise before removing them from the prompt data. Although the storage space has to be controlled since acquiring the randoms separately doubles the size of the saved data (Meikle & Badawi, 2005).

1.1.5.4 Scatter correction

Scatter events cause a loss of contrast and resolution in the measured PET signal. This makes correcting scattered events a very important step in data processing. Some of the most used methods are discussed below.

a) The dual energy window methods. These methods make use of the assumption that the highest proportion of scatter events occur in the region of the single photon energy spectrum, below the photopeak, or above a certain upper energy limit where only unscattered photons are detected. Thus, different energy windows can be used to estimate and remove the scatter distribution within the photopeak window (350 to 650 keV). The Estimation of Trues method uses an energy window between 511 keV and 650 keV which overlaps with the upper part of the photopeak window (Figure 18a) (Meikle & Badawi, 2005). On the other hand, the Dual Energy Window method uses an energy window lower than the photopeak window (Figure 18b). Extensions of these methods with 3 or more energy windows are often used to achieve a more accurate measurement of scattered data (Figure 18c).

b) The convolution method. While the energy window methods use auxiliary windows to estimate the scatter distribution, the convolution methods use the integral transformation of the projections detected in the photopeak window to model this distribution. The location and size of the source, detection angle and other factors are taken into account in an iterative process to estimate the scatter. The best estimate of the scatter is scaled and subtracted from the acquired image

(Saha, 2010a). This process works well in relatively homogeneous environments, such as in neurological studies, but it does not work well on more complex bodies such as the thorax (Meikle & Badawi, 2005).

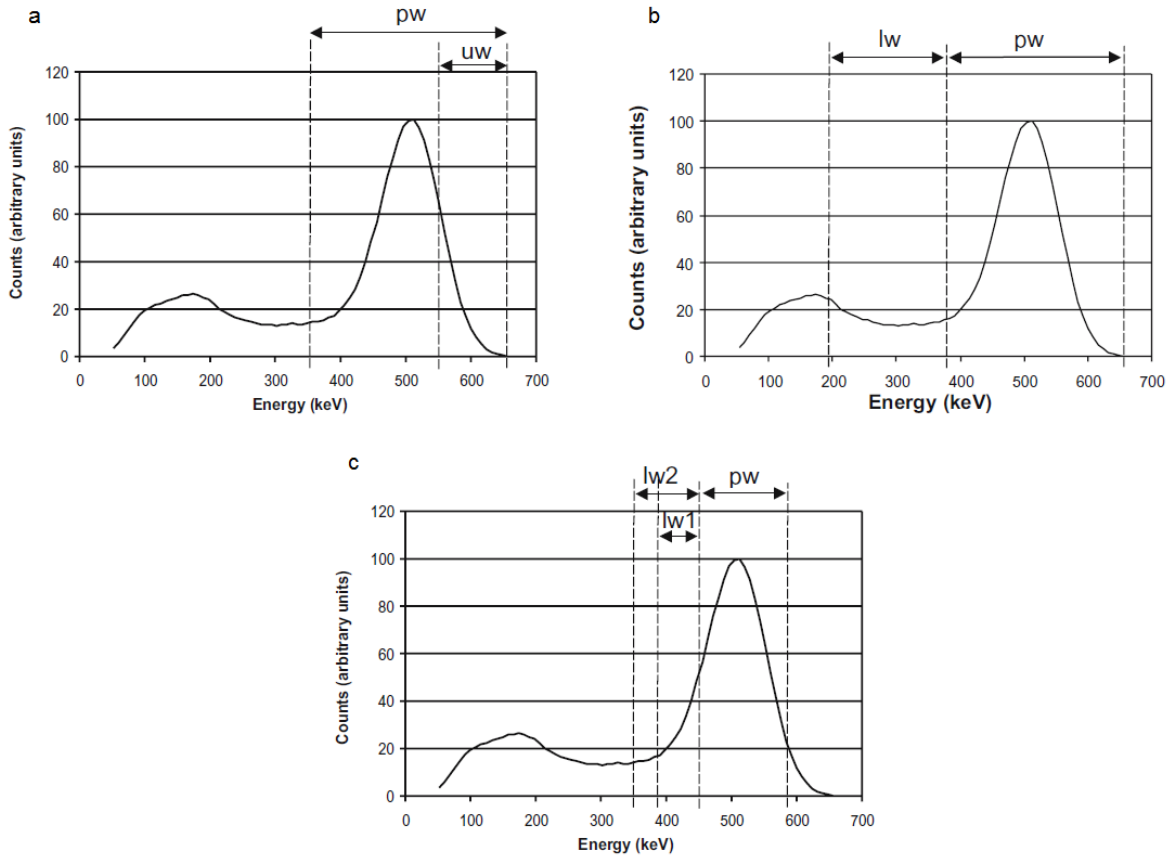

Figure 18: Energy window methods for scatter distribution estimation: Estimation of Trues (a), Dual Energy (b) and multiple energy (c). Adapted with permission of Springer Nature from (Meikle & Badawi, 2005).

c) Single Scatter Simulation methods. Another way to estimate the scatter contribution to projections is through simulation techniques starting from an attenuation map and another with the initial distribution of the radiotracer without scatter. A first approach is through Single Scatter Simulation methods (Ollinger, 1996; C. C. Watson et al., 1996). These methods assume that the scatter events detected in a LOR are generated by single Compton events. A random distribution of scatter points is performed to later calculate the number of events that contribute to the LORs using the Klein-Nishima formula. The scatter sinogram is obtained by interpolation and it is scaled and subtracted from the acquired sinogram before reconstructing the image (Ollinger, 1996; C. C. Watson et al., 1996). These methods, despite having reasonable precision in most cases, have some drawbacks, such as that in obese bodies they can present difficulties, they are computationally expensive and when calculations are performed on uncorrected data, there is an overestimation of the scatter distribution (Meikle & Badawi, 2005). To improve these aspects, more efficient versions have been developed and are implemented in reconstruction process (Accorsi et al., 2004; Polycarpou et al., 2011; Tsoumpas et al., 2004, 2005; Werling et al., 2002).

d) MC Simulation methods. A better way to use simulation to correct scatter events is through Monte Carlo (MC) simulations. Unlike previous analytical simulation methods, MC simulations generates scattered and unscattered data separately. This makes it a great tool to perform scatter correction for any specified attenuation and emission distribution or PET configurations. In this method, a 2D reconstruction of the blank and transmission data or a CT image is used as the attenuation map and an image reconstructed by FBP as an initial estimate of the activity distribution. This initial image is assumed to represent the true radiotracer distribution with no scatter events. The algorithm then generates photon pairs according to the initial activity distribution and tracks the random interactions through the scattering medium according to the attenuation map. From the simulation, the scattered sinograms are generated, which are smoothed and removed from the measured data to obtain the unscattered data. This process can be repeated to reduce the initial error by assuming that the reconstructed image has no scatter. MC is one of the most accurate that we have discussed. However, it requires great computational power to carry out the necessary simulations and to have sufficient counting statistics for an accurate scatter correction, since a large part of the tracked photons will undergo energy or trajectory changes that will impair their detection (Meikle & Badawi, 2005; Saha, 2010a).

1.1.5.5 Dead time correction

Between the detection of one coincidence event and the next one, the PET scanner and in particular the detector block need a recovery time. At this time that goes from a photon interacts with the scintillator crystal until it is processed as a count, it is classified as a coincidence event when another photon reaches another detector in the same time window and the detector is again available to receive the next event is called dead time of the PET scanner.

Dead time sources are highly dependent on the architecture and design of the PET scanner. An influencing factor is the integration time of the charge of a photon in the PMT after depositing the energy on the scintillator crystal. If a new photon reaches the crystal while the previous one is still being integrated (called pulse pileup phenomenon) it can happen that both events are discarded or considered as a single event but with incorrect energy and position (Figure 19), which leads to distortions in the image. There are other factors such as the "reset" time of the electronics detectors or the time to process a coincident event that do not allow accepting new coincidences and contribute significantly to the scanner dead time. To improve in this sense, pulse pileup rejection circuits, high-speed electronics or buffers to retain overlapping events during the dead time are often used (Saha, 2010a).

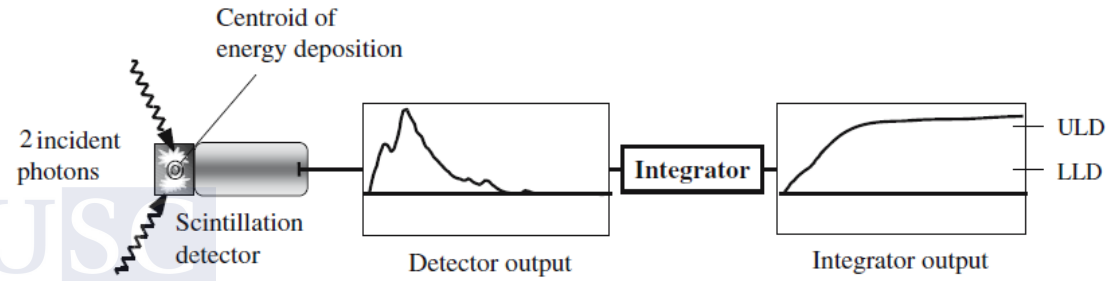

Figure 19: Pulse pileup phenomenon. Adapted with permission of Springer Nature from (Meikle & Badawi, 2005).

A basic option to correct the dead time is to collect data from observed count-rates of decay sources, calculate correction factors and apply them to the acquired data. However, this method does not take into account the spatial variations in the distribution of activity that can alter the count-rate in each part of the system. Therefore, a more precise option is to construct a model where the correction factors from all sources are applied to each subsystem of the scanner (Meikle & Badawi, 2005).

Dead time models are often made up of two components: paralyzable and non-paralyzable (Knoll, 2000). The paralyzable time refers to when the system cannot process any events for a time after each event, but the system is not considered dead. For example, when the charge of a photon is being integrated into a PMT but more photons arrive to deposit energy on the crystal, which must decay before being able to process the next event. In the non-paralyzed case, the system is considered dead, so additional events are ignored. These two components are often used in series in PET scanners.

1.2 BRAIN IMAGING

Since this thesis is focused on epilepsy, in this section we discuss some of the main types of brain images that have been gradually introduced into the clinical routine for the study of epilepsy and other important neurological diseases and how they complement each other to achieve a better diagnosis. We will also see different ways of evaluating these studies to observe the changes caused in the brain due to the disease, be able to differentiate pathologies or even obtain information on its initial states.

1.2.1 MRI

MRI has become an essential tool for diagnosis and research in medicine, becoming the gold standard for the study of brain structures, with a particular focus on the study and differentiation of neurological and psychiatric diseases such as epilepsy, dementias, parkinsonisms and other disorders. The main advantage of MRI compared to other types of images is its great spatial and temporal resolution, showing a strong contrast between the different tissues of the brain, something impossible in other modalities.

1.2.1.1 Clinical use

a) Epilepsy

In clinical routine, structural MRI is an essential tool for the diagnosis and study of the underlying pathophysiology of epilepsy, since it contributes greatly to the detection of the structural brain abnormalities involved. In the most common type of epilepsy, temporal lobe epilepsy (TLE), MRI favors the detection of gliosis and impairments in the temporal lobe, hippocampus and amygdala (R. Kuzniecky et al., 1987; D. H. Lee et al., 1998). In frontal lobe epilepsy, focal frontal lobe or multilobar abnormalities usually appear (Lorenzo et al., 1995) and in occipital lobe epilepsy, a less frequent type, occipital cortical dysplasia or occipital periventricular heterotopia among other syndromes (Taylor et al., 2003). In Figure 20 we can see some examples of the different types of epilepsy and their manifestations on MRI.

Furthermore, MRI has an important role in presurgical evaluation in patients with refractory epilepsy (seizures cannot be properly controlled using antiepileptic drugs). MRI can help visualize and detect over 60% of frontal lobe lesions and over 80% of temporal lobe lesions (Álvarez-Linera Prado, 2012). In particular structural impairments such as hippocampal sclerosis, cortical dysplasias or focal lesions are good indicators on MRI to select candidates for surgery since surgical treatment of focal cortical malformations has a high probability of cure (Duncan, 1997; Dupont & Baulac, 2004; R. I. Kuzniecky, 2005).

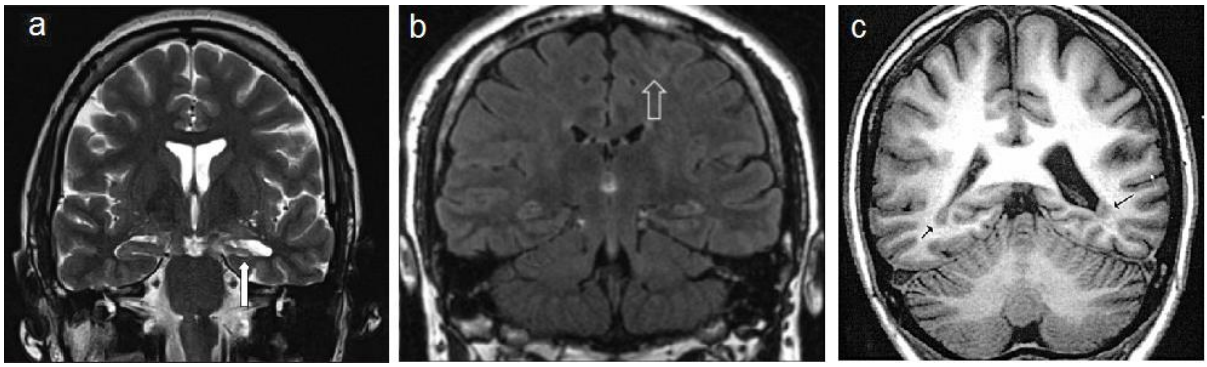

Figure 20: Coronal MR images show a decrease in the volume of the left hippocampus in a case of TLE (a), a focal cortical dysplasia of the left superior frontal sulcus in a case of frontal lobe epilepsy (b) and bioccipital periventricular heterotopia in a case of occipital lobe epilepsy. Adapted with permission of Wolters Kluwer Medknow Publications and Oxford University Press from (Singh et al., 2013; Taylor et al., 2003; Winston et al., 2013).

b) Other clinical uses

Regarding the study of other neurological diseases such as dementia, MRI can show the degree of anatomical deterioration of different regions or reveal atrophy patterns associated with the appearance of certain dementias (Raposo Rodríguez et al., 2018). Among all dementias, Alzheimer's disease (AD) is the most widespread in the population, frequently being the phase after mild cognitive impairment (MCI). Numerous structural imaging studies have been performed to find brain atrophies and other factors that characterize the progression of MCI to AD (Frankó et al., 2013; S. H. Lee et al., 2016; Whitwell et al., 2008). In Figure 21 we can see T1-weighted MRI images of how gray matter (GM) atrophy evolves from a healthy subject to a subject with MCI and a subject with AD.

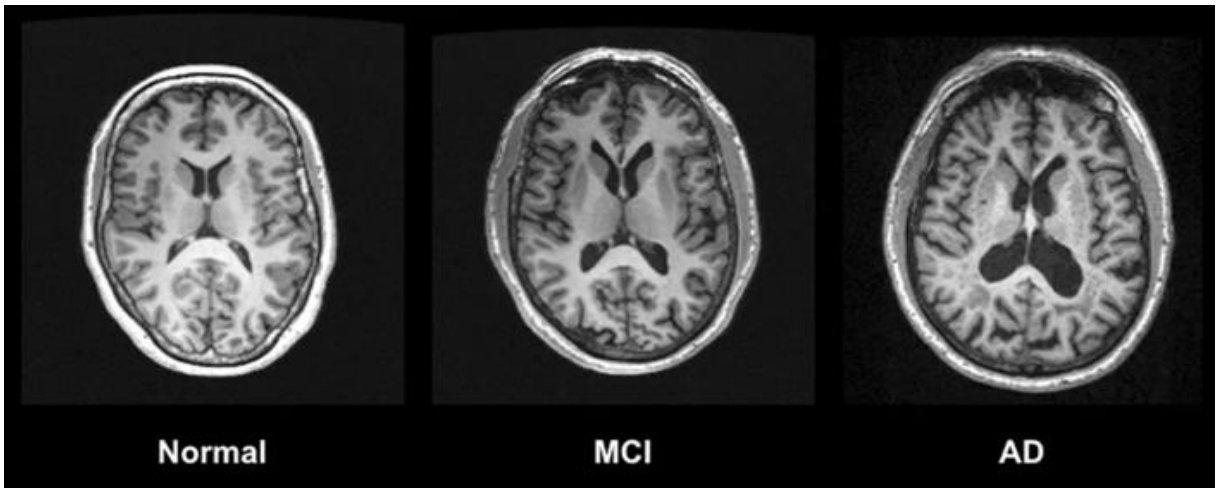

Figure 21: T1-weighted images showing GM volume reduction in a healthy subject, in a MCI patient and in an AD patient. Reproduced with permission of Springer Nature from (Chandra et al., 2019).

Another of the main advantages of using MRI for the study of dementias is to be able to observe the patterns of structural deterioration and discriminate between AD and other dementias as frontotemporal lobe dementia (FTLD) or dementia with Lewy bodies (DLB). In Figure 22 we can see examples of some characteristic patterns of AD, FTLD and DLB.

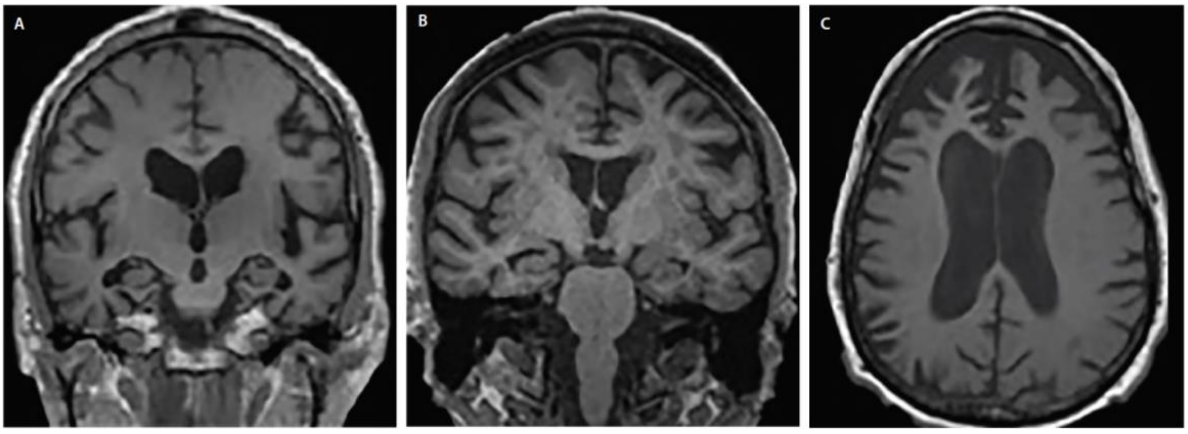

Figure 22: Atrophy patters in AD (A), DLB (B) and FTLD (C). Coronal T1-weighted images show cortical deterioration in general but with greater atrophy in the hippocampus in AD (A) than in DLB (B). Axial T1-weighted image show a deterioration in the frontal and prefrontal cortices in FTLD case (C). Adapted with permission from (Ayers et al., 2019).

In relation to Parkinson's disease (PD), traditional MRI does not usually show changes in the anatomy of the brain. For this reason, more advanced MRI techniques are often considered, such as functional MRI or diffusion imaging (Pyatigorskaya et al., 2014).

1.2.1.2 Image analysis

a) Quantification methods

In MRI, different patterns of sclerosis, lesions or dysplasias are associated with specific diseases. Traditionally, visual analysis has been the most efficient method to analyze these pathologies. However, this does not help to refine the degree of atrophy present (Vemuri & Jack, 2010) or it may not allow detect the lesion (Muhlhofer et al., 2017; Wang & Alexopoulos, 2016). It is also a subjective evaluation and time consuming used in large groups of subjects. This has led to the development of automatic and semi-automatic quantitative techniques that allow post-processing and evaluating morphological changes in single subjects with greater efficiency and precision. One of the most popular options is voxel-based morphometry (VBM) (Ashburner & Friston, 2000) using T1-weighted images because it provides biologically reliable results by performing statistical tests at voxel level in the whole brain. The most common situation is to find atrophy patterns between a patient and a group of healthy controls. Then a t-test would be performed on each voxel of the brain to obtain regions with significant morphological differences.

Before the statistical analysis, it is necessary to preprocess the images, since we need the location of each anatomical structure to be the same in all subjects so that they coincide at the voxel level. The basic pipeline has the following steps: segmentation, spatial normalization and smoothing of the images (Whitwell, 2009), as can be seen in Figure 23:

a. Inhomogeneity correction and segmentation: an inhomogeneity correction is applied to the T1-weighted images. The images are then segmented into different tissue compartments: GM, white matter (WM), cerebrospinal fluid and others.

b. Spatial normalization: it consists of applying to each segmented image a series of mathematical transformations to place all the images of the different subjects in the same standard space. In particular, a set of linear transformations are

performed to transform the space followed by non-linear deformations. In this way, the images will not only be in the same standard space, but the anatomical structures will have a similar shape, so that they coincide point by point.

c. Spatial smoothing: the segmented images in standard space are smoothed, so that the intensity value in each voxel is weighted by the average of the adjacent voxels, obtaining a blurred image of each segmented image. This helps to decrease intersubject variability during statistical analysis.

Once the preprocessing is done, the images are ready to be used in the statistical analysis. This analysis is usually a t-test where the null hypothesis is that the difference of a tissue volume between the groups is zero, although depending on the images and parameters with which we work, there may be other types of tests. Depending on the chosen p-value, the t-test will generate a map of t-statistical values with all voxels where the null hypothesis is not fulfilled and, therefore, there are significant differences between the groups.

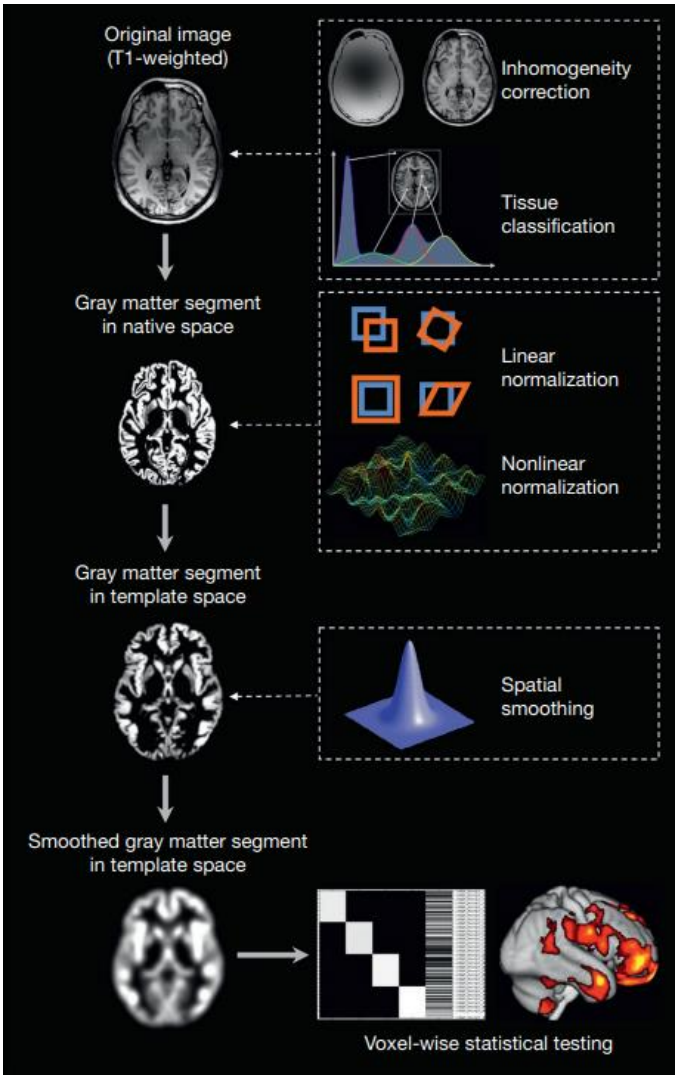

Figure 23: Workflow of a VBM analysis using T1-weighted images. Reproduced with permission of Elsevier from (Kurth et al., 2015).

b) Examples

In epilepsy, it has provided essential information for the detection of cortical abnormalities, especially in nonlesional MRI situations in the context of epilepsy pre-surgical evaluation (Wang & Alexopoulos, 2016). In cases of TLE, the VBM analysis usually shows an asymmetrical volume distribution mainly in hippocampus and less frequently in parahippocampal, entorhinal cortex and contralateral hippocampus (Keller & Roberts, 2008; Mueller et al., 2006) (Figure 24). In extratemporal lobe atrophies, there is a more bilateral distribution of lesions mainly affecting the parietal lobe and thalamus (Keller & Roberts, 2008).

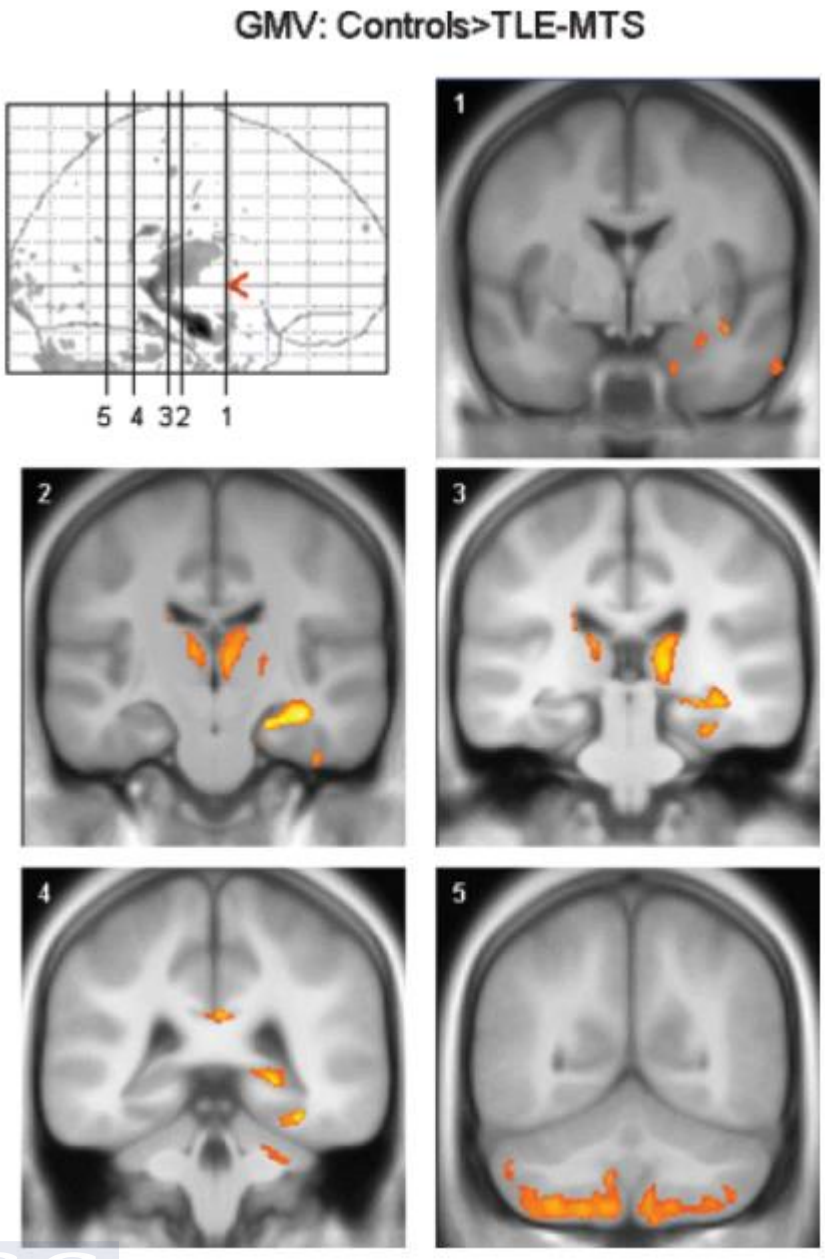

Figure 24: Differences in the volume of GM between a control group and a group with TLE. The loss of volume extends to hippocampus, extrahippocampal and extralimbic areas. Adapted from (Mueller et al., 2006).

Regarding dementias, the VBM analysis is a useful tool to characterize the reduction of GM volume in patients compared to a control group, across the whole brain. Atrophic changes in temporal lobe structures (hippocampus, parahippocampal cortex, lingual and fusiform gyri, amygdala) are commonly found in multiple studies for cases of MCI and AD (Busatto et al., 2008; Chételat et al., 2005; Ferreira et al., 2011; Yao et al., 2011).

Another notable role of VBM analysis in dementias is its usefulness in the differentiating diagnosis between AD and other dementias such as FTLD or DLB. In FTLD, the VBM analysis shows evidence that GM patients undergo volume reduction in frontal cortex, insula, and striatum (Pan et al., 2012), less frequent areas in AD. While in DLB patients, the higher level of atrophy in the dorsal brain stem and the better preservation of the medial temporal lobe, hippocampus and amygdala compared to AD patients improve differentiation (see Figure 25) (Burton et al., 2002; Matsuda et al., 2019; R. Watson et al., 2012).

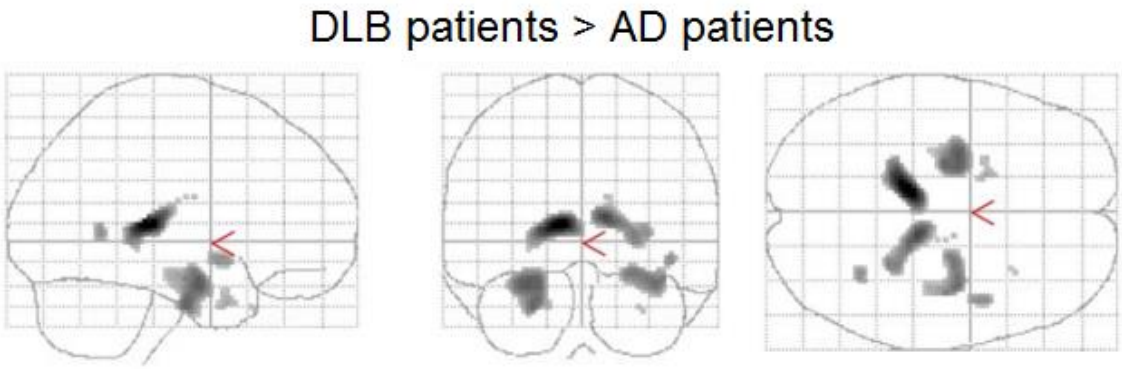

Figure 25: Statistical parametric maps of the most preserved areas in a group of DLB patients compared to a group of AD patients. Adapted with permission of Elsevier from (Burton et al., 2002).

The main limitation of the VBM is that it is designed to test differences between groups, being neither optimized nor sufficiently validated for the detection of areas with great variability between patients, such as in cases of epilepsy with focal cortical dysplasia (Yasuda et al., 2010), for the diagnosis of individual cases. There is validated software for performing VBM in single subject cases, such as Neurocloud Vol (https://www.qubiotech.com/soluciones/neurocloud-vol/), but it is not present in all clinical centers. Despite this limitation, the VBM analysis is an important tool for the investigation of different aspects in groups of patients, providing a better knowledge of the morphological damage suffered in the brain and complementary to other modalities and types of analysis, as we will see in the following sections.

1.2.2 FDG-PET

The compound 2-Deoxy-2-[^{18}F]fluoro-D-glucose (FDG) consists of a molecule similar to glucose where an OH group has been replaced by the radioisotope ^{18}F. FDG, like glucose, enters cells through glucose transporters. FDG and glucose are phosphorylated by hexokinase. However, unlike glucose, the FDG molecule is not metabolized and is trapped in tissue (see Figure 26).

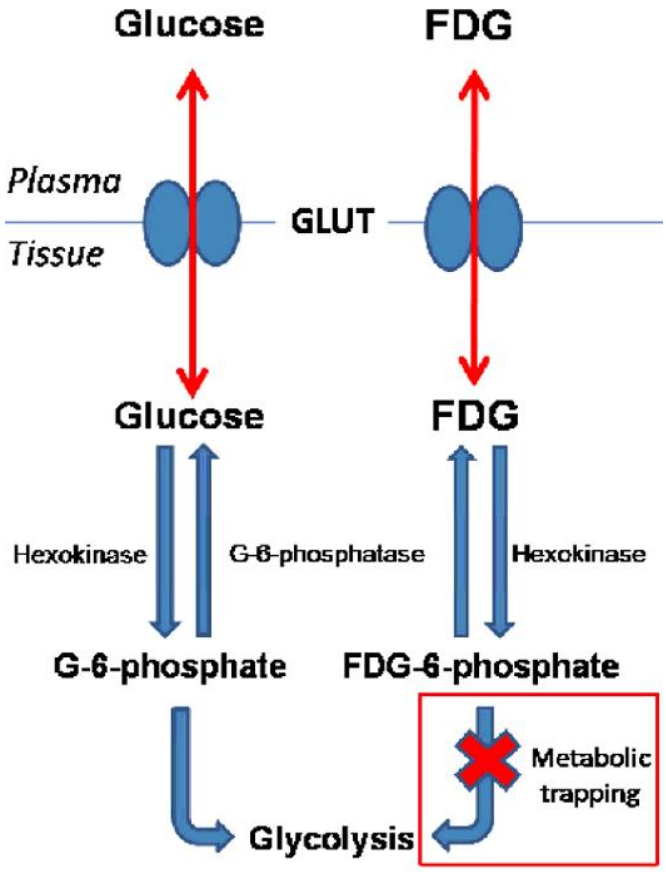

Figure 26: Comparison of glucose and FDG cellular uptake and metabolism. Reproduced with permission of Elsevier from (Filho et al., 2011).

As glucose is the main source of energy for the brain, this trapping makes possible to study cellular metabolism and see the physiological and biochemical changes in the brain. The alteration of brain metabolism in different areas would reflect an alteration in synaptic activity resulting from a combination of processes involved in the pathogenesis of neurodegenerative diseases. For this reason, FDG is one of the most widely used biomarkers for diagnosis in neurology.

1.2.2.1 Clinical use

The main indications for the use of the brain FDG-PET are presurgical evaluation of refractory epilepsy, early and differential diagnosis of dementia and differential diagnosis between Parkinson disease (PD) and other atypical parkinsonisms; less common cases of patients with stroke or psychiatric disorders (Schöll et al., 2014).

a) Epilepsy

FDG-PET has proven to be a valuable tool in clinical routine to support MRI in the non-invasive localization of epileptogenic brain regions in intractable epilepsy for surgery for many years (Casse et al., 2002; Willmann et al., 2007), especially in cases where no signs of lesions on MRI (Cendes, 2013; Jaisani et al., 2020; Muhlhofer et al., 2017; Rathore et al., 2014) proving to have a higher sensitivity than other kind of images (Sarikaya, 2015). In particular,

the documented sensitivity of FDG-PET is around 85% -90% in cases of TLE, while it drops to values around 55% in frontal lobe epilepsy or even lower in cases of occipital lobe epilepsy (Kumar & Chugani, 2017). In any case, it is a very useful imaging modality for presurgical evaluation, especially if it is supported by quantitative analyzes to improve diagnostic confidence. Sometimes it is the only imaging method with a positive result to evaluate the option of surgical intervention.

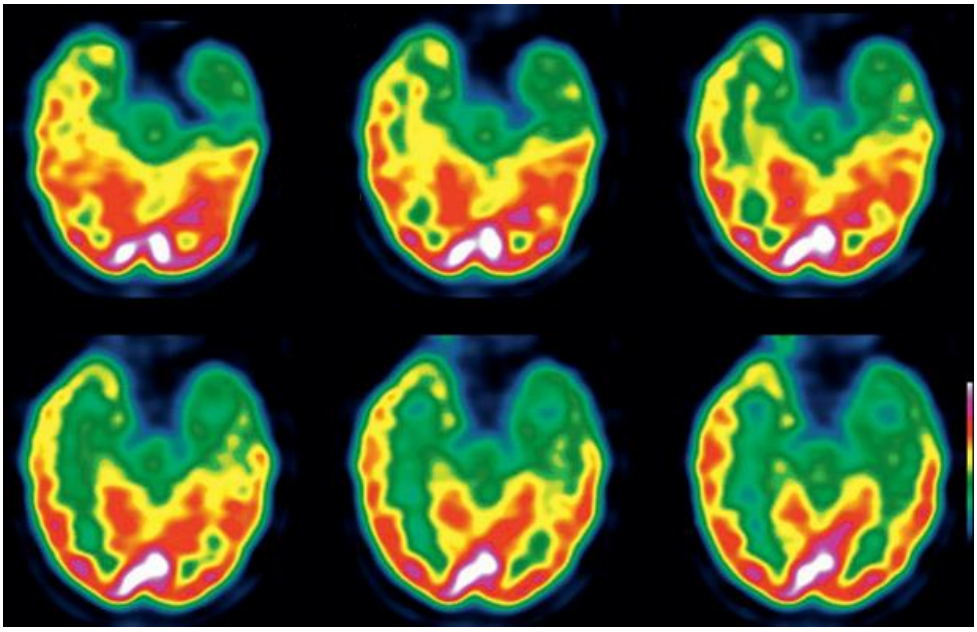

Figure 27: Interictal FDG-PET study in a patient with temporal lobe epilepsy. Reproduced with permission of Elsevier from (Kumar et al., 2012).

The most common is to perform the acquisition of the FDG-PET study in an interictal period, due to the short life of FDG and technical difficulties in acquiring ictal studies in patients with infrequent epileptic seizures. The characteristic observed in the FDG-PET studies are small areas or foci with low glucose uptake (hypometabolism) during the interictal period (Figure 27). The reasons why these hypometabolic foci appear during the interictal period are not clear, but they may be due to different mechanisms such as neuronal or synaptic density loss (Willmann et al., 2007).

Ictal PET, although less frequent, can also be performed. Several authors (Meltzer et al., 2000; Nooraine et al., 2013) have reported ictal PET studies where areas of hypermetabolism have been observed in frontal and occipital regions. The correlation between these hypermetabolic areas and the good postoperative results support the usefulness of ictal PET, especially in cases of frontal or occipital epilepsy (Ladrón De Guevara, 2013).

Some limitations of FDG PET for the localization of epileptogenic foci are: the low resolution of PET studies and the fact that the observed changes in metabolism usually extend beyond the real ictal zone. Therefore, it is important to rely on other imaging modalities when defining surgical borders.

In addition to the location of epileptogenic foci, FDG-PET also shows the general status of the other areas of the brain. This may lead to correlations between epileptogenic zones and the malfunction of other regions of the brain or functional deficit zones (Jaisani et al., 2020; Sarikaya, 2015; Vielhaber et al., 2003), forming a dysfunctional neural network more extensive than the specific epileptogenic zone. Therefore, FDG-PET studies provide prognostic value in

the evolution of neural networks associated with epilepsy. On the other hand, the findings observed in the FDG-PET studies will also influence the post-operative status, especially in cases with limited hypometabolic extent where the probability of a good outcome is greater (Verger et al., 2018).

b) Other clinical uses

Regarding dementias, in MCI cases the role of FDG-PET is to evaluate the reduction in brain metabolism in relation to neural injury or synaptic dysfunction and provide information to predict whether this MCI will evolve to AD or other dementias, such as DLB or FTLD (DeCarli, 2003; Drzezga et al., 2003; Ito et al., 2015; Pagani et al., 2017). Among all types of dementia, AD is the most common, especially in subjects over 65 years of age with 50-60% of cases of dementia (Bohnen et al., 2012). Many FDG-PET studies are performed to study this disease (J. M. Hoffman et al., 2000; Mosconi et al., 2006). In Figure 28 we can see a representation of how healthy levels of metabolism decrease in cases of MCI and subsequently form different patterns of hypometabolism in AD.

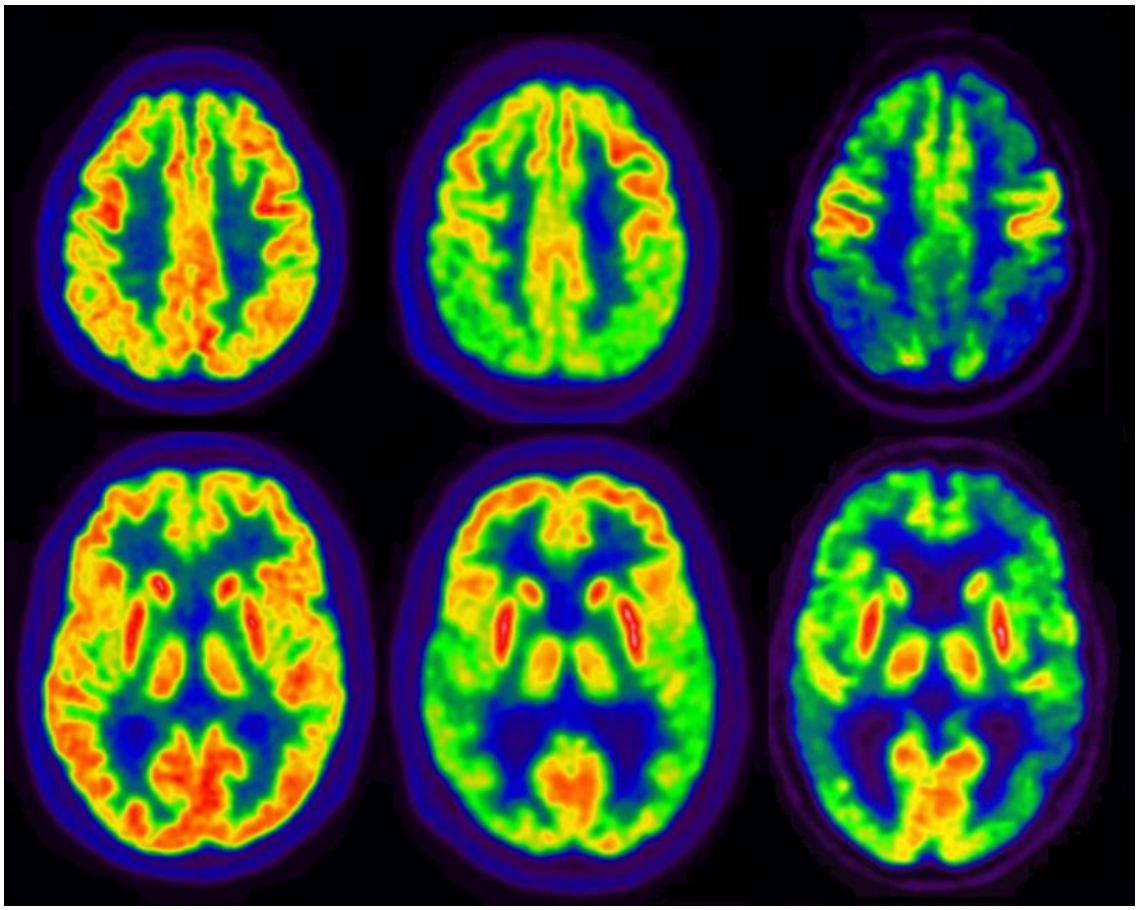

Figure 28: Representative FDG-PET images of a group of healthy people without cognition impairment (NCI), another group with MCI and another with AD. Adapted with permission from (Arbizu et al., 2015).

On the other hand, hypometabolism patterns are characteristic of each neurodegenerative disorder (see Figure 29), leading to a fairly widespread use of FDG-PET as a tool to differentiate AD from other neurodegenerative dementias (Bohnen et al., 2012; Guillén et al., 2020; Kato et al., 2016).

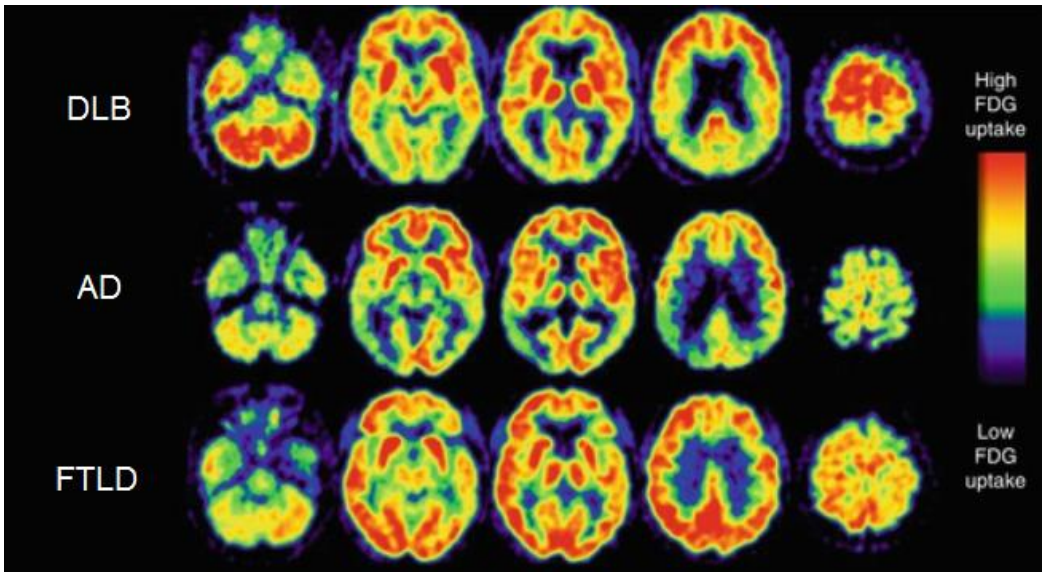

Figure 29: Common hypometabolic patters in neurodegenerative dementias using FDG-PET. Adapted with permission from (Heinen et al., 2013).

Regarding Parkinson's disease, there is a fairly widespread clinical use of FDG-PET as a modality to identify patients with idiopathic PD and facilitate their distinction from other forms of parkinsonism such as progressive supranuclear palsy syndromes (PSP), multiple system atrophy (MSA) or corticobasal syndrome (CBS). In Figure 30 we can see some of the typical metabolism patterns of the different forms of parkinsonism.

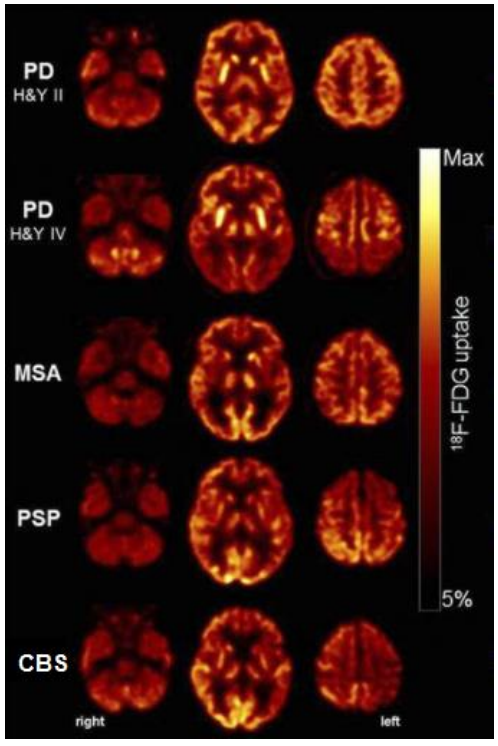

Figure 30: Typical FDG-PET findings in patients with different parkinsonism. Cross-sections at levels of cerebellum, basal ganglia and dorsal frontoparietal cortex in PD (stage 1 and 4), PSP, MSA and CBS. Adapted with permission of JNM from (Meyer et al., 2017).

1.2.2.2 Image analysis

a) Quantification methods

Visual-based qualitative analysis is the most widespread method for the evaluation of FDG-PET images (Varrone et al., 2009). However, this evaluation is affected by an important variability depending on who makes the evaluation or even on the changes of criteria experienced by the same nuclear physician (Bohnen et al., 2012). The differential characteristic of PET compared to other imaging modalities is that it allows the quantitative study of the molecular processes that occur in vivo, increasing its sensitivity. This makes possible to more accurately detect changes in metabolism that go unnoticed by the expert eye. In addition, the use of statistical analyzes allows to observe the differences in metabolism with respect to a control group or the effects due to a certain condition making FDG-PET a very useful modality in the early and differential diagnosis of neurological diseases (Mayoral et al., 2019; Meyer et al., 2017; Perani et al., 2014). As a consequence, various ways of extracting quantitative values from PET images have been implemented with the aim of supporting visual analysis and leading to a more objective diagnosis. A simple form used in clinical routine is the standard uptake value (SUV), which measures the absolute number of counts in a VOI. However, this method is not usually used in brain imaging because it is highly variable from one subject to another, and even within the same subject depending on different factors.

In recent years, more complex and automated quantitative analyzes have been developed. These allow for more complete statistical analyzes to be carried out and to greatly standardize the steps to be followed in brain PET processing for a better comparison between subjects. These methods are voxel-based analyzes (VBA), in which, point by point, a statistical map of p-values that reflects the differences observed between subjects under certain conditions is generated. The software that implements this type of analysis is very diverse and even today they continue to be developed (Niñerola-Baizán et al., 2020).

Before the statistical evaluation, a preprocessing of the images is required since the head will not be in the same position, nor will the structures have the same shape when comparing images from different patients or acquired at different times. This is essential for VBA as we need a point-by-point correspondence between all the images. The preprocessing for VBA consists of a series of mathematical transformations that are carried out to the images in order that the same voxel corresponds to the same anatomical region for all the images. These mathematical techniques are realignment, co-registration, spatial normalization, and smoothing.

The realignment consists of rigid-body transformations that modify the original coordinate space of the images to bring them to a common space in a voxel-to-voxel correspondence. This technique is frequently used when we want to compare images of the same patient and modality but acquired at different times, such as PET studies before and after a treatment. The transformations applied in this movement correction can be seen in Figure 31a and Figure 31b. The process consists of an iterative algorithm that, based on initial spatial correlation values, tests different combinations until the rotation-translation parameters that minimize the sum of squared difference between the images are found.

The co-registration are the mathematical transformations applied to place images belonging to the same patient but of different modalities, in the same space. For instance, when we want to merge a PET image with the corresponding MRI of the patient, placing them in the same coordinate space. This process is widely used, not only as part of the preprocessing of a VBA, but also for the diagnosis of the PET image itself, since by co-registering it with the MRI we can anatomically locate the metabolic changes reflected in the PET, improving the diagnosis (Ding et al., 2018; Salamon et al., 2008). The transformations in this process are similar to the

realignment (Figure 31a-b) with the difference that in realignment the images have the same voxel size while, in this case, the MRI has a higher resolution than the PET image. Therefore, a resampling has to be also applied to the data. The co-registered PET image has the same resolution and orientation as the reference MRI (see Figure31c). The resampling of the values of each voxel is carried out based on the values of the adjoining voxels, applying types of linear interpolations.

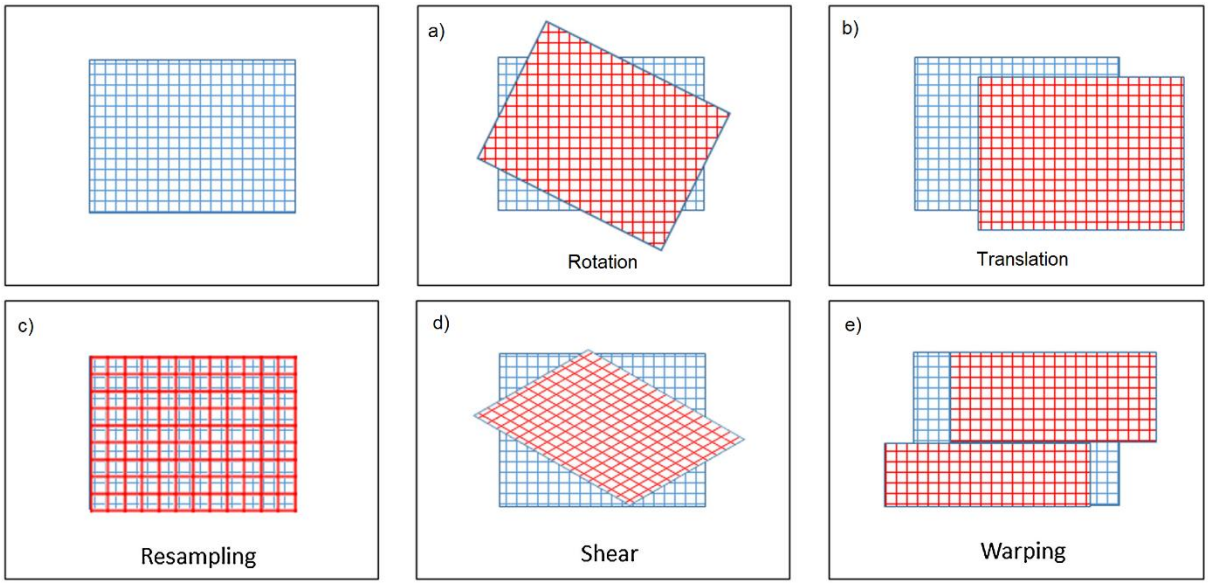

Figure 31: Mathematical spatial transformations applied to images during preprocessing. Adapted with permission from (Niñerola-Baizán et al., 2020).

As in the VBM analysis, the spatial normalization rewrites images of the same modality but of different subjects in a standard space (Collins et al., 1998). This normalization is a fairly standardized process because it not only allows group analyzes to be carried out, but also cross study comparisons by reporting the results in the same standard space. As in the previous processes, normalization begins by applying rotations and translations, but later also shear (Figure 31d) and warping (Figure 31e) deformations. In many cases, applying shear-type linear deformations should be enough. However, in cases where there are important differences in the shape of the brain structures, it is necessary to apply non-linear transformations using deformation fields. This is known as warping and can generate artifacts in the images, so it is necessary to verify the normalized images. On the other hand, the transformations to normalize can be done directly based on each PET image. However, if there is an MRI corresponding to each PET image, it is more appropriate to co-register the PET to the MRI and normalize taking advantage of the higher resolution of the MRI. These transformations are then applied to the co-registered PET image to bring it to the standard space.

Once all the images are in a reference space, the same smoothing process as in the VBM analysis is applied. Smoothing is used to increase the signal to noise ratio in PET images, reducing the random noise.

Finally, the smoothed PET images are intensity normalized before analysis. There are different ways to perform intensity normalization: by the total activity in the whole brain, by means of the average uptake on a defined reference region (Borghammer et al., 2008), using a template image, etc. This heterogeneity in the normalization methods strongly influence the

brain FDG-PET quantification. The most suitable normalization method and its possible effects on the quantification output are still being studied.

After preprocessing, the images are ready for VBA. The statistical analysis of the VBA is similar to that seen in the VBM for MRIs. It consists of performing statistical tests configured to observe significant differences between groups of subjects, although other types of statistics can also be performed. In the case of FDG-PET, the statistical maps generated show the areas with significant metabolic differences between groups.

b) Examples

These statistical analyzes have a lot of applications for the evaluation and diagnosis of neurological diseases.

In epilepsy, the quantification of FDG-PET studies is an important support in the visual diagnosis of frontal (Kim et al., 2002) and temporal lobe epilepsy (see Figure 32), even in cases where the visual evaluation is negative (Mayoral et al., 2016), and a useful tool for locating epileptogenic foci in cases of cortical dysplasia. Furthermore, quantification of asymmetry allows generating prognostic indices capable of predicting whether a patient will stop having seizures after surgery (Niñerola-Baizán et al., 2020).

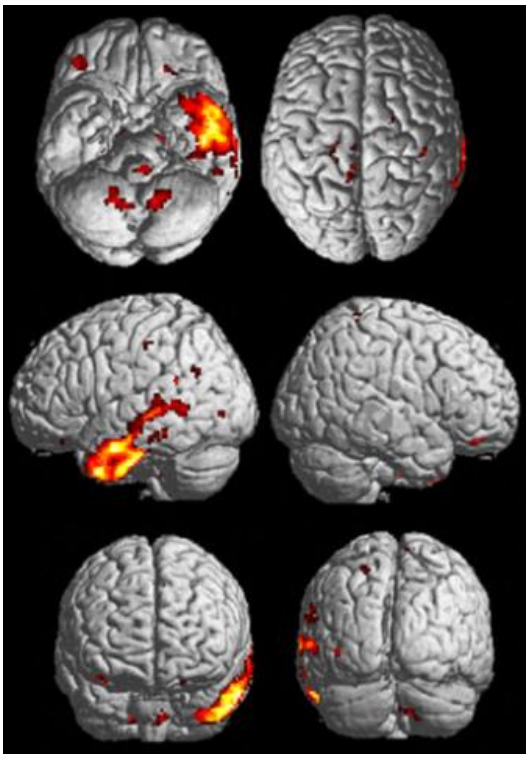

Figure 32: Differences obtained in a VBA between a patient with temporal lobe epilepsy and a control group. Adapted with permission from (Niñerola-Baizán et al., 2020).

Regarding other neurological diseases, such as dementia and parkinsonism, the quantitative analysis is similar to that performed for epilepsy. In particular, VBAs help to observe patterns of hypometabolism to distinguish between different pathologies (see Figure 33) or to study the stage of the disease.

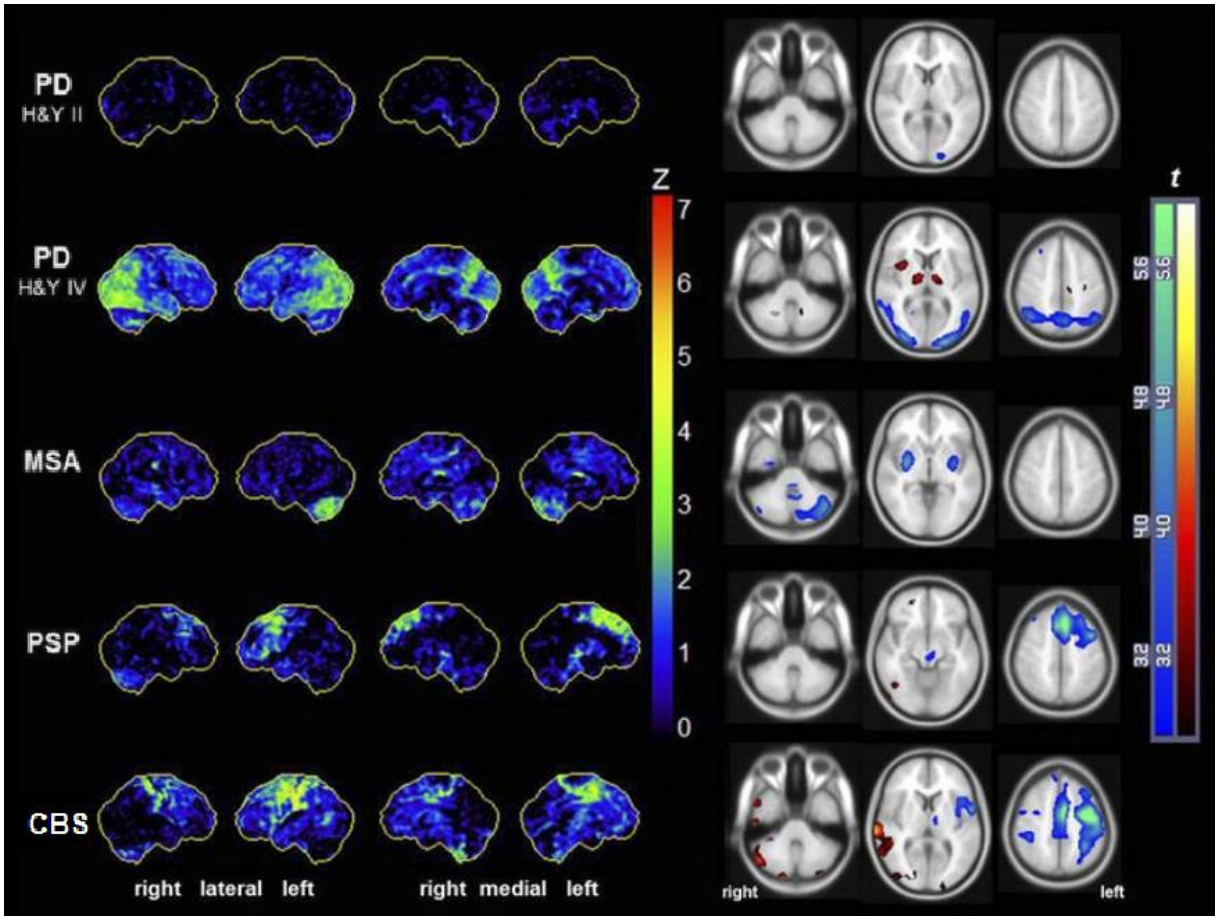

Figure 33: FDG-PET patterns associated to the different parkinsonisms. The first panel shows metabolic deficits compared with control subjects as z-scores. Second panel shows patient vs control results of a VBA as t maps. Adapted with permission of JNM from (Meyer et al., 2017).

As we have seen, the quantification of FDG-PET studies is a great complementary tool to other neuroimaging analyzes and visual as it improves the diagnosis and early detection of different neurological diseases, as well as a greater degree of confidence.

However, FDG-PET may not provide sufficient functional information for the diagnosis of some neurological diseases and it may be necessary to complement or replace FDG with other more specific radiotracers. (Chételat et al., 2020; Emsen et al., 2020; Kumar & Chugani, 2017; Ortner, 2018). Among them, amyloid-PET tracers stand out in the detection of AD and other dementias.

1.2.3 Amyloid-PET

To achieve a better early and differential diagnosis of neurodegenerative disorders leading to dementia, the use of new biomarkers, such as amyloid tracers, is increasingly present. Amyloid-PET allows in vivo and non-invasive observation of the presence of beta-amyloid ($A\beta$) plaques, one of the most common neuropathological features of AD (Chételat et al., 2020). The first abnormalities in AD possibly occur at the functional level with the $A\beta$ involved. Some studies affirm that the spread of amyloid plaques occurs in phases, beginning with the neocortex and extending through the cingulate, striatum, cerebellum and other regions (Vandenberghe et al., 2013).

Multiple radiotracers for clinical and research in amyloid-PET have been developed. N-methyl-[^{11}C]2-(4-methylaminophenyl)-6-hydroxybenzothiazole (^{11}C-PIB) was the first radiotracer described for the study of $A\beta$ plaques, allowing uptake patterns to be found in AD patients. However, the short half-life of ^{11}C (20 minutes) has caused its use in the clinic to be greatly restricted and it is more widely used in research or in centers with cyclotrons (Camacho et al., 2018). This led to the development of ^{18}F-labeled and amyloid-related radiotracers. Currently there are 3 radiotracers for amyloid-PET synthesized with ^{18}F and that are approved for clinical use by different international organizations: ^{18}F-florbetaben (^{18}F-AV-1), ^{18}F-flutemetamol ([^{18}F]3'-F-PIB) and ^{18}F-florbetapir (^{18}F-AV-45). In general terms, the three radiopharmaceuticals do not present notable differences (see Figure 34). They have a similar biodistribution and ability to bind $A\beta$, with a sensitivity of 89-97% and a specificity of 63-93% for detecting AD cases compared to controls. They also show a localization of amyloid in the cerebral cortex similar to ^{11}C-PIB, although they appear to have a greater nonspecific binding to WM than ^{11}C-PIB (Camacho et al., 2018).

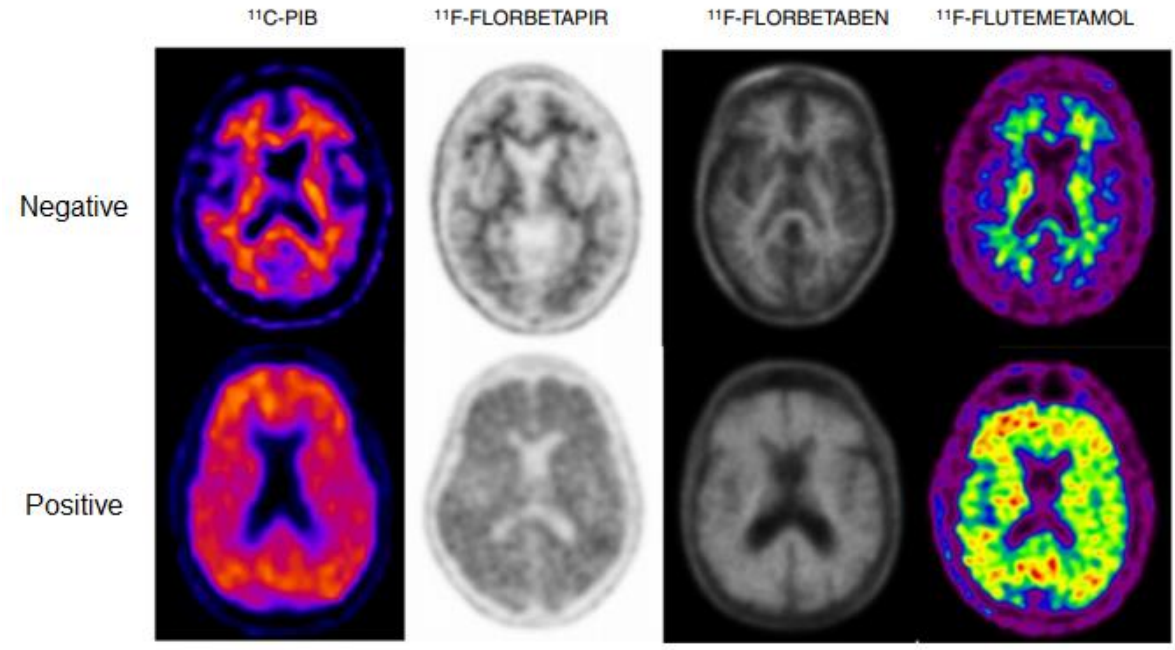

Figure 34: Negative and positive amyloid-PET images for the main radiotracers. Adapted with permission from (Camacho et al., 2018).

1.2.3.1 Clinical use

a) Dementia

Amyloid-PET has various clinical applications. One of the main ones is the early detection of the progression of MCI cases to AD. This is based on the fact approximately 50% of MCI patients have a positive amyloid scan (Chételat et al., 2020; Vandenberghe et al., 2013), being usually negative in FTLD patients and positive in AD patients (Camacho et al., 2018; Chételat et al., 2020). However, we cannot say the same in BLD patients, since some studies show that 66% of BLD patients have positive amyloid-PET in the cerebral cortex, so it is not useful to differentiate BLD patients from AD or FTLD patients (Camacho et al., 2018). A particular situation in amyloid-PET is that healthy subjects can be positive for $A\beta$ plaques, since the cortical deposit increases in advanced age, even in cognitively asymptomatic cases.

In these cases, the importance of amyloid-PET resides in whether it is negative, since it allows to exclude AD as a possible cause of dementia (Camacho et al., 2018; Shivamurthy et al., 2015).

b) Other clinical uses

Other uses that are beginning to be made of amyloid-PET are in cases of PD, down syndrome, multiple sclerosis and in the evaluation of AD therapies (Camacho et al., 2018).

In relation to the other imaging modalities, Amyloid-PET has shown to be better than FDG-PET and MRI in detecting AD in early stages, while FDG PET is superior in predicting the progression from MCI to AD and MRI is useful to assess the severity of damage and disease progression in more advanced stages. Therefore, the combination of different modalities can lead to better prognostic values, especially when they are atypical AD situations, a strange cognitive evolution or the presence of another disease that limits a good diagnosis (Camacho et al., 2018).

1.2.3.2 Evaluation

a) Quantification methods

In clinical practice, when an amyloid-PET is evaluated as positive or negative, it is usually done qualitatively, that is, by visual analysis. As in the case of FDG-PET and other imaging modalities, this can sometimes lead to incorrect diagnoses or dependent on the experience of the clinician (Mountz et al., 2015; Yamane et al., 2017). For this reason, the use of quantitative methods, as a complement to the visual evaluation of amyloid-PET, has recently been promoted. One of the most widely used, both in clinical and research, is the standardized uptake value ratio (SUVr), which is calculated as the ratio between the SUV of a cortical ROI and the SUV of a reference region. Depending on the radiotracer, positive amyloid cases are usually considered when the SUVr is between 1.12 and 1.45 (Arbizu et al., 2015), although it is usually converted to the Centiloid scale (Klunk et al., 2015) that has standardized values and allows comparison between different amyloid tracers.

To calculate the SUVr, PET images have to be also preprocessed. In this case, it usually consists of a spatial normalization of the images to a standard space, the manual definition of the ROI and the calculation of the SUVr (Tsubaki et al., 2020). There are several commercial software that perform this process such as PMOD (PMOD Technologies, Switzerland), HERMES Brass (Hermes Medical Solutions, Sweden), MIMneuro (MIM Software, USA) or Siemens Syngo VIA Amyloid Plaque (Siemens Medical Solutions Inc., USA) in addition to other tools under development (Tsubaki et al., 2020). However, each software has its peculiarities in the preprocessing and there is no standard in the methods for SUVr calculations (Curry et al., 2019; Knesaurek et al., 2014).

b) Examples

The SUVr has an important role in longitudinal studies on the evolution of amyloid deposits (Landau et al., 2015), in the detection of early stages of AD (Yamane et al., 2017) as well as in the evaluation of cognitively healthy older people where there is a low deposition of amyloid difficult to detect visually. Thanks to SUVr, this detection of less widespread beta-amyloid can be improved and individuals at increased risk of having AD can be identified (Harn et al., 2017).

On the other hand, SUVr has several limitations: SUVr values depend not only on the chosen reference and interest regions but also on the particular radiotracer being used (Matsuda et al., 2021). In addition, they are values that can be altered by partial volume effects. For this

reason, new ways to improve the preprocessing for the calculation of the SUVr are still being investigated, new quantitative measures of amyloid are being implemented, such as the Centiloid scaling method mentioned above (Klunk et al., 2015) and the AMYQ index (Pegueroles et al., 2021), or the usefulness of other analyzes are being evaluated such as VBA in amyloid-PET (Akamatsu, Ikari, et al., 2019).

1.3 MONTE CARLO SIMULATION IN BRAIN PET

In this section we talk about MC simulation techniques and its different applications, particularly in nuclear medicine and brain PET imaging. In addition to the main advantages and limitations of using MC simulation compared to other methods.

1.3.1 Description

MC simulation techniques are statistical methods used to solve mathematical problems, especially those that cannot be solved analytically or when experimental measurements may be impractical, (Raeside, 1976; Zaidi, 1999). In this way, the aim is to reproduce the behavior of real situations to later analyze their characteristics and study how they will evolve. These techniques have multiple applications in medical physics such as diagnostic radiology and nuclear medicine, radiotherapy physics or radiation protection (Andreo, 1991). In this case, we are going to focus on their uses in nuclear medical imaging, particularly in brain PET imaging.

In PET imaging, these techniques are very useful thanks to the stochastic nature of positron emission. MC simulation allows the random generation of photons in order to study the physical processes that occur inside the scanner. This is achieved by assuming that the behavior of the system can be defined using probability density functions (PDF's). These PDF's use random numbers uniformly distributed in an interval [0,1] to generate and sample primary photons, projections, scattered photons, etc. (see Figure 35) (Zaidi, 1999). In this way, MC simulations make it possible to generate synthetic images of brain PET in a theoretical framework of reference (ground-truth) and thus evaluate different processes on controlled images (García et al., 2020).

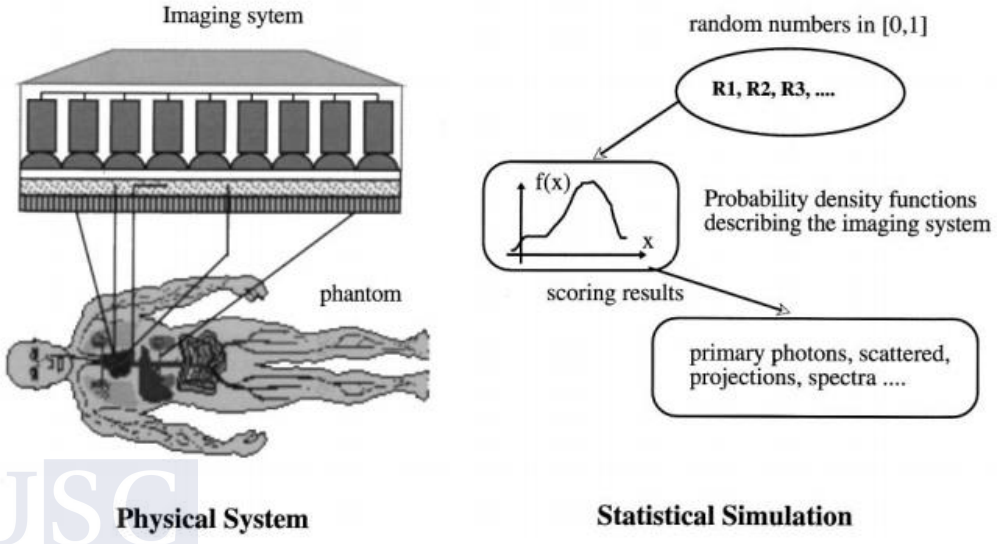

Figure 35: Physical system compared to Monte Carlo simulation. Reproduced with permission of John Wiley and Sons from (Zaidi, 1999).

1.3.2 Applications in brain PET

MC simulations are present in many fields of neuroimaging such as evaluation of PET protocols, quantification methods, visual detectability studies, generation of datasets, among others (Andreo, 1991; Zaidi, 1999).

1.3.2.1 Evaluation of acquisition protocols and reconstruction methods

MC simulation is commonly used for the evaluation of some of the different steps that are involved in the generation of the PET images, such as data acquisition and reconstruction protocols, to later establish a better configuration or improve image correction techniques. On the one hand, MC simulations are widely used to evaluate acquisition protocols and predict the performance of new PET scanner prototypes (Antonecchia et al., 2020; Guerra et al., 2018; Kochebina et al., 2019; Sheikhzadeh et al., 2017). On the other hand, MC simulations are very useful when evaluating reconstruction algorithms because the reconstructed images obtained from the different reconstruction methods under evaluation can be compared to a ground-truth image (see Figure 36). Thus, MC simulations can be used to compare different PET image reconstruction methods (Reilhac et al., 2008) or to develop new, more accurate and efficient reconstruction algorithms (Hashimoto et al., 2022; Kontaxakis, 2002) among other applications.

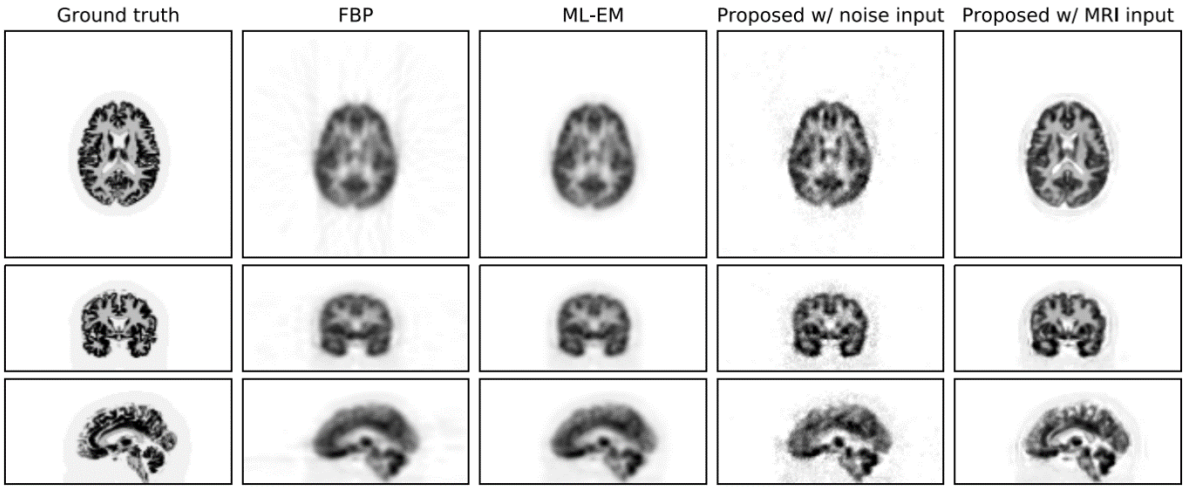

Figure 36: Example of simulated and reconstructed images using different reconstruction methods. From left to right we have the ground truth, the images reconstructed with FBP and ML-EM, and those generated with new methods using noise and MRI information as input. Adapted with permission of IEEE from (Hashimoto et al., 2022).

Regarding attenuation and scatter correction techniques in brain PET, MC simulations have an important role since they allow separating the simulated data into scattered and unscattered events and correcting these effects using an algorithm (Levin et al., 1995), as we saw in the section Scatter correction. In addition to being part of a correction method, MC simulations of PET images or different spatial distributions (see Figure 37) can also be used to evaluate different attenuation or scatter correction techniques respectively (Castiglioni et al., 1999; García et al., 2020), see the effects of scatter correction when comparing attenuation maps (Burgos et al., 2014), and more.

MC simulations also have some relevance in seeing how the noise and the spatial resolution of the data affect how realistic the simulated PET images can be compared to studies obtained with real protocols in the clinical routine (Stute et al., 2011).

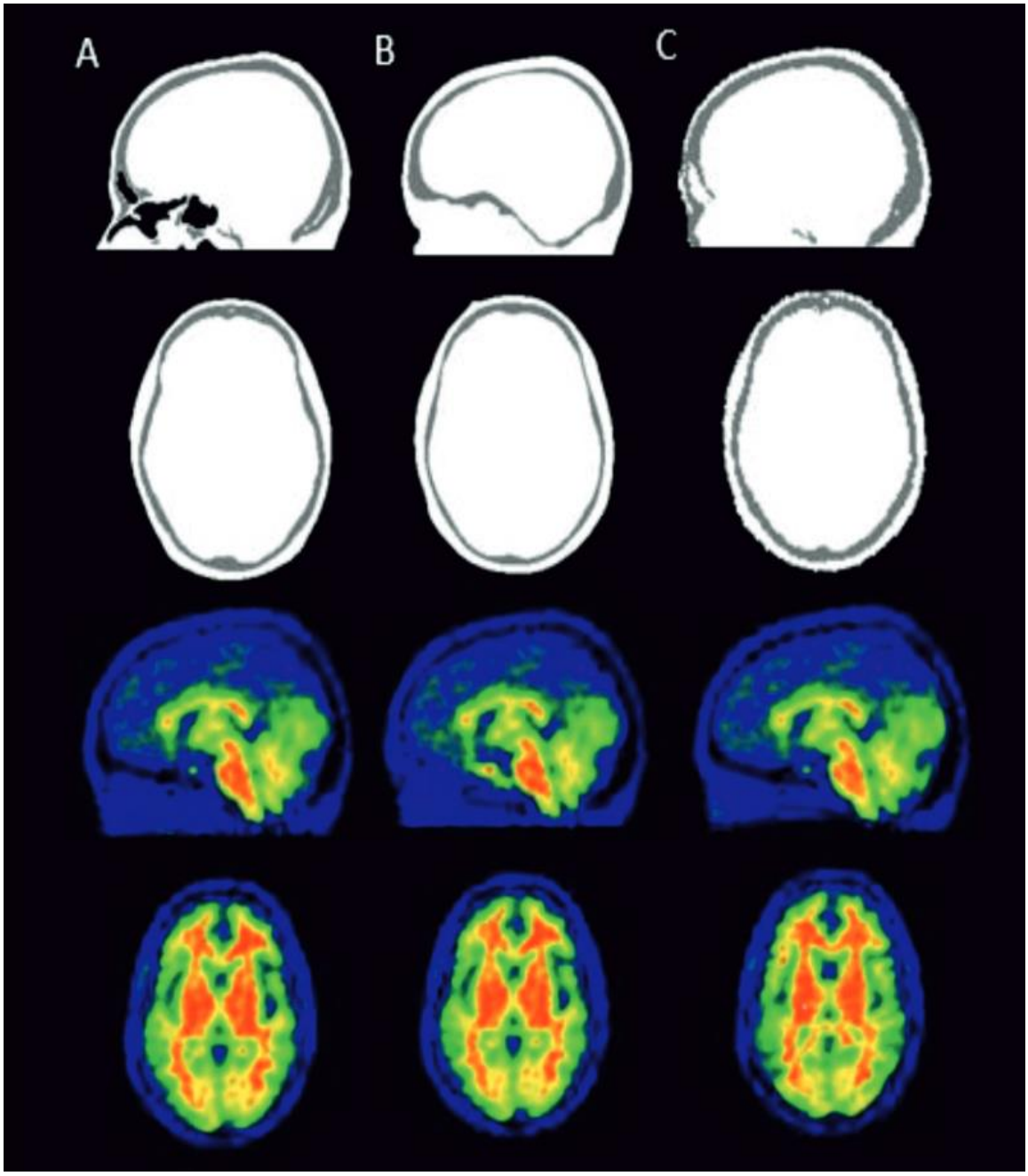

Figure 37: Attenuation maps and simulated brain PET of the same subject using different attenuation correction methods based on a CT image of the patient (A), an MRI of the patient (B) or an average CT image (C). Reproduced with permission of Sociedad Española de Física Médica from (García et al., 2020).

1.3.2.2 Evaluation and optimization of quantification methods

As we have seen in previous sections, quantification methods are an important complement to visual evaluation in the study of various neurological diseases. However, the presence of quantitative analyzes in clinical routine has been diminished by the lack of standardization in quantification protocols. For this reason, MC simulations are especially useful in this task since they allow the generation of realistic images of brain PET and can be considered as ground-truth when studying different processes involved in quantification.

In recent years there are more and more works that use MC simulations for the study and optimization of processes involved in the quantification of PET images. Generation of images to compare correction methods for the partial-volume effect (Frouin et al., 2002); evaluation of how anatomical variability, reconstruction algorithm, special normalization algorithm, and other aspects affect sensitivity and specificity in statistical analyzes (Aguiar et al., 2008; Davatzikos et al., 2001; Ishii et al., 2001; Schoenahl et al., 2003) are just some examples from the variety of applications that simulations have in the field of PET quantification.

1.3.2.3 Visual detectability studies

One type of study that is beginning to benefit from the realistic brain PET images generated by MC simulations are visual sensitivity studies in the detection of pathologies. Most detectability studies are done using a clinical ground-truth based on the response to treatments, surgeries or postmortem observations. But thanks to MC simulations, brain PET images can be generated by controlling with great precision the location and degree of development of a pathology of interest, being a better ground-truth. These works allow to study the reliability of the images acquired to show certain abnormalities in the brain, discover the detection limit of the radiotracer and study the variability in diagnosis among clinical experts.

1.3.2.4 Generation of datasets and other uses

As we have seen, the MC simulation of realistic brain PET images has many applications as it allows evaluating and improving a multitude of aspects in terms of acquisition and reconstruction algorithms, quantification methods, image post-processing, etc. All the commented applications make use, to a greater or lesser extent, of realistic synthetic brain PET databases. Therefore, another proper application of MC simulation in brain PET is the ability to generate datasets for all types of works. Some datasets are available for public use by doctors or researchers (Mota et al., 2015; Papadimitroulas et al., 2013; Reilhac et al., 2005).

1.3.3 Limitations

Despite all the advantages and applications that we have seen of MC simulations in brain PET, it also has some limitations.

The main limitation of the MC techniques is the great computational power required to simulate a number of events that is representative of the reality of the PET scanner and that converges to the solution in a time reasonable (Buvat & Castiglioni, 2002; Zaidi, 1999). This is something that affects most experts or research groups who want to make use of these methods and who need to acquire very powerful computing equipment.

On the other hand, thanks to the advances of the internet, in recent years multiple general and PET-specific MC codes have been made available to the public (Buvat & Castiglioni, 2002). However, their complexity of use and the knowledge that is needed to get the most out of it, has greatly limited its dissemination and use by researchers or health personnel who do not have the knowledge of physics, mathematics or programming required.

1.4 JUSTIFICATION

PET imaging is one of the most widely used modalities in neurology to detect the early stage of a disease, diagnose its current progress, the changes associated with different treatments or therapies that have been practiced, and even predict the evolution of symptoms from the current state. This is achieved thanks to the use of different radiotracers that allow studying different functional aspects of the brain. In particular, FDG-PET is one of the most widespread modalities and provides important information about glucose metabolism in different areas of the brain.

The clinical assessment of PET images, in particular FDG-PET, have normally been visually evaluated, being an important support for other more traditional morphological tests such as MRI. However, as we have seen in previous sections, numerous studies have shown the importance of quantitative analysis of PET images as a complement to visual analysis and thus be able to obtain their maximum potential as tools to support the diagnosis of neurological diseases, highlighting epilepsy. FDG-PET quantification allows detecting hypometabolism in different types of epilepsy, locate epileptogenic foci even in cases of cortical epilepsy with difficult visual detection, and study metabolic asymmetry to predict how epilepsy will evolve after surgery. In fact, the European Journal of Nuclear Medicine (EANM) suggests the use of quantification methods for the study of brain PET in one of its recent clinical guidelines (Varrone et al., 2009). This has led to the emergence of different software focused on performing quantitative analysis on PET images. However, the quantitative analysis of brain PET is not still widespread in the clinical routine. It is mainly due to lack of standardization between different quantification strategies and software solutions, which can be substantially different from each other. These methods can involve different intensity normalization methods, spatial normalization transformations, anatomical templates, statistical criteria, etc. In epilepsy there are usually cases with smaller lesions that are difficult to locate visually, causing situations that are highly dependent on the quantification methods used. There are even situations, such as in many cases of TLE, where the precision of the diagnosis or the good result of the surgical operation depends on the evaluation of the hypometabolisms obtained by quantification. In addition, many of the brain PET quantification methods need databases of healthy subjects, which are not being used properly, since it is not possible to have healthy databases for each scanner model, each particular acquisition protocol or each reconstruction method. All this together leads to a huge variability between quantification outputs that should be urgently addressed.

The challenge of the standardization requires having a ground truth against which each quantification strategy can be validated. One of the most common tools for the generation of ground truth values has been the use of physical phantoms, such as Hoffman phantom (E. J. Hoffman et al., 1990). However, physical phantoms have a very inflexible configuration, leading in many cases to unrealistic images of the brain, such as uniform uptake or lack of anatomical variability between subjects. An alternative tool is the use of MC simulation, which allows the generation of multiple datasets under configurable conditions. From digital phantoms, PET sinograms can be simulated and then reconstructed in order to obtain simulated PET images. Through MC simulation we can control the activity of different brain regions with greater precision and, in the case of epilepsy, generate databases with induced hypometabolism that simulate cases of cortical epilepsy. This database with a known level and location of hypometabolisms can serve as a real ground-truth for the evaluation of all types of neuroimaging protocols in epilepsy. However, the generation of useful and versatile PET databases requires the use of realistic digital phantoms, which involves additional MC simulations, greatly increasing the computing requirements. Moreover, the use of MC techniques need advanced knowledge in physics, programming, and statistics. Nowadays, there are several open MC simulation codes available for PET community, but the mentioned requirements have limited its use to researchers with solid background in MC simulation.

These issues have led to the need for MC tools specially developed for non-expert researchers with limited programming skills or computational resources. This tool should include an user-friendly environment, pre-validated scanners and certain automatic processes, but keeping a degree of customization to allow a flexible generation of PET databases.

1.5 OBJECTIVES

The main objective of the thesis is the design, development and validation of a web-based platform for the generation of simulated brain PET datasets using MC simulation techniques.

1.5.1 Specific objectives

a) Validation of MC simulation models of commercial PET scanners

b) Design and development of the web-based platform for MC simulation of brain PET images: SimPET.

c) Generation of healthy simulated PET image datasets with different configurations for SimPET validation.

d) Application of SimPET to generate a simulated PET database representative of subjects with cortical epilepsy.

METHODS

2 METHODS

Part of the content of this chapter has already been published as Paredes-Pacheco, J. [1,2], López-González, F.J. [1,2], Silva-Rodríguez, J. [3,4], Efthimiou, N. [5], Niñerola-Baizán, A. [6,7], Ruibal, Á. [1,3], Roé-Vellvé, N. [7] and Aguiar, P. [1,3] SimPET-An open online platform for the Monte Carlo simulation of realistic brain PET data. Validation for 18 F-FDG scans. Med Phys. 2021 May; 48(5):2482-2493. doi: 10.1002/mp.14838. PMID: 33713354; PMCID: PMC8252452.

[1] *Radiology and Psychiatry Department, Faculty of Medicine, Universidade de Santiago de Compostela, Galicia, Spain.*

[2] *Molecular Imaging Unit, Centro de Investigaciones Médico-Sanitarias, General Foundation of the University of Málaga, Málaga, Spain.*

[3] *Nuclear Medicine Department & Molecular Imaging Research Group, University Hospital (SERGAS) & Health Research Institute of Santiago de Compostela (IDIS), Galicia, Spain.*

[4] *R&D Department, Qubiotech Health Intelligence SL, A Coruña, Galicia, Spain.*

[5] *Positron Emission Tomography Research Centre, University of Hull, Hull, HU6 7RX, UK.*

[6] *Nuclear Medicine Department, Hospital Clinic Barcelona, Universitat de Barcelona, Barcelona, Spain.*

[7] *Biomedical Research Networking Center of Bioengineering, Biomaterials and Nanomedicine (CIBER-BBN), Barcelona, Spain.*

2.1 PATIENT DATABASES

This section describes the different image databases that we have used to carry out the work presented in this thesis. Databases were obtained from patient cohorts obtained at Centro de Investigaciones Médico-Sanitarias (CIMES, Málaga), Complexo Hospitalario Universitario de Santiago (CHUS, Santiago de Compostela), Hospital Clinic of Barcelona and the public database of the Alzheimer's Disease Neuroimaging Initiative (ADNI) (*ADNI | Alzheimer's Disease Neuroimaging Initiative*, n.d.).

2.1.1 Our cohort (CIMES)

Group 1: PET studies from 25 healthy subjects (mean age: 58 ± 5 years; range: 48–67 years) were acquired on a GE Discovery ST PET/CT (General Electric, Milwaukee, WI) installed at CIMES (Málaga, Spain) with a bedtime of 1200 s after the intravenous injection of approximately 245 MBq (3.3 MBq/Kg) of 18F-FDG. PET images were reconstructed using 3D OSEM with CT-based attenuation correction, and scatter correction (Voxel size, 1.95 x 1.95 x 3.27 mm; Matrix size, 128 x 128 x 47).

These healthy subjects also underwent MRI studies performed on a 3-T MRI scanner (Philips Intera, Best, The Netherlands). High-resolution T1 structural images of the whole brain were acquired with three-dimensional magnetization prepared rapid acquisition gradient echo (3D-MPRAGE) sequence. The acquisition parameters were: repetition time (TR) about 9.9 ms;

echo time (TE) about 4.6 ms; acquisition matrix 240/200; turbo field echo (TFE) factor 200; field of view 240; flip angle 8°; reconstruction voxel size 1×0.94×0.94 mm; 190 contiguous slices; total acquisition time of the sequences about 170 s.

2.1.2 Our cohort (CHUS)

Group 2: PET images from 25 healthy subjects (mean age: 60 ± 4 years; range: 54–65 years) were acquired on a GE Advance NXi PET scanner placed at CHUS for 1800 s on 3D mode (no septa) after the injection of 370 MBq (4.7 MBq/Kg) of 18F-FDG. These images were reconstructed using 2D OSEM after attenuation (using a 68Ge source), scatter and randoms pre-correction and FORE rebinning (Voxel size, 2.05 x 2.05 x 4.3 mm; Matrix size, 128 x 128 x 35).

2.1.3 Our cohort (Hospital Clinic de Barcelona)

Group 3: PET images from 25 healthy controls (mean age: 53 ± 10 years; range: 35–66 years) were acquired on the Siemens Biograph mCT PET scanner at the Hospital Clinic (Barcelona, Spain), after injecting a dose of 185 MBq (2.5 MBq/Kg) of 18F-FDG, with a bedtime of 900 s. The images were reconstructed using time-of-flight OSEM including resolution recovery (TrueX), attenuation, scatter, random, dead time, and decay corrections. (Voxel size, 1.02 x 1.02 x 1.50 mm; Matrix size, 400 x 400 x 148).

2.1.4 ADNI

ADNI was founded as a private-public partnership in 2004 by Dr. Michael W. Weiner. This multicenter project brings together neuroimaging datasets, patient clinical information and neuropsychological evaluations with the aim of being a public domain research source that facilitates the study of early detection and progression of MCI and AD, and improves intervention processes. In our case, a group of amyloid-PET images were obtained from the ADNI database.

Group 4: PET images from 5 healthy controls were acquired on a GE Discovery ST PET/CT (General Electric, Milwaukee, WI) with acquisitions of 5-min frames from 30 to 60 min after an injection of 370 MBq of 18F-AV-45. The acquired frames were co-registered to the first to correct movement artifacts. The co-registered frames were averaged to have a 30 min static PET image. All preprocessed PET images of healthy controls were reviewed by the ADNI PET Quality Control team and downloaded from the ADNI database (*ADNI | PET Analysis*, n.d.).

2.2 MC SIMULATION

Multiple MC simulation codes are currently free available to PET community (Buvat & Castiglioni, 2002), both general purpose codes with a specific application to PET studies, such as GEANT4 (Agostinelli et al., 2003) or ITS3 (Halbleib et al., 1993), and dedicated codes for PET. General purpose codes are more widespread than the dedicated ones and, therefore, their support, community, development, testing, reliability and versatility are considerable. The degree of customization and versatility of the code is especially relevant for implementing novel scanner geometries. However, using these general codes to simulate clinical PET scanners can be challenging, since implementing the geometry of a scanner from scratch is not trivial, and furthermore, these codes include many unnecessary or irrelevant options that only consume resources. Thus, dedicated codes become the preferred option for simulating PET data from well-known clinical scanners. Some of the most used PET-specific MC simulation codes are

GATE (Jan et al., 2004), PETSIM (Thompson et al., 1992), EGS5 (Hirayama et al., 2006), FLUKA (Ferrari et al., 2005), SimSET (Lewellen et al., 1998) and PeneloPET (España et al., 2009).

2.2.1 SimSET code

The SimSET code (https://depts.washington.edu/simset) was the preferred choice to integrate in our platform. It was released in 1993 by the Division of Nuclear Medicine of University of Washington. Since then, SimSET has undergone continuous evolution, implementing the technologies incorporated in the recent scanners (R. L. Harrison et al., 2006; Poon et al., 2015), and becoming a tool freely available to PET community.

The SimSET tool uses MC techniques to simulate the particle physical processes of interest in nuclear emission imaging. Its operation is based on modules that share information and data (see Figure 38). The core of the system is the Photon History Generator (PHG). The PHG simulates a decay and the resulting photons are tracked through a digital phantom. This phantom defines both the activity and attenuation maps used as input of the simulation. Tracked photons are projected into the scanner, whose geometry and detector characteristics are described in the Detector Module. The detector model can be of various types: "simple pet", the simplest as it not simulate a specific detector block type, but simply applies a Gaussian blurring to the incident photons; "cylindrical", more sophisticated since it performs the simulations considering a cylindrical scanner model; among others. Detected photons are finally sorted by the Binning Module, firstly into coincidences and then in the form of a sinogram. If a simulation process is interrupted between modules, a History File (a record of the decays and generated photons) is generated to be able to resume the process later. There is also a Random Coincidence Generation Module that adds random events to the history file.

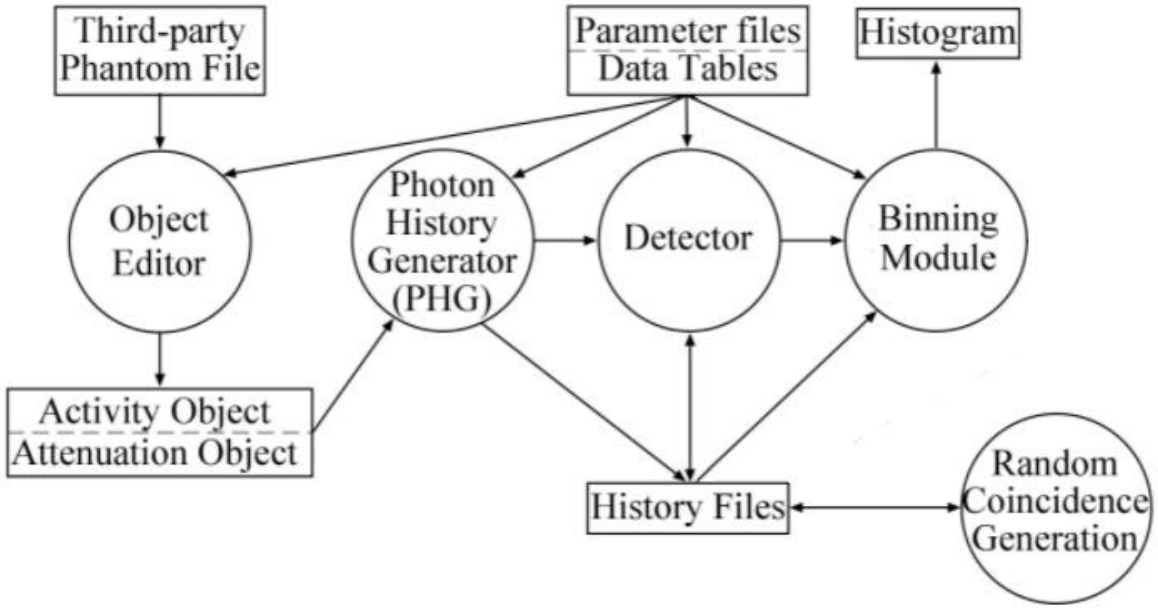

Figure 38: Workflow of SimSET simulation tool for PET imaging. Adapted with permission of SimSET team from (https://depts.washington.edu/simset/html/user_guide/user_guide_index.html)

The straightforward use of the SimSET workflow requires extensive scripting work to combine the inputs and outputs of each module, and particularly to incorporate the geometry of each

clinical scanner. This has somewhat hampered the use of SimSET by all researchers. In our project we have used scripting code previously implemented by our group for the simulation of GE Discovery ST, GE Advance NXi and Siemens Biograph mCT PET scanners. The MC simulation model of the GE Discovery ST was specifically implemented and validated in this project, while the MC simulation models of GE Advance NXi and Siemens Biograph mCT PET scanners from previously implemented and validated by collaborators and our group (Barret et al., 2005; Poon et al., 2015; Silva-Rodríguez et al., 2014).

2.3 TOMOGRAPHIC RECONSTRUCTION SOFTWARE

Another issue that has hampered the extensive use of simulation tools that simulated PET data has still to be reconstructed to generate simulated PET images, and obviously, the tomographic reconstruction codes are not included in the MC simulation codes. Several freely available codes are currently being used by the PET community, such as STIR (Thielemans et al., 2012), NiftyRec (Pedemonte et al., 2010) and CASToR (Merlin et al., 2018).

2.3.1 STIR

STIR (http://stir.sourceforge.net/) was the preferred choice to integrate in our platform. It originally belonged to the PARAPET project, a joint project of the European Union for the development of 3D PET image reconstruction libraries (Labbe, Thielemans, Belluzzo, et al., 1999; Labbe, Thielemans, Zaidi, et al., 1999), to later be readapted as an Open Source project. This tool is implemented in C++ code and its main purpose is provide an Object-oriented framework to reconstruct and process tomographic images, mainly PET imaging but could also be used in other imaging modalities. This library has a modular structure with options that interact with each other in many ways, making it difficult to define a single workflow. Its main characteristic is to be able to preprocess the acquired data and reconstruct tomographic images using multiple reconstruction algorithms and scanner geometries. It also has different utilities such as format converters, image manipulators, data filters, Poisson noise generator, automatic testing functions among others.

Again, the straightforward use of STIR library requires in-depth knowledge of the code to combine sinogram formats and scanner geometries. In our project, we take advantage of the extensive background of the group in STIR to integrate it into the platform in order to reconstruct the simulated PET data from the different scanners. Assuming slight differences between the algorithms implemented in STIR and the algorithms implemented in the clinical PET scanners, all reconstruction parameters were set as closely as possible to the settings specified by the manufacturers.

2.4 CHARACTERIZATION OF PET SCANNERS

A well-known way to characterize and define a PET scanner is to measure a series of basic operating performance parameters, such as sensitivity, uniformity, spatial resolution or contrast, so that an objective comparison between scanners can be carried out. This includes the possibility of validating MC simulation models of PET scanners, searching for the model closest to the performance of the real scanner. The procedures to perform these measurements is well described by the National Electrical Manufacturers Association (NEMA) protocols (National Electrical Manufacturers Association, 2007).

2.4.1 NEMA protocols

The first version of the NEMA guidelines were created in 1994 by NEMA with a committee of experts from all manufacturers of PET scanners as well as members of the Society of Nuclear Medicine (National Electrical Manufacturers Association, 1994). These protocols were updated to more recent versions with the evolution and improvement in the technology of PET scanners. The main objective of the NEMA protocols is to verify that the performance of a scanner corresponds to that indicated by the manufacturer, thus establishing the appropriate parameters for all future acquisitions and then optimal performance of the PET scanner and its characterization are guaranteed. The main parameters used for the characterization of a PET scanners in the NEMA guidelines are briefly described below:

a) Spatial resolution: it refers to the precision of the PET scanner to distinguish two spatially separated sources of radioactivity in the reconstructed image and serves as an indicator of the minimal detectable structure or lesion. It is an especially useful to characterize the highest achievable performance of the scanner. The main element that influences the spatial resolution is the size of the scintillating crystals, although this can be accompanied by other factors such as the reconstruction algorithm, the non-collinearity of the photons, the crystal size, the positron range, the penetration of photons into crystals before being detected or the number of scintillating crystals in each detector (Moses, 2011).

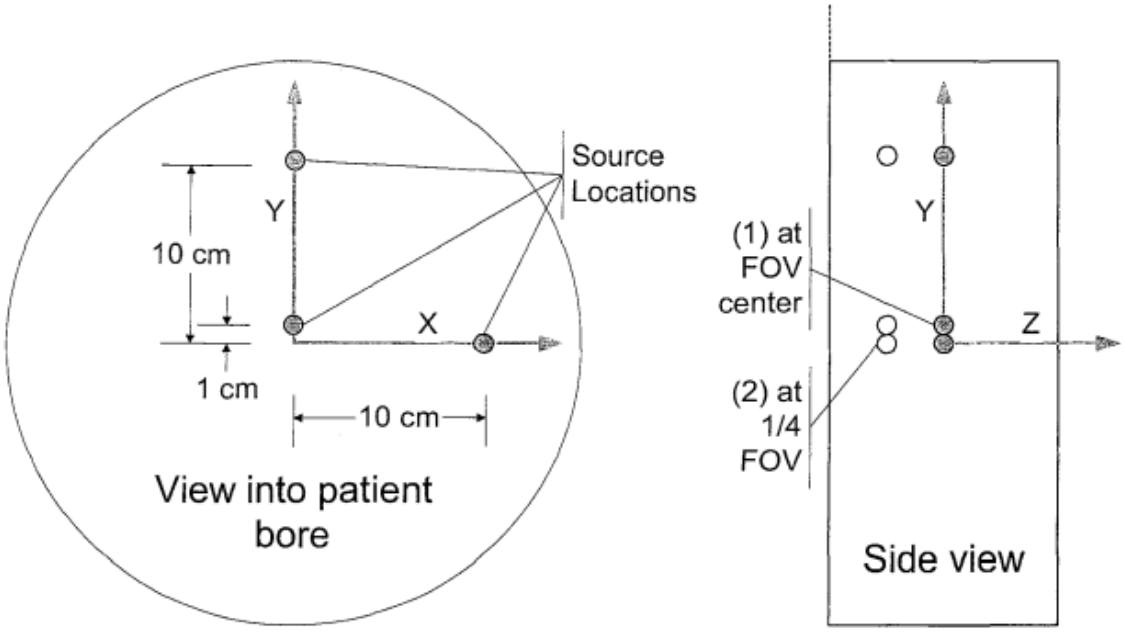

Figure 39: Radioactive source positions for spatial resolution measurements. Reproduced from (National Electrical Manufacturers Association, 2007).

To evaluate the spatial resolution of the tomograph, the NEMA protocol indicates that an ^{18}F point source of less than 1x1x1 mm should be taken inside a glass tube and placed in 6 different positions (see Figure 39) to make the data collection in at least one hundred thousand counts in each response function. Subsequently, the data is reconstructed with the FBP algorithm. The information from the point source response functions is adjusted to a Gaussian distribution in order to define the spatial resolution in terms of the Full Width Half Maximum (FWHM) and

Full Width Tenth Maximum (FWTM). In particular, tangential and axial resolutions (FWHM and FWTH) at 1 cm and radial, tangential and axial resolutions at 10 cm are calculated (National Electrical Manufacturers Association, 2007).

b) Sensitivity: it can be expressed as the ratio of counts per second that a scanner can detect per unit of radioactive activity. As we have seen in previous chapters, the sensitivity of the scanner depends mainly on the physical characteristics of the tomograph, such as the width of the energy window, the dead time of the system or the efficiency of the scintillating crystals.

NEMA proposes a way to infer the sensitivity of a specific scanner from different sensitivity values obtained using a sensitivity phantom. The procedure consists of filling a 700 mm long plastic tube with water and a certain amount of ^{18}F. This activity has to be low enough so that the lost counts are less than 1% and the rate of random events less than 5%. The tube is then placed in the center of the scanner, in the axial direction, and covered by aluminum tubes of different thicknesses simulating known attenuation values. The acquisition is made for the central position and 10 cm from the center of the tomograph. Then, the data acquired for the different thicknesses is fitted to an exponential equation to calculate the ratio of counts without attenuation R_0. Finally, the system sensitivity S is calculated by the following formula:

$$S = \frac{R_0}{A_{cal}} \quad (16)$$

where A_{cal} is the used activity in MBq (National Electrical Manufacturers Association, 2007).

c) Image quality: although it should be assessed using clinical imaging conditions, such as phantoms with a variety of patient shapes, sizes, and structures, it would be very cumbersome and multiple phantoms should be acquired. Due to this, NEMA protocol proposes the use of a specific phantom (see Figure 40) for this purpose, which is made up of several parts: a 180 mm body phantom, a cylindrical insert filled with a low atomic number material to simulate lung attenuation, a test phantom for different scatter and randoms measurements and 6 spheres of different diameters (10, 13, 17, 22, 28 and 37 mm). The two largest spheres are filled with water to simulate cold lesion imaging and the remaining ones with ^{18}F to simulate hot lesion imaging. The concentration of radioactivity in the hot spheres will be 4 times the concentration of the background activity in the phantom (5.3 kBq/cc).

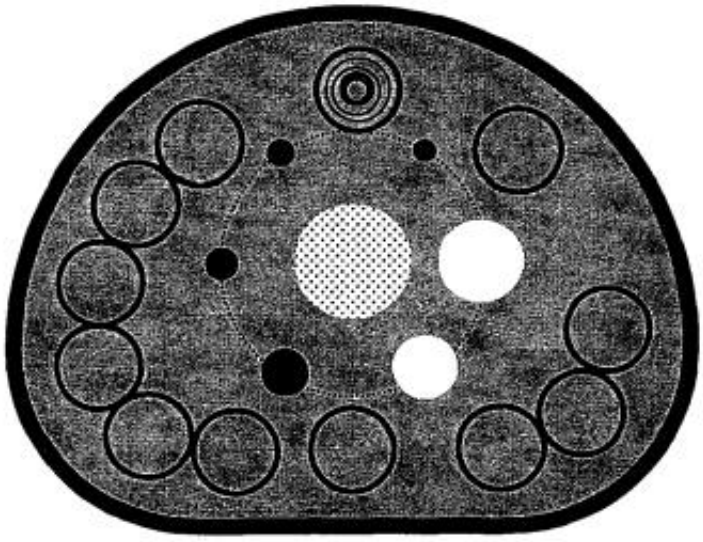

Figure 40: Image quality phantom with background ROIs. Reproduced from (National Electrical Manufacturers Association, 2007).

For image quality analysis, a cross-sectional image centered on the hot and cold spheres is used. In this image, some ROIs are drawn inside the spheres and, on the other hand, other ROIs of the same size are drawn in the background of the phantom, as they appear in Figure 40. In particular, twelve 37-mm diameter ROIs are drawn in the background and ROIs of the smaller sizes (10, 13, 17, 22, and 28 mm) are drawn concentric to the 37-mm background ROIs. These same background ROIs are drawn in slices +/- 1 and +/- 2 making a total of 60 background ROIs of each size, 12 in each slice. Background variability and image contrast ratios in the spheres are the measures considered as image quality (National Electrical Manufacturers Association, 2007). The contrast ratio $Q_{H,j}$ in each hot sphere j follows this formula:

$$Q_{H,j} = \frac{C_{H,j}/C_{B,j} - 1}{a_H/a_B - 1} * 100\% \qquad (17)$$

where $C_{H,j}$ is the average counts in the inside ROI for j, $C_{B,j}$ is the average of the background ROI counts for j, a_H is the activity concentration in all hot spheres, and a_B is the activity concentration in the background.

The contrast ratio $Q_{C,j}$ in each cold sphere j is calculated by:

$$Q_{C,j} = \left(1 - \frac{C_{C,j}}{C_{B,j}}\right) * 100\% \qquad (18)$$

where $C_{B,j}$ is the average of the background ROI counts for j, and $C_{C,j}$ is the average counts in the ROI for j.

The percentage of background variability N_j for each sphere j follows the equation:

$$N_j = \frac{SD_j}{C_{B,j}} * 100\% \qquad (19)$$

where SD_j is the standard deviation of the background ROI counts for j.

In this work, the MC models of the PET scanners implemented in SimPET were tested using the previous protocols detailed in the NEMA-NU 2007 standard (National Electrical Manufacturers Association, 2007). In this way the simulated NEMA results were validated for each scanner as detailed in Chapter 3.1 of the Results. The validated MC simulation models were integrated into the web platform.

2.5 WEB-BASED PLATFORM

The SimPET platform is an adaptation from Neurocloud®, a commercial online platform hosting quantification tools (https://qubiotech.com/en/neurocloud) (Qubiotech Health Intelligence SL, A Coruña, Spain). It has a multilayered architecture, with three main layers: presentation (GUI), domain logic, and data storage (see Figure 41). Each layer is built with its own technologies and can be independently upgraded, debugged, and repaired.

The web portal (www.sim-pet.org) provides a simple graphical user interface (GUI). The application manages the web server, computational processes, and file storage. The platform distributes load to parallel processing "workers" that perform the simulation/reconstruction. The underlying scripts are written in various programming languages, such as Bash, MATLAB, C, and Python. Various well-validated libraries are used under-the-hood, such as SimSET, STIR, SPM12, FSL (Jenkinson et al., 2012), and the Python NiBabel (Brett et al., 2019).

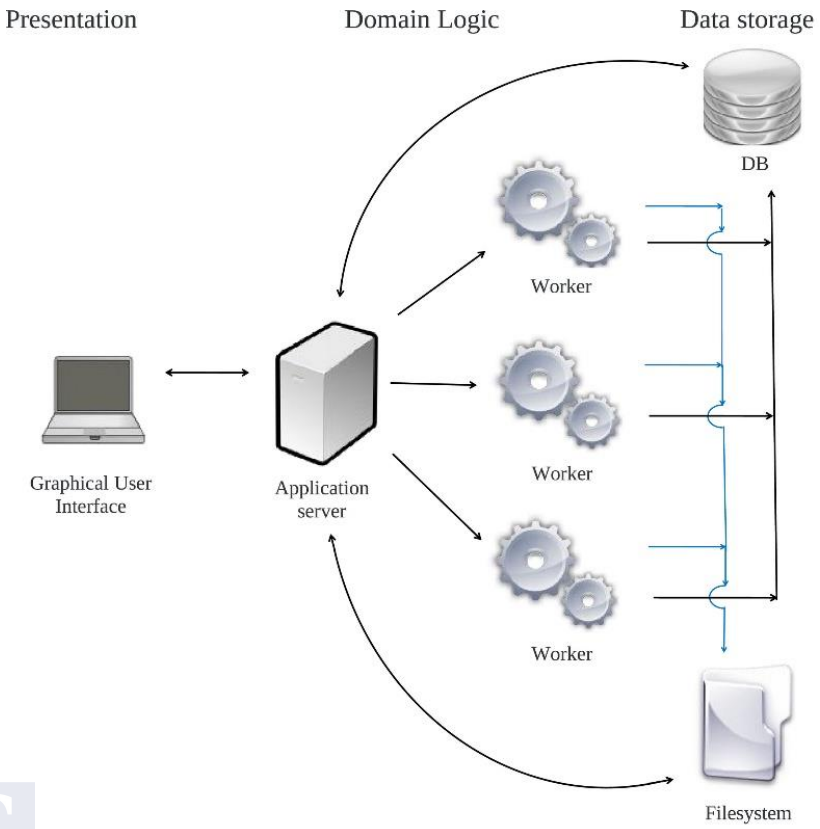

Figure 41: System architecture of SimPET with the three layers: Presentation, domain logic, and data storage.

The whole system (including the web application + two simulation workers) is currently deployed on a Lenovo ThinkStation P920 with two Intel Zeon Silver 4114 processors (twenty 2.20 GHz cores and forty threads in total), 126 GB RAM and 6 TB disk space in a mirroring configuration using Ubuntu 16.04 LTS. In addition, thanks to the platform features inherited from Neurocloud, the platform is ready to be deployed in a full cloud-computing configuration, with the ability of managing autoscaling of the number of simulation cores depending on the load.

2.6 GENERATION OF HEALTHY DATABASES

The validation of the platform was based on the simulation of realistic healthy patient's FDG-PET images databases for the included scanner models. To this end, FDG-PET/CT and MRI images from 25 healthy subjects were scanned with the GE Discovery ST (Group 1) and used for the phantom generation. The 25 generated activity and attenuation maps were then used as inputs for the simulation of synthetic data.

25 brain FDG-PET control subjects were simulated in SimPET using the GE Discovery ST MC model. Real noise, a whole-body injected dose of 245 MBq and a study duration of 1200 s were simulated. Scatter correction was performed during simulation of the sinograms. These sinograms were reconstructed using the OSEM reconstruction algorithm with attenuation correction, 32 iterations and 7 subsets. The images generated have a voxel size of 1x1x0.96 mm and a matrix size of 256x256x256, the same as the activity maps used as a reference.

25 brain FDG-PET control subjects have been simulated with the SimPET platform using the MC model of the GE Advance NXi scanner. Real noise, a whole-body injected dose of 370 MBq and a study duration of 1800 s were the input parameters to simulate. Scatter and attenuation correction were performed in the simulation of the sinograms. The sinograms were reconstructed with the OSEM reconstruction algorithm with 56 iterations and 14 subsets. The images generated have a voxel size of 1x1x0.96 mm and a matrix size of 256x256x256, the same as the activity maps used as a reference.

Regarding the dataset with the MC model of the Siemens mCT, 23 brain FDG-PET control subjects were simulated with the SimPET platform. In this case, real noise, a whole-body injected dose of 185 MBq and a study duration of 900 s were considered as input parameters. Scatter correction was performed during simulation and the sinograms were reconstructed using the OSEM reconstruction algorithm with attenuation correction, 130 iterations and 26 subsets. As in the previous cases, the images generated have a voxel size of 1x1x0.96 mm and a matrix size of 256x256x256.

The validation was carried out by performing different statistical analyzes between the simulated datasets and real subject FDG-PET images acquired on each of the scanners.

2.7 GENERATION OF AN EPILEPSY DATABASE

After the validation of the platform, SimPET was used for generating a highly realistic database including different types of hypometabolisms typical of MRI-negative epilepsy.

The methodology used to generate the simulated image dataset can be seen in Figure 42. The 25 GE Discovery ST activity and attenuation maps generated for the SimPET validation were used as the basis for the generation of hypometabolisms in typical regions of cortical dysplasia. In these 25 activities maps we induce different intensities hypometabolisms in randomly selected regions of the cerebral cortex, not including subcortical structures. In particular, the algorithm intersects the probabilistic brain atlas of Hammers (Hammers et al., 2003) with a gray matter probability map to extract a random ROI where to apply hypometabolism. The Hammers atlas is a label-based maximum probability map of the

neuroanatomy of a population and allows, among other things, the anatomical labeling of the different regions of the brain. A labeled list with the regions that can be selected can be seen in (Hammers et al., 2003). The gray matter probability map is obtained from the MRI segmentation used during the generation of each activity map. Once the ROI is selected, we consider two types of synthetic hypometabolisms that are usually present in cases of cortical dysplasia. We define type 1 hypometabolism as punctual hypometabolisms that act as epileptogenic foci within the ROI and type 2 hypometabolism as extensive hypometabolisms that usually affect a large part of the ROI. In this way, we provide the database with greater variability and diversity of hypometabolisms that reflect the real situations that would arise. In particular, we use the selected ROI to generate one of the two types of hypometabolisms considered. Type 1 hypometabolism consists of selecting a voxel within the ROI as the center of a cube with side 2 cm. This cube has a value of 1 in the center and will gradually decrease until it is 0.5 at the edges to generate a homogeneous and realistic hypometabolism in the simulated PET image. Masking the ROI with this cube and multiplying the values by a level of hypometabolism (60, 75 or 90%), we obtain a type 1 hypometabolic region. Type 2 hypometabolism consists of selecting a voxel within the ROI as the center of the hypometabolic region. In this case, the ROI will have a value of 1 in the center of the voxel and will decrease to 0 at the edges of the ROI, thus achieving a complete hypometabolic ROI. This hypometabolic ROI is multiplied by a level of hypometabolism (30 or 40%) to obtain a type 2 hypometabolic region. All these hypometabolic regions separately were applied to the activity maps (3 type 1 hypometabolic region and 1 type 2 hypometabolic region to each activity map). These activity maps with different induced hypometabolisms, together with the corresponding original attenuation maps, were simulated with SimPET (GE Discovery ST model, whole body injected dose = 245 MBq and study duration = 1200 s) to generate a dataset of 100 synthetic images with different cases of cortical epilepsy.

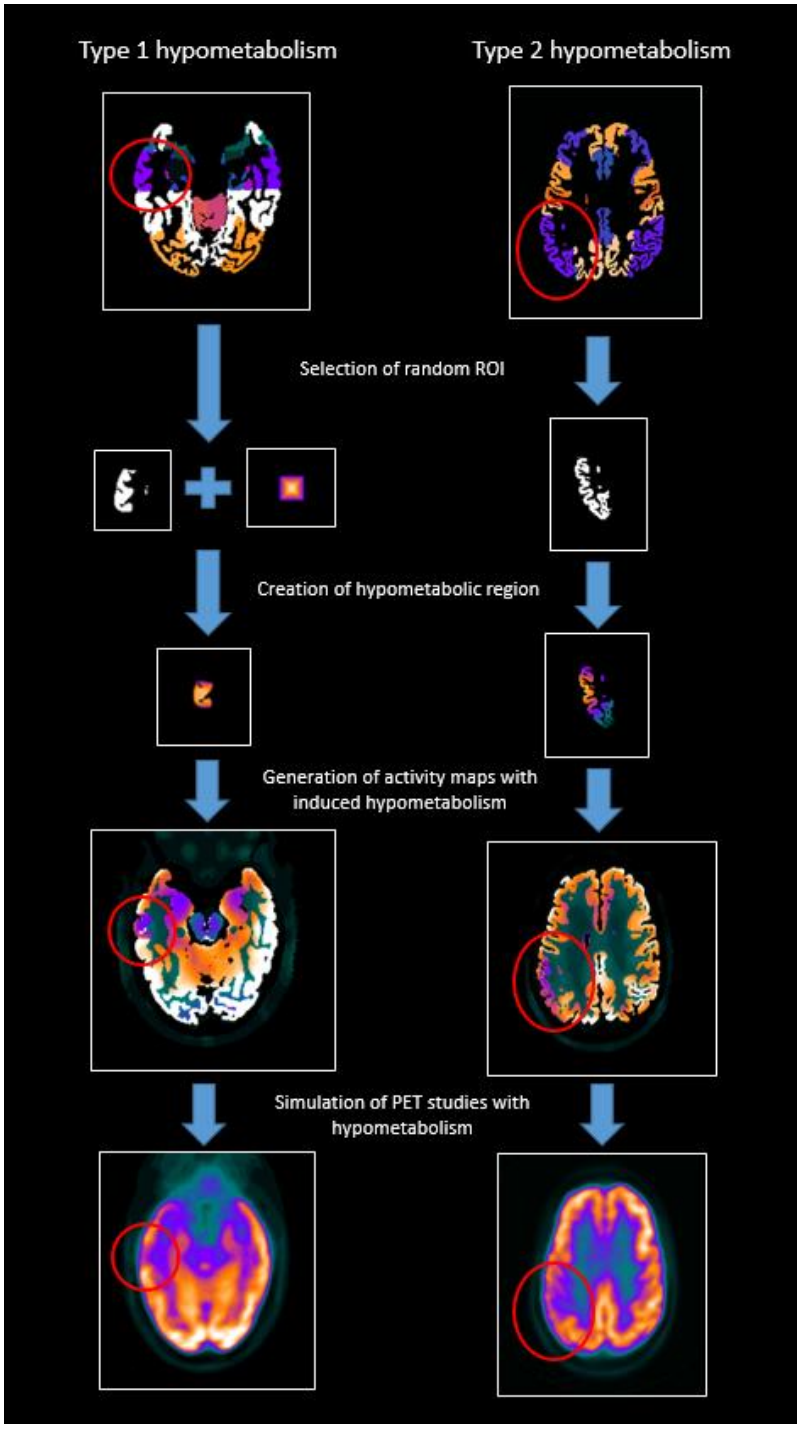

Figure 42: Generation of simulated PET images with two types of induced hypometabolism from randomly selected regions.

Each individual simulated image was reviewed several times by a nuclear medicine physician with previous experience in epilepsy for validating that the images and the induced metabolisms were realistic for the eyes of an expert. If it was not a realistic study, it would be generated again taking into account the comments of the nuclear medicine physician. Thus, the simulated database is refined until finally certifying that all the simulated studies form a dataset of realistic

cases of cortical dysplasia. In addition, the 25 brain FDG-PET control subjects simulated with the GE Discovery ST model described in chapter 2.6 were included in the final dataset.

To complement the visual assessment and validate the simulated epilepsy database, a quantitative analysis was performed between the healthy simulated subjects and each of the simulated subjects with induced hypometabolism.

2.8 IMAGE PROCESSING AND QUANTIFICATION

The quantitative analysis of PET images requires previous image processing, mainly in terms of spatial and intensity normalization, which can be carried out using well-known software packages such as SPM.

2.8.1 SPM

SPM is a free software package created for preprocessing and statistical evaluation by hypothesis testing of different types of neuroimaging, including anatomical or functional images. This package was developed in 1994 by Karl Friston and other researchers at the Wellcome Center for Human Neuroimaging at the University College of London (Friston, 2007). Since then it has undergone different updates to the current version, SPM12. This version is the one used in this project.

This software allowed us to preprocess different PET image datasets and perform VBAs. For the works present in this thesis, the preprocessing of the real or simulated PET images is similar to that described in the image analysis section of FDG-PET (see Figure 43). In particular, we used a 6-parameter rigid body transformation to co-register the acquired and simulated PET images to the space of the T1-weighted images corresponding to each subject. The PET studies were spatially normalized onto the MNI space (voxel size of 2 × 2 × 2 mm) using a ^{18}F-FDG template and the 12-parameter affine normalization provided by SPM. This is followed by a nonlinear deformation using a mean squared difference matching function (Ashburner & Friston, 2000). A Gaussian kernel of 8 mm was used to smooth the normalized PET studies. In the intensity normalization step there is no established standard method but there are different options inside and outside of SPM that can offer good results. In our case, histogram-based intensity normalization was performed. In this method, all the smoothed PET images were voxel-wise divided by the mean of the smooth acquired images. Histogram of these ratio images were generated and each smoothed image was divided by the most prevalent value in its ratio image.

Once all PET images are pre-processed, they are ready for voxel-level statistical analyzes. These VBAs allow to find the significant differences between the different groups of PET images under a certain configuration. The statistical analyzes carried out for the different works are described in the following section.

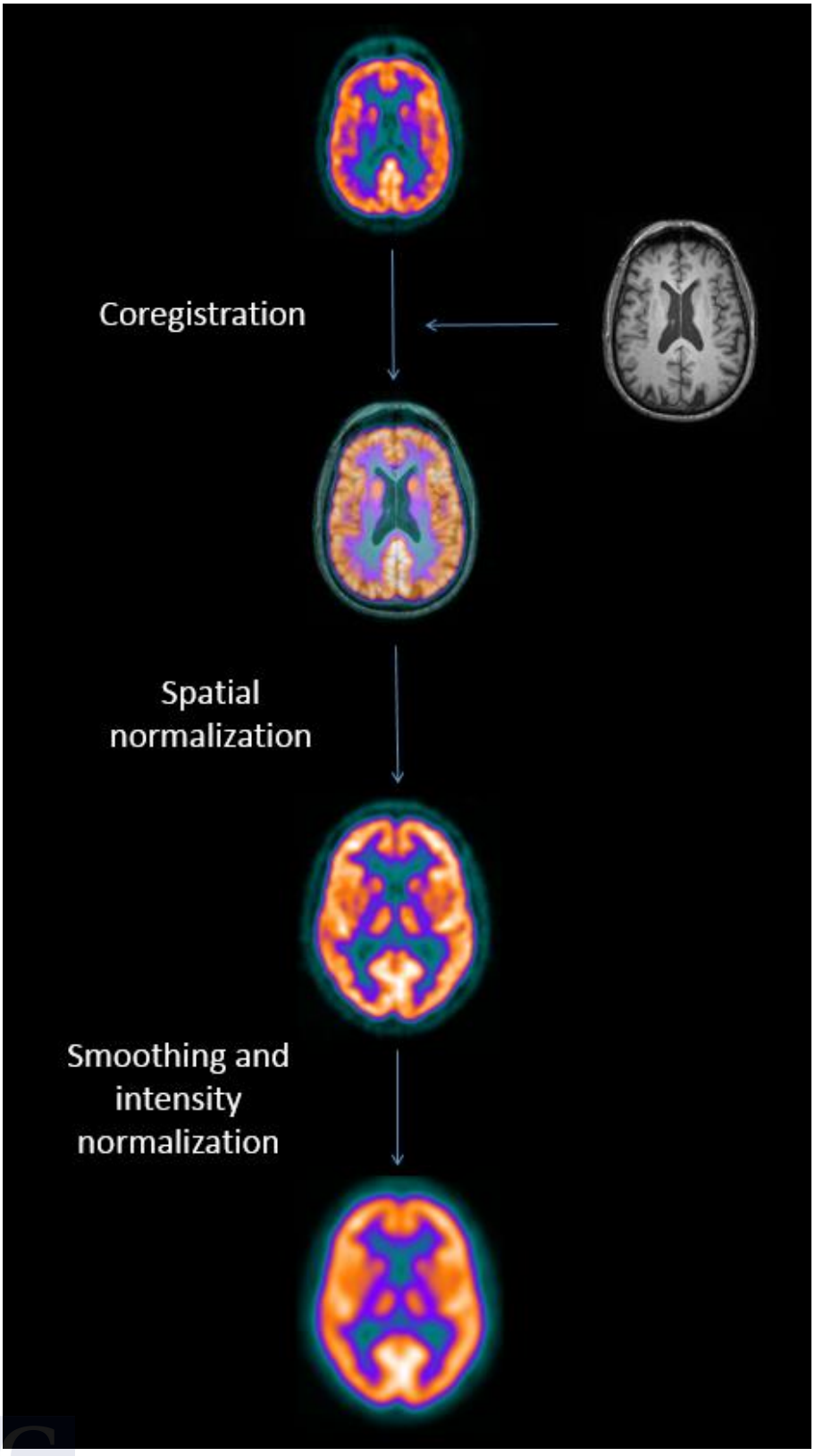

Figure 43: Preprocessing brain PET images with SPM

2.9 STATISTICS

In the evolution of research with PET neuroimaging, statistics have played a fundamental role, since it allows statistical inference between groups of images and to study the significant differences in the activation of different brain regions, carry out functional connectivity studies, see the functional differences in the brain before and after a treatment, study the correlation between a biological variable and the changes observed in a group, or predict the evolution of a patient, among other analyzes.

Initially, the statistical analysis of PET images was based mostly on performing a voxel-level t-test between groups to study significant differences between PET images. However, later the general linear model (GLM) was also implemented in SPM as follows:

$$y = X\beta + e \qquad (20)$$

where y are the input values of the PET images, X the design matrix with the explanatory variables of the model, β the regressors to be estimated and e the errors. With the GLM defined, the regressors are estimated using ordinary least squares such that the sum of the squared errors is minimal.

Once the model has been fitted and the beta regressors estimated for each voxel, statistical inference is carried out using hypothesis tests on the beta regressors. In SPM, a contrast is defined as a vector of weights that indicates the participation of each regressor in the definition of the null hypothesis. The hypothesis is then evaluated in each voxel by performing a statistical test, providing maps of t-values following a Gaussian distribution. Thus, each t-value has an associated probability value, p-value and finally a threshold (significance level, α) has to be defined to determine the voxels showing significant differences between groups. The most common α value is 0.05 (although 0.1 or 0.01 are also used). Applying this threshold we would obtain all the voxels where the null hypothesis is rejected. Adjacent voxels are grouped into clusters. These clusters form a statistical parametric map of significant differences. The minimum cluster size considered for the formation of the statistical map is defined in SPM by a parameter K. Due to the large number of voxels and t-tests that are carried out, there is the problem of multiple comparisons. If the significance level of α is set to 0.05, there is a 5% chance of providing significant differences. Considering the large number of voxels of the PET images, the proportion of false positives included in the statistical parametric map can be important. To compensate this issue, SPM implemented several correction methods, such as Bonferroni or Family Wise Error (FWE), which are applied during thresholding (Han & Glenn, 2017).

In Figure 44 we can see a diagram of the entire process to obtain the statistical parametric map with SPM. In the course of this thesis, we have used the GLM implemented in SPM configured as two-sample t-test and paired t-test to compare simulated and patient brain PET images. This type of analysis allows to assess regional/systematic differences between the simulated/real groups. In addition, we have also used Bland-Altman plot to study the correlation between two groups of PET data.

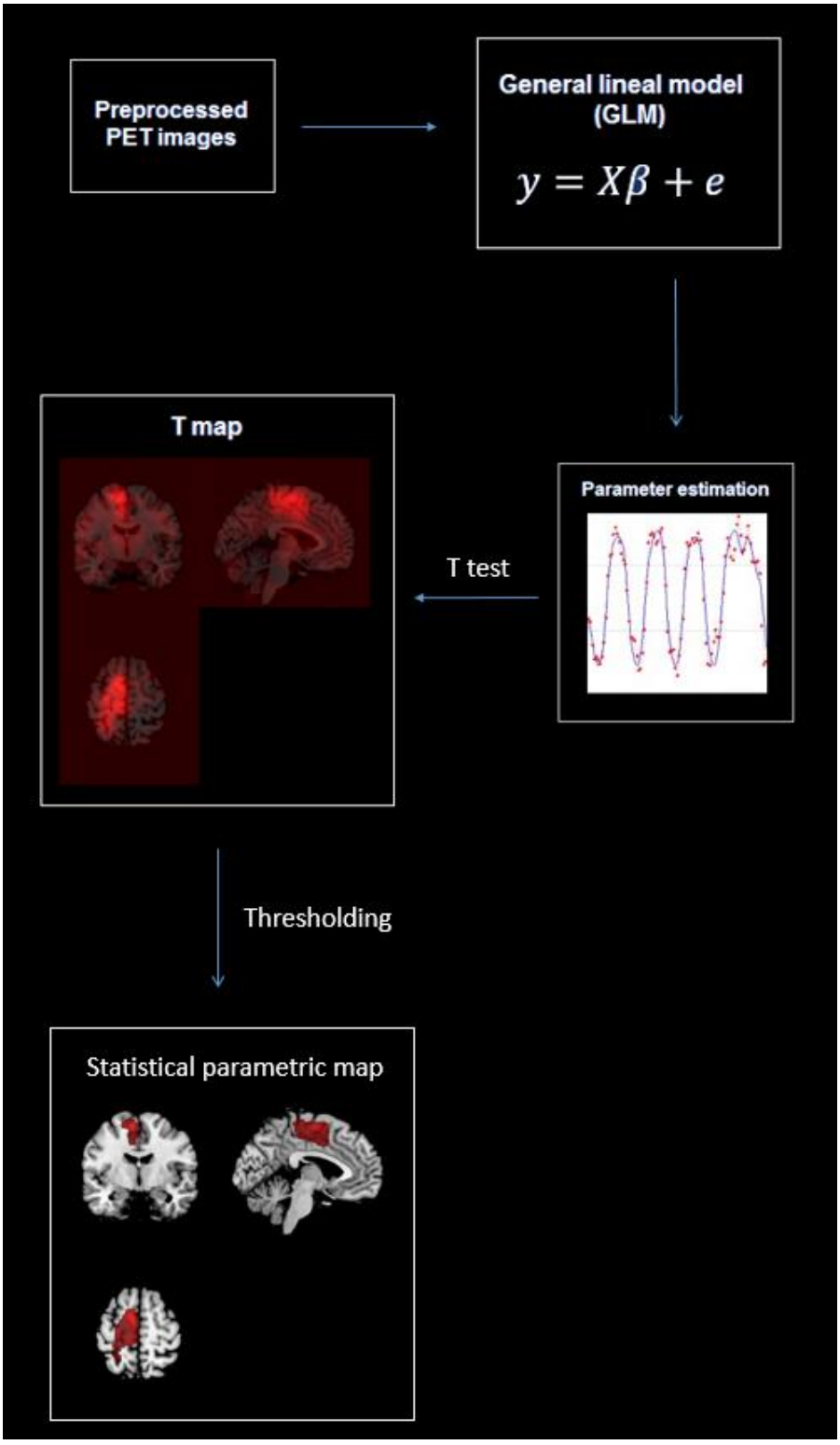

Figure 44: Generation of a statistical parametric map using the GLM with SPM. The preprocessed PET images are the input of the GLM, where y is the intensity value in each voxel and takes a different value for each subject, X is the design matrix that describes the classification of the images in groups, β are the regressors to estimate and e the errors. The β parameters of the model are fitted by regression on each voxel taking into account the values in all subjects. Different t-tests and thresholds are applied to the estimated model to obtain statistical parametric maps.

2.9.1 Two-sample t-test

The two-sample t-test is one of the most widely used t-tests to determine whether the mean values between two independent data groups are significantly different or not, the null hypothesis being that the mean value is the same. Applied to the VBAs, we used them to assess the significant differences at the voxel level between the mean images of two independent groups of pre-processed PET images.

The two-sample t-test design matrix in SPM includes variables to indicate the group to which the input PET images belong and other optional covariates with quantitative information about the subjects such as age or sex. In our case, we directly compared the images between groups without other covariates.

After the model has been configured and estimated, the contrast to be evaluated is chosen. This contrast indicates how the mean values are subtracted to obtain the significant differences for a particular comparison. Once the contrast is selected, the value from which a voxel is significantly different is determined by the significance level α. An FWE correction is applied to reduce the probability of false positives in the results. A minimum cluster size, K, for the formation of the statistical parametric map is set. In the validation of the simulated healthy databases, two different contrasts were used to assess areas with significant differences: the real group metabolism > the simulated group metabolism and the real group metabolism < the simulated group metabolism. A statistic threshold of $p < 0.01$ and a cluster size $k = 300$ was applied. In the validation of the simulated epilepsy database, the contrast simulated control group > each subject with simulated hypometabolism was used to verify the areas with induced hypometabolism. A statistic threshold of $p < 0.05$ and a cluster size $k = 250$ was applied. In any case, family wise error (FWE) correction was applied to assess for multiple comparisons. In this way, we obtain a tridimensional maps with the significantly different regions for each contrast.

2.9.2 Paired t-test

The paired t-test is similar to the two-sample t-test described above, but must be used for different data structures. The paired t-test is designed to be used with pair-correlated data. For example, if we want to compare the same group of subjects with PET images generated under two different conditions or at two different times. Furthermore, while in the two-sample t-test the data have the same variance and are normally distributed, in the paired t-test the data only have to be normally distributed (Fralick et al., 2017).

In the thesis we use the paired t-test to compare the real and simulated GE Discovery ST images as the activity and attenuation maps were derived from the real GE Discovery ST images. For the rest of comparisons, we used the previously commented two-sample t-test.

2.9.3 Bland-Altman comparison analysis

Bland-Altman comparison analysis is a graphical method to study the differences between two measurements. This type of graphic analysis is especially useful when we study the correlation or similarity between two sets of data with respect to the same variable but acquired in a different way. It usually consists of representing the differences or ratios between two sets of data against the mean of all the data. Alternatively it can also be done with respect to one of the two data sets, if this is a reference set, instead of using the mean.

In the validation of the simulated healthy databases, we adapt this analysis to study the similarity between groups of simulated PET images and real PET images for each scanner. In particular, the simulated images were compared with the real images by performing a Bland-Altman-like analysis, where for each voxel, we calculated voxel-based differences ($\in_{voxel}$) as:

$$\in_{voxel} = 2 * \frac{(V_{real} - V_{simulated})}{(V_{real} + V_{simulated})} \qquad (21)$$

where V_{real} is the average value of the real images and $V_{simulated}$ is the average value of the simulated images. The resulting values were histogrammed for presentation purposes. In order to considerer potential differences between the real database of the GE Discovery ST (Group 1), which was the input to generate the activity and attenuation maps for the simulations, and the real databases of the GE Advance NXi (Group 2) and the Siemens Biograph mCT (Group 3), the same process was performed between the real databases for comparison and included in the corresponding figure when needed.

This graphical analysis in combination with the three-dimensional statistical parametric maps provides a complete framework to validate the simulated PET images generated by the SimPET platform.

RESULTS

3 RESULTS

Part of the content of this chapter has already been published as Paredes-Pacheco, J. et al. SimPET-An open online platform for the Monte Carlo simulation of realistic brain PET data. Validation for 18 F-FDG scans. Med Phys. 2021 May; 48(5):2482-2493. doi: 10.1002/mp.14838. PMID: 33713354; PMCID: PMC8252452.

3.1 VALIDATION OF MC SIMULATION MODELS

3.1.1 Validation of GE Discovery ST

The main configurable parameters in the MC model were obtained from technical information of the scanner in order to reproduce the physical characteristics of the scanner and thereby simulate PET data as similar to the real data as possible. The results of the validation are presented following the NEMA protocol, comparing spatial resolution, sensitivity and image quality tests on the real and simulated scanner.

The spatial resolution results obtained for both the GE Discovery ST scanner and the model simulated with SimSET can be seen in Table 3.

Table 3. Spatial resolution results for the GE Discovery ST scanner and its simulated model in SimSET applying the NEMA protocol.

	1 cm			
	FWHM		FWTM	
	Transverse	Axial	Transverse	Axial
Real GE Discovery ST	6.05185	5.63324	11.59110	10.91120
Simulated GE Discovery ST	5.42109	3.88172	11.12496	18.88881

	10 cm					
	FWHM			FWTM		
	Radial	Tangential	Axial	Radial	Tangential	Axial
Real GE Discovery ST	7.46702	6.50139	5.96881	13.24310	11.32690	12.04400
Simulated GE Discovery ST	6.15523	6.05442	4.11792	11.44435	11.67943	19.18272

The mean difference in spatial resolution between the real scanner and the SimSET simulated model is approximately 2.7 for 1 cm and 2.15 for 10 cm, obtaining more relevant differences in the Axial component.

Regarding the sensitivity obtained, for the real scanner it was $S_{real} = 8.87957\ counts/sec/kBq$, while for the simulated scanner with SimSET it was $S_{sim} = 57.3576\ counts/sec/kBq$. This difference leads to taking into account a ratio of $S_{sim}/S_{real} \approx 6.46$ to divide the study duration when simulating the GE Discovery ST using SimSET. In this way, the simulated model achieves a sensitivity similar to the real acquisition, obtaining a realistic statistical variability.

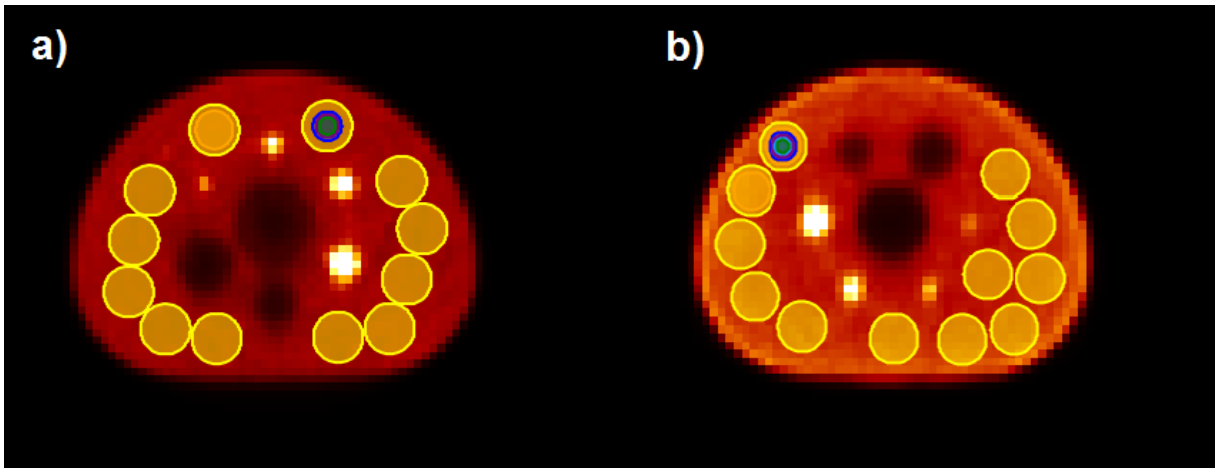

Figure 45: PET images generated to perform the image quality test on the real GE Discovery ST scanner (a) and on the simulated model in SimSET (b).

Following the NEMA protocol, in Figure 45 we can see the image acquired in the real scanner (Figure 45a) and the image generated with the simulated model in SimSET (Figure 45b) to study the image quality. For each of the 6 sizes of ROIs considered, the NEMA results obtained for the real and simulated scanner in terms of image quality are shown in Table 4. The mean difference between the real GE Discovery ST scanner and the simulated model is approximately 0.29% in background variability, 4.33% in hot contrast, and 3.86% in cold contrast.

Table 4: Image quality results applying the NEMA protocol to the real GE Discovery ST scanner and the model simulated by SimSET.

		37 mm	28 mm	22 mm	17 mm	13 mm	10 mm
Background variability	Real GE Discovery ST	2.00 %	2.20 %	2.50 %	2.70 %	3.00 %	3.20 %
	Simulated GE Discovery ST	2.32 %	2.24 %	2.25 %	2.43 %	2.61 %	2.75 %
Hot contrast	Real GE Discovery ST	-	-	46.60 %	38.00 %	25.80 %	9.70 %
	Simulated GE Discovery ST	-	-	47.53 %	32.95 %	15.43 %	8.75 %
Cold contrast	Real GE Discovery ST	62.20 %	54.80 %	-	-	-	-
	Simulated GE Discovery ST	66.75 %	51.64 %	-	-	-	-

3.1.2 Validation of GE Advance NXi

The validation of the MC simulation model of the GE Advance NXi scanner was already carried out in different previous works by our group (Barret et al., 2005; Silva-Rodríguez et al., 2014), so the validated configurations have simply been adapted to our case.

3.1.3 Validation of Siemens Biograph mCT

The validation of the MC simulation model of the Siemens mCT scanner was based on previous works (Poon et al., 2015) and measurements carried out by our collaborators at the Hospital Clínic, so the validated configurations have simply been adapted to our case.

3.1.4 Validated MC simulation models

Table 5a and Table 5b show three validated MC simulation models (GE Discovery ST, GE Advance NXi and Siemens mCT) that includes the main configurable parameters for each scanner, mainly based on the technical characteristics of the scanners (Barret et al., 2005; Ghabrial et al., 2021; Guerin & El Fakhri, 2008) but also those parameters which have to be directly derived from the validation test.

Table 5a: Main physical parameters implemented in the simulation model of each scanner

Scanner model	*Scanner description*										
Parameter	*Detector model*	*Number of rings*	*Number of detectors per ring*	*Inner ring diameter*	*Average depth of interaction*	*Distance between rings*	*Min / Max z*	*Num aa bins*	*Num td bins*	*Min / Max td*	*Min energy window*
Definition	Detector block model type to simulate	Number of rings (axial slices)	Number of detectors per ring in total	Inner detector ring diameter	Mean distance traveled by a photon when interacting with the scintillator cristal	Space between rings	FOV limits in axial plane	Number of azimuthal angle bins	Number of transaxial distance bins	Limits of transaxial distance	Minimum value of the energy window
GE Discovery ST	Simple pet (only apply gaussian blurring)	24	420	88.62 cm	0.84 cm	0.654 cm	-7.85 / 7.85	210	249	-35.12 / 35.12	375 keV
GE Advance NXi	Simple pet (only apply gaussian blurring)	18	672	92.7 cm	0.01 cm	0.844 cm	-7.6 / 7.6	336	281	-56.2 / 56.2	375 keV
Siemens Biograph mCT	Simple pet (only apply gaussian blurring)	52	624	84.90 cm	0.1 cm	0.419 cm	-10.9 / 10.9	312	312	-31.2 / 31.2	435 keV

Table 5b: Main parameters configured in the simulation/reconstruction model of each scanner.

	Simulation				*Reconstruction*					
Parameter	***PSF value***	***Add noise***	***Apply att correction***	***Scatt correction factor***	***Zoom factor***	***XY output size***	***Reconstruction type***	***Num iterations***	***Num subsets***	***Max segment***
Definition	Value of the Point Spread Function applied to blurring the sinograms	Add poisson noise to sinograms	Apply attenuation correction	Factor by which the scatter is corrected (0.15 is 85% corrected scatter)	Zoom factor in X and Y dimensions	X and Y sizes in reconstructed matrix	Reconstruction algorithm	Number of iterations in the reconstruction algorithm	Number of blocks into which the image reconstruction is divided	Maximum ring difference on the reconstruction
GE Discovery ST	1.125	-	Yes	0.15	1.23	128	OSEM 3D	32	7	23
GE Advance NXi	1.125	0.01	Yes	0.15	2	128	OSEM 3D	56	14	11
Siemens Biograph mCT	1	-	Yes	0.15	1	200	OSEM 3D	130	26	49

3.2 SimPET - An open online platform for the Monte Carlo simulation of realistic brain PET data

3.2.1 SimPET platform

After the validation of the MC simulation models in the three commercial scanners, the subsequent result of this thesis was the creation of the SimPET platform. In this chapter we present SimPET (www.sim-pet.org), a free, easy-to-use, cloud-based platform for the generation of synthetic PET images with a special focus on brain imaging. The source code is free and can be downloaded from GitHub (https://github.com/txusser/brainviset_simset). The SimPET collaboration is an initiative of the Health Research Institute of Santiago (IDIS) with partners such as the General Foundation of the University of Malaga (FGUMA), University of Barcelona (UB) and Qubiotech Health Intelligence SL. The platform allows the automatic generation of realistic digital brain phantoms derived from patient PET/CT and MRI images by using SimSET and STIR within the Brain-VISET (voxel-based iterative simulation for emission tomography) method previously published by our group (Marti-Fuster et al., 2014), and the simulation and reconstruction of these or other user-defined phantoms using the validated scanner models included in the platform. The interested reader can find past use cases in our published work (Silva-Rodríguez et al., 2014, 2015, 2016).

3.2.2 GUI and functionalities

Figure 46 shows the GUI, that users can access freely through www.sim-pet.org, after filling a registration form with their email and some additional information. The main menu is structured in three modules: Phantom generation (map generation), simulation, and reconstruction. After each process, intermediate files can be downloaded/uploaded, allowing the user to introduce extra steps in the process. An interactive online image viewer is also included for evaluating the results without the need of downloading any file. The different boxes in Figure 46 provide an overview of the different interaction panels in the platform. The user profile, an online manual and online support can also be found in the main page.

The platform accepts inputs in the Digital Imaging and Communications in Medicine (DICOM) and NifTI-1 formats. When uploading DICOM, the images are anonymized and converted to NifTI-1, which is a more convenient format for mathematical manipulation. The platform outputs the generated digital brain phantoms (activity and attenuation maps), sinograms, and reconstructed PET images in NifTI-1.

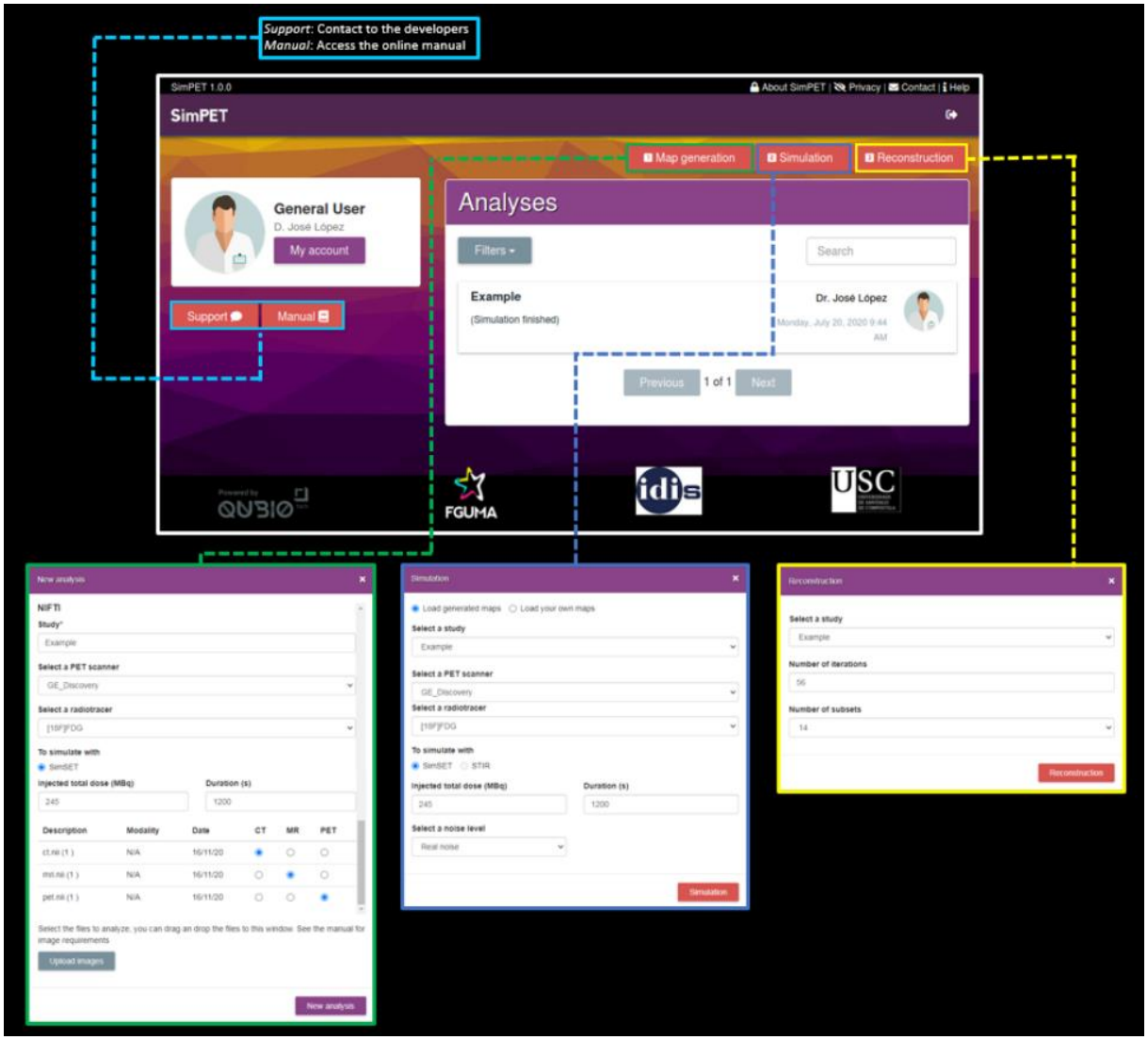

Figure 46: Web-based Graphical User Interface of SimPET (www.sim-pet.org). Surrounding boxes show the pop-up menus for patient-derived map generation (green), Monte Carlo simulation (dark blue), Tomographic reconstruction (yellow) and we highlight the different support options (light blue).

A typical workflow is illustrated in Figure 47, including (i) loading PET, CT, and MR images of the same subject, as input parameters, and configuring a scanner model, a radiotracer, injected dose (MBq), and scan duration (s) for generating activity and attenuation maps using Brain-VISET; (ii) generating simulated sinograms from previously generated maps or from uploaded attenuation and activity maps using SimSET. For these, the user must set the desired injected dose (MBq), the scan duration (s), and the noise level, which can be allowed to easily generate noise-free simulations independently of the selected parameters; and finally (iii) reconstructing the above sinograms using STIR. Once the different images are generated, these can be viewed online or downloaded. For more details or an usage example, see the online manual at www.sim-pet.org (Figure 46, light blue box).

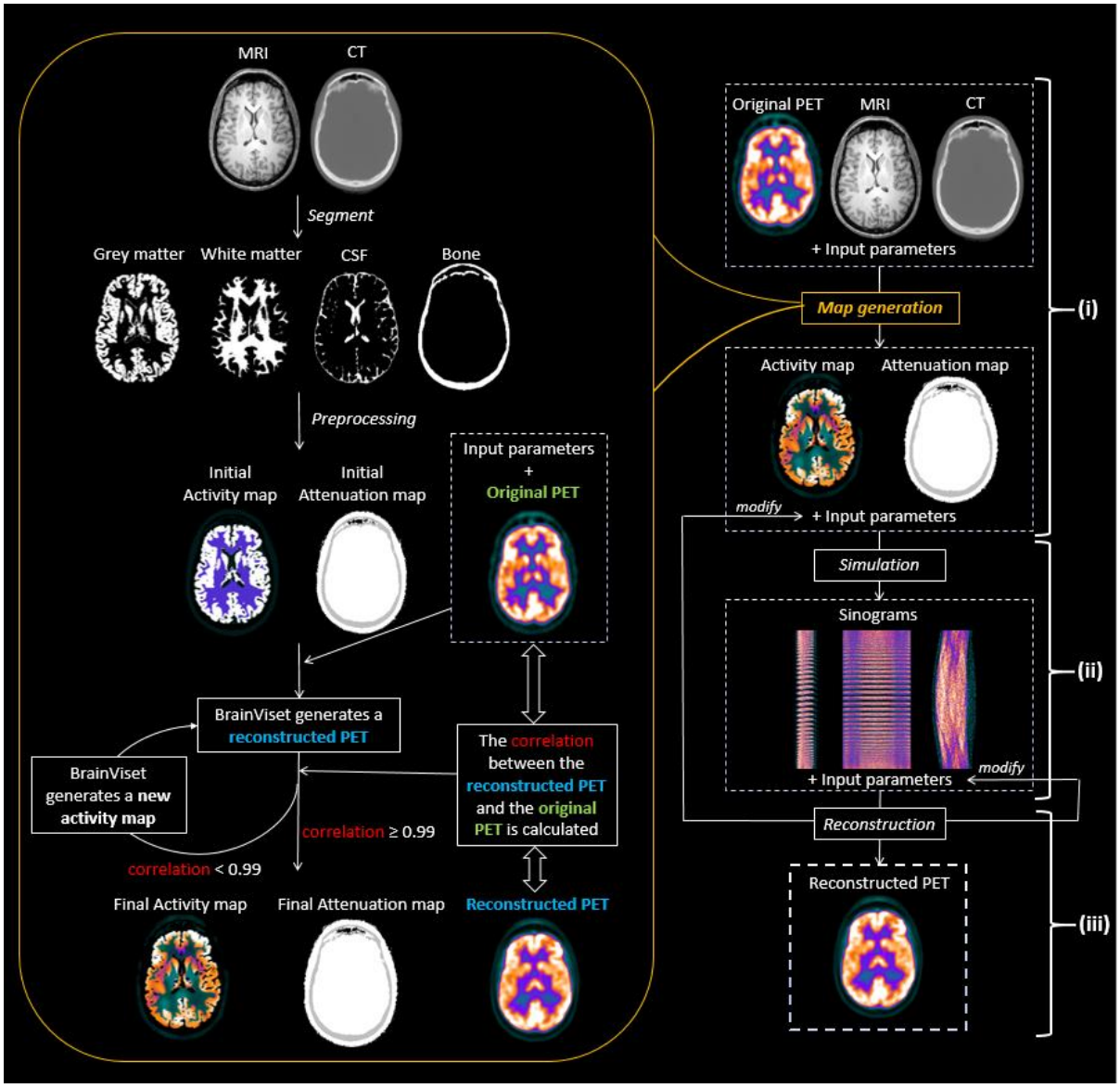

Figure 47: Typical workflow of SimPET. (i) First PET/CT and MRI images are considered as inputs for the activity and attenuation map generation. (ii) Next, the attenuation and activity maps are simulated for obtaining PET sinograms. (iii) Finally, the reconstructed PET images are generated by reconstructing these sinograms. The simulation and reconstruction steps can be repeated after changing the input parameters until the final image is satisfactory.

3.2.3 Internal processing

The MC simulation is performed using SimSET (v.2.9.2), which includes the simulation of all the physical processes for the energies of interest in nuclear medicine (below 1 MeV) (R. Harrison et al., 2008; R. E. Schmitz et al., 2007). The generated data are then reconstructed by using STIR (v.3.1) (https://github.com/UCL/STIR). Currently, three commercial PET scanners are supported, namely the GE Discovery ST (GE Healthcare, Chicago, United States), The GE Advance NXi (GE Healthcare, Chicago, United States) and the Siemens Biograph mCT (Siemens Healthineers, Erlanger, Germany). Additional scanners will be progressively added in the future. Part of the parameters of the models of the three implemented scanners are based on previously published works (Barret et al., 2005; Guerin & El Fakhri, 2008; Poon et al., 2015). The scanner models are validated as shown in the results of section 3.1. The images are

reconstructed using the ordered subsets expectation maximization (OSEM) algorithm as implemented in STIR, setting the reconstruction parameters to match those set in the scanner as closely as possible.

Realistic activity and attenuation maps including nonuniform activities and physiological variability can be fully automatically extracted from patient images by using the Brain-VISET iterative method. This method has been previously presented in detail (Marti-Fuster et al., 2014) and can be seen schematically in the orange box of Figure 47. In brief, PET/CT images are coregistered to the T1-weighted MRIs using FLIRT (https://fsl.fmrib.ox.ac.uk/fsl). Bone tissue images are extracted from the CTs using a 600 Hounsfield unit threshold. The T1 MRI is segmented to gray matter, white matter, and cerebrospinal fluid using SPM12. An initial activity map is generated by filling the segmented tissues with uniform activities. An initial attenuation map is created joining bone tissue image (attenuation value = 3) with outskin image (attenuation value = 4). The bone tissue image is generated from thresholded CT and the outskin image came from joining all segments generated with SPM12. The initial maps are then simulated using the MC model for the selected scanner. Postsimulation, the reconstructed image is compared with the original PET image studying the correlation coefficient. In case the correlation coefficient is < 0.99, the original PET image is divided by the reconstructed image to generate a ratio image and the activity map is multiplied by this ratio image to be updated. This process is repeated iteratively until the correlation coefficient is ≥ 0.99.

3.3 GENERATION OF HEALTHY DATABASES

For SimPET validation, realistic simulated databases of healthy subjects were generated from digital phantoms for each of the scanners implemented in the SimPET platform: the GE Discovery ST, the GE Advance NXi and the Siemens mCT. The CPU time for the generation of digital phantoms was about 3–4 h for GE Discovery ST, reaching convergence after four or five BrainVISET iterations. Figure 48 shows a subset of Group 1 (row 1) and the corresponding generated digital phantoms (row 2).

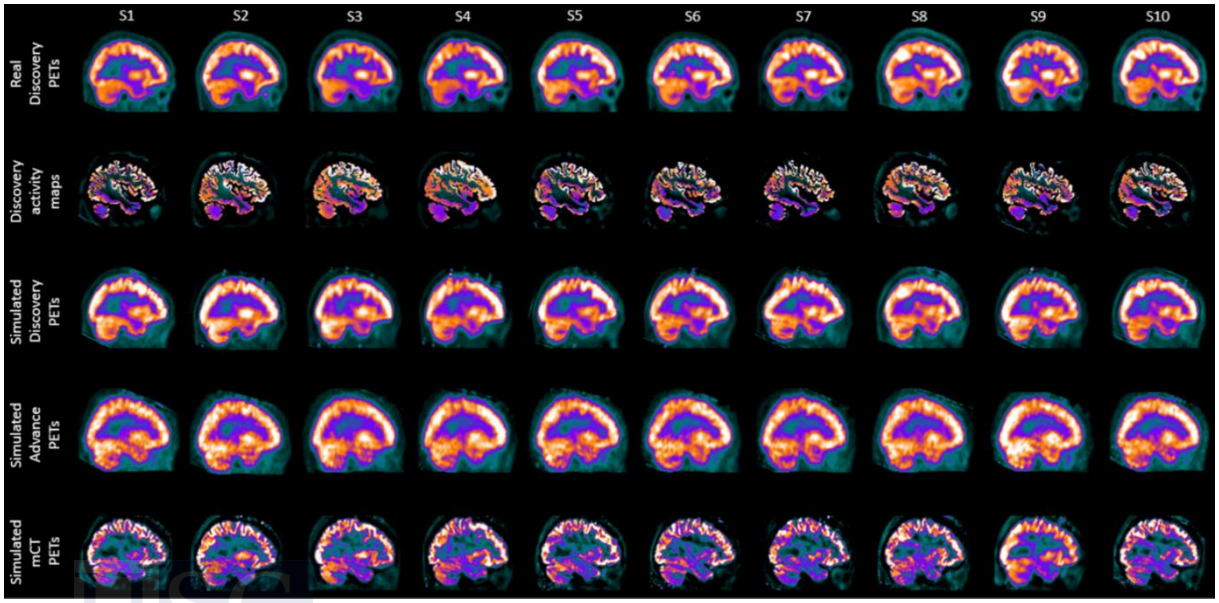

Figure 48: Sample of ten healthy control PET images acquired on GE Discovery ST (Group 1), the corresponding generated digital phantoms, and the corresponding simulated PET images obtained in the different commercial scanners using SimPET.

The computation time for the simulation of the generated phantoms was about 50 min per subject, while the reconstruction time was 20 min for the GE Discovery ST and GE Advance NXi, and 40–60 min for the Siemens Biograph mCT scanner. This difference in reconstruction times was caused by the difference in times for the calculation of attenuation sinograms between the different scanners. Figure 48 (rows 3–5) shows the corresponding simulations of this subset of Group 1 in the three scanners.

On the other hand, the results of the Bland-Altman analysis are shown in Figure 49.

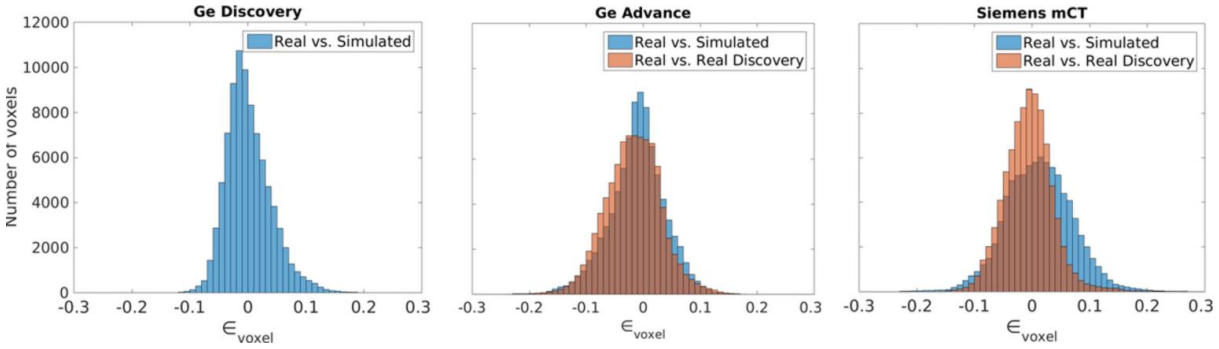

Figure 49: Bland-Altman comparison between the real and simulated databases, for the GE Discovery ST (left), the GE Advance (center) and the Siemens mCT (right).

In the left blue histogram, we can observe the differences between the real and the simulated images for the GE Discovery ST, showing that 83.02% of voxels showed differences of < 5%, while 98.09% were below 10%. For the GE Advance NXi (center), the blue histogram represents the differences between the real and the simulated images, showing that 71.98% of the voxels had differences lower than 5%, while 95.09% were below 10%. These results were similar when comparing between real databases for the GE Discovery ST (Group 1) and the GE Advance NXi (Group 2). The red histogram shows that 68.42% voxels had differences lower than 5% while 94.55% are below 10%, pointing to the fact that most of the observed differences between the real and the simulated images for the GE Advance NXi, they were due to differences between the real databases. Finally, for the Siemens Biograph mCT (right), the blue histogram shows that 62.22% of the voxels showed differences of less than 5%, while 91.35% were below 10%. Instead, when comparing between real databases for GE Discovery ST (Group 1) and Siemens Biograph mCT (Group 3), the red histogram shows differences lower than 5% for 79.03% of the voxels, and below 10% for 97.60%, showing that the model of the Siemens Biograph mCT provides the worst correspondence along the used scanner models.

Figure 50 shows the voxel-wise statistical comparisons (mean and statistical differences) between acquired and simulated images for the different scanners. As it can be observed in Figure 50 (rows 1–2), good visual agreement between the mean simulated and acquired images was achieved. Voxel-wise analysis (Figure 50, row 3) showed some regional differences, including regions of higher activity in the right temporal lobe of the simulated group and a bilateral region showing lower activity for the simulated group in the upper frontal lobe. As for the GE Discovery ST, a good visual agreement between simulated and real images is observed for GE Advance NXi (Figure 50, rows 4–5). The voxel-wise analysis showed some areas of higher metabolism for the simulated group on the frontal lobe, while reduced activity was observed in the temporal lobe and the internal structures (Figure 50, row 6). For the Siemens Biograph mCT we observed the greater visual differences between the simulations and the

acquisitions (Figure 50, rows 7–8). Artifacts can be observed in the simulated images, such as slight asymmetries on the occipital and temporal lobes that are not observed for the other scanners. The voxel-wise analysis showed higher simulated activity in the cerebellum, the internal structures and some small cortical areas in the right frontal lobe and the left occipital lobe. In contrast, we observed reduced simulated metabolism in several small clusters distributed along the cortex. The three simulated databases are freely available via SimPET web (www.sim-pet.org) in the Datasets section.

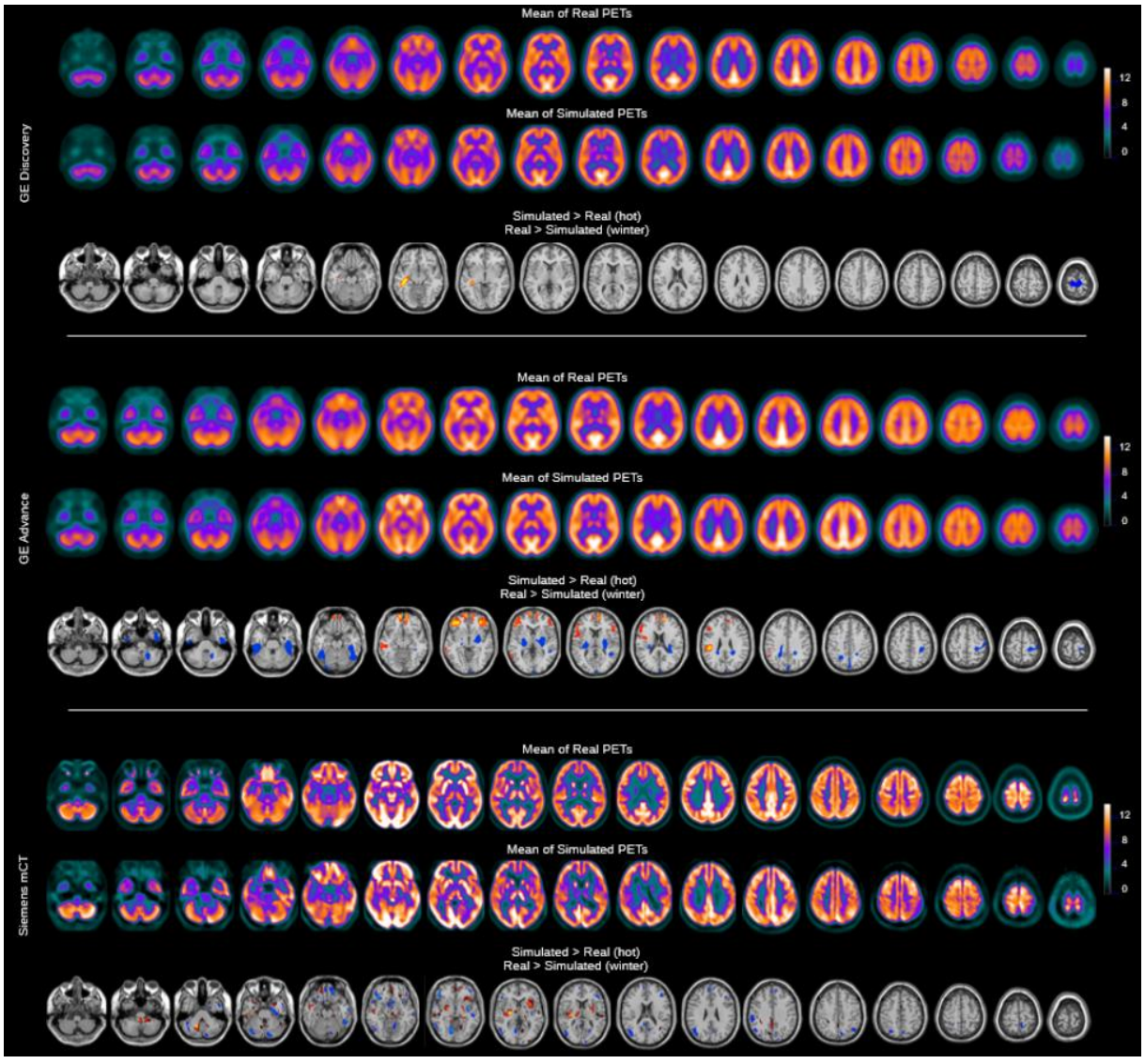

Figure 50: Voxel-based analysis results for the comparison between the simulated images and real FDG-PET images for the three simulated scanners. A threshold of P < 0.01 corrected and k = 300 is applied.

3.4 GENERATION OF AN EPILEPSY DATABASE

Initially, three levels of type 1 hypometabolism were considered for each activity map. Thus, 25 maps with an induced hypometabolism of 60%, 25 maps with a hypometabolism of 75% and 25 maps with a hypometabolism of 90% were created and then a total of 75 simulated images were obtained, which were visually validated by the experienced nuclear physician. This visual validation resulted in a significant proportion of non-realistic hypometabolisms that

were discarded because they showed too subtle epileptogenic foci, undetected or areas of low metabolic activity that could be confused with the epileptogenic foci.
This process of review and simulation of new studies was repeated several times until we obtained a first database visually validated by our nuclear medicine physician. In this way, we ended up with 25 PET studies with an induced hypometabolism of 60%, 31 studies with a hypometabolism of 75% and 19 studies with a hypometabolism of 90%. All hypometabolisms in small random regions of the cerebral cortex (type 1 hypometabolisms).

Following the recommendations of our epilepsy expert to increase the variability of the dataset, we decided to include 25 additional cases with 2 levels of type 2 hypometabolism. Thus, after some review by our expert, 15 PET studies with an induced hypometabolism of 40% and 10 studies with a hypometabolism of 30% were simulated. These hypometabolisms affect whole regions of the cerebral cortex (hypometabolism type 2).

If we add the 25 simulated PET studies without induced hypometabolism to the dataset simulated with hypometabolism, we form the definitive database with a total of 125 simulated images (100 simulated PET images with induced hypometabolism + 25 simulated PET images of healthy controls). The characteristics of each of the 100 simulated PET studies with induced hypometabolism can be seen in Table 6a and Table 6b.

Table 6a: Characteristics of simulated PET studies with induced hypometabolism in the cerebral cortex.

Subject	Type of hypometabolism	% of hypometabolism	Hypometabolism región (atlas of Hammers)
1	Type 1	60	7-Anterior temporal lobe lateral part
2	Type 1	60	30-Posterior temporal lobe
3	Type 1	75	20-Insula
4	Type 1	60	49-Precentral gyrus
5	Type 1	75	55-Inferior frontal gyrus Brocca's area
6	Type 1	90	3-Amygdala
7	Type 1	60	56-Inferior frontal gyrus Brocca's area
8	Type 1	60	14-Middle and inferior temporal gyrus
9	Type 1	90	32-Inferiolateral remainder of parietal
10	Type 1	75	64-Lingual gyrus
11	Type 1	75	13-Middle and inferior temporal gyrus
12	Type 1	75	25-Gyrus cinguli posterior part
13	Type 1	75	49-Precentral gyrus
14	Type 1	75	65-Cuneus
15	Type 1	90	7-Anterior temporal love lateral part
16	Type 1	75	62-Precuneus
17	Type 1	75	26-Gyrus cinguli posterior part
18	Type 1	90	64-Lingual gyrus
19	Type 1	75	4-Amygdala
20	Type 1	75	1-Hippocampus
21	Type 1	90	16-Fusiform gyrus
22	Type 1	60	53-Anterior orbital gyrus
23	Type 1	75	56-Inferior frontal gyrus Brocca's area
24	Type 1	75	55-Inferior frontal gyrus Brocca's area
25	Type 1	60	60-Postcentral gyrus
26	Type 1	90	63-Lingual gyrus
27	Type 1	75	12-Temporal superior posterior part
28	Type 1	60	58-Superior frontal gyrus
29	Type 1	75	32-Inferiolateral remainder of parietal
30	Type 1	90	58-Superior frontal gyrus
31	Type 1	60	5-Anterior temporal lobe medial part
32	Type 1	75	30-Posterior temporal lobe
33	Type 1	90	13-Middle and inferior temporal gyrus
34	Type 1	60	64-Lingual gyrus
35	Type 1	60	13-Middle and inferior temporal gyrus
36	Type 1	90	54-Anterior orbital gyrus
37	Type 1	60	7-Anterior temporal love lateral part
38	Type 1	75	27-Middle frontal gyrus
39	Type 1	75	6-Anterior temporal lobe medial part
40	Type 1	60	59-Postcentral gyrus
41	Type 1	75	50-Precentral gyrus
42	Type 1	90	1-Hippocampus
43	Type 1	60	50-Precentral gyrus
44	Type 1	75	11-Temporal superior posterior part
45	Type 1	90	56-Inferior frontal gyrus Brocca's area
46	Type 1	60	28-Middle frontal gyrus
47	Type 1	90	2-Hippocampus
48	Type 1	90	14-Middle and inferior temporal gyrus
49	Type 1	60	20-Insula
50	Type 1	75	56-Inferior frontal gyrus Brocca's area

Table 6b: Characteristics of simulated PET studies with induced hypometabolism in the cerebral cortex.

Subject	Type of hypometabolism	% of hypometabolism	Hypometabolism region (atlas of Hammers)
51	Type 1	60	21-Lateral remainder of occipital lobe
52	Type 1	60	55-Inferior frontal gyrus Brocca's area
53	Type 1	75	49-Precentral gyrus
54	Type 1	75	23-Gyrus cinguli anterior part
55	Type 1	60	55-Inferior frontal gyrus Brocca's area
56	Type 1	75	27-Middle frontal gyrus
57	Type 1	90	62-Precuneus
58	Type 1	60	10-Parahippocampal gyrus
59	Type 1	75	15-Fusiform gyrus
60	Type 1	90	8-Anterior temporal lobe lateral part
61	Type 1	60	31-Inferiolateral remainder of parietal lobe
62	Type 1	75	29-Posterior temporal lobe
63	Type 1	90	51-Straight gyrus
64	Type 1	60	53-Anterior orbital gyrus
65	Type 1	75	27-Middle frontal gyrus
66	Type 1	90	6-Anterior temporal lobe medial part
67	Type 1	60	4-Amygdala
68	Type 1	75	2-Hippocampus
69	Type 1	75	60-Postcentral gyrus
70	Type 1	60	31-Inferiolateral remainder of parietal lobe
71	Type 1	75	28-Middle frontal gyrus
72	Type 1	90	50-Precentral gyrus
73	Type 1	60	10-Parahippocampal gyrus
74	Type 1	75	56-Inferior frontal gyrus Brocca's area
75	Type 1	90	64-Lingual gyrus
76	Type 2	40	22-Lateral remainder of occipital lobe
77	Type 2	40	56-Inferior frontal gyrus Brocca's area
78	Type 2	30	29-Posterior temporal lobe
79	Type 2	30	32-Inferiolateral remainder of parietal lobe
80	Type 2	30	30-Posterior temporal lobe
81	Type 2	40	53-Anterior orbital gyrus
82	Type 2	40	57-Superior frontal gyrus
83	Type 2	40	49-Precentral gyrus
84	Type 2	30	64-Lingual gyrus
85	Type 2	30	28-Middle frontal gyrus
86	Type 2	30	59-Postcentral gyrus
87	Type 2	40	56-Inferior frontal gyrus Brocca area
88	Type 2	40	61-Precuneus
89	Type 2	30	60-Postcentral gyrus
90	Type 2	30	25-Gyrus cinguli posterior part
91	Type 2	40	14-Middle and inferior temporal gyrus
92	Type 2	40	21-Lateral remainder of occipital lobe
93	Type 2	40	50-Precentral gyrus
94	Type 2	40	27-Middle frontal gyrus
95	Type 2	40	31-Inferiolateral remainder of parietal lobe
96	Type 2	40	14-Middle and inferior temporal gyrus
97	Type 2	30	28-Middle frontal gyrus
98	Type 2	30	58-Superior frontal gyrus
99	Type 2	40	11-Temporal supeior posterior part
100	Type 2	40	61-Precuneus

Regarding the quantitative analysis of this simulated database, we can observe a sample of 5 of the subjects in Figure 51. As we can see, a good visual agreement has been achieved between the ROI of the cerebral cortex where hypometabolism has been induced in the activity maps and the hypometabolism shown in the simulated PETs (Figure 51, rows 1- 2). The simulated epilepsy database is quantitatively validated thanks to the VBA results where the most

significant differences between the simulated PET group of healthy controls and each simulated subject with hypometabolism are shown in the same region where hypometabolism has been induced in each simulated subject (Figure 51, rows 1-3). The complete simulated epilepsy dataset is freely available via SimPET web (www.sim-pet.org) in the Datasets section.

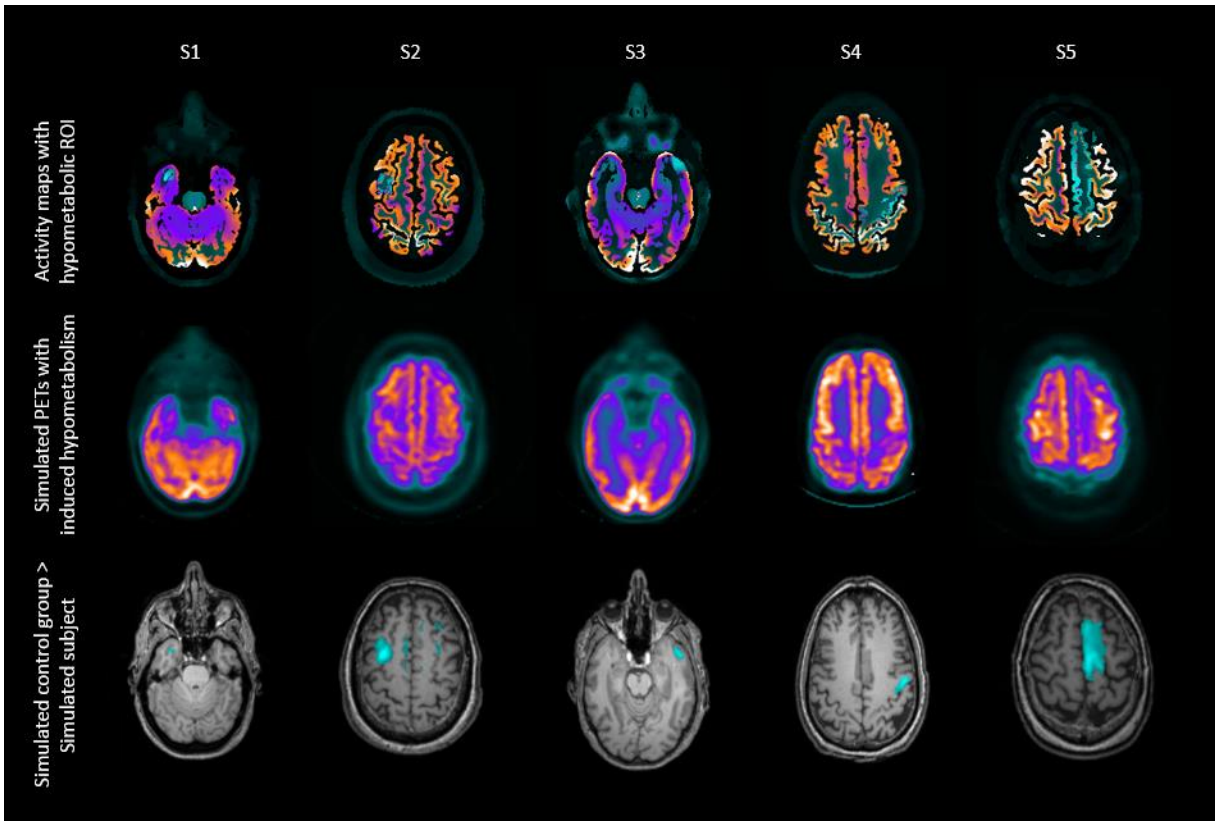

Figure 51: Sample of five subjects from the simulated epilepsy database. Row 1 shows the activity maps with the ROI of hypometabolism, row 2 shows the corresponding hypometabolic simulated PETs, and row 3 shows the VBA results where the metabolic activity of the simulated subject with induced hypometabolism is lower than the activity from the simulated PET group of healthy controls.

DISCUSSION

4 DISCUSSION

Part of the content from this chapter has already been published as Paredes-Pacheco, J. et al. SimPET-An open online platform for the Monte Carlo simulation of realistic brain PET data. Validation for 18 F-FDG scans. Med Phys. 2021 May; 48(5):2482-2493. doi: 10.1002/mp.14838. PMID: 33713354; PMCID: PMC8252452.

As we have seen, validating simulation models of commercial PET scanners was the first step to perform simulations of realistic PET brain studies. The NEMA tests carried out to validate the GE Discovery ST simulation model gave quite satisfactory results while for the other scanners more differences were observed (Barret et al., 2005; Poon et al., 2015; Silva-Rodríguez et al., 2014). However, the NEMA results obtained in this and other works were good and realistic enough to consider the three MC simulation models validated for their implementation in the simulation platform developed in this thesis, SimPET. There are other MC simulation codes (España et al., 2009; Ferrari et al., 2005; Jan et al., 2004; Thompson et al., 1992), but SimPET is the first online platform that allows the simulation of realistic brain PET studies in an easy and efficient way, in commercial scanner models, without the need for strong computational resources or technical knowledge and with a high level of validation of the results from the NEMA tests on the simulation models to the validation carried out on the healthy databases generated on the platform. After obtaining a fully functional and validated platform such as SimPET, the possibility of performing multiple simulation works quickly and easily is available. In this thesis we focused on the direct application of the platform to the simulation of epilepsy cases. The simulation of known and controlled cortical hypometabolisms gave rise to an epilepsy database valid as real ground-truth for all types of work. Currently our epilepsy database is being used in an international detectability study that will yield more accurate results and conclusions than any other similar work that relies on the variability of real patient data or less validated simulation software. On the other hand, the works with FDG-PET in epilepsy are not the only ones that can benefit from the platform. Studies in neurological diseases as important as AD, Parkinson's disease or different types of epilepsy, as well as more specific PET study modalities, such as amyloid-PET, can also take advantage of the characteristics of SimPET. As an example, in the Appendices chapter we included complementary simulations of AD and TLE cases, as well as amyloid-PET simulations. These experiments may serve as examples to illustrate the variety of applications that SimPET can have when simulating different tracers and to present the users with appropriate workflows for evaluation of quantification protocols.

4.1 VALIDATION OF MC SIMULATION MODELS

When evaluating acquisition and quantification protocols using MC simulation, we need to use models best integrate the physical and acquisition characteristics of commercial PET scanners. For this we used the NEMA protocol (National Electrical Manufacturers Association, 2007). This standard provided us with a guide to evaluate the performance of our simulation models, as well as the corresponding real scanner. These measurements allowed us to configure and validate the simulation models. However, some of the configuration of these models could vary from one simulation software to another. One of the most widespread simulation toolkits is

GATE (Jan et al., 2004). GATE has the tools to build good simulation models close to real scanners, as we can see in these works (Geramifar et al., 2009; Schmidtlein, Turner, et al., 2006). However, the greater degree of complexity, long computational times and the need for a large amount of resources for its correct operation made us choose SimSET for the creation of the simulation models. SimSET is more intuitive, focuses on PET simulation, and is accurate enough to give quite realistic results at a lower cost of resources.

Focusing on the use of SimSET for the construction of a simulation model of the GE Discovery ST and its validation through the NEMA protocol, we found some works (Guerin & El Fakhri, 2008). If we calculate the mean differences in the NEMA tests performed by Guerin and El Fakhri between the simulation model implemented in SimSET and the real GE Discovery ST scanner, we have approximately 2.62 for 1 cm and 3.61 for 10 cm in spatial resolution, approximately 2.34 in sensitivity and, regarding image quality, 19% in cold contrast and 28% in hot contrast. Looking at the results of our NEMA tests for the real GE Discovery ST scanner and our simulated model in SimSET, we could also observe certain differences. These differences were more present in image quality contrasts, with a mean difference of 4.33% in hot contrast and 3.86% in cold contrast, and less marked in spatial resolution, with a mean difference of 2.7 for 1 cm and 2.15 for 10 cm, and with almost no difference in sensitivity. This supports that our NEMA results are within expectations, being better or similar than the results published in other works for the GE Discovery ST scanner.

The differences observed in our NEMA tests for the GE Discovery ST scanner could be due to, among other reasons, the detector block model used to simulate: “simple pet”. This is the most basic model of SimSET, since it does not reproduce any particular geometry and only takes into account the object photon interaction by applying a Gaussian blurring. There are other detector block models like the “cylindrical” model. This model reproduces a geometry formed by a series of adjacent regular right cylinders with some transaxial layers. This allows us to simulate photon interactions such as scatter, absorption or depth of interaction, although there are no blocks and therefore no gap effects. This makes the "cylindrical" model more accurate than the "simple pet" model, although it is a much more time consuming model to simulate and still has some features in development, especially if we want to use SimSET to simulate brain PET images in the selected scanners. So we chose the simpler SimSET models for integration into SimPET. Besides this, another important limitation was not having the reconstruction algorithm used in the real scanner. This led us to validate the simulation model in an atypical way, since the most appropriate option would have been to validate the simulation and subsequently the reconstruction. However, this was not possible since our reconstruction software, STIR, did not have the reconstruction algorithm developed by General Electric implemented in the GE Discovery ST scanner. For this reason we had to jointly validate the simulation and reconstruction processes using the OSEM iterative reconstruction algorithm as an approximate solution to the real reconstruction.

Regarding the GE Advance NXi and Siemens Biograph mCT scanners, both simulation models were validated both in previous works of our group (Silva-Rodríguez et al., 2014) and other authors (Barret et al., 2005; Poon et al., 2015). In the case of the GE Advance NXi, the NEMA tests of the simulation model and the real scanner had a good correlation (within 5%) regarding spatial resolution, sensitivity and image quality, having a good balance between all (Silva-Rodríguez et al., 2014). In the case of the Siemens Biograph mCT scanner, in addition to the tests carried out by collaborators of the Hospital Clinic, there is a study that has already evaluated the simulation model for this scanner (Poon et al., 2015). Observing the NEMA protocol results of this study, we can get that the mean difference between the simulated model and the real acquisition is 1.45 for 1 cm and approximately 1.42 for 10 cm regarding spatial

resolution. This is a pretty good result considering that the Siemens Biograph mCT is a more modern scanner than the other two and with new technologies for data acquisition, such as Time of Flight (Jakoby et al., 2011), which increase the complexity of the simulation.

Considering the simulation models of the three commercial PET scanners evaluated for SimSET and fixing the physical parameters that describe the geometry of each scanner, different configurations of number of iterations in the reconstruction, PSF values, etc. were tested looking to reduce the differences obtained between the real and the simulated scanners. These tests were necessary since some of these parameters were not known a priori, and the manufacturers of the PET scanners do not usually provide them with precision. An individual improvement in the results of spatial resolution, sensitivity or image quality of the simulated scanner could be achieved using values other than those in Table 5a and Table 5b. However, improving the results in one of the tests could worsen the results in another. For example, for the GE Discovery ST simulation model, the number of iterations selected for the reconstruction minimized the errors in the NEMA tests with respect to the real scanner in general, since if we lower this parameter, the difference in the contrasts of the spheres of the image quality test decreases a little but increases the difference in background variability. On the other hand, if we increase the number of iterations, the difference in the image quality test increases in general. Also, applying lower or higher values of PSF could increase the difference in one component of the spatial resolution and decrease in the others or directly increase the difference in the whole spatial resolution.

Taking all of the above into account, the configurations shown in Table 5a and Table 5b provide a better balance and lower global differences between the real and simulated scanners in the different NEMA tests, considering the MC simulation models validated under the conditions described in chapter 3.1.

4.2 SimPET - An open online platform for the Monte Carlo simulation of realistic brain PET data

The evaluation and standardization of quantification methods in brain PET require the analysis of large pools of PET images, ideally against a well-known ground truth. While physical phantoms (Akamatsu et al., 2019; Harries et al., 2020; E. J. Hoffman et al., 1990; Iida et al., 2013; Wong et al., 1984) provide a way forward, they have quite a few limitations. They are complicated devices to fill properly, so acquiring many phantom images can be tedious and time consuming. They are often limited to simple geometric shapes. The generated studies do not show variability in the uptake of WM and GM since they are uniformly filled. Even the materials used in the phantom making have a limited ability to reproduce tissue characteristics such as density or attenuation (Filippou & Tsoumpas, 2018). All this leads to acquiring unrealistic images. Therefore, simulations can be of value in this case. In recent works, easy-to-use platforms for analytical simulation were presented (Pfaehler et al., 2018). The analytic PET simulators have low computational time costs and are especially useful in evaluation works of image processing methods and, in general, in works that require generating a large number of images. However, analytical simulations cannot be used, for example, to evaluate detector designs due to their low accuracy. This has led to most PET simulators being based on MC methods. MC methods allow to simulate the processes of acquisition and generation of projection data in a much more precise way, as well as to model different scanner designs and detector materials. However, great technical expertise and high computing power are required. To overcome these limitations without losing the precision provided by MC methods, we expanded the range of simulation software available by offering a free, intuitive, and efficient tool for MC simulation of realistic PET images, with a focus on brain imaging. SimPET is the

first web platform to have user-friendly tools for generating realistic activity and attenuation maps from patient data, simulating sinograms by combining previous generated digital phantoms with well-validated scanner models as well as reconstructing realistic synthetic brain PET images from the previously simulated sinograms. In addition, the modular design of the GUI allows the user to repeat any of the steps using different configurations, saving time and making it easy to customize simulated databases without restarting the entire process. Downloading different files of interest generated during the simulation, as well as previewing some of them through an online viewer are some of the additional features that the GUI has.

SimPET is a project in continuous development and is open, since all the simulation and reconstruction code is fully available on Github (https://github.com/txusser/brainviset_simset), allowing other users to contribute new features. Currently, new more detailed detector models, such as "cylindrical" model are being tested and implemented, as well as more sophisticated features not included so far, such as time-of-flight, resolution recovery and a list-mode for reconstruction (Efthimiou et al., 2019; Karakatsanis et al., 2016; Surti, 2015). These features are currently under development and will be available on a future release (Silva-Rodríguez et al., 2019). In addition to these features, the modular architecture of the platform favors collaboration with different centers for the incorporation of new models of commercial PET scanners. These scanners can have very different geometries, from preclinical equipment to total-body PET scanners, passing through the most current PET scanners. Many of these scanners already have a validated MC simulation model (Ahmed et al., 2020; Cañadas et al., 2011; Lu et al., 2016; Monnier et al., 2015; Schmidtlein, Kirov, et al., 2006), which would facilitate their future implementation on the platform. Our future goal is to build an open and diverse scientific community of users and developers. The platform currently has more than 80 registered users since it was published online in 2020.

4.3 GENERATION OF HEALTHY DATABASES

To demonstrate the capabilities of the platform, we generated synthetic databases of healthy patients for the three scanner models included in the library. For this, we generated realistic activity and attenuation maps derived from 25 healthy patients acquired on the GE Discovery ST, which were then simulated using different scanner models. Despite the images generated by the platform were visually close to the real images for all scanners (see Figure 48), statistical analysis revealed significant differences, especially for the GE Advance and the Siemens mCT. In this regard, quantitative analysis was performed by comparing simulated images with the real ones acquired on each scanner by Bland-Altman analysis and SPM statistical analysis (see Figure 49 and 50). In both cases, the GE Discovery ST showed the smallest differences between the acquired and simulated images (83.02% of voxels have differences of < 5%). This is not surprising, as this was the most favorable comparison, since the simulated images were compared with the FDG-PET images from which the digital phantoms were derived. Results from the other scanners (GE Advance NXi and Siemens Biograph mCT) showed bigger differences. Unlike the GE Discovery ST, where the differences observed are due solely to the quality of the simulation, the differences obtained for GE Advance NXi and Siemens Biograph mCT were due to both the simulation and the physiological differences between the control groups (see Figure 49) because different subjects were compared and the size of each group was relatively small. In addition, this validation had the handicap that the simulation images of the three scanners were generated from the same activity and attenuation maps. More work will be needed to decrease the variability between the databases and new features are being developed to improve MC simulation models in order to minimize the differences (Silva-Rodríguez et al., 2019). Despite the differences, the tests supported the idea that simulated PET

studies provided good realistic results according to the simulation complexity of each implemented scanner. In this way, the simulation models currently implemented in the platform were considered validated.

These databases can serve as a control group in the study of many pathological cases as well as a test bench for the evaluation of PET neuroimaging protocols, eliminating the need to acquire or have a database of real controls. In addition, they are easily expandable through the platform thanks to the implemented PET scanner models. Our simulated healthy databases are an important addition to the low availability of simulated databases of realistic brain PET studies (Batan et al., 2004; Mota et al., 2015; Reilhac et al., 2005) and they have some advantages over other datasets. Our databases were validated by different statistical analyses and respect the physical characteristics of the implemented commercial PET scanners, which makes them especially realistic and useful in works involving these or other commercial scanners. Furthermore, our datasets have a realistic variability of activity values since the digital phantoms used in the simulation were generated by the Brain-VISET iterative method (Marti-Fuster et al., 2014). All this makes our healthy databases an important contribution to the development of PET scanners, clinical diagnosis and research.

4.4 GENERATION OF AN EPILEPSY DATABASE

As a central element of this thesis focused on the validation of new PET protocols for epilepsy, we proceeded to simulate a cortical epilepsy database using the previously generated activity maps for the GE Discovery ST scanner model. We induced activity maps with different levels and types of known hypometabolism in ROIs of the cerebral cortex to then generate simulated PET studies of cortical epilepsy. It is a unique database, both for the variety of cases of cortical epilepsy present with hypometabolism of various sizes, levels of intensity and affected regions, as well as for the visual review of each case by our experienced nuclear medicine physician and the subsequent quantitative validation. Currently there are few works that simulate PET studies with realistic hypometabolism in neurological diseases and, in particular, in epilepsy. (Baete et al., 2004) simulates hypometabolisms in the cerebral cortex from a digital phantom to evaluate the performance of a reconstruction algorithm for the detection of these hypometabolic regions in epilepsy. However, they use a digital phantom without variability in the uptake of WM and GM and perform the simulation without using a validated model or software, leading to unrealistic images. Contrary to simulated studies from our epilepsy database. This highlights the quality of the simulated database as well as the ability of the SimPET platform to simulate realistic pathological PET studies.

The first application we have proposed for our database is to evaluate the visual detectability of FDG-PET in patients with epilepsy. In this type of work, the visual sensitivity of different experts in epilepsy to detect epileptogenic foci is evaluated. Most detectability studies in epilepsy are done without simulation and, therefore, without real ground-truth. Instead, the clinical history of the patients, an operative report after surgery or other medical tests are used as the reference standard (Kikuchi et al., 2021; Paldino et al., 2017; Struck & Westover, 2015). However, this entails a series of limitations such as the introduction of some patient selection bias, the possible non-existence of hypometabolism despite the success of surgery or directly the lack of knowledge of the hypometabolism that really exists since all these references are subject to errors or interpretations. With SimPET we do not have these limitations since it allows the simulation of epilepsy cases in a controlled environment, thus generating the described database. Our simulated epilepsy database constitutes a real and known ground-truth for the evaluation of epilepsy neuroimaging protocols. It is currently undergoing an international detectability study with nuclear medicine physicians from different

countries (Spain, France and Italy) with the aim of assessing the ability of visual analysis to locate epileptogenic foci in the cerebral cortex compared to quantitative analysis. To this end, a platform has been created from which nuclear medicine physicians can access the epilepsy database, download the quantitative analysis if necessary, and send a report with the region of the brain in which they have detected hypometabolism and the degree of confidence in the selection. Once we have all the reports from the experts, the sensitivity and specificity will be analyzed.

Another application could be as a visual reference for the creation of epilepsy guidelines, taking advantage of the wide variety of cortical hypometabolisms in the database. Also as a tool to train nuclear physicians with simulated PET images with induced hypometabolism giving them the ability to accurately locate epileptogenic foci. For example, a study with several phases of training could be proposed, starting with extensive hypometabolisms as easy level and, little by little, increasing the difficulty with lighter or smaller hypometabolisms. If the database is expanded to many more cases, it could serve not only as training for nuclear physicians but also as a source of information for training machine learning algorithms. These types of algorithms need a large amount of pre-classified training data to work accurately. This is a major drawback in epilepsy works dependent on real PET studies, since there is usually a limited number of images available and it is difficult and time consuming to locate and delimit epileptogenic foci. These problems can be overcome thanks to simulated, extensible and validated databases such as the one presented in this thesis. Our database will allow training machine learning algorithms for automatic detection of hypometabolic cortical regions, classifiers of different types of hypometabolism associated with epilepsy or predictors of surgical outcome, among other uses.

CONCLUSIONS

5 CONCLUSIONS

We have successfully developed a new computer simulation web platform designed for brain PET studies and validated in FDG-PET images, specifically in epilepsy patients.

For this, we have achieved different milestones summarized in the following conclusions:

a) As an initial step, MC simulation models of three commercial PET scanners were validated and configured to be implemented into a simulation web platform. The validation of the GE Discovery ST scanner was carried out using our NEMA measurements, while the validation of GE Advance and mCT Siemens were derived from works previously developed in our group. All of them resulted in small differences between the simulated model and the real scanners.

b) The simulation web platform to integrate all MC simulation models was developed as a free, user-friendly and efficient tool that allows the automatic generation of realistic digital brain phantoms and the simulation of brain PET studies. It was validated through the simulation of three databases of healthy controls, one for each implemented commercial scanner, showing an excellent agreement between simulated and real brain PET studies.

c) Finally, the simulation web platform was efficiently used to generate simulated brain PET images of epilepsy patients in order to evaluate different protocols in epilepsy. A new methodology was developed to induce known and controlled hypometabolic cortical areas in digital brain phantoms and generate a well-validated database of simulated FDG-PET images of epilepsy patients.

BIBLIOGRAPHY

6 BIBLIOGRAPHY

Accorsi, R., Adam, L.-E., Werner, M. E., & Karp, J. S. (2004). Optimization of a fully 3D single scatter simulation algorithm for 3D PET. *Physics in Medicine and Biology*, *49*(12), 2577–2598. https://doi.org/10.1088/0031-9155/49/12/008

ADNI | Alzheimer's Disease Neuroimaging Initiative. (n.d.). Retrieved 3 September 2021, from http://adni.loni.usc.edu/

ADNI | PET Analysis. (n.d.). Retrieved 3 September 2021, from http://adni.loni.usc.edu/methods/pet-analysis-method/pet-analysis/

Agostinelli, S., Allison, J., Amako, K., Apostolakis, J., Araujo, H., Arce, P., Asai, M., Axen, D., Banerjee, S., Barrand, G., Behner, F., Bellagamba, L., Boudreau, J., Broglia, L., Brunengo, A., Burkhardt, H., Chauvie, S., Chuma, J., Chytracek, R., … Zschiesche, D. (2003). Geant4—A simulation toolkit. *Nuclear Instruments and Methods in Physics Research Section A: Accelerators, Spectrometers, Detectors and Associated Equipment*, *506*(3), 250–303. https://doi.org/10.1016/S0168-9002(03)01368-8

Aguiar, P., Pareto, D., Gispert, J. D., Crespo, C., Falcón, C., Cot, A., Lomeña, F., Pavía, J., & Ros, D. (2008). Effect of anatomical variability, reconstruction algorithms and scattered photons on the SPM output of brain PET studies. *NeuroImage*, *39*(3), 1121–1128. https://doi.org/10.1016/j.neuroimage.2007.09.055

Ahmed, A. M., Chacon, A., Rutherford, H., Akamatsu, G., Mohammadi, A., Nishikido, F., Tashima, H., Yoshida, E., Yamaya, T., Franklin, D. R., Rosenfeld, A., Guatelli, S., & Safavi-Naeini, M. (2020). A validated Geant4 model of a whole-body PET scanner with four-layer DOI detectors. *Physics in Medicine &amp$\mathsemicolon$ Biology*, *65*(23), 235051. https://doi.org/10.1088/1361-6560/abaa24

Akamatsu, G., Ikari, Y., Ohnishi, A., Matsumoto, K., Nishida, H., Yamamoto, Y., Senda, M., & Japanese Alzheimer's Disease Neuroimaging Initiative. (2019). Voxel-based statistical analysis and quantification of amyloid PET in the Japanese Alzheimer's disease neuroimaging initiative (J-ADNI) multi-center study. *EJNMMI Research*, *9*(1), 91. https://doi.org/10.1186/s13550-019-0561-2

Akamatsu, G., Tashima, H., Iwao, Y., Wakizaka, H., Maeda, T., Yoshida, E., & Yamaya, T. (2019). A 3-dimensional hemispherical brain phantom for compact dedicated brain PET scanners. *Biomedical Physics & Engineering Express*, *5*(2), 025013. https://doi.org/10.1088/2057-1976/aaf77f

Alessio, A., & Kinahan, P. (2005). *PET Image Reconstruction*. https://www.semanticscholar.org/paper/PET-Image-Reconstruction-Alessio-Kinahan/c7e24d3a664656ea0bf9e52de4622cdb0d0f394d

Álvarez-Linera Prado, J. (2012). Resonancia magnética estructural en la epilepsia. *Radiología*, *54*(1), 9–20. https://doi.org/10.1016/j.rx.2011.07.007

Anderson, C. D. (1932). The Apparent Existence of Easily Deflectable Positives. *Science*, *76*(1967), 238–239. https://doi.org/10.1126/science.76.1967.238

Andreo, P. (1991). Monte Carlo techniques in medical radiation physics. *Physics in Medicine and Biology*, *36*(7), 861–920. https://doi.org/10.1088/0031-9155/36/7/001

Antonecchia, E., Chu, Q., Costanzo, A. D., Li, Z., Wan, L., D'Ascenzo, N., & Xie, Q. (2020). Simulation study on sensitivity performance of a helmet-shaped brain PET scanner based on the Plug&amp$\mathsemicolon$Imaging detector design. *Journal of Instrumentation*, *15*(05), C05071–C05071. https://doi.org/10.1088/1748-0221/15/05/C05071

Arbizu, J., García-Ribas, G., Carrió, I., Garrastachu, P., Martínez-Lage, P., & Molinuevo, J. L. (2015). Recomendaciones para la utilización de biomarcadores de imagen PET en el proceso diagnóstico de las enfermedades neurodegenerativas que cursan con demencia: Documento de consenso SEMNIM y SEN. *Revista Española de Medicina Nuclear e Imagen Molecular*, *34*(5), 303–313. https://doi.org/10.1016/j.remn.2015.03.002

Ashburner, J., & Friston, K. J. (2000). Voxel-based morphometry—The methods. *NeuroImage*, *11*(6 Pt 1), 805–821. https://doi.org/10.1006/nimg.2000.0582

Ayers, M., Svaldi, D., & Apostolova, L. (2019). *Brain Imaging in Differential Diagnosis of Dementia*. Practical Neurology; Bryn Mawr Communications. https://practicalneurology.com/articles/2019-june/brain-imaging-in-differential-diagnosis-of-dementia

Baete, K., Nuyts, J., Van Paesschen, W., Suetens, P., & Dupont, P. (2004). Anatomical-based FDG-PET reconstruction for the detection of hypo-metabolic regions in epilepsy. *IEEE Transactions on Medical Imaging*, *23*(4), 510–519. https://doi.org/10.1109/TMI.2004.825623

Bailey, D. L. (2005). Data Acquisition and Performance Characterization in PET. In D. L. Bailey, D. W. Townsend, P. E. Valk, & M. N. Maisey (Eds.), *Positron Emission Tomography: Basic Sciences* (pp. 41–62). Springer. https://doi.org/10.1007/1-84628-007-9_3

Bailey, D. L., Karp, J. S., & Surti, S. (2005). Physics and Instrumentation in PET. In D. L. Bailey, D. W. Townsend, P. E. Valk, & M. N. Maisey (Eds.), *Positron Emission Tomography: Basic Sciences* (pp. 13–39). Springer. https://doi.org/10.1007/1-84628-007-9_2

Barret, O., Carpenter, T., Clark, J., Ansorge, R., & Fryer, T. (2005). Monte Carlo simulation and scatter correction of the GE Advance PET scanner with SimSET and Geant4. *Physics in Medicine and Biology*, *50*, 4823–4840. https://doi.org/10.1088/0031-9155/50/20/006

Batan, G., Reilhac, A., Grova, C., Collins, L., Tohka, J., Costes, N., & Evans, A. C. (2004). A database of simulated PET volumes with anatomical variability. *IEEE Symposium Conference Record Nuclear Science 2004.*, *6*, 3699–3702. https://doi.org/10.1109/NSSMIC.2004.1466684

Biersack, H.-J., & Freeman, L. M. (2008). *Clinical Nuclear Medicine*. Springer Science & Business Media.

Bohnen, N. I., Djang, D. S. W., Herholz, K., Anzai, Y., & Minoshima, S. (2012). Effectiveness and safety of 18F-FDG PET in the evaluation of dementia: A review of the recent literature. *Journal of Nuclear Medicine: Official Publication, Society of Nuclear Medicine*, *53*(1), 59–71. https://doi.org/10.2967/jnumed.111.096578

Borghammer, P., Jonsdottir, K. Y., Cumming, P., Ostergaard, K., Vang, K., Ashkanian, M., Vafaee, M., Iversen, P., & Gjedde, A. (2008). Normalization in PET group comparison studies—The importance of a valid reference region. *NeuroImage*, *40*(2), 529–540. https://doi.org/10.1016/j.neuroimage.2007.12.057

Brett, M., Markiewicz, C. J., Hanke, M., Côté, M.-A., Cipollini, B., McCarthy, P., Cheng, C. P., Halchenko, Y. O., Cottaar, M., Ghosh, S., Larson, E., Wassermann, D., Gerhard, S., Lee, G. R., Kastman, E., Rokem, A., Madison, C., Morency, F. C., Moloney, B., … freec84. (2019). *nipy/nibabel: 2.5.1*. Zenodo. https://doi.org/10.5281/zenodo.3458246

Brownell, G. L. (1999). A HISTORY OF POSITRON IMAGING. *Celebration of the 50th Year of Services of GL Brownell*, 11.

Burgos, N., Thielemans, K., Cardoso, M. J., Markiewicz, P., Jiao, J., Dickson, J., Duncan, J. S., Atkinson, D., Arridge, S. R., Hutton, B. F., & Ourselin, S. (2014). Effect of scatter correction when comparing

attenuation maps: Application to brain PET/MR. *2014 IEEE Nuclear Science Symposium and Medical Imaging Conference (NSS/MIC)*, 1–5. https://doi.org/10.1109/NSSMIC.2014.7430775

Burton, E. J., Karas, G., Paling, S. M., Barber, R., Williams, E. D., Ballard, C. G., McKeith, I. G., Scheltens, P., Barkhof, F., & O'Brien, J. T. (2002). Patterns of cerebral atrophy in dementia with Lewy bodies using voxel-based morphometry. *NeuroImage*, *17*(2), 618–630.

Busatto, G. F., Diniz, B. S., & Zanetti, M. V. (2008). Voxel-based morphometry in Alzheimer's disease. *Expert Review of Neurotherapeutics*, *8*(11), 1691–1702. https://doi.org/10.1586/14737175.8.11.1691

Buvat, I., & Castiglioni, I. (2002). Monte Carlo simulations in SPET and PET. *The Quarterly Journal of Nuclear Medicine: Official Publication of the Italian Association of Nuclear Medicine (AIMN) [and] the International Association of Radiopharmacology (IAR)*, *46*(1), 48–61.

Camacho, V., Gómez-Grande, A., Sopena, P., García-Solís, D., Gómez Río, M., Lorenzo, C., Rubí, S., & Arbizu, J. (2018). PET amiloide en enfermedades neurodegenerativas que cursan con demencia. *Revista Española de Medicina Nuclear e Imagen Molecular*, *37*(6), 397–406. https://doi.org/10.1016/j.remn.2018.03.004

Cañadas, M., Arce, P., & Rato Mendes, P. (2011). Validation of a small-animal PET simulation using GAMOS: A GEANT4-based framework. *Physics in Medicine and Biology*, *56*(1), 273–288. https://doi.org/10.1088/0031-9155/56/1/016

Casse, R., Rowe, C. C., Newton, M., Berlangieri, S. U., & Scott, A. M. (2002). Positron Emission Tomography and Epilepsy. *Molecular Imaging & Biology*, *4*(5), 338–351. https://doi.org/10.1016/S1536-1632(02)00071-9

Castiglioni, I., Cremonesi, O., Gilardi, M. C., Bettinardi, V., Rizzo, G., Savi, A., Bellotti, E., & Fazio, F. (1999). Scatter correction techniques in 3D PET: A Monte Carlo evaluation. *IEEE Transactions on Nuclear Science*, *46*(6), 2053–2058. https://doi.org/10.1109/23.819282

Cendes, F. (2013). Neuroimaging in investigation of patients with epilepsy. *Continuum (Minneapolis, Minn.)*, *19*(3 Epilepsy), 623–642. https://doi.org/10.1212/01.CON.0000431379.29065.d3

Chandra, A., Dervenoulas, G., Politis, M., & for the Alzheimer's Disease Neuroimaging Initiative. (2019). Magnetic resonance imaging in Alzheimer's disease and mild cognitive impairment. *Journal of Neurology*, *266*(6), 1293–1302. https://doi.org/10.1007/s00415-018-9016-3

Cherry, S., & Dahlbom, M. (2006). *PET: Physics, Instrumentation, and Scanners*. https://doi.org/10.1007/0-387-34946-4_1

Chételat, G., Arbizu, J., Barthel, H., Garibotto, V., Law, I., Morbelli, S., Giessen, E. van de, Agosta, F., Barkhof, F., Brooks, D. J., Carrillo, M. C., Dubois, B., Fjell, A. M., Frisoni, G. B., Hansson, O., Herholz, K., Hutton, B. F., Jack, C. R., Lammertsma, A. A., … Drzezga, A. (2020). Amyloid-PET and 18F-FDG-PET in the diagnostic investigation of Alzheimer's disease and other dementias. *The Lancet Neurology*, *19*(11), 951–962. https://doi.org/10.1016/S1474-4422(20)30314-8

Chételat, G., Landeau, B., Eustache, F., Mézenge, F., Viader, F., de la Sayette, V., Desgranges, B., & Baron, J.-C. (2005). Using voxel-based morphometry to map the structural changes associated with rapid conversion in MCI: A longitudinal MRI study. *NeuroImage*, *27*(4), 934–946. https://doi.org/10.1016/j.neuroimage.2005.05.015

Collins, D. L., Zijdenbos, A. P., Kollokian, V., Sled, J. G., Kabani, N. J., Holmes, C. J., & Evans, A. C. (1998). Design and construction of a realistic digital brain phantom. *IEEE Transactions on Medical Imaging*, *17*(3), 463–468. https://doi.org/10.1109/42.712135

Curry, S., Patel, N., Fakhry-Darian, D., Khan, S., Perry, R. J., Malhotra, P. A., Nijran, K. S., & Win, Z. (2019). Quantitative evaluation of beta-amyloid brain PET imaging in dementia: A comparison between two commercial software packages and the clinical report. *The British Journal of Radiology*, *92*(1101), 20181025. https://doi.org/10.1259/bjr.20181025

Daube-Witherspoon, M., Carson, R. E., & Green, M. V. (1988). Post-injection transmission attenuation measurements for PET. *IEEE Transactions on Nuclear Science*, *35*(1), 757–761. https://doi.org/10.1109/23.12827

Davatzikos, C., Li, H. H., Herskovits, E., & Resnick, S. M. (2001). Accuracy and Sensitivity of Detection of Activation Foci in the Brain via Statistical Parametric Mapping: A Study Using a PET Simulator. *NeuroImage*, *13*(1), 176–184. https://doi.org/10.1006/nimg.2000.0655

DeCarli, C. (2003). Mild cognitive impairment: Prevalence, prognosis, aetiology, and treatment. *The Lancet Neurology*, *2*(1), 15–21. https://doi.org/10.1016/S1474-4422(03)00262-X

Ding, Y., Zhu, Y., Jiang, B., Zhou, Y., Jin, B., Hou, H., Wu, S., Zhu, J., Wang, Z. I., Wong, C. H., Ding, M., Zhang, H., Wang, S., & Tian, M. (2018). 18F-FDG PET and high-resolution MRI co-registration for pre-surgical

evaluation of patients with conventional MRI-negative refractory extra-temporal lobe epilepsy. *European Journal of Nuclear Medicine and Molecular Imaging*, *45*(9), 1567–1572. https://doi.org/10.1007/s00259-018-4017-0

Drzezga, A., Lautenschlager, N., Siebner, H., Riemenschneider, M., Willoch, F., Minoshima, S., Schwaiger, M., & Kurz, A. (2003). Cerebral metabolic changes accompanying conversion of mild cognitive impairment into Alzheimer's disease: A PET follow-up study. *European Journal of Nuclear Medicine and Molecular Imaging*, *30*(8), 1104–1113. https://doi.org/10.1007/s00259-003-1194-1

Duncan, J. S. (1997). Imaging and epilepsy. *Brain*, *120*(2), 339–377. https://doi.org/10.1093/brain/120.2.339

Dupont, S., & Baulac, M. (2004). [Contribution of MRI to the exploration of partial refractory epilepsy]. *Revue Neurologique*, *160 Spec No 1*, 5S91-97.

Efthimiou, N., Emond, E., Wadhwa, P., Cawthorne, C., Tsoumpas, C., & Thielemans, K. (2019). Implementation and validation of time-of-flight PET image reconstruction module for listmode and sinogram projection data in the STIR library. *Physics in Medicine and Biology*, *64*(3), 035004. https://doi.org/10.1088/1361-6560/aaf9b9

Emsen, B., Villafane, G., David, J.-P., Evangelista, E., Chalaye, J., Lerman, L., Authier, F.-J., Gracies, J.-M., & Itti, E. (2020). Clinical impact of dual-tracer FDOPA and FDG PET/CT for the evaluation of patients with parkinsonian syndromes. *Medicine*, *99*(45). https://doi.org/10.1097/MD.0000000000023060

España, S., Herraiz, J. L., Vicente, E., Vaquero, J. J., Desco, M., & Udias, J. M. (2009). PeneloPET, a Monte Carlo PET simulation tool based on PENELOPE: Features and validation. *Physics in Medicine and Biology*, *54*(6), 1723–1742. https://doi.org/10.1088/0031-9155/54/6/021

Fahey, F. (2002). Data acquisition in PET imaging. *Journal of Nuclear Medicine Technology*, *30*, 39–49.

Ferrari, A., Sala, P., Fasso, A., & Ranft, J. (2005). FLUKA: A multi-particle transport code. *CERN Yellow Report*, *2005–10*. https://doi.org/10.2172/877507

Ferreira, L. K., Diniz, B. S., Forlenza, O. V., Busatto, G. F., & Zanetti, M. V. (2011). Neurostructural predictors of Alzheimer's disease: A meta-analysis of VBM studies. *Neurobiology of Aging*, *32*(10), 1733–1741. https://doi.org/10.1016/j.neurobiolaging.2009.11.008

Filho, J. L. G. C., Lima, R. de S. L., Neto, L. de S. M., Bittencourt, L. K., Domingues, R. C., & Fonseca, L. M. B. da. (2011). PET/CT and vascular disease: Current concepts. *European Journal of Radiology*, *80*(1), 60–67. https://doi.org/10.1016/j.ejrad.2010.12.102

Filippou, V., & Tsoumpas, C. (2018). Recent advances on the development of phantoms using 3D printing for imaging with CT, MRI, PET, SPECT, and ultrasound. *Medical Physics*, *45*(9), e740–e760. https://doi.org/10.1002/mp.13058

Finocchiaro, P., Campisi, A., Corso, D., Cosentino, L., Fallica, G., Lombardo, S., Mazzillo, M., Musumeci, F., Piazza, A., Privitera, G., Privitera, S., Rimini, E., Sanfilippo, D., Sciacca, E., Scordino, A., & Tudisco, S. (2006). Test of scintillator readout with single photon avalanche photodiodes. *Nuclear Science, IEEE Transactions On*, *52*, 3040–3046. https://doi.org/10.1109/TNS.2005.862912

Fralick, D., Zheng, J. Z., Wang, B., Tu, X. M., & Feng, C. (2017). The Differences and Similarities Between Two-Sample T-Test and Paired T-Test. *Shanghai Archives of Psychiatry*, *29*(3), 184–188. https://doi.org/10.11919/j.issn.1002-0829.217070

Frankó, E., Joly, O., & Initiative, for the A. D. N. (2013). Evaluating Alzheimer's Disease Progression Using Rate of Regional Hippocampal Atrophy. *PLOS ONE*, *8*(8), e71354. https://doi.org/10.1371/journal.pone.0071354

Friston, K. J. (2007). *Statistical parametric mapping: The analysis of functional brain images*. Elsevier / Academic Press.

Frouin, V., Comtat, C., Reilhac, A., & Grégoire, M.-C. (2002). Correction of Partial-Volume Effect for PET Striatal Imaging: Fast Implementation and Study of Robustness. *Journal of Nuclear Medicine*, *43*(12), 1715–1726.

García, J. P. C., Sala-Llonch, R., Fernández, R. T., Puig, D. R., Segura, J. P., & Baizán, A. N. (2020). Corrección de atenuación en equipos PET-RM. Comparación de métodos mediante simulación Monte Carlo. *Revista de Física Médica*, *21*(2), 43–52. https://doi.org/10.37004/sefm/2020.21.2.004

Geramifar, P., Ay, M. R., Shamsaie Zafarghandi, M., Loudos, G., & Rahmim, A. (2009). Performance comparison of four commercial GE discovery PET/CT scanners: A monte carlo study using GATE. *Iranian Journal of Nuclear Medicine*, *17*(2), 26–33.

Ghabrial, A., Franklin, D. R., & Zaidi, H. (2021). A Monte Carlo simulation study of scatter fraction and the impact of patient BMI on scatter in long axial field-of-view PET scanners. *Zeitschrift Für Medizinische Physik*, *31*(3), 305–315. https://doi.org/10.1016/j.zemedi.2021.01.006

Guerin, B., & El Fakhri, G. (2008). Realistic PET Monte Carlo Simulation With Pixelated Block Detectors, Light Sharing, Random Coincidences and Dead-Time Modeling. *IEEE Transactions on Nuclear Science*, *55*(3), 942–952. https://doi.org/10.1109/TNS.2008.924064

Guerra, A. D., Ahmad, S., Avram, M., Belcari, N., Berneking, A., Biagi, L., Bisogni, M. G., Brandl, F., Cabello, J., Camarlinghi, N., Cerello, P., Choi, C.-H., Coli, S., Colpo, S., Fleury, J., Gagliardi, V., Giraudo, G., Heekeren, K., Kawohl, W., … Consortium, T. (2018). TRIMAGE: A dedicated trimodality (PET/MR/EEG) imaging tool for schizophrenia. *European Psychiatry*, *50*, 7–20. https://doi.org/10.1016/j.eurpsy.2017.11.007

Guillén, E. F., Rosales, J. J., Lisei, D., Grisanti, F., Riverol, M., & Arbizu, J. (2020). Current role of 18F-FDG-PET in the differential diagnosis of the main forms of dementia. *Clinical and Translational Imaging*, *8*(3), 127–140. https://doi.org/10.1007/s40336-020-00366-0

Halbleib, J. A., Kensek, R. P., Valdez, G. D., Mehlhorn, T. A., Seltzer, S. M., & Berger, M. J. (1993). *ITS Version 30: The Integrated TIGER Series of coupled electron/photon Monte Carlo transport codes* (p. 7).

Hammers, A., Allom, R., Koepp, M. J., Free, S. L., Myers, R., Lemieux, L., Mitchell, T. N., Brooks, D. J., & Duncan, J. S. (2003). Three-dimensional maximum probability atlas of the human brain, with particular reference to the temporal lobe. *Human Brain Mapping*, *19*(4), 224–247. https://doi.org/10.1002/hbm.10123

Han, H., & Glenn, A. L. (2017). *Evaluating Methods of Correcting for Multiple Comparisons Implemented in SPM12 in Social Neuroscience fMRI Studies: An Example from Moral Psychology* (p. 129734). https://doi.org/10.1101/129734

Harn, N. R., Hunt, S. L., Hill, J., Vidoni, E., Perry, M., & Burns, J. M. (2017). Augmenting Amyloid PET Interpretations with Quantitative Information Improves Consistency of Early Amyloid Detection. *Clinical Nuclear Medicine*, *42*(8), 577–581. https://doi.org/10.1097/RLU.0000000000001693

Harries, J., Jochimsen, T. H., Scholz, T., Schlender, T., Barthel, H., Sabri, O., & Sattler, B. (2020). A realistic phantom of the human head for PET-MRI. *EJNMMI Physics*, *7*(1), 52. https://doi.org/10.1186/s40658-020-00320-z

Harrison, R., Gillispie, S., Schmitz, R., & Lewellen, T. (2008). Modeling block detectors in SimSET. *Journal of Nuclear Medicine: Official Publication, Society of Nuclear Medicine*, *49 Suppl 1*, 410P.

Harrison, R. L., Gillispie, S. B., & Lewellen, T. K. (2006). Design and Implementation of a Block Detector Simulation in SimSET. *IEEE Nuclear Science Symposium Conference Record. Nuclear Science Symposium*, *5*, 3151–3153. https://doi.org/10.1109/NSSMIC.2006.356543

Hashimoto, F., Ote, K., & Onishi, Y. (2022). PET Image Reconstruction Incorporating Deep Image Prior and a Forward Projection Model. *IEEE Transactions on Radiation and Plasma Medical Sciences*, 1–1. https://doi.org/10.1109/TRPMS.2022.3161569

Heinen, L., Teune, L., & Leenders, N. (2013). Het cerebrale glucose-metabolisme bij neurodegeneratieve hersenaandoeningen. *Tijdschrift Voor Neuropsychiatrie En Gedragsneurologie*, *1*, 51–59. https://doi.org/10.1007/s40533-013-0011-9

Hirayama, H., Namito, Y., Bielajew, A., Wilderman, S., & Nelson, W. (2006). *The EGS5 code system*. https://doi.org/10.2172/877459

Hoffman, E. J., Cutler, P. D., Digby, W. M., & Mazziotta, J. C. (1990). 3-D phantom to simulate cerebral blood flow and metabolic images for PET. *IEEE Transactions on Nuclear Science*, *37*(2), 616–620. https://doi.org/10.1109/23.106686

Hoffman, J. M., Welsh-Bohmer, K. A., Hanson, M., Crain, B., Hulette, C., Earl, N., & Coleman, R. E. (2000). FDG PET imaging in patients with pathologically verified dementia. *Journal of Nuclear Medicine: Official Publication, Society of Nuclear Medicine*, *41*(11), 1920–1928.

Hudson, H. M., & Larkin, R. S. (1994). Accelerated image reconstruction using ordered subsets of projection data. *IEEE Transactions on Medical Imaging*, *13*(4), 601–609. https://doi.org/10.1109/42.363108

Humm, J. L., Rosenfeld, A., & Del Guerra, A. (2003). From PET detectors to PET scanners. *European Journal of Nuclear Medicine and Molecular Imaging*, *30*(11), 1574–1597. https://doi.org/10.1007/s00259-003-1266-2

Iida, H., Hori, Y., Ishida, K., Imabayashi, E., Matsuda, H., Takahashi, M., Maruno, H., Yamamoto, A., Koshino, K., Enmi, J., Iguchi, S., Moriguchi, T., Kawashima, H., & Zeniya, T. (2013). Three-dimensional brain phantom containing bone and grey matter structures with a realistic head contour. *Annals of Nuclear Medicine*, *27*(1), 25–36. https://doi.org/10.1007/s12149-012-0655-7

Ishii, K., Willoch, F., Minoshima, S., Drzezga, E., Ficaro, E. P., Cross, D. J., Kuhl, D. E., & Schwaiger, M. (2001). *Statistical brain mapping of 18F-FDG PET in Alzheimer's disease: Validation of anatomic standardization for atrophied brains*.

Ito, K., Fukuyama, H., Senda, M., Ishii, K., Maeda, K., Yamamoto, Y., Ouchi, Y., Ishii, K., Okumura, A., Fujiwara, K., Kato, T., Arahata, Y., Washimi, Y., Mitsuyama, Y., Meguro, K., Ikeda, M., & Group, S.-J. S. (2015). Prediction of Outcomes in Mild Cognitive Impairment by Using 18F-FDG-PET: A Multicenter Study. *Journal of Alzheimer's Disease*, *45*(2), 543–552. https://doi.org/10.3233/JAD-141338

Jaisani, Z., Miletich, R. S., Ramanathan, M., & Weinstock, A. L. (2020). Clinical FDG-PET Findings in Patients with Temporal Lobe Epilepsy: Concordance with EEG and MRI. *Journal of Neuroimaging: Official Journal of the American Society of Neuroimaging*, *30*(1), 119–125. https://doi.org/10.1111/jon.12671

Jakoby, B. W., Bercier, Y., Conti, M., Casey, M. E., Bendriem, B., & Townsend, D. W. (2011). Physical and clinical performance of the mCT time-of-flight PET/CT scanner. *Physics in Medicine and Biology*, *56*(8), 2375–2389. https://doi.org/10.1088/0031-9155/56/8/004

Jan, S., Santin, G., Strul, D., Staelens, S., Assié, K., Autret, D., Avner, S., Barbier, R., Bardiès, M., Bloomfield, P. M., Brasse, D., Breton, V., Bruyndonckx, P., Buvat, I., Chatziioannou, A. F., Choi, Y., Chung, Y. H., Comtat, C., Donnarieix, D., … Morel, C. (2004). GATE - Geant4 Application for Tomographic Emission: A simulation toolkit for PET and SPECT. *Physics in Medicine and Biology*, *49*(19), 4543–4561.

Jenkinson, M., Beckmann, C. F., Behrens, T. E. J., Woolrich, M. W., & Smith, S. M. (2012). FSL. *NeuroImage*, *62*(2), 782–790. https://doi.org/10.1016/j.neuroimage.2011.09.015

Kak, A. C., & Slaney, M. (2001). 3. Algorithms for Reconstruction with Nondiffracting Sources. In *Principles of Computerized Tomographic Imaging* (Vol. 1–0, pp. 49–112). Society for Industrial and Applied Mathematics. https://doi.org/10.1137/1.9780898719277.ch3

Karakatsanis, N. A., Lodge, M. A., Rahmim, A., & Zaidi, H. (2016). Introducing time-of-flight and resolution recovery image reconstruction to clinical whole-body PET parametric imaging. *2014 IEEE Nuclear*

Science Symposium and Medical Imaging Conference, NSS/MIC 2014, 7430771. https://doi.org/10.1109/NSSMIC.2014.7430771

Kato, T., Inui, Y., Nakamura, A., & Ito, K. (2016). Brain fluorodeoxyglucose (FDG) PET in dementia. *Ageing Research Reviews*, *30*, 73–84. https://doi.org/10.1016/j.arr.2016.02.003

Keller, S. S., & Roberts, N. (2008). Voxel-based morphometry of temporal lobe epilepsy: An introduction and review of the literature. *Epilepsia*, *49*(5), 741–757. https://doi.org/10.1111/j.1528-1167.2007.01485.x

Kikuchi, K., Togao, O., Yamashita, K., Momosaka, D., Nakayama, T., Kitamura, Y., Kikuchi, Y., Baba, S., Sagiyama, K., Ishimatsu, K., Kamei, R., Mukae, N., Iihara, K., Suzuki, S. O., Iwaki, T., & Hiwatashi, A. (2021). Diagnostic accuracy for the epileptogenic zone detection in focal epilepsy could be higher in FDG-PET/MRI than in FDG-PET/CT. *European Radiology*, *31*(5), 2915–2922. https://doi.org/10.1007/s00330-020-07389-1

Kim, Y. K., Lee, D. S., Lee, S. K., Chung, C. K., Chung, J.-K., & Lee, M. C. (2002). 18F-FDG PET in Localization of Frontal Lobe Epilepsy: Comparison of Visual and SPM Analysis. *Journal of Nuclear Medicine*, *43*(9), 1167–1174.

Kinahan, P. E., Defrise, M., & Clackdoyle, R. (2004). CHAPTER 20—Analytic Image Reconstruction Methods. In M. N. Wernick & J. N. Aarsvold (Eds.), *Emission Tomography* (pp. 421–442). Academic Press. https://doi.org/10.1016/B978-012744482-6.50023-5

Klunk, W. E., Koeppe, R. A., Price, J. C., Benzinger, T. L., Devous, M. D., Jagust, W. J., Johnson, K. A., Mathis, C. A., Minhas, D., Pontecorvo, M. J., Rowe, C. C., Skovronsky, D. M., & Mintun, M. A. (2015). The Centiloid Project: Standardizing quantitative amyloid plaque estimation by PET. *Alzheimer's & Dementia: The Journal of the Alzheimer's Association*, *11*(1), 1-15.e1-4. https://doi.org/10.1016/j.jalz.2014.07.003

Knesaurek, K., Warnock, G., Sideras, P., & Burger, C. (2014). Comparison of SUVr calculations in amyloid PET brain imaging. *Journal of Nuclear Medicine*, *55*(supplement 1), 1873–1873.

Knoll, G. F. (2000). *Radiation detection and measurement* (3rd ed). Wiley.

Kochebina, O., Jan, S., Stute, S., Sharyy, V., Verrecchia, P., Mancardi, X., & Yvon, D. (2019). Performance Estimation for the High Resolution CaLIPSO Brain PET Scanner: A Simulation Study. *IEEE Transactions on Radiation and Plasma Medical Sciences*, *3*(3), 363–370. https://doi.org/10.1109/TRPMS.2018.2880811

Kontaxakis, G. (2002). Iterative Image Reconstruction for Clinical PET Using Ordered Subsets, Median Root Prior, and a Web-Based Interface. *Molecular Imaging & Biology*, *4*(3), 219–231. https://doi.org/10.1016/S1536-1632(02)00004-5

Kumar, A., & Chugani, H. T. (2017). The Role of Radionuclide Imaging in Epilepsy, Part 1: Sporadic Temporal and Extratemporal Lobe Epilepsy. *Journal of Nuclear Medicine Technology*, *45*(1), 14–21. https://doi.org/10.2967/jnumed.112.114397

Kumar, A., Semah, F., Chugani, H. T., & Theodore, W. H. (2012). Chapter 26 - Epilepsy diagnosis: Positron emission tomography. In H. Stefan & W. H. Theodore (Eds.), *Handbook of Clinical Neurology* (Vol. 107, pp. 409–424). Elsevier. https://doi.org/10.1016/B978-0-444-52898-8.00026-4

Kurth, F., Luders, E., & Gaser, C. (2015). Voxel-Based Morphometry. In *Brain Mapping* (pp. 345–349). Elsevier. https://doi.org/10.1016/B978-0-12-397025-1.00304-3

Kuzniecky, R., de la Sayette, V., Ethier, R., Melanson, D., Andermann, F., Berkovic, S., Robitaille, Y., Olivier, A., Peters, T., & Feindel, W. (1987). Magnetic resonance imaging in temporal lobe epilepsy: Pathological correlations. *Annals of Neurology*, *22*(3), 341–347. https://doi.org/10.1002/ana.410220310

Kuzniecky, R. I. (2005). Neuroimaging of Epilepsy: Therapeutic Implications. *NeuroRx*, *2*(2), 384–393.

Labbe, C., Thielemans, K., Belluzzo, D., Bettinardi, V., Gilardi, M., Hague, D., Jacobson, M., Kaiser, S., Levkovitz, R., Margalit, T., Mitra, G., Morel, C., Spinks, T., Valente, P., Zaidi, H., & Zverovich, A. (1999). *An Object-Oriented Library for 3D PET Reconstruction Using Parallel Computing*. https://doi.org/10.1007/978-3-642-60125-5_50

Labbe, C., Thielemans, K., Zaidi, H., & Morel, C. (1999). *An object-oriented library incorporating efficient projection/backprojection operators for volume reconstruction in 3D PET*.

Ladrón De Guevara, D. (2013). Rol del PET/CT en epilepsia. *Revista Médica Clínica Las Condes*, *24*(6), 973–977. https://doi.org/10.1016/S0716-8640(13)70251-7

Landau, S. M., Fero, A., Baker, S. L., Koeppe, R., Mintun, M., Chen, K., Reiman, E. M., & Jagust, W. J. (2015). Measurement of Longitudinal β-Amyloid Change with 18F-Florbetapir PET and Standardized Uptake Value Ratios. *Journal of Nuclear Medicine : Official Publication, Society of Nuclear Medicine*, *56*(4), 567–574. https://doi.org/10.2967/jnumed.114.148981

Lecoq, P., & Gundacker, S. (2021). SiPM applications in positron emission tomography: Toward ultimate PET time-of-flight resolution. *The European Physical Journal Plus*, *136*(3), 292. https://doi.org/10.1140/epjp/s13360-021-01183-8

Lee, D. H., Gao, F.-Q., Rogers, J. M., Gulka, I., Mackenzie, I. R. A., Parrent, A. G., Kubu, C. S., Munoz, D. G., McLachlan, R. S., Blume, W. T., & Girvin, J. P. (1998). MR in Temporal Lobe Epilepsy: Analysis with Pathologic Confirmation. *AJNR. American Journal of Neuroradiology*, *19*(1), 9.

Lee, S. H., Bachman, A. H., Yu, D., Lim, J., & Ardekani, B. A. (2016). Predicting progression from mild cognitive impairment to Alzheimer's disease using longitudinal callosal atrophy. *Alzheimer's & Dementia: Diagnosis, Assessment & Disease Monitoring*, *2*, 68–74. https://doi.org/10.1016/j.dadm.2016.01.003

Levin, C. S., Dahlbom, M., & Hoffman, E. J. (1995). A Monte Carlo correction for the effect of Compton scattering in 3-D PET brain imaging. *IEEE Transactions on Nuclear Science*, *42*(4), 1181–1185. https://doi.org/10.1109/23.467880

Lewellen, T. K., Harrison, R. L., & Vannoy, S. (1998). The SimSET program, in Monte Carlo Calculations in Nuclear Medicine: Applications in Diagnostic Imaging. *Institute of Physics Publication, Bristol, UK*.

Lorenzo, N. Y., Parisi, J. E., Cascino, G. D., Jack, C. R., Marsh, W. R., & Hirschorn, K. A. (1995). Intractable frontal lobe epilepsy: Pathological and MRI features. *Epilepsy Research*, *20*(2), 171–178. https://doi.org/10.1016/0920-1211(94)00072-5

Lu, L., Zhang, H., Bian, Z., Ma, J., Feng, Q., & Chen, W. (2016). Validation of a Monte Carlo simulation of the Inveon PET scanner using GATE. *Nuclear Instruments and Methods in Physics Research Section A: Accelerators, Spectrometers, Detectors and Associated Equipment*, *828*, 170–175. https://doi.org/10.1016/j.nima.2016.04.059

Maisey, M. N. (2005). Positron Emission Tomography in Clinical Medicine. In D. L. Bailey, D. W. Townsend, P. E. Valk, & M. N. Maisey (Eds.), *Positron Emission Tomography: Basic Sciences* (pp. 1–12). Springer. https://doi.org/10.1007/1-84628-007-9_1

Marshall, R. A., & Cully, C. M. (2020). Atmospheric effects and signatures of high-energy electron precipitation. In *The Dynamic Loss of Earth's Radiation Belts* (pp. 199–255). Elsevier. https://doi.org/10.1016/B978-0-12-813371-2.00007-X

Marti-Fuster, B., Esteban, O., Thielemans, K., Setoain, X., Santos, A., Ros, D., & Pavia, J. (2014). Including anatomical and functional information in MC simulation of PET and SPECT brain studies. Brain-VISET: A voxel-based iterative method. *IEEE Transactions on Medical Imaging*, *33*(10), 1931–1938. https://doi.org/10.1109/TMI.2014.2326041

Matsuda, H., Ito, K., Ishii, K., Shimosegawa, E., Okazawa, H., Mishina, M., Mizumura, S., Ishii, K., Okita, K., Shigemoto, Y., Kato, T., Takenaka, A., Kaida, H., Hanaoka, K., Matsunaga, K., Hatazawa, J., Ikawa, M., Tsujikawa, T., Morooka, M., … Sato, N. (2021). Quantitative Evaluation of 18F-Flutemetamol PET in Patients With Cognitive Impairment and Suspected Alzheimer's Disease: A Multicenter Study. *Frontiers in Neurology*, *11*, 578753. https://doi.org/10.3389/fneur.2020.578753

Matsuda, H., Yokoyama, K., Sato, N., Ito, K., Nemoto, K., Oba, H., Hanyu, H., Kanetaka, H., Mizumura, S., Kitamura, S., Shinotoh, H., Shimada, H., Suhara, T., Terada, H., Nakatsuka, T., Kawakatsu, S., Hayashi, H., Asada, T., Ono, T., … Shigemori, K. (2019). Differentiation Between Dementia With Lewy Bodies And Alzheimer's Disease Using Voxel-Based Morphometry Of Structural MRI: A Multicenter Study. *Neuropsychiatric Disease and Treatment*, *15*, 2715–2722. https://doi.org/10.2147/NDT.S222966

Mayoral, M., Marti-Fuster, B., Carreño, M., Carrasco, J. L., Bargalló, N., Donaire, A., Rumià, J., Perissinotti, A., Lomeña, F., Pintor, L., Boget, T., & Setoain, X. (2016). Seizure-onset zone localization by statistical parametric mapping in visually normal 18F-FDG PET studies. *Epilepsia*, *57*(8), 1236–1244. https://doi.org/10.1111/epi.13427

Mayoral, M., Niñerola-Baizán, A., Marti-Fuster, B., Donaire, A., Perissinotti, A., Rumià, J., Bargalló, N., Sala-Llonch, R., Pavia, J., Ros, D., Carreño, M., Pons, F., & Setoain, X. (2019). Epileptogenic Zone Localization With 18FDG PET Using a New Dynamic Parametric Analysis. *Frontiers in Neurology*, *10*. https://doi.org/10.3389/fneur.2019.00380

Mazzillo, M., Fallica, G., Ficarra, E., Messina, A., Romeo, M., & Zafalon, R. (2011). Solid state photodetectors for nuclear medical imaging applications. In *Proceedings -Design, Automation and Test in Europe, DATE* (p. 512). https://doi.org/10.1109/DATE.2011.5763091

Meikle, S. R., & Badawi, R. D. (2005). Quantitative Techniques in PET. In D. L. Bailey, D. W. Townsend, P. E. Valk, & M. N. Maisey (Eds.), *Positron Emission Tomography: Basic Sciences* (pp. 93–126). Springer. https://doi.org/10.1007/1-84628-007-9_5

Meltzer, C. C., Adelson, P. D., Brenner, R. P., Crumrine, P. K., Van Cott, A., Schiff, D. P., Townsend, D. W., & Scheuer, M. L. (2000). Planned ictal FDG PET imaging for localization of extratemporal epileptic foci. *Epilepsia*, *41*(2), 193–200. https://doi.org/10.1111/j.1528-1157.2000.tb00139.x

Merlin, T., Stute, S., Benoit, D., Bert, J., Carlier, T., Comtat, C., Filipovic, M., Lamare, F., & Visvikis, D. (2018). CASToR: A generic data organization and processing code framework for multi-modal and multi-dimensional tomographic reconstruction. *Physics in Medicine and Biology*, *63*. https://doi.org/10.1088/1361-6560/aadac1

Meyer, P. T., Frings, L., Rücker, G., & Hellwig, S. (2017). 18F-FDG PET in Parkinsonism: Differential Diagnosis and Evaluation of Cognitive Impairment. *Journal of Nuclear Medicine*, *58*(12), 1888–1898. https://doi.org/10.2967/jnumed.116.186403

Monnier, F., Fayad, H., Bert, J., Schmidt, H., & Visvikis, D. (2015). Validation of a simultaneous PET/MR system model for PET simulation using GATE. *EJNMMI Physics*, *2*(1), A45. https://doi.org/10.1186/2197-7364-2-S1-A45

Mosconi, L., De Santi, S., Li, Y., Li, J., Zhan, J., Tsui, W. H., Boppana, M., Pupi, A., & de Leon, M. J. (2006). Visual rating of medial temporal lobe metabolism in mild cognitive impairment and Alzheimer's disease using FDG-PET. *European Journal of Nuclear Medicine and Molecular Imaging*, *33*(2), 210–221. https://doi.org/10.1007/s00259-005-1956-z

Moses, W. W. (2011). Fundamental Limits of Spatial Resolution in PET. *Nuclear Instruments & Methods in Physics Research. Section A, Accelerators, Spectrometers, Detectors and Associated Equipment*, *648 Supplement 1*, S236–S240. https://doi.org/10.1016/j.nima.2010.11.092

Mota, A., Cuplov, V., Schott, J., Hutton, B., Thielemans, K., Drobnjak, I., Dickson, J., Bert, J., Burgos, N., Cardoso, J., Modat, M., Ourselin, S., & Erlandsson, K. (2015). Establishment of an open database of realistic simulated data for evaluation of partial volume correction techniques in brain PET/MR. *EJNMMI Physics*, *2*(1), A44. https://doi.org/10.1186/2197-7364-2-S1-A44

Mountz, J. M., Laymon, C. M., Cohen, A. D., Zhang, Z., Price, J. C., Boudhar, S., McDade, E., Aizenstein, H. J., Klunk, W. E., & Mathis, C. A. (2015). Comparison of qualitative and quantitative imaging characteristics of [11C]PiB and [18F]flutemetamol in normal control and Alzheimer's subjects. *NeuroImage. Clinical*, *9*, 592–598. https://doi.org/10.1016/j.nicl.2015.10.007

Mueller, S. G., Laxer, K. D., Cashdollar, N., Buckley, S., Paul, C., & Weiner, M. W. (2006). Voxel-based Optimized Morphometry (VBM) of Gray and White Matter in Temporal Lobe Epilepsy (TLE) with and without Mesial Temporal Sclerosis. *Epilepsia*, *47*(5), 900–907. https://doi.org/10.1111/j.1528-1167.2006.00512.x

Muhlhofer, W., Tan, Y.-L., Mueller, S. G., & Knowlton, R. (2017). MRI-negative temporal lobe epilepsy—What do we know? *Epilepsia*, *58*(5), 727–742. https://doi.org/10.1111/epi.13699

National Electrical Manufacturers Association. (1994). Standards Publication NU-2-1994: Performance measurements of positron emission tomography. *Washington DC: National Electrical Manufacturers Association*.

National Electrical Manufacturers Association. (2007). *NEMA Standards Publication NU 2-2007: Performance Measurements of Positron Emission Tomographs*. National Electrical Manufacturers Association. https://books.google.es/books?id=WhutMwEACAAJ

Niñerola-Baizán, A., Aguiar, P., Cabrera-Martín, M. N., Vigil, C., Gómez-Grande, A., Lorenzo, C., Rubí, S., Sopena, P., Camacho, V., & por el Grupo de Neuroimagen SEMNIM. (2020). Relevance of quantification in brain PET studies with 18F-FDG. *Revista Espanola De Medicina Nuclear E Imagen Molecular*, *39*(3), 184–192. https://doi.org/10.1016/j.remn.2020.03.003

Nooraine, J., Iyer, R. B., & Raghavendra, S. (2013). Ictal PET in presurgical workup of refractory extratemporal epilepsy. *Annals of Indian Academy of Neurology*, *16*(4), 676–677. https://doi.org/10.4103/0972-2327.120475

Ollinger, J. M. (1996). Model-based scatter correction for fully 3D PET. *Physics in Medicine & Biology*, *41*(1), 153. https://doi.org/10.1088/0031-9155/41/1/012

Ortner, M. M. (2018). The Use of 18F-FDG PET in the Diagnostic Workup of Alzheimer's Dementia. In R. Perneczky (Ed.), *Biomarkers for Alzheimer's Disease Drug Development* (pp. 213–219). Springer. https://doi.org/10.1007/978-1-4939-7704-8_14

Pagani, M., Nobili, F., Morbelli, S., Arnaldi, D., Giuliani, A., Öberg, J., Girtler, N., Brugnolo, A., Picco, A., Bauckneht, M., Piva, R., Chincarini, A., Sambuceti, G., Jonsson, C., & De Carli, F. (2017). Early identification of MCI converting to AD: A FDG PET study. *European Journal of Nuclear Medicine and Molecular Imaging*, *44*(12), 2042–2052. https://doi.org/10.1007/s00259-017-3761-x

Paldino, M. J., Yang, E., Jones, J. Y., Mahmood, N., Sher, A., Zhang, W., Hayatghaibi, S., Krishnamurthy, R., & Seghers, V. (2017). Comparison of the diagnostic accuracy of PET/MRI to PET/CT-acquired FDG brain exams for seizure focus detection: A prospective study. *Pediatric Radiology*, *47*(11), 1500–1507. https://doi.org/10.1007/s00247-017-3888-8

Pan, P. L., Song, W., Yang, J., Huang, R., Chen, K., Gong, Q. Y., Zhong, J. G., Shi, H. C., & Shang, H. F. (2012). Gray Matter Atrophy in Behavioral Variant Frontotemporal Dementia: A Meta-Analysis of Voxel-Based Morphometry Studies. *Dementia and Geriatric Cognitive Disorders*, *33*(2–3), 141–148. https://doi.org/10.1159/000338176

Papadimitroulas, P., Loudos, G., Le Maitre, A., Hatt, M., Tixier, F., Efthimiou, N., Nikiforidis, G. C., Visvikis, D., & Kagadis, G. C. (2013). Investigation of realistic PET simulations incorporating tumor patient's specificity using anthropomorphic models: Creation of an oncology database. *Medical Physics*, *40*(11), 112506. https://doi.org/10.1118/1.4826162

Pedemonte, S., Bousse, A., Erlandsson, K., Modat, M., Arridge, S., Hutton, B. F., & Ourselin, S. (2010). GPU accelerated rotation-based emission tomography reconstruction. In *IEEE Nuclear Science Symposium Conference Record* (p. 2661). https://doi.org/10.1109/NSSMIC.2010.5874272

Pegueroles, J., Montal, V., Bejanin, A., Vilaplana, E., Aranha, M., Santos-Santos, M. A., Alcolea, D., Carrió, I., Camacho, V., Blesa, R., Lleó, A., Fortea, J., Alzheimer Disease Neuroimaging Initiative, & Australian Imaging, Biomarkers and Lifestyle Research Group. (2021). AMYQ: An index to standardize quantitative amyloid load across PET tracers. *Alzheimer's & Dementia: The Journal of the Alzheimer's Association*. https://doi.org/10.1002/alz.12317

Perani, D., Della Rosa, P. A., Cerami, C., Gallivanone, F., Fallanca, F., Vanoli, E. G., Panzacchi, A., Nobili, F., Pappatà, S., Marcone, A., Garibotto, V., Castiglioni, I., Magnani, G., Cappa, S. F., & Gianolli, L. (2014). Validation of an optimized SPM procedure for FDG-PET in dementia diagnosis in a clinical setting. *NeuroImage : Clinical*, *6*, 445–454. https://doi.org/10.1016/j.nicl.2014.10.009

Pfaehler, E., De Jong, J. R., Dierckx, R. A. J. O., van Velden, F. H. P., & Boellaard, R. (2018). SMART (SiMulAtion and ReconsTruction) PET: An efficient PET simulation-reconstruction tool. *EJNMMI Physics*, *5*(1), 16. https://doi.org/10.1186/s40658-018-0215-x

Phelps, M. E., Hoffman, E. J., Mullani, N. A., & Ter-Pogossian, M. M. (1975). Application of annihilation coincidence detection to transaxial reconstruction tomography. *Journal of Nuclear Medicine: Official Publication, Society of Nuclear Medicine*, *16*(3), 210–224.

Polycarpou, I., Thielemans, K., Manjeshwar, R., Aguiar, P., Marsden, P. K., & Tsoumpas, C. (2011). Comparative evaluation of scatter correction in 3D PET using different scatter-level approximations. *Annals of Nuclear Medicine*, *25*(9), 643–649. https://doi.org/10.1007/s12149-011-0514-y

Poon, J. K., Dahlbom, M. L., Casey, M. E., Qi, J., Cherry, S. R., & Badawi, R. D. (2015). Validation of the SimSET simulation package for modeling the Siemens Biograph mCT PET scanner. *Physics in Medicine and Biology*, *60*(3), N35-45. https://doi.org/10.1088/0031-9155/60/3/N35

Portnow, L. H., Vaillancourt, D. E., & Okun, M. S. (2013). The history of cerebral PET scanning. *Neurology*, *80*(10), 952–956. https://doi.org/10.1212/WNL.0b013e318285c135

Pyatigorskaya, N., Gallea, C., Garcia-Lorenzo, D., Vidailhet, M., & Lehericy, S. (2014). A review of the use of magnetic resonance imaging in Parkinson's disease. *Therapeutic Advances in Neurological Disorders*, *7*(4), 206–220. https://doi.org/10.1177/1756285613511507

Raeside, D. E. (1976). Monte Carlo principles and applications. *Physics in Medicine and Biology*, *21*(2), 181–197. https://doi.org/10.1088/0031-9155/21/2/001

Raposo Rodríguez, L., Tovar Salazar, D. J., Fernández García, N., Pastor Hernández, L., & Fernández Guinea, Ó. (2018). Magnetic resonance imaging in dementia. *Radiología (English Edition)*, *60*(6), 476–484. https://doi.org/10.1016/j.rxeng.2018.07.004

Rathore, C., Dickson, J. C., Teotónio, R., Ell, P., & Duncan, J. S. (2014). The utility of 18F-fluorodeoxyglucose PET (FDG PET) in epilepsy surgery. *Epilepsy Research*, *108*(8), 1306–1314. https://doi.org/10.1016/j.eplepsyres.2014.06.012

Reilhac, A., Batan, G., Michel, C., Grova, C., Tohka, J., Collins, D. L., Costes, N., & Evans, A. C. (2005). PET-SORTEO: Validation and development of database of Simulated PET volumes. *IEEE Transactions on Nuclear Science*, *52*(5), 1321–1328. https://doi.org/10.1109/TNS.2005.858242

Reilhac, A., Tomeï, S., Buvat, I., Michel, C., Keheren, F., & Costes, N. (2008). Simulation-based evaluation of OSEM iterative reconstruction methods in dynamic brain PET studies. *NeuroImage*, *39*(1), 359–368. https://doi.org/10.1016/j.neuroimage.2007.07.038

Saha, G. B. (2010a). *Basics of PET Imaging: Physics, Chemistry, and Regulations* (2nd ed.). Springer-Verlag. https://doi.org/10.1007/978-1-4419-0805-6

Saha, G. B. (2010b). PET Scanning Systems. In G. B. Saha (Ed.), *Basics of PET Imaging: Physics, Chemistry, and Regulations* (pp. 19–39). Springer. https://doi.org/10.1007/978-1-4419-0805-6_2

Salamon, N., Kung, J., Shaw, S. J., Koo, J., Koh, S., Wu, J. Y., Lerner, J. T., Sankar, R., Shields, W. D., Engel, J., Fried, I., Miyata, H., Yong, W. H., Vinters, H. V., & Mathern, G. W. (2008). FDG-PET/MRI coregistration improves detection of cortical dysplasia in patients with epilepsy. *Neurology*, *71*(20), 1594–1601. https://doi.org/10.1212/01.wnl.0000334752.41807.2f

Sarikaya, I. (2015). PET studies in epilepsy. *American Journal of Nuclear Medicine and Molecular Imaging*, *5*(5), 416–430.

Schmidtlein, C., Kirov, A., Nehmeh, S., Erdi, Y., Humm, J., Amols, H., Bidaut, L., Ganin, A., Stearns, C. W., McDaniel, D., & Hamacher, K. (2006). Validation of GATE Monte Carlo simulations of the GE Advance/Discovery LS PET scanners. *Medical Physics*, *33*, 198–208. https://doi.org/10.1118/1.2089447

Schmidtlein, C., Turner, A., Nehmeh, S., Mawlawi, O., Erdi, Y., Humm, J., Amols, H., & Kirov, A. (2006). A Monte Carlo model of the Discovery ST PET scanner. *Medical Physics - MED PHYS*, *33*. https://doi.org/10.1118/1.2240294

Schmitz, R., Alessio, A., & Kinahan, P. (2013). *The Physics of PET / CT scanners*. https://www.semanticscholar.org/paper/The-Physics-of-PET-%2F-CT-scanners-Schmitz-Alessio/0dfac4fe22a290c5a036b5cf67d732d227ed701f

Schmitz, R. E., Gillispie, S. B., Harrison, R. L., MacDonald, L. R., Kinahan, P. E., & Lewellen, T. K. (2007). Expanding SimSET to include block detectors: Performance with pseudo-blocks and a true block model. *2007 IEEE Nuclear Science Symposium Conference Record*, *6*, 4275–4278. https://doi.org/10.1109/NSSMIC.2007.4437061

Schoenahl, F., Montandon, M.-L., Slosman, D., & Zaidi, H. (2003). *Assessment of the performance of SPM analysis in PET neuroactivation studies: A Monte Carlo investigation*. https://www.semanticscholar.org/paper/Assessment-of-the-performance-of-SPM-analysis-in-%3A-Schoenahl-Montandon/36984e412b0a89e21a8e0526c9a806d93faec8dc

Schöll, M., Damián, A., & Engler, H. (2014). Fluorodeoxyglucose PET in Neurology and Psychiatry. *PET Clinics*, *9*(4), 371–390, v. https://doi.org/10.1016/j.cpet.2014.07.005

Sheikhzadeh, P., Sabet, H., Ghadiri, H., Geramifar, P., Mahani, H., Ghafarian, P., & Ay, M. R. (2017). Development and validation of an accurate GATE model for NeuroPET scanner. *Physica Medica: PM: An International Journal Devoted to the Applications of Physics to Medicine and Biology: Official Journal of the Italian Association of Biomedical Physics (AIFB)*, *40*, 59–65. https://doi.org/10.1016/j.ejmp.2017.07.008

Shepp, L. A., & Vardi, Y. (1982). Maximum likelihood reconstruction for emission tomography. *IEEE Transactions on Medical Imaging*, *1*(2), 113–122. https://doi.org/10.1109/TMI.1982.4307558

Shivamurthy, V. K. N., Tahari, A. K., Marcus, C., & Subramaniam, R. M. (2015). Brain FDG PET and the Diagnosis of Dementia. *American Journal of Roentgenology*, *204*(1), W76–W85. https://doi.org/10.2214/AJR.13.12363

Silva-Rodríguez, J., Aguiar, P., Domínguez-Prado, I., Fierro, P., & Ruibal, Á. (2015). Simulated FDG-PET studies for the assessment of SUV quantification methods. *Revista Española de Medicina Nuclear e Imagen Molecular*, *34*(1), 13–18. https://doi.org/10.1016/j.remn.2014.07.006

Silva-Rodríguez, J., Aguiar, P., Sanchez-Garcia, M., Mosquera, J., Luna Vega, V., Cortés, J., Garrido, M., Cameán, M., & Ruibal, A. (2014). Correction for FDG PET dose extravasations: Monte Carlo validation and quantitative evaluation of patient studies. *Medical Physics*, *41*, 052502. https://doi.org/10.1118/1.4870979

Silva-Rodríguez, J., Pineiro-Fiel, M., Archibald, S. J., Aguiar, P., & Efthimiou, N. (2019). A SimSET-STIR hybrid Monte Carlo model for the Philips Vereos Digital PET. *2019 IEEE Nuclear Science Symposium and Medical Imaging Conference (NSS/MIC)*, 1–4. https://doi.org/10.1109/NSS/MIC42101.2019.9059645

Silva-Rodríguez, J., Tsoumpas, C., Domínguez-Prado, I., Pardo-Montero, J., Ruibal, Á., & Aguiar, P. (2016). Impact and correction of the bladder uptake on 18 F-FCH PET quantification: A simulation study using the XCAT2 phantom. *Physics in Medicine and Biology*, *61*(2), 758–773. https://doi.org/10.1088/0031-9155/61/2/758

Singh, D., Garg, A., Gupta, A., & Bansal, A. R. (2013). Mesial temporal lobe epilepsy with hippocampal sclerosis preceded by eclampsia: A rare association. *Neurology India*, *61*(4), 421. https://doi.org/10.4103/0028-3886.117585

Struck, A. F., & Westover, M. B. (2015). Variability in clinical assessment of neuroimaging in temporal lobe epilepsy. *Seizure - European Journal of Epilepsy*, *30*, 132–135. https://doi.org/10.1016/j.seizure.2015.06.011

Stute, S., Carlier, T., Cristina, K., Noblet, C., Martineau, A., Hutton, B., Barnden, L., & Buvat, I. (2011). Monte Carlo simulations of clinical PET and SPECT scans: Impact of the input data on the simulated images. *Physics in Medicine and Biology*, *56*(19), 6441–6457. https://doi.org/10.1088/0031-9155/56/19/017

Surti, S. (2015). Update on Time-of-Flight PET Imaging. *Journal of Nuclear Medicine*, *56*(1), 98–105. https://doi.org/10.2967/jnumed.114.145029

Taylor, I., Scheffer, I. E., & Berkovic, S. F. (2003). Occipital epilepsies: Identification of specific and newly recognized syndromes. *Brain*, *126*(4), 753–769. https://doi.org/10.1093/brain/awg080

Thielemans, K., Tsoumpas, C., Mustafovic, S., Beisel, T., Aguiar, P., Dikaios, N., & Jacobson, M. W. (2012). STIR: Software for tomographic image reconstruction release 2. *Physics in Medicine and Biology*, *57*(4), 867–883. https://doi.org/10.1088/0031-9155/57/4/867

Thompson, C. J., Moreno-Cantu, J., & Picard, Y. (1992). PETSIM: Monte Carlo simulation of all sensitivity and resolution parameters of cylindrical positron imaging systems. *Physics in Medicine and Biology*, *37*(3), 731–749. https://doi.org/10.1088/0031-9155/37/3/017

Tsoumpas, C., Aguiar, P., Nikita, K. S., Ros, D., & Thielemans, K. (2004). Evaluation of the single scatter simulation algorithm implemented in the STIR library. *IEEE Symposium Conference Record Nuclear Science 2004.*, *6*, 3361-3365 Vol. 6. https://doi.org/10.1109/NSSMIC.2004.1466455

Tsoumpas, C., Aguiar, P., Ros, D., Dikaios, N., & Thielemans, K. (2005). Scatter simulation including double scatter. *IEEE Nuclear Science Symposium Conference Record, 2005*, *3*, 5 pp. – 1619. https://doi.org/10.1109/NSSMIC.2005.1596628

Tsubaki, Y., Akamatsu, G., Shimokawa, N., Katsube, S., Takashima, A., Sasaki, M., & Japanese Alzheimer's Disease Neuroimaging Initiative. (2020). Development and evaluation of an automated quantification tool for amyloid PET images. *EJNMMI Physics*, *7*(1), 59. https://doi.org/10.1186/s40658-020-00329-4

Vandenberghe, R., Adamczuk, K., Dupont, P., Laere, K. V., & Chételat, G. (2013). Amyloid PET in clinical practice: Its place in the multidimensional space of Alzheimer's disease. *NeuroImage : Clinical*, *2*, 497–511. https://doi.org/10.1016/j.nicl.2013.03.014

Varrone, A., Asenbaum, S., Vander Borght, T., Booij, J., Nobili, F., Någren, K., Darcourt, J., Kapucu, Ö. L., Tatsch, K., Bartenstein, P., & Van Laere, K. (2009). EANM procedure guidelines for PET brain imaging using [18F]FDG, version 2. *European Journal of Nuclear Medicine and Molecular Imaging*, *36*(12), 2103–2110. https://doi.org/10.1007/s00259-009-1264-0

Vemuri, P., & Jack, C. R. (2010). Role of structural MRI in Alzheimer's disease. *Alzheimer's Research & Therapy*, *2*(4), 23. https://doi.org/10.1186/alzrt47

Verger, A., Lagarde, S., Maillard, L., Bartolomei, F., & Guedj, E. (2018). Brain molecular imaging in pharmacoresistant focal epilepsy: Current practice and perspectives. *Revue Neurologique*, *174*(1–2), 16–27. https://doi.org/10.1016/j.neurol.2017.05.001

Vielhaber, S., Von Oertzen, J. H., Kudin, A. F., Schoenfeld, A., Menzel, C., Biersack, H.-J., Kral, T., Elger, C. E., & Kunz, W. S. (2003). Correlation of hippocampal glucose oxidation capacity and interictal FDG-PET in temporal lobe epilepsy. *Epilepsia*, *44*(2), 193–199. https://doi.org/10.1046/j.1528-1157.2003.38102.x

Wang, Z. I., & Alexopoulos, A. V. (2016). MRI Post-processing in Pre-surgical Evaluation. *Current Opinion in Neurology*, *29*(2), 168–174. https://doi.org/10.1097/WCO.0000000000000305

Watson, C. C., Newport, D., & Casey, M. E. (1996). A Single Scatter Simulation Technique for Scatter Correction in 3D PET. In P. Grangeat & J.-L. Amans (Eds.), *Three-Dimensional Image Reconstruction in Radiology and Nuclear Medicine* (pp. 255–268). Springer Netherlands. https://doi.org/10.1007/978-94-015-8749-5_18

Watson, R., O'Brien, J. T., Barber, R., & Blamire, A. M. (2012). Patterns of gray matter atrophy in dementia with Lewy bodies: A voxel-based morphometry study. *International Psychogeriatrics*, *24*(4), 532–540. https://doi.org/10.1017/S1041610211002171

Werling, A., Bublitz, O., Doll, J., Adam, L.-E., & Brix, G. (2002). Fast implementation of the single scatter simulation algorithm and its use in iterative image reconstruction of PET data. *Physics in Medicine & Biology*, *47*(16), 2947. https://doi.org/10.1088/0031-9155/47/16/310

Whitwell, J. L. (2009). Voxel-Based Morphometry: An Automated Technique for Assessing Structural Changes in the Brain. *The Journal of Neuroscience*, *29*(31), 9661–9664. https://doi.org/10.1523/JNEUROSCI.2160-09.2009

Whitwell, J. L., Shiung, M. M., Przybelski, S., Weigand, S. D., Knopman, D. S., Boeve, B. F., Petersen, R. C., & Jack, C. R. (2008). MRI patterns of atrophy associated with progression to AD in amnestic Mild Cognitive Impairment. *Neurology*, *70*(7), 512–520. https://doi.org/10.1212/01.wnl.0000280575.77437.a2

Willmann, O., Wennberg, R., May, T., Woermann, F. G., & Pohlmann-Eden, B. (2007). The contribution of 18F-FDG PET in preoperative epilepsy surgery evaluation for patients with temporal lobe epilepsy. *Seizure*, *16*(6), 509–520. https://doi.org/10.1016/j.seizure.2007.04.001

Winston, G., Micallef, C., Kendell, B., Bartlett, P., Williams, E., Burdett, J., & Duncan, J. (2013). The value of repeat neuroimaging for epilepsy at a tertiary referral centre: 16 years of experience. *Epilepsy Research*, *105*. https://doi.org/10.1016/j.eplepsyres.2013.02.022

Wong, D. F., Links, J. M., Molliver, M. E., Hengst, T. C., Clifford, C. M., Buhle, L., Bryan, M., Stumpf, M., & Wagner, H. N. Jr. (1984). An anatomically realistic brain phantom for quantification with positron tomography. *Journal of Nuclear Medicine*, *25*(5), 108.

Yamane, T., Ishii, K., Sakata, M., Ikari, Y., Nishio, T., Ishii, K., Kato, T., Ito, K., Senda, M., & J-ADNI Study Group. (2017). Inter-rater variability of visual interpretation and comparison with quantitative evaluation of 11C-PiB PET amyloid images of the Japanese Alzheimer's Disease Neuroimaging Initiative (J-ADNI) multicenter study. *European Journal of Nuclear Medicine and Molecular Imaging*, *44*(5), 850–857. https://doi.org/10.1007/s00259-016-3591-2

Yao, Z., Hu, B., Zhao, L., & Liang, C. (2011). Analysis of Gray Matter in AD Patients and MCI Subjects Based Voxel-Based Morphometry. In B. Hu, J. Liu, L. Chen, & N. Zhong (Eds.), *Brain Informatics* (pp. 209–217). Springer. https://doi.org/10.1007/978-3-642-23605-1_22

Yasuda, C. L., Betting, L. E., & Cendes, F. (2010). Voxel-based morphometry and epilepsy. *Expert Review of Neurotherapeutics*, *10*(6), 975–984. https://doi.org/10.1586/ern.10.63

Zaidi, H. (1999). Relevance of accurate Monte Carlo modeling in nuclear medical imaging. *Medical Physics*, *26*(4), 574–608. https://doi.org/10.1118/1.598559

Zaidi, H., Montandon, M.-L., & Alavi, A. (2007). Advances in Attenuation Correction Techniques in PET. *PET Clinics*, *2*(2), 191–217. https://doi.org/10.1016/j.cpet.2007.12.002

Zanzonico, P. (2004). Positron emission tomography: A review of basic principles, scanner design and performance, and current systems. *Seminars in Nuclear Medicine*. https://doi.org/10.1053/J.SEMNUCLMED.2003.12.002

Zvolský, M. (2014, November 28). *Tomographic Image Reconstruction. - An Introduction.* https://www.desy.de/~garutti/LECTURES/BioMedical/Lecture7_ImageReconstruction.pdf

Zvolský, M., Horns, D., & Garutti, E. (2017). *Simulation, Image Reconstruction and SiPM Characterisation for a Novel Endoscopic Positron Emission Tomography Detector* [Universität Hamburg]. https://bib-pubdb1.desy.de/record/398074/files/PhDThesis_published.pdf

APPENDICES

7 APPENDICES

The content of this chapter has already been published as Paredes-Pacheco, J. et al. SimPET-An open online platform for the Monte Carlo simulation of realistic brain PET data. Validation for 18 F-FDG scans. Med Phys. 2021 May; 48(5):2482-2493. doi: 10.1002/mp.14838. PMID: 33713354; PMCID: PMC8252452.

7.1 SIMULATION OF PATHOLOGICAL MAPS

SimPET can be used to validate quantitative methods in different pathologies, in addition to cortical epilepsy. Users can download the generated activity maps, and modify them to introduce known hypometabolism patterns, which can be used as ground-truth for the quantification after the simulation and reconstruction. As an example, one of the generated 18F-FDG activity maps was downloaded, and two different hypometabolism were added manually in predefined ROIs reflecting patterns typically observed in AD and TLE. The simulations of this patterns in the three scanners are showcased in Figure A1, allowing for the different representation of the exact same metabolism in the different scanners to be easily observed.

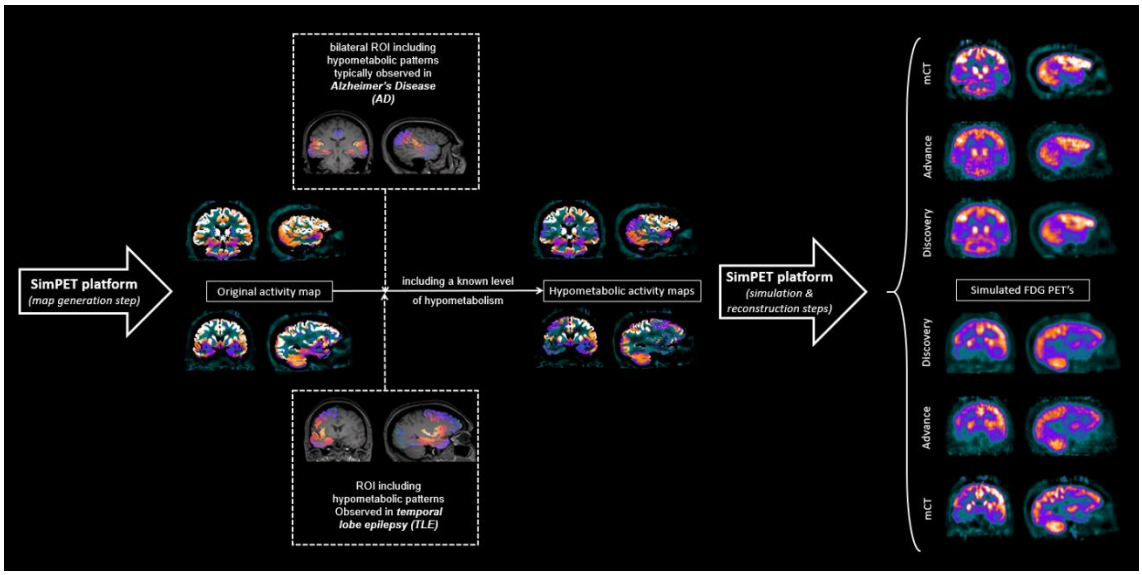

Figure A1: Pipeline used to simulate pathological PET images of AD and TLE cases using activity maps generated on SimPET and including a known level of hypometabolism.

After simulating the generated patterns using the platform, measurements on the different scanners can be compared, allowing the users to validate quantification and harmonization protocols.

7.2 AMYLOID-PET SIMULATION

In addition to 18F-FDG, SimPET also allows users to simulate amyloid-PET images with 18F-Florbetapir as a tracer. For demonstrating this capability, we include a simple example case. Five amyloid-negative patients, acquired on the GE Discovery ST, were uploaded to the platform to obtain amyloid-PET realistic activity maps. These maps were then simulated on the three implemented scanners and the results are showcased for demonstration purposes, showing the differences between scanners in amyloid-PET assessments.

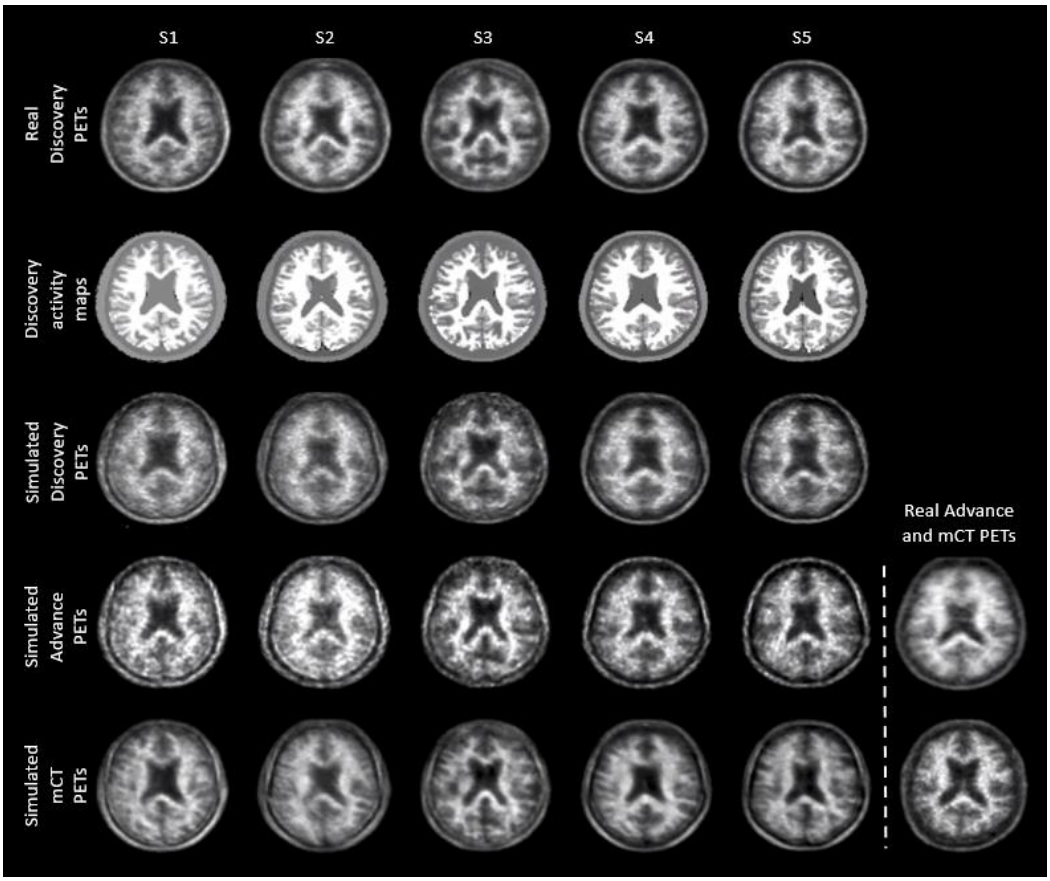

Figure A2: Sample of five amyloid-negative patient PET images acquired on GE Discovery ST, the corresponding generated activity maps, and the simulated PET images obtained in the different commercial scanners, GE Advance NXi and Siemens Biograph mCT images are included for comparison.

Figure A2 shows the results of the performed amyloid-PET simulations. Five amyloid-negative PET patients and the obtained activity maps are shown in rows 1 and 2, followed by the simulated PETs obtained with the platform for the GE Discovery ST, GE Advance NXi and Siemens Biograph mCT scanner models (rows 3-5). Real amyloid-negative PET examples for the GE Advance NXi and Siemens Biograph mCT scanners are included for comparison.

DECLARATIONS

8 DECLARATIONS: USE OF IMAGES, TABLES AND PUBLISHED CONTENT

8.1 JOURNAL AUTHORIZATIONS FOR THE USE OF IMAGES AND TABLES

- Table 1 and Figure 12

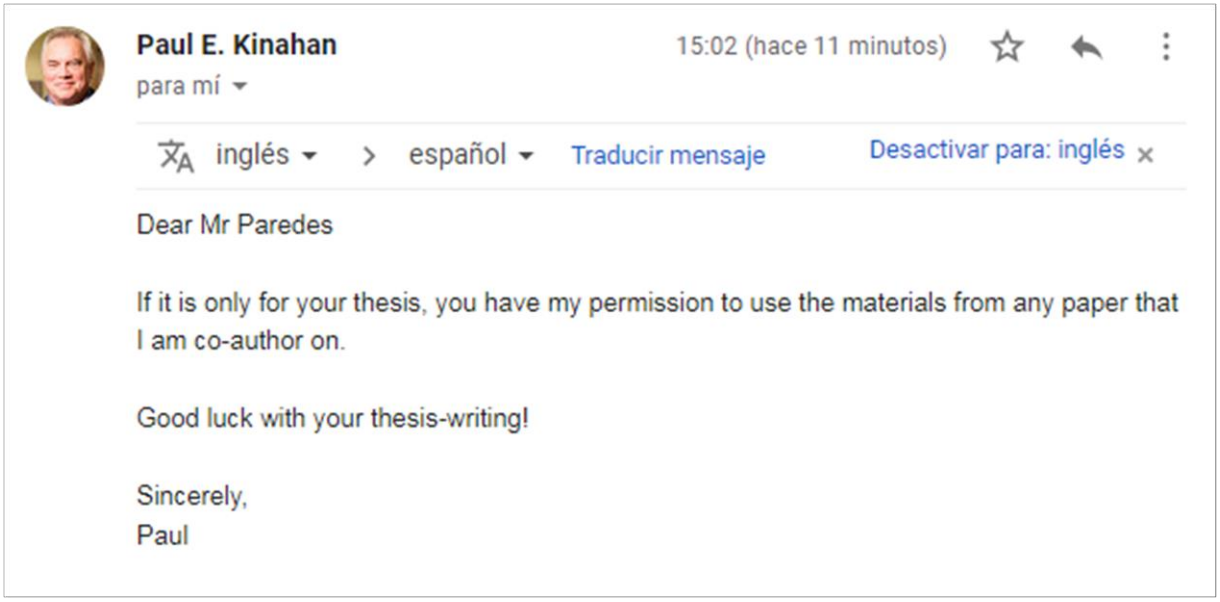

Paul E. Kinahan 15:02 (hace 11 minutos)

para mí

inglés > español Traducir mensaje Desactivar para: inglés ×

Dear Mr Paredes

If it is only for your thesis, you have my permission to use the materials from any paper that I am co-author on.

Good luck with your thesis-writing!

Sincerely,
Paul

- Figure 2 and Table 2

SPRINGER NATURE LICENSE TERMS AND CONDITIONS

Apr 22, 2022

This Agreement between Mr. José Paredes-Pacheco ("You") and Springer Nature ("Springer Nature") consists of your license details and the terms and conditions provided by Springer Nature and Copyright Clearance Center.

License Number	5294150552274
License date	Apr 22, 2022
Licensed Content Publisher	Springer Nature
Licensed Content Publication	Springer eBook
Licensed Content Title	Physics and Instrumentation in PET
Licensed Content Author	Dale L Bailey ARCP (London), FIPEM, MACPSEM, Joel S Karp PhD, Suleman Surti PhD
Licensed Content Date	Jan 1, 2005
Type of Use	Thesis/Dissertation
Requestor type	academic/university or research institute
Format	print and electronic
Portion	figures/tables/illustrations
Number of figures/tables/illustrations	2
Will you be translating?	no
Circulation/distribution	1 - 29
Author of this Springer Nature content	no
Title	Desarrollo de una plataforma web para la evaluación de protocolos de neuroimagen PET: SimPET
Institution name	University of Santiago de Compostela
Expected presentation date	Jun 2022
Portions	Figure 2.10, Table 2.4

- Figure 3

ELSEVIER LICENSE TERMS AND CONDITIONS

Apr 22, 2022

This Agreement between Mr. José Paredes-Pacheco ("You") and Elsevier ("Elsevier") consists of your license details and the terms and conditions provided by Elsevier and Copyright Clearance Center.

License Number	5294260371497
License date	Apr 22, 2022
Licensed Content Publisher	Elsevier
Licensed Content Publication	Elsevier Books
Licensed Content Title	The Dynamic Loss of Earth's Radiation Belts
Licensed Content Author	Robert A. Marshall,Chris M. Cully
Licensed Content Date	Jan 1, 2020
Licensed Content Pages	57
Start Page	199
End Page	255
Type of Use	reuse in a thesis/dissertation
Portion	figures/tables/illustrations
Number of figures/tables/illustrations	1
Format	both print and electronic
Are you the author of this Elsevier chapter?	No
Will you be translating?	No
Title	Desarrollo de una plataforma web para la evaluación de protocolos de neuroimagen PET: SimPET
Institution name	University of Santiago de Compostela
Expected presentation date	Jun 2022
Portions	Figure 7.6

- Figure 4

SPRINGER NATURE LICENSE TERMS AND CONDITIONS

Apr 22, 2022

This Agreement between Mr. José Paredes-Pacheco ("You") and Springer Nature ("Springer Nature") consists of your license details and the terms and conditions provided by Springer Nature and Copyright Clearance Center.

License Number	5294270249019
License date	Apr 22, 2022
Licensed Content Publisher	Springer Nature
Licensed Content Publication	Springer eBook
Licensed Content Title	PET Scanning Systems
Licensed Content Author	Gopal B. Saha Ph.D.
Licensed Content Date	Jan 1, 2010
Type of Use	Thesis/Dissertation
Requestor type	academic/university or research institute
Format	print and electronic
Portion	figures/tables/illustrations
Number of figures/tables/illustrations	1
Will you be translating?	no
Circulation/distribution	1 - 29
Author of this Springer Nature content	no
Title	Desarrollo de una plataforma web para la evaluación de protocolos de neuroimagen PET: SimPET
Institution name	University of Santiago de Compostela
Expected presentation date	Jun 2022
Portions	Figure 2.1

- Figure 5

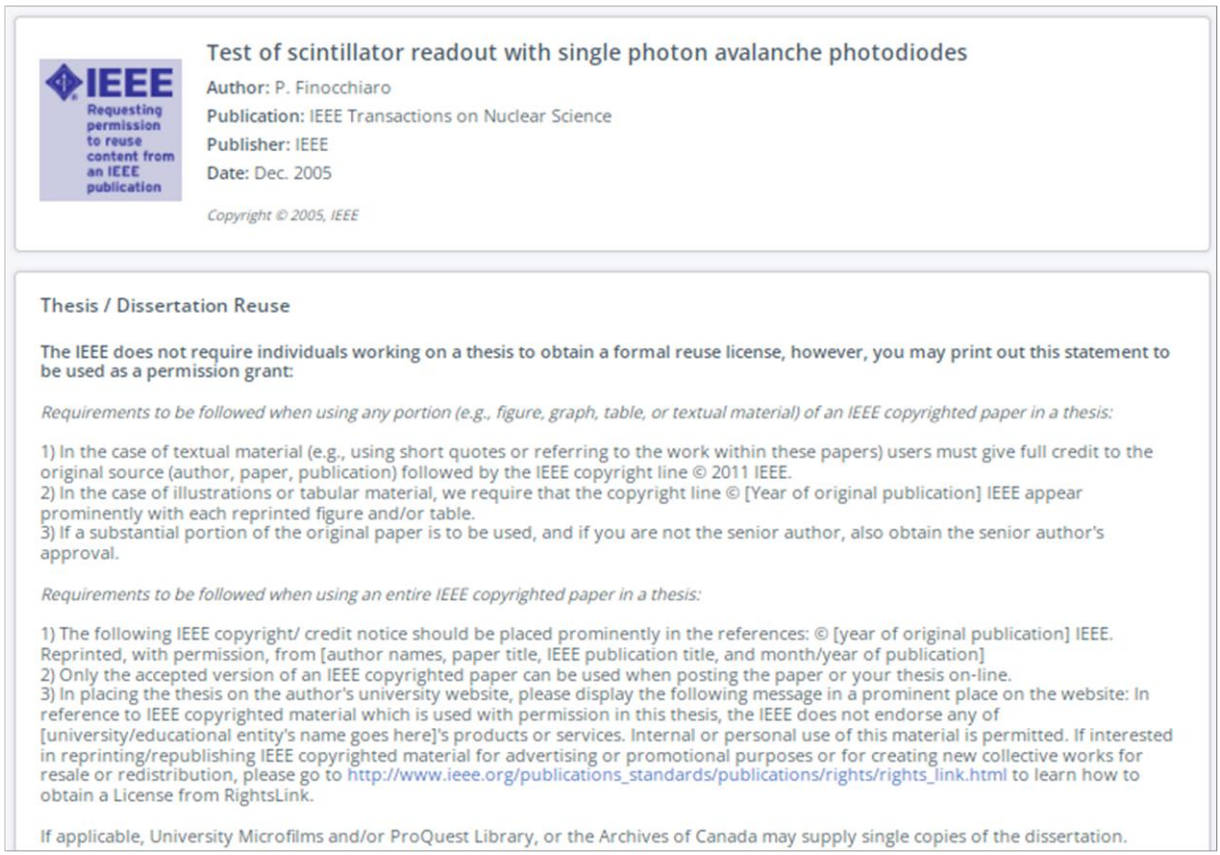

IEEE
Requesting permission to reuse content from an IEEE publication

Test of scintillator readout with single photon avalanche photodiodes

Author: P. Finocchiaro
Publication: IEEE Transactions on Nuclear Science
Publisher: IEEE
Date: Dec. 2005

Thesis / Dissertation Reuse

The IEEE does not require individuals working on a thesis to obtain a formal reuse license, however, you may print out this statement to be used as a permission grant:

Requirements to be followed when using any portion (e.g., figure, graph, table, or textual material) of an IEEE copyrighted paper in a thesis:

1) In the case of textual material (e.g., using short quotes or referring to the work within these papers) users must give full credit to the original source (author, paper, publication) followed by the IEEE copyright line © 2011 IEEE.
2) In the case of illustrations or tabular material, we require that the copyright line © [Year of original publication] IEEE appear prominently with each reprinted figure and/or table.
3) If a substantial portion of the original paper is to be used, and if you are not the senior author, also obtain the senior author's approval.

Requirements to be followed when using an entire IEEE copyrighted paper in a thesis:

1) The following IEEE copyright/ credit notice should be placed prominently in the references: © [year of original publication] IEEE. Reprinted, with permission, from [author names, paper title, IEEE publication title, and month/year of publication]
2) Only the accepted version of an IEEE copyrighted paper can be used when posting the paper or your thesis on-line.
3) In placing the thesis on the author's university website, please display the following message in a prominent place on the website: In reference to IEEE copyrighted material which is used with permission in this thesis, the IEEE does not endorse any of [university/educational entity's name goes here]'s products or services. Internal or personal use of this material is permitted. If interested in reprinting/republishing IEEE copyrighted material for advertising or promotional purposes or for creating new collective works for resale or redistribution, please go to http://www.ieee.org/publications_standards/publications/rights/rights_link.html to learn how to obtain a License from RightsLink.

If applicable, University Microfilms and/or ProQuest Library, or the Archives of Canada may supply single copies of the dissertation.

- Figure 6, Figure 7, Figure 16 and Figure 17

SPRINGER NATURE LICENSE TERMS AND CONDITIONS

Apr 22, 2022

This Agreement between Mr. José Paredes-Pacheco ("You") and Springer Nature ("Springer Nature") consists of your license details and the terms and conditions provided by Springer Nature and Copyright Clearance Center.

License Number	5294290079846
License date	Apr 22, 2022
Licensed Content Publisher	Springer Nature
Licensed Content Publication	Springer eBook
Licensed Content Title	PET: Physics, Instrumentation, and Scanners
Licensed Content Author	Simon R. Cherry, Magnus Dahlbom
Licensed Content Date	Jan 1, 2006
Type of Use	Thesis/Dissertation
Requestor type	academic/university or research institute
Format	print and electronic
Portion	figures/tables/illustrations
Number of figures/tables/illustrations	4
Will you be translating?	no
Circulation/distribution	1 - 29
Author of this Springer Nature content	no
Title	Desarrollo de una plataforma web para la evaluación de protocolos de neuroimagen PET: SimPET
Institution name	University of Santiago de Compostela
Expected presentation date	Jun 2022
Portions	Figure 20, Figure 21, Figure 53, Figure 55

- Figure 8 and Figure 10

SPRINGER NATURE LICENSE TERMS AND CONDITIONS

Apr 23, 2022

This Agreement between Mr. José Paredes-Pacheco ("You") and Springer Nature ("Springer Nature") consists of your license details and the terms and conditions provided by Springer Nature and Copyright Clearance Center.

License Number	5294710688921
License date	Apr 23, 2022
Licensed Content Publisher	Springer Nature
Licensed Content Publication	Springer eBook
Licensed Content Title	Data Acquisition and Performance Characterization in PET
Licensed Content Author	Dale L Bailey PhD, ARCP (London), FIPEM, MACPSEM
Licensed Content Date	Jan 1, 2005
Type of Use	Thesis/Dissertation
Requestor type	academic/university or research institute
Format	print and electronic
Portion	figures/tables/illustrations
Number of figures/tables/illustrations	2
Will you be translating?	no
Circulation/distribution	1 - 29
Author of this Springer Nature content	no
Title	Desarrollo de una plataforma web para la evaluación de protocolos de neuroimagen PET: SimPET
Institution name	University of Santiago de Compostela
Expected presentation date	Jun 2022
Portions	Figure 3.1, Figure 3.3

- Figure 9

Permissions

JNMT Permission Policies

Non-Commercial

JNMT allows reuse of excerpted original material, such as abstracts, short text excerpts, figures, and tables, provided appropriate credit is given to the copyright holder and the material is not used for commercial purposes. Non-commercial uses include articles in peer-review journals, classroom/teaching material, and academic theses/dissertations. Full article reprints require explicit permission with exceptions as noted below. For bulk reprints, see our reprint page.

- Figure 11

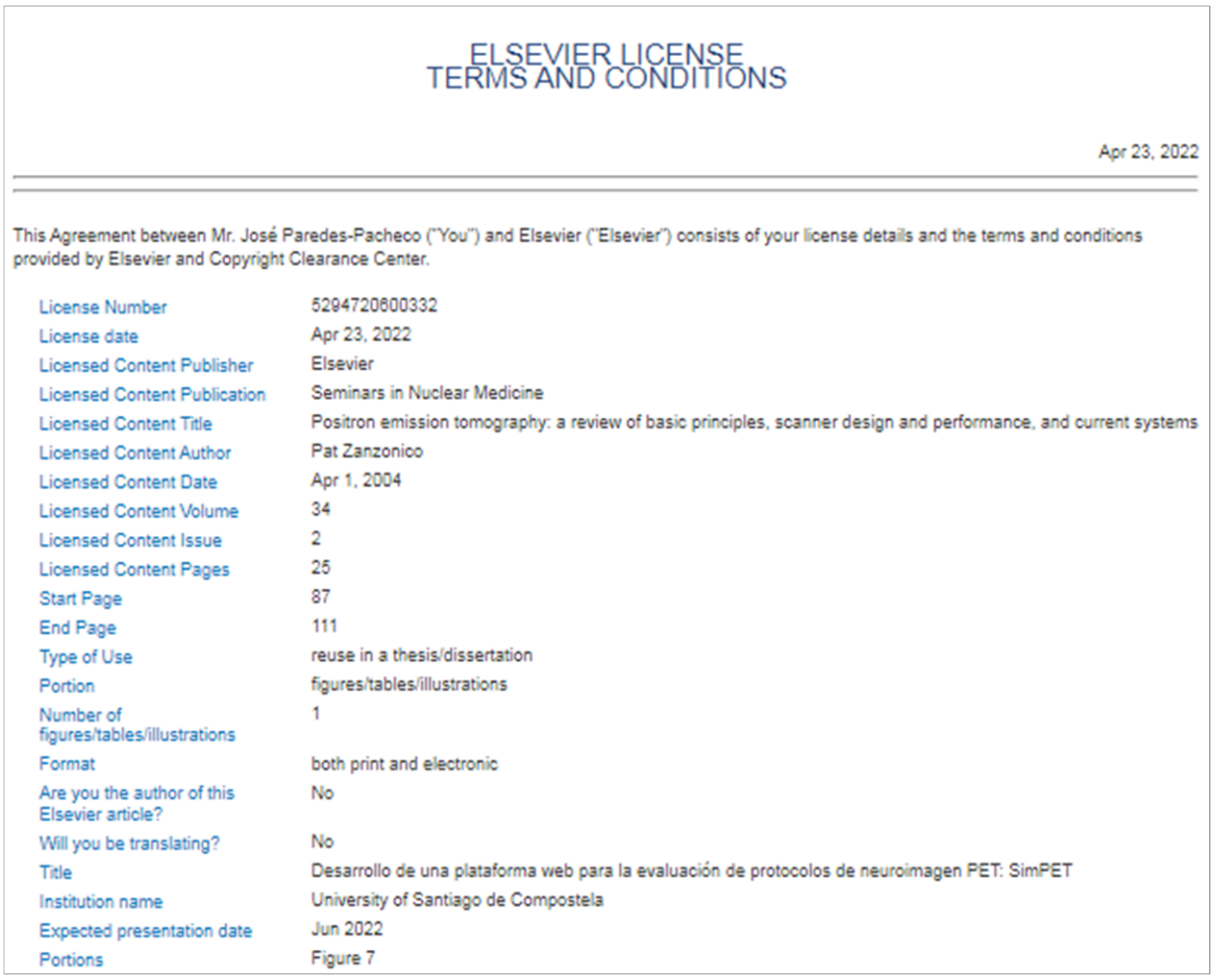

ELSEVIER LICENSE
TERMS AND CONDITIONS

Apr 23, 2022

This Agreement between Mr. José Paredes-Pacheco ("You") and Elsevier ("Elsevier") consists of your license details and the terms and conditions provided by Elsevier and Copyright Clearance Center.

License Number	5294720600332
License date	Apr 23, 2022
Licensed Content Publisher	Elsevier
Licensed Content Publication	Seminars in Nuclear Medicine
Licensed Content Title	Positron emission tomography: a review of basic principles, scanner design and performance, and current systems
Licensed Content Author	Pat Zanzonico
Licensed Content Date	Apr 1, 2004
Licensed Content Volume	34
Licensed Content Issue	2
Licensed Content Pages	25
Start Page	87
End Page	111
Type of Use	reuse in a thesis/dissertation
Portion	figures/tables/illustrations
Number of figures/tables/illustrations	1
Format	both print and electronic
Are you the author of this Elsevier article?	No
Will you be translating?	No
Title	Desarrollo de una plataforma web para la evaluación de protocolos de neuroimagen PET: SimPET
Institution name	University of Santiago de Compostela
Expected presentation date	Jun 2022
Portions	Figure 7

- Figure 13 and Figure 15

They are figures from teaching material and publicly available online from the University of Hamburg, so no permission is needed since the reproduced material does not exceed 10% of the length of the document (Condition indicated by EDIUS).

- Figure 14

ELSEVIER LICENSE
TERMS AND CONDITIONS

Apr 23, 2022

This Agreement between Mr. José Paredes-Pacheco ("You") and Elsevier ("Elsevier") consists of your license details and the terms and conditions provided by Elsevier and Copyright Clearance Center.

License Number	5294731055482
License date	Apr 23, 2022
Licensed Content Publisher	Elsevier
Licensed Content Publication	Elsevier Books
Licensed Content Title	Emission Tomography
Licensed Content Author	PAUL E. KINAHAN,MICHEL DEFRISE,ROLF CLACKDOYLE
Licensed Content Date	Jan 1, 2004
Licensed Content Pages	22
Start Page	421
End Page	442
Type of Use	reuse in a thesis/dissertation
Portion	figures/tables/illustrations
Number of figures/tables/illustrations	1
Format	both print and electronic
Are you the author of this Elsevier chapter?	No
Will you be translating?	No
Title	Desarrollo de una plataforma web para la evaluación de protocolos de neuroimagen PET: SimPET
Institution name	University of Santiago de Compostela
Expected presentation date	Jun 2022
Portions	Figure 10

- Figure 18 and Figure 19

SPRINGER NATURE LICENSE TERMS AND CONDITIONS

Apr 23, 2022

This Agreement between Mr. José Paredes-Pacheco ("You") and Springer Nature ("Springer Nature") consists of your license details and the terms and conditions provided by Springer Nature and Copyright Clearance Center.

License Number	5294740849464
License date	Apr 23, 2022
Licensed Content Publisher	Springer Nature
Licensed Content Publication	Springer eBook
Licensed Content Title	Quantitative Techniques in PET
Licensed Content Author	Steven R Meikle BAppSc, PhD, Ramsey D Badawi PhD
Licensed Content Date	Jan 1, 2005
Type of Use	Thesis/Dissertation
Requestor type	academic/university or research institute
Format	print and electronic
Portion	figures/tables/illustrations
Number of figures/tables/illustrations	2
Will you be translating?	no
Circulation/distribution	1 - 29
Author of this Springer Nature content	no
Title	Desarrollo de una plataforma web para la evaluación de protocolos de neuroimagen PET: SimPET
Institution name	University of Santiago de Compostela
Expected presentation date	Jun 2022
Portions	Figure 5.12, Figure 5.15

- Figure 20

(Singh et al., 2013)

Wolters Kluwer

Mesial temporal lobe epilepsy with hippocampal sclerosis preceded by eclampsia: A rare association

Author: Singh D, Garg A, Gupta A, Bansal AR
Publication: Neurology India
Publisher: Wolters Kluwer Medknow Publications
Date: Jul 1, 2013

Welcome to RightsLink

Wolters Kluwer Medknow Publications has partnered with Copyright Clearance Center's RightsLink service to offer a variety of options for reusing this content.

(Taylor et al., 2003)

OXFORD UNIVERSITY PRESS LICENSE TERMS AND CONDITIONS

Apr 23, 2022

This Agreement between Mr. José Paredes-Pacheco ("You") and Oxford University Press ("Oxford University Press") consists of your license details and the terms and conditions provided by Oxford University Press and Copyright Clearance Center.

License Number	5294840036557
License date	Apr 23, 2022
Licensed Content Publisher	Oxford University Press
Licensed Content Publication	Brain
Licensed Content Title	Occipital epilepsies: identification of specific and newly recognized syndromes
Licensed Content Author	Taylor, Isabella; Scheffer, Ingrid E.
Licensed Content Date	Apr 1, 2003
Type of Use	Thesis/Dissertation
Institution name	
Title of your work	Desarrollo de una plataforma web para la evaluación de protocolos de neuroimagen PET: SimPET
Publisher of your work	University of Santiago de Compostela
Expected publication date	Jun 2022
Permissions cost	0.00 EUR
Value added tax	0.00 EUR
Total	**0.00 EUR**
Title	Desarrollo de una plataforma web para la evaluación de protocolos de neuroimagen PET: SimPET
Institution name	University of Santiago de Compostela
Expected presentation date	Jun 2022
Portions	Figure 3

(Winston et al., 2013)

Publisher: Elsevier

Creative Commons

- Figure 21

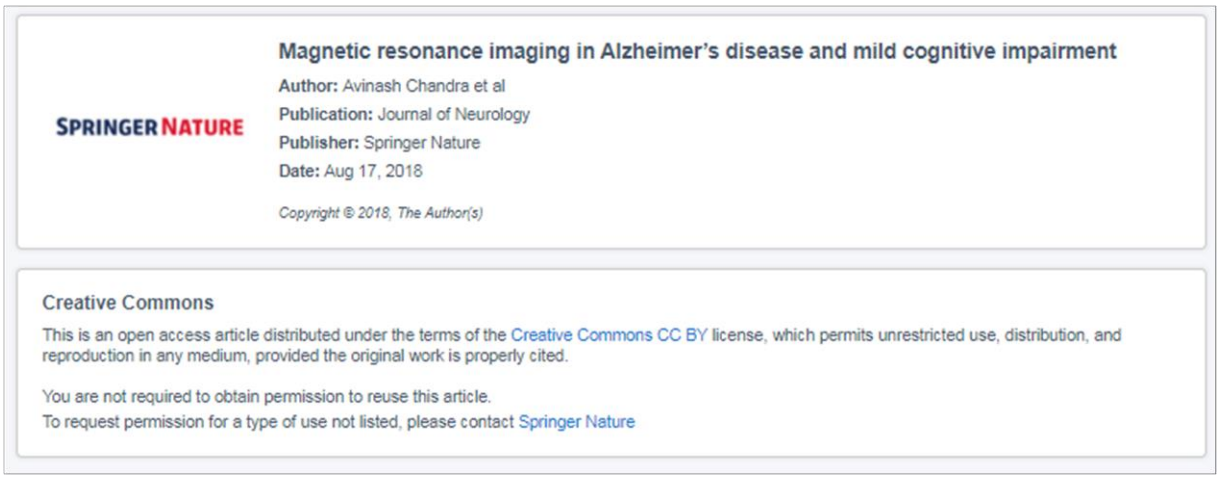

SPRINGER NATURE

Magnetic resonance imaging in Alzheimer's disease and mild cognitive impairment

Author: Avinash Chandra et al
Publication: Journal of Neurology
Publisher: Springer Nature
Date: Aug 17, 2018

- Figure 22

WHAT WE PUBLISH AND HOW IT MAY BE USED

Practical Neurology publishes review articles, case reports, news, and interviews and welcomes submissions from around the world. No author or article-processing fees are charged. All submissions are subject to our peer-review processes. Published materials are available online to all users and may be shared freely. Commercial reuse requires permission.

- Figure 23

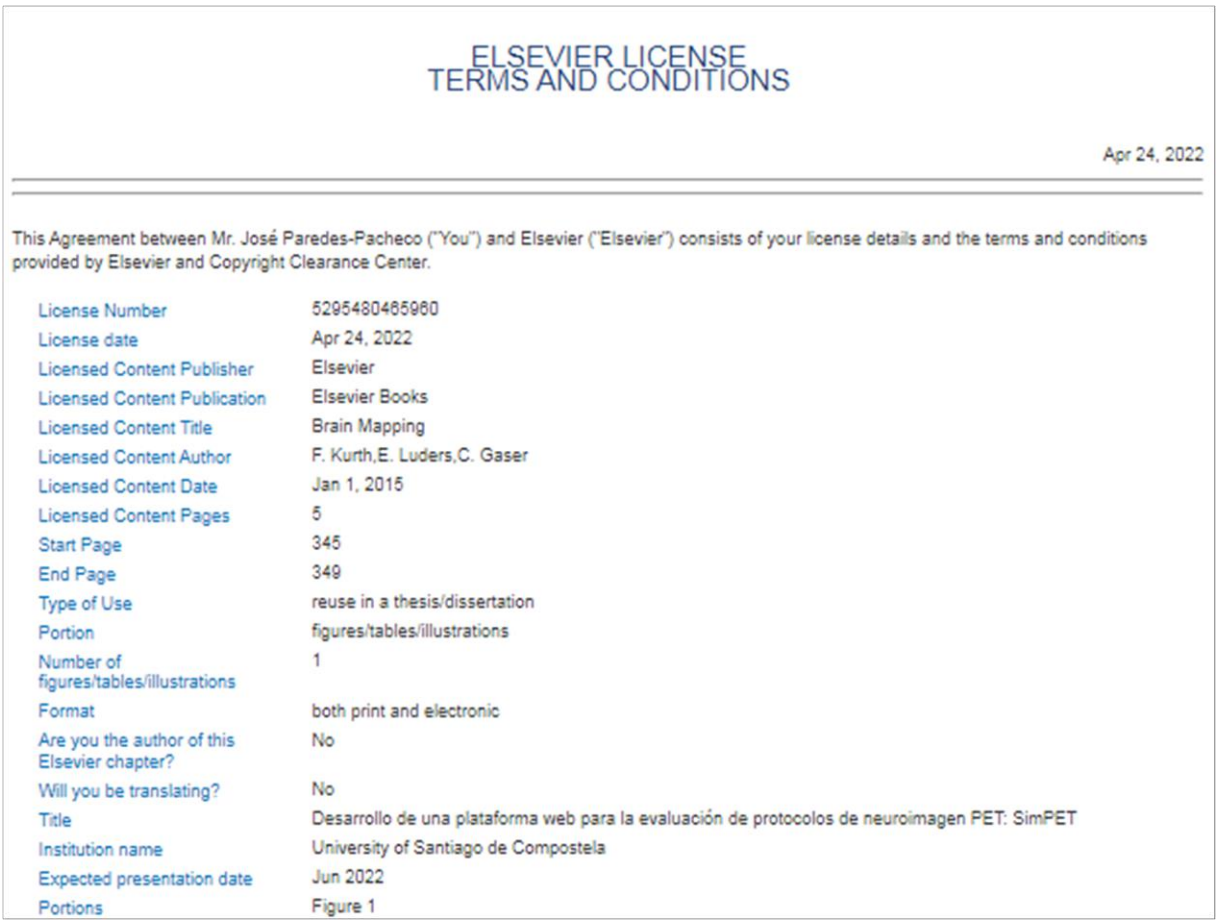

ELSEVIER LICENSE
TERMS AND CONDITIONS

Apr 24, 2022

This Agreement between Mr. José Paredes-Pacheco ("You") and Elsevier ("Elsevier") consists of your license details and the terms and conditions provided by Elsevier and Copyright Clearance Center.

License Number	5295480465960
License date	Apr 24, 2022
Licensed Content Publisher	Elsevier
Licensed Content Publication	Elsevier Books
Licensed Content Title	Brain Mapping
Licensed Content Author	F. Kurth,E. Luders,C. Gaser
Licensed Content Date	Jan 1, 2015
Licensed Content Pages	5
Start Page	345
End Page	349
Type of Use	reuse in a thesis/dissertation
Portion	figures/tables/illustrations
Number of figures/tables/illustrations	1
Format	both print and electronic
Are you the author of this Elsevier chapter?	No
Will you be translating?	No
Title	Desarrollo de una plataforma web para la evaluación de protocolos de neuroimagen PET: SimPET
Institution name	University of Santiago de Compostela
Expected presentation date	Jun 2022
Portions	Figure 1

- Figure 24

JOHN WILEY AND SONS LICENSE TERMS AND CONDITIONS

May 03, 2022

This Agreement between Mr. José Paredes-Pacheco ("You") and John Wiley and Sons ("John Wiley and Sons") consists of your license details and the terms and conditions provided by John Wiley and Sons and Copyright Clearance Center.

License Number	5301400007043
License date	May 03, 2022
Licensed Content Publisher	John Wiley and Sons
Licensed Content Publication	Epilepsia
Licensed Content Title	Voxel-based Optimized Morphometry (VBM) of Gray and White Matter in Temporal Lobe Epilepsy (TLE) with and without Mesial Temporal Sclerosis
Licensed Content Author	Michael W. Weiner, Crystal Paul, Shannon Buckley, et al
Licensed Content Date	May 8, 2006
Licensed Content Volume	47
Licensed Content Issue	5
Licensed Content Pages	8
Type of Use	Dissertation/Thesis
Requestor type	University/Academic
Format	Print and electronic
Portion	Figure/table
Number of figures/tables	1
Will you be translating?	No
Title	Desarrollo de una plataforma web para la evaluación de protocolos de neuroimagen PET: SimPET
Institution name	University of Santiago de Compostela
Expected presentation date	Jun 2022
Portions	Figure 1

- Figure 25

ELSEVIER LICENSE TERMS AND CONDITIONS

Apr 24, 2022

This Agreement between Mr. José Paredes-Pacheco ("You") and Elsevier ("Elsevier") consists of your license details and the terms and conditions provided by Elsevier and Copyright Clearance Center.

License Number	5295481344663
License date	Apr 24, 2022
Licensed Content Publisher	Elsevier
Licensed Content Publication	NeuroImage
Licensed Content Title	Patterns of Cerebral Atrophy in Dementia with Lewy Bodies Using Voxel-Based Morphometry
Licensed Content Author	E.J. Burton,G. Karas,S.M. Paling,R. Barber,E.D. Williams,C.G. Ballard,I.G. McKeith,P. Scheltens,F. Barkhof,J.T. O'Brien
Licensed Content Date	Oct 1, 2002
Licensed Content Volume	17
Licensed Content Issue	2
Licensed Content Pages	13
Start Page	618
End Page	630
Type of Use	reuse in a thesis/dissertation
Portion	figures/tables/illustrations
Number of figures/tables/illustrations	1
Format	both print and electronic
Are you the author of this Elsevier article?	No
Will you be translating?	No
Title	Desarrollo de una plataforma web para la evaluación de protocolos de neuroimagen PET: SimPET
Institution name	University of Santiago de Compostela
Expected presentation date	Jun 2022
Portions	Figure 8

- Figure 26

ELSEVIER LICENSE
TERMS AND CONDITIONS

Apr 24, 2022

This Agreement between Mr. José Paredes-Pacheco ("You") and Elsevier ("Elsevier") consists of your license details and the terms and conditions provided by Elsevier and Copyright Clearance Center.

License Number	5295490176436
License date	Apr 24, 2022
Licensed Content Publisher	Elsevier
Licensed Content Publication	European Journal of Radiology
Licensed Content Title	PET/CT and vascular disease: Current concepts
Licensed Content Author	José Leite Gondim Cavalcanti Filho,Ronaldo de Souza Leão Lima,Luiz de Souza Machado Neto,Leonardo Kayat Bittencourt,Romeu Côrtes Domingues,Lea Mirian Barbosa da Fonseca
Licensed Content Date	Oct 1, 2011
Licensed Content Volume	80
Licensed Content Issue	1
Licensed Content Pages	8
Start Page	60
End Page	67
Type of Use	reuse in a thesis/dissertation
Portion	figures/tables/illustrations
Number of figures/tables/illustrations	1
Format	both print and electronic
Are you the author of this Elsevier article?	No
Will you be translating?	No
Title	Desarrollo de una plataforma web para la evaluación de protocolos de neuroimagen PET: SimPET
Institution name	University of Santiago de Compostela
Expected presentation date	Jun 2022
Portions	Figure 1

- Figure 27

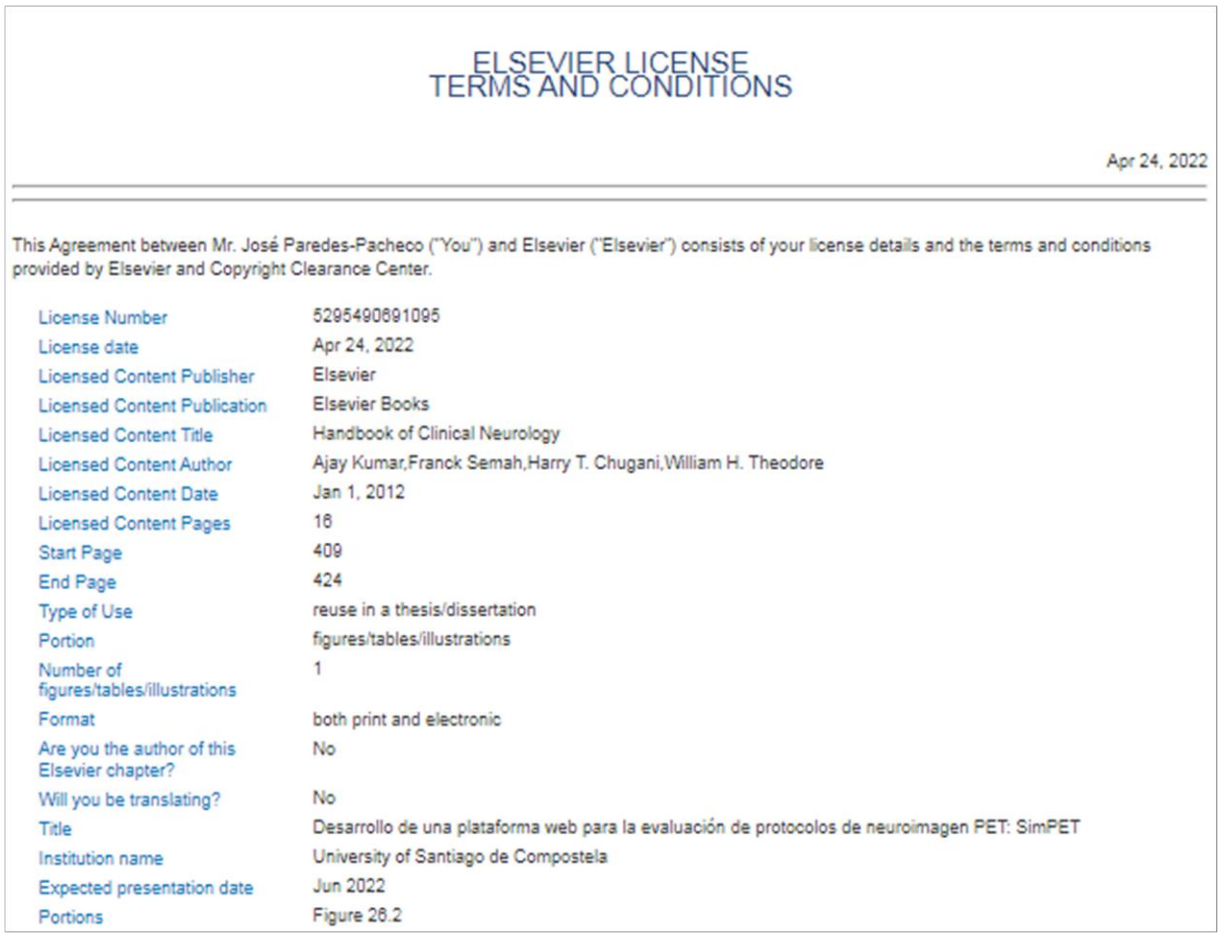

ELSEVIER LICENSE
TERMS AND CONDITIONS

Apr 24, 2022

This Agreement between Mr. José Paredes-Pacheco ("You") and Elsevier ("Elsevier") consists of your license details and the terms and conditions provided by Elsevier and Copyright Clearance Center.

License Number	5295490691095
License date	Apr 24, 2022
Licensed Content Publisher	Elsevier
Licensed Content Publication	Elsevier Books
Licensed Content Title	Handbook of Clinical Neurology
Licensed Content Author	Ajay Kumar,Franck Semah,Harry T. Chugani,William H. Theodore
Licensed Content Date	Jan 1, 2012
Licensed Content Pages	16
Start Page	409
End Page	424
Type of Use	reuse in a thesis/dissertation
Portion	figures/tables/illustrations
Number of figures/tables/illustrations	1
Format	both print and electronic
Are you the author of this Elsevier chapter?	No
Will you be translating?	No
Title	Desarrollo de una plataforma web para la evaluación de protocolos de neuroimagen PET: SimPET
Institution name	University of Santiago de Compostela
Expected presentation date	Jun 2022
Portions	Figure 26.2

- Figure 28

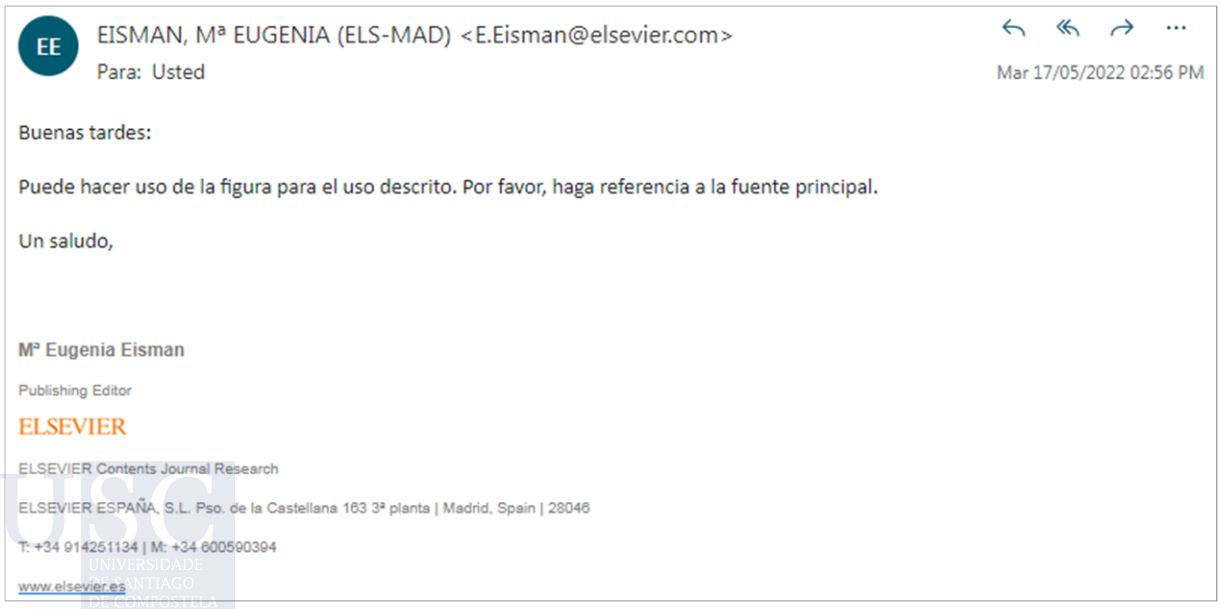

EE EISMAN, Mª EUGENIA (ELS-MAD) <E.Eisman@elsevier.com>

Para: Usted

Mar 17/05/2022 02:56 PM

Buenas tardes:

Puede hacer uso de la figura para el uso descrito. Por favor, haga referencia a la fuente principal.

Un saludo,

Mª Eugenia Eisman

Publishing Editor

ELSEVIER

ELSEVIER Contents Journal Research

ELSEVIER ESPAÑA, S.L. Pso. de la Castellana 163 3ª planta | Madrid, Spain | 28046

T: +34 914251134 | M: +34 600590394

www.elsevier.es

- Figure 29

De: Joyce Rodenhuis <joyce.rodenhuis@bsl.nl>
Enviado: jueves, 19 de mayo de 2022 12:01 p. m.
Para: j.p789@hotmail.com <j.p789@hotmail.com>; joseparedespacheco90@gmail.com <joseparedespacheco90@gmail.com>
Asunto: Reuse a figure in my thesis

Dear Jose,

Your question about the reuse of a Springer-figure came through me through our Customer Services Department.
We are unable to trace the figure.
I suggest you use the figure stating the correct source and that you have done your utmost in asking for permission from the publisher. This statement should than be incorporated in the colophon page of your thesis.

Hope this helps.
Good luck with your thesis.

With best wishes,

Joyce

Joyce Rodenhuis
Uitgever GGZ-Jeugd
(afwezig op woensdag)

Walmolen 1 | 3994 DL | Houten
Postbus 246 | 3990 GA | Houten
Tel +31 30 638 37 13 | Mobiel +31 (0) 6 479 477 42

www.bsl.nl

- Figure 30 and Figure 33

Permissions

JNM Permission Policies

Non-Commercial

JNM allows reuse of excerpted original material, such as abstracts, short text excerpts, figures, and tables, provided appropriate credit is given to the copyright holder and the material is not used for commercial purposes. Non-commercial uses include articles in peer-review journals, classroom/teaching material, and academic theses/dissertations. Full article reprints require explicit permission with exceptions as noted below. For bulk reprints, see our reprint page.

- Figure 31 and Figure 32

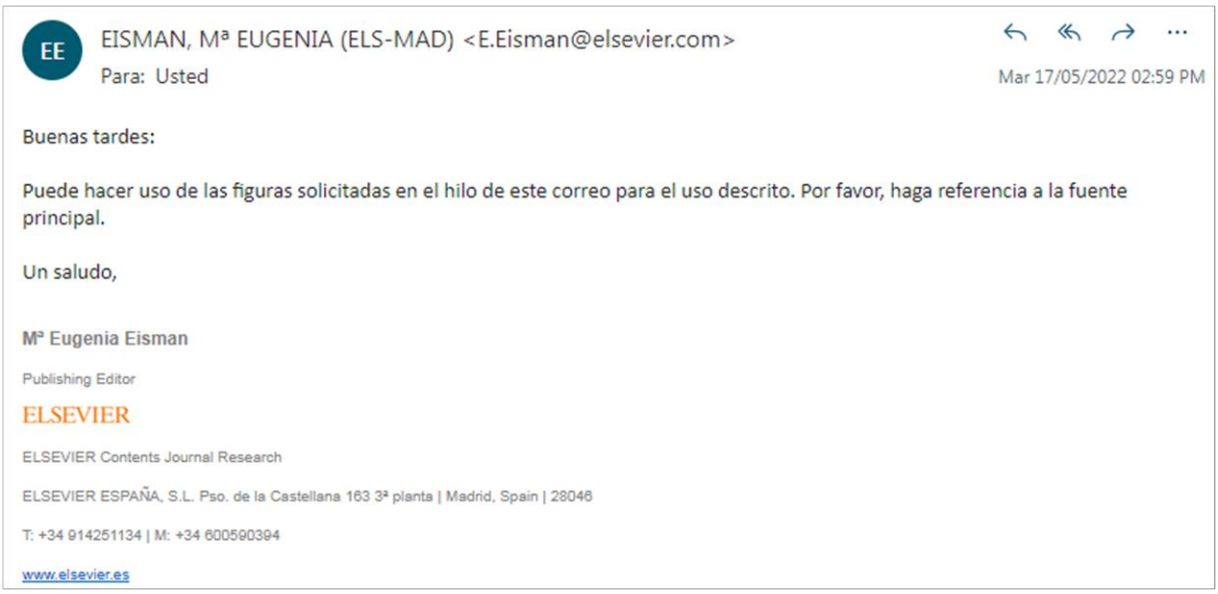

EE

EISMAN, Mª EUGENIA (ELS-MAD) <E.Eisman@elsevier.com>

Para: Usted

Mar 17/05/2022 02:59 PM

Buenas tardes:

Puede hacer uso de las figuras solicitadas en el hilo de este correo para el uso descrito. Por favor, haga referencia a la fuente principal.

Un saludo,

Mª Eugenia Eisman

Publishing Editor

ELSEVIER

ELSEVIER Contents Journal Research

ELSEVIER ESPAÑA, S.L. Pso. de la Castellana 163 3ª planta | Madrid, Spain | 28046

T: +34 914251134 | M: +34 600590394

www.elsevier.es

- Figure 34

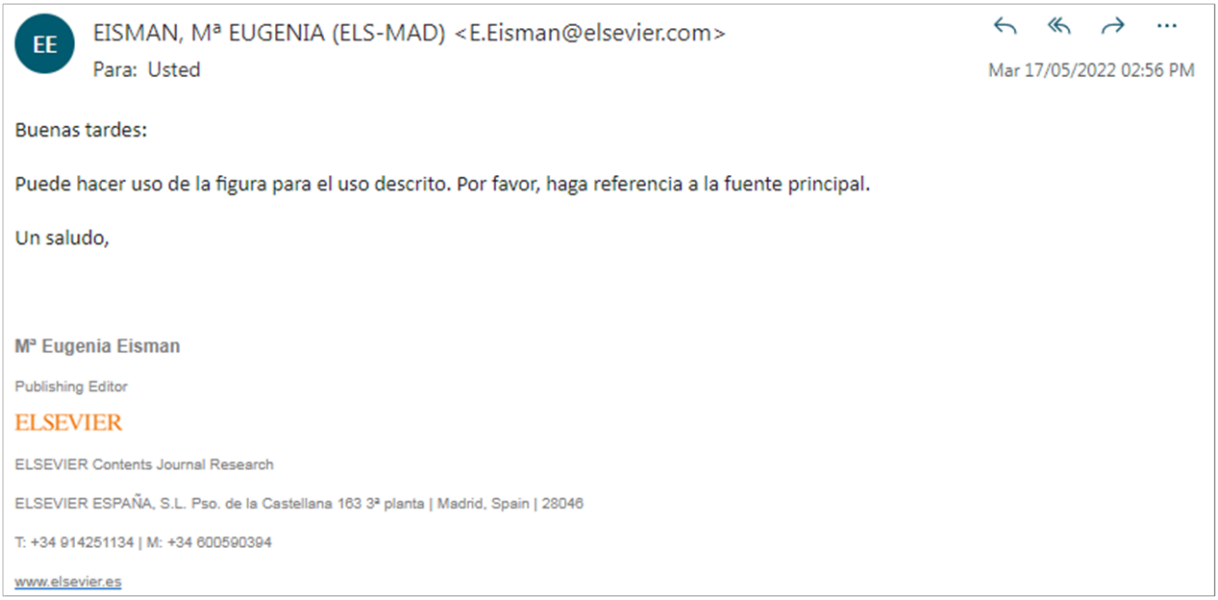

EE

EISMAN, Mª EUGENIA (ELS-MAD) <E.Eisman@elsevier.com>

Para: Usted

Mar 17/05/2022 02:56 PM

Buenas tardes:

Puede hacer uso de la figura para el uso descrito. Por favor, haga referencia a la fuente principal.

Un saludo,

Mª Eugenia Eisman

Publishing Editor

ELSEVIER

ELSEVIER Contents Journal Research

ELSEVIER ESPAÑA, S.L. Pso. de la Castellana 163 3ª planta | Madrid, Spain | 28046

T: +34 914251134 | M: +34 600590394

www.elsevier.es

- Figure 35

JOHN WILEY AND SONS LICENSE TERMS AND CONDITIONS

Apr 26, 2022

This Agreement between Mr. José Paredes-Pacheco ("You") and John Wiley and Sons ("John Wiley and Sons") consists of your license details and the terms and conditions provided by John Wiley and Sons and Copyright Clearance Center.

License Number	5296560512056
License date	Apr 26, 2022
Licensed Content Publisher	John Wiley and Sons
Licensed Content Publication	Medical Physics
Licensed Content Title	Relevance of accurate Monte Carlo modeling in nuclear medical imaging
Licensed Content Author	Habib Zaidi
Licensed Content Date	Apr 9, 1999
Licensed Content Volume	26
Licensed Content Issue	4
Licensed Content Pages	35
Type of Use	Dissertation/Thesis
Requestor type	University/Academic
Format	Print and electronic
Portion	Figure/table
Number of figures/tables	1
Will you be translating?	No
Title	Desarrollo de una plataforma web para la evaluación de protocolos de neuroimagen PET: SimPET
Institution name	University of Santiago de Compostela
Expected presentation date	Jun 2022
Portions	Figure 2

- Figure 36

IEEE Requesting permission to reuse content from an IEEE publication

PET Image Reconstruction Incorporating Deep Image Prior and a Forward Projection Model

Author: Fumio Hashimoto
Publication: IEEE Transactions on Radiation and Plasma Medical Sciences
Publisher: IEEE
Date: Dec 31, 1969

Thesis / Dissertation Reuse

The IEEE does not require individuals working on a thesis to obtain a formal reuse license, however, you may print out this statement to be used as a permission grant:

Requirements to be followed when using any portion (e.g., figure, graph, table, or textual material) of an IEEE copyrighted paper in a thesis:

1) In the case of textual material (e.g., using short quotes or referring to the work within these papers) users must give full credit to the original source (author, paper, publication) followed by the IEEE copyright line © 2011 IEEE.
2) In the case of illustrations or tabular material, we require that the copyright line © [Year of original publication] IEEE appear prominently with each reprinted figure and/or table.
3) If a substantial portion of the original paper is to be used, and if you are not the senior author, also obtain the senior author's approval.

- Figure 37

- Figure 38

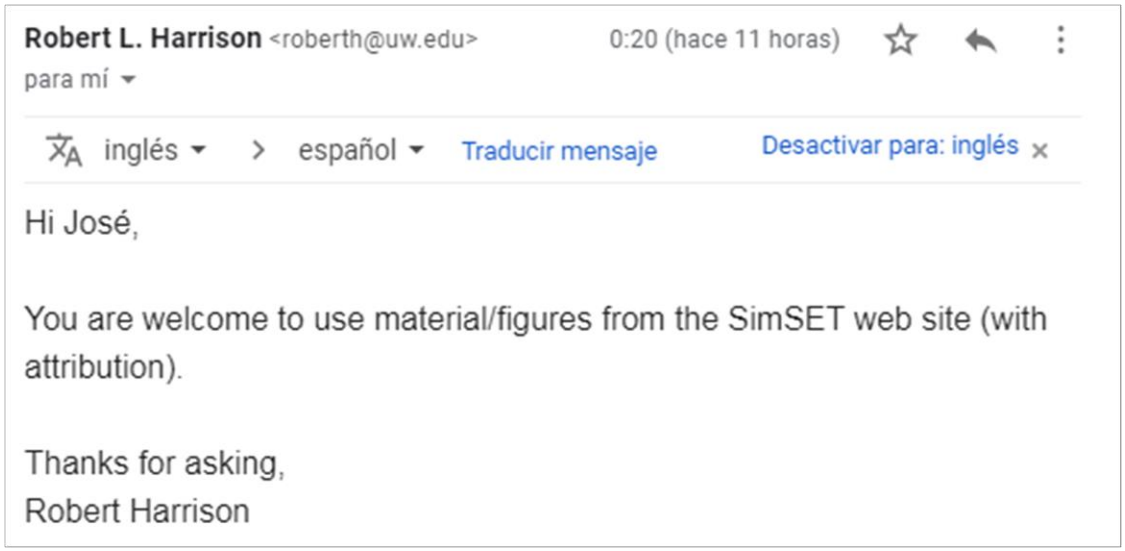

- Figure 39 and Figure 40

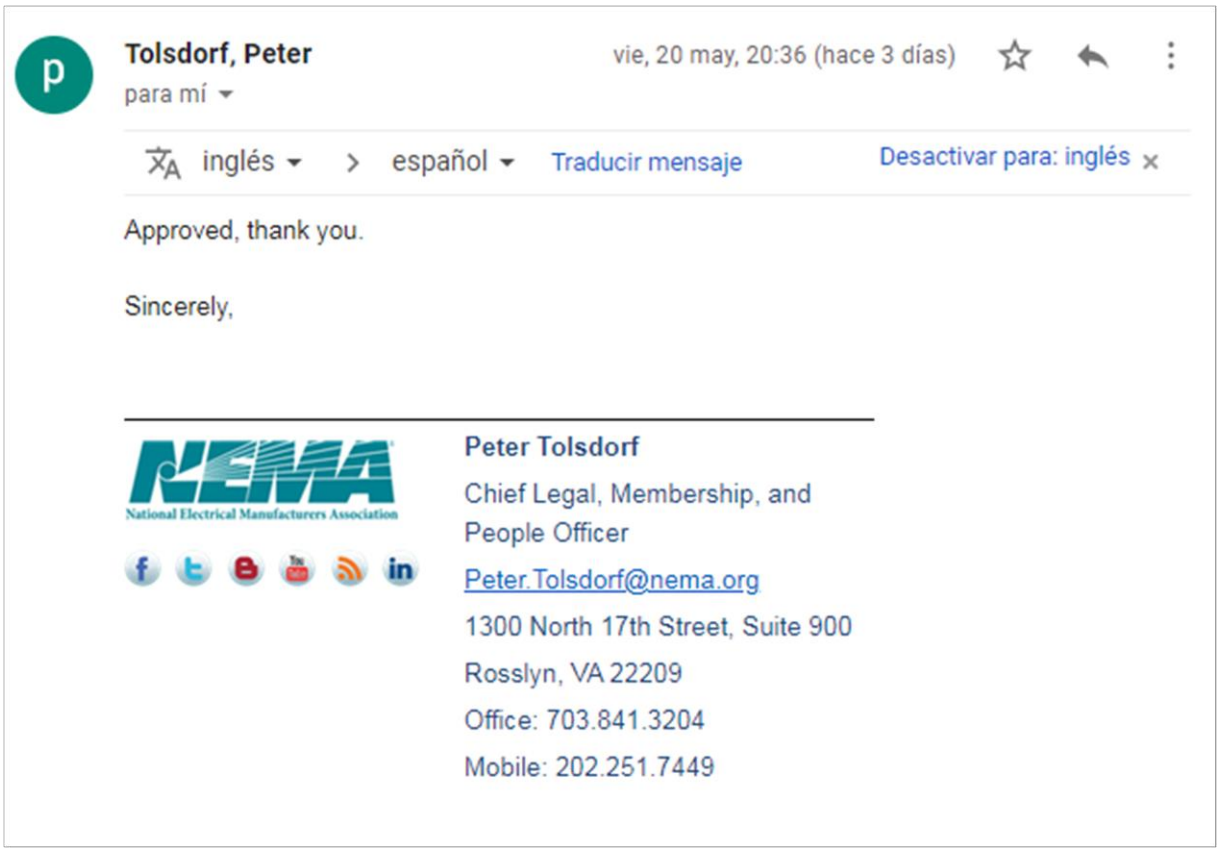

8.2 LIST OF THESIS PUBLICATIONS

8.2.1 SimPET – An online platform for the Monte Carlo simulation of realistic brain PET data. Validation for 18F-FDG scans

Medical Physics, volume 48, p. 2482-2493, 2021
DOI: https://doi.org/10.1002/mp.14838

Specific contribution in the publication:

State of the art research. Development and implementation of the SimPET platform. Generation of datasets and subsequent statistical analysis for SimPET validation. Drafting and revision of the original manuscript.

Quality índices:

The journal where part of the content of chapter 3.2 was published currently has an impact factor of 4.21 (2020), a CiteScore index of 6.1 (calculated by Scopus on May 5, 2021) and the following position: quartile 1 (Q1) in Biophysics, Q1 in Medicine (miscellaneous) and Q1 in Radiology, Nuclear Medicine and Imaging (SJR 2020 of 1,473) calculated by Scimago: https://www.scimagojr.com/journalsearch.php?q=17871&tip=sid

Journal authorization:

The Medical Physics journal, belonging to John Wiley and Sons, where part of chapter 3.2 has been published, allows the reuse of the article by the author as part of his thesis as it is an Open Access article.

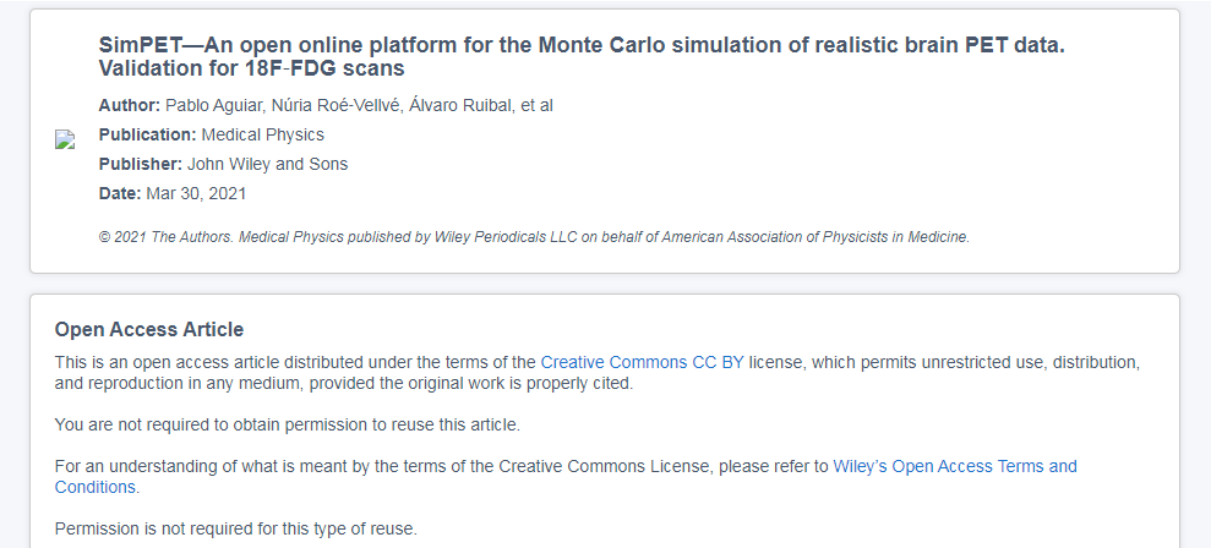

SimPET—An open online platform for the Monte Carlo simulation of realistic brain PET data. Validation for 18F-FDG scans

Author: Pablo Aguiar, Núria Roé-Vellvé, Álvaro Ruibal, et al

Publication: Medical Physics

Publisher: John Wiley and Sons

Date: Mar 30, 2021

CONFLICT OF INTEREST

9 CONFLICT OF INTEREST

The doctoral candidate declares no conflicts of interest related to his tesis.

Monte Carlo simulation of PET studies is a reference tool for the evaluation and standardization of PET protocols. However, current Monte Carlo software codes require a high degree of knowledge in physics, mathematics and programming languages, in addition to a high cost of time and computational resources. These drawbacks make their use difficult for a large part of the scientific community. In order to overcome these limitations, a free and an efficient web-based platform was designed, implemented and validated for the simulation of realistic brain PET studies, and specifically employed for the generation of a well-validated large database of brain FDG-PET studies of patients with refractory epilepsy.